Spin Transfer Torque Magnetisation Switching in MgO Based Magnetic Tunnel Junctions

A thesis submitted to the University of Dublin, Trinity College

in application for the degree of Doctor of Philosophy

by

Kaan Oguz

School of Physics

Trinity College Dublin

October 2010

Declaration

This thesis is submitted by the undersigned for examination for the degree Doctor of Philosophy at the University of Dublin. It has not been submitted as an exercise for a degree at any other University or other degree-giving institution.

This thesis, apart from the advice, assistance and joint effort mentioned in the acknowledgements and in the text, is entirely my own work.

I, the undersigned, agree that Trinity College Library may lend or copy this thesis upon request.

To my lovely wife, Deniz Gezer Oguz

Summary

Magnetic tunnel junctions (MTJ) are important magnetic elements that are used as memory and sensor devices. In this thesis, first, the fundamentals of MTJs were explored by investigating different tunnel barrier materials, then, a new physical phenomenon called spin transfer torque magnetisation switching (STS) was investigated in nanopillars with magnesium oxide based MTJs with a view to reducing the critical current density (J_c) required to switch the magnetisation. This is a technological challenge at present.

MTJs with the different tunnel barriers, namely aluminium oxide (Al_2O_3), strontium titanate ($SrTiO_3$) and magnesium oxide (MgO) were produced by sputtering, patterned by UV and e-beam lithography and characterized by x-ray diffraction, electron microscopy, transport and magnetic measurements. The basics of tunnelling and magnetoresistance were appreciated by first studying the AlO_x based MTJs. A typical tunnelling magnetoresistance (TMR) ratio of 23 % was observed at room temperature (RT) and it was found to be independent of annealing temperature. The effect of O_2 injection during AlO_x sputtering was investigated and a detrimental effect on the TMR ratio was ascribed to formation of a dead layer at the bottom CoFe / AlO_x interface owing to oxidation of bottom CoFe surface.

Dead layer formation in ultrathin ferromagnetic layers is critical for MTJ performance. Therefore, the dead layers in ultrathin $Co_{40}Fe_{40}B_{20}$ films deposited on SiO_2 and MgO buffer layers were investigated. The magnetisation of films grown on MgO and SiO_2 substrates disappeared at RT below a thickness of 0.6 nm; a dead layer due to an interdiffused non-magnetic layer of 0.5 nm was found for the films on SiO_2 substrates whereas on MgO, CoFeB films less than 1.0 nm thick were granular and behaved superparamagnetically.

The $SrTiO_3$ (STO) based MTJs with CoFeB electrodes exhibited a small TMR ratio of 2.0 % at RT. The low TMR ratio can be understood in terms of the lack of (001) crystal orientation of the STO barrier, which needed to produce a spin filtering effect. It seems that low-temperature growth of STO on a ferromagnetic

metal electrode can't produce the quality and orientation of the barrier layer required for large TMR.

The main focus of the thesis was to develop high performance and reliable magnetic tunnel junctions with MgO barriers. It was possible to realize MgO MTJs with TMR ratios exceeding 250 % at RT by optimizing the process parameters. A low resistance × area (RA) (< 50 $\Omega\mu m^2$) together with a high TMR ratio (> 120 %) was also achieved. The low RA is critical to observe spin transfer torque magnetisation reversal. Meanwhile, we developed a new technique to produce high quality MgO barrier layers for MTJs-good (001) oriented MgO was grown by e-beam evaporation in UHV conditions and MTJs with high TMR ratios (> 240 %) were produced.

Three amorphous ferromagnetic alloy systems were investigated to reduce the saturation magnetisation (M_s) with a view to reducing J_c. These systems, $Co_{40}Fe_{40-x}Cr_xB_{20}$, $Co_{40}Fe_{40-x}Ni_xB_{20}$ and $Co_{40}Ni_{40-x}Cr_xB_{20}$, were grown by co-sputtering. It was possible to reduce M_s in all three. For CoFeNiB, M_s decreases only slowly with increasing Ni content. On the other hand, M_s decays very rapidy in CoNiCrB with increasing Cr content and it becomes non-magnetic above 10 % of Cr content. Of the three systems, CoFeCrB is found to be best in terms of reducing the M_s.

STS was demonstrated in three different nano-scale MgO-based MTJ devices, namely single barrier MTJ, dual barrier MTJ and MTJ with a synthetic antiferromagnetic (SAF) free layer. The nanopillars had dimensions < 100 x 200 nm^2. J_c was reduced by a factor of four in single barrier MTJs to 5 x 10^5 A/cm^2 using the CoFeCrB free layer. The reduction in J_c is mainly due to the reduced M_s of the free layer. The effect of using dual barrier stack was shown to reduce J_c by a factor of three due to an increase in the torque efficiency. The reduction of J_c in MTJs with SAF free layer was also observed. The effect of consecutive switchings is found to be minimal on the resistance and TMR ratio of our devices.

Acknowledgements

First, I would like to thank Prof. Michael Coey who gave me the opportunity and the support to work in his lab and complete a PhD there. I still remember my interview with him over the phone in early 2006. It was a very nervous and exciting interview ☺. It is now more than 4 years and I'm finishing my thesis with him. I wouldn't be able to gain this much knowledge and experience without his support. Here, I also want to emphasize how helpful and understanding he was throughout my PhD study. I also appreciate all his efforts during my hard times to bring my wife over here.

I want to thank my love, Deniz, for her endless support and motivation during this challenging period. I regret every moment that we spent separated during the first two years of my PhD. Even though, it was difficult at those times, she always supported and encouraged me to keep going. My success would be meaningless without her. Here, I also want to thank my family who always believed in me. I am thankful for all their support throughout my education.

It is very difficult to complete a PhD without the help and motivation of lab-mates. One of the most important figures in my work is Ciaran (I was calling him Fowley at the beginning and I still don't know which one he prefers). I am really thankful to him for everything, especially dealing with my bossy attitude in the lab and in the office. Honestly, I can't ignore his continuous support to my poor English writing. He corrected so many visa letters and abstracts that I can't count. We shared so many rooms together during conferences and I am sorry for any inconvenience that I caused (snoring ☺).

I am especially thankful to everybody who contributed a lot to my work; starting with Venky for all SQUID measurements and valuable discussions, Tomohiko Niizeki for all scientific discussions and Formula 1 conversations ☺, Savas Ulucan, Henrik Szucs and Huseyin Tokuc for being nice house-mates, Huseyin Kurt for all his help for my experiments, Plamen for important scientific and experimental discussions, Karsten for informative/challenging scientific discussions, Darragh for very interesting conversations like oil-wrestling ☺, Cathy, Damaris, Peter and Fiona. I also want to thank everybody in Group D for their help and support during my study. I have to express my gratitude to two summer students, Prateek and Yongchang, that I worked with. They both worked very hard.

I have to mention the contributions from the people in CRANN and CRANN Advanced Microscopy Laboratory. I used almost all of the equipment and the facilities within CRANN. I want to express my gratitude to Colm Faulkner and Marcus Boese for preparing and analyzing my TEM samples. I know how difficult and frustrating it is.

Last but not least, I need to express my thankfulness to the people from Intel Corp. whom indirectly helped quite a bit. We discussed and solved very important issues in this thesis during fortnightly conference calls. I especially want to thank Chris Murray, Brian Doyle, Gavin D'Arcy and Matthew Shaw. I was able to realize very nice experiments with their continuous samples, support and motivation. I also benefited from their experience and equipment by visiting their labs both in Ireland and USA.

This work was supported by Science Foundation Ireland (SFI) as part of the MANSE project Grant No: SFI 05/IN/1850.

Table of Contents

List of Figures

List of Tables

Chapter 1

Introduction

1.1 Spintronics

The fundamental properties of the electron, its charge and now its spin, play a key role in the technological devices. The controlling of the charge of the electron in semiconductors yielded unexpected developments starting with the invention of the transistor back in 1947 [1]. This breakthrough formed the basis for the electronics revolution. But until recently conventional electronics ignored the spin, the other fundamental property of the electron besides its mass. Unlike conventional electronics, spin electronics (spintronics or magnetoelectronics) aims to control both the spin and the charge of the electron in order to produce novel device functionality. The spin of the electrons in a small ferromagnetic electrode can be controlled via an external magnetic field and due to this fact spintronic devices show non-volatility so long as the direction of magnetisation of the electrode remains stable. The discovery of the giant magnetoresistance (GMR) effect in 1988 rapidly accelerated research in the field. The 2007 Physics Nobel prize was shared by Albert Fert and Peter Grünberg for their discovery of the GMR effect in magnetic multilayer stacks.

In the following sections, GMR effect, tunnel magnetoresistance (TMR) and spin torque related effects will be introduced. The chapter will end with a section on the applications of magnetic tunnel junctions.

1.2. Giant magnetoresistance effect

Primarily, magnetoresistance is the change in electrical resistance of any magnetic system due to magnetic field. The first observation of magnetoresistance was the anisotropic magnetoresistance (AMR) in magnetic materials in which the resistance of the material depends on the relative angle between the current direction and the magnetisation direction. It is a small effect (~ 1 %) related to spin-orbit coupling. The giant magnetoresistance (GMR) effect is observed in a multilayer stack consisting of just two ferromagnetic (FM) electrodes separated by a conductive spacer layer; this is also referred to as spin valve structure and is illustrated in Figure 1.1. The GMR effect was first found in Fe/Cr multilayers by Baibich *et al.* [2] and Binasch *et al.* [3] in 1988. The relative angle between the magnetisations of the FM layers determines the resistance value of the overall multilayer structure. The horizontal arrows in the graph indicate the magnetisation direction of the FM layers. If the magnetisations of the two FM layers are parallel, the spin valve shows low resistance; alternatively the resistance is higher by ~ 10 % if the magnetisations are aligned in the anti-parallel orientation. There are two types of spin valves; current in plane (CIP) spin valve and current perpendicular to plane (CPP) spin valve as shown in Figure 1.1. CIP GMR sensors were widely used as hard disk read heads in computer industry until recently. In addition, GMR sensors where the pinned and

free layers have their magnetisations perpendicular are commonly used as magnetic sensors in the automotive industry [4] and biological research [5].

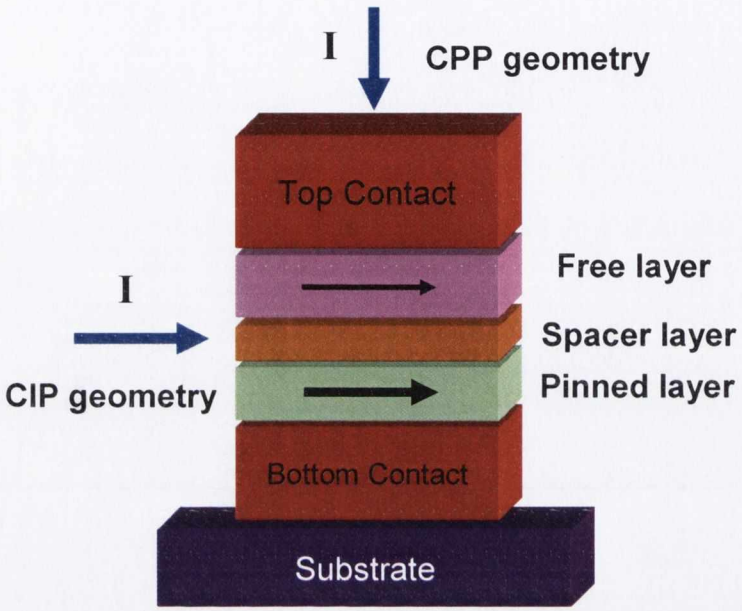

Figure 1. 1. Spin valve structure showing CIP and CPP geometries (blue arrows). Black arrows indicate the magnetisation directions of the two ferromagnetic layers.

The GMR effect is observable by either having two FM electrodes with different coercivities (soft and hard ferromagnets) or else one FM is exchange biased by an adjacent antiferromagnetic layer (pinning) which causes exchange anisotropy and shifts the hysteresis loop of the ferromagnet [6-7]. The resistance change

$$GMR = \frac{R_{ap} - R_p}{R_p} \times 100$$

is called the GMR ratio. The effect was found to be around 10 % at room temperature and increases to more than 50 % at low temperatures in the early experiments as shown in Figure 1.2. These values were much higher (one order of

magnitude) than the resistance changes due to the anisotropic magnetoresistance [8-9] which originates from the spin-orbit interaction [10] and was used in early thin film hard disk read heads. Therefore this new effect was called the *giant* magnetoresistance effect. The origin of the effect relies on the spin dependent scattering of electrons primarily, at the interfaces and will not be discussed in detail here, for the physics and theory of GMR effect, the reader should refer to [11-12].

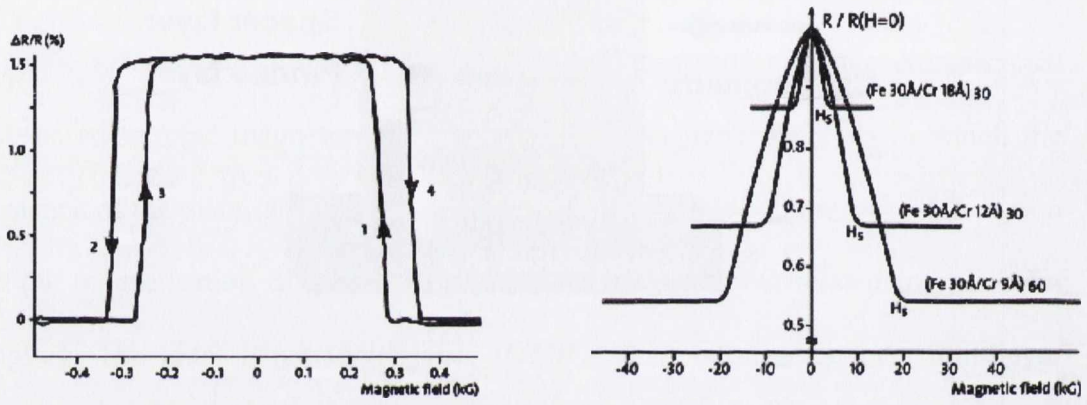

Figure 1. 2. (a) Magnetoresistance measurements (room temperature) for the trilayer system Fe / Cr / Fe [2]. (b) Magnetoresistance measurements (4.2 K) for the multilayer system $(Fe / Cr)_n$ [3] (10 kG = 1 T).

1.3. Tunnel magnetoresistance and magnetic tunnel junctions

Soon after the discovery of high GMR effects at room temperature, researchers from Japan and USA were able to realize another interesting phenomenon related to magnetoresistance at room temperature (RT). This effect was observed in tunnel junctions and is called *tunnelling* magnetoresistance (TMR). Like a GMR spin valve, a magnetic tunnel junction (MTJ) consists of two FM layers

separated by a spacer layer but this time the spacer is an insulator (Figure 1.3). The conduction in this case is due to the quantum mechanical tunnelling. The resistance changes also depend on the relative angle between the magnetisations of two FM layers but the effect is much higher, ~ 100 %, in MTJs. This is mainly due to the high efficiency of the tunnelling process in which the electron does not flip its spin orientation during tunnelling. A typical magnetoresistance curve of an MTJ is shown in Figure 1.3. Sharp change of resistance around zero field is due to the switching of free layer. The parallel (P) and antiparallel (AP) states are shown in the figure with red arrows.

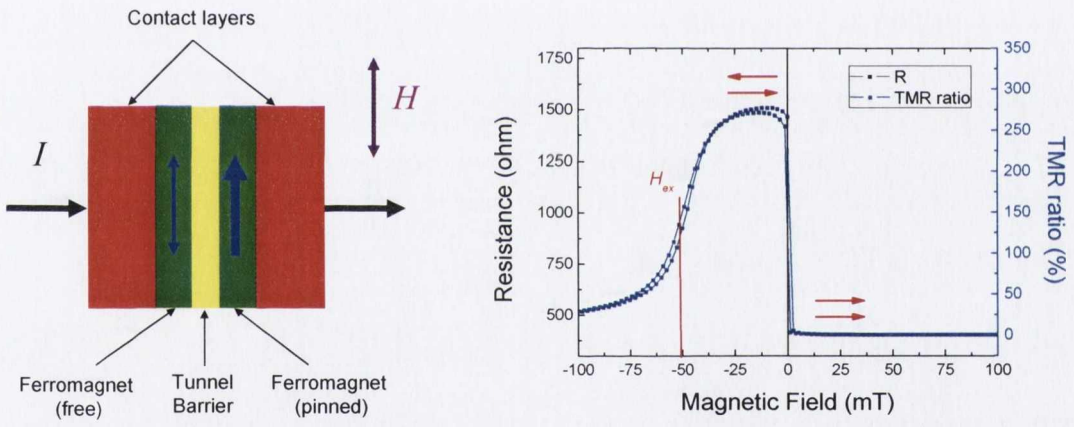

Figure 1. 3. Schematic illustration of a basic magnetic tunnel junction composed of FM/I/FM trilayer and magnetoresistance curves of an MgO MTJ with an exchange biased pinned layer. TMR ratio is > 250 % and exchange bias field (H_{ex}) is > 50 mT.

The change in the resistance is called TMR ratio and calculated by the formula;

$$TMR \equiv \left(\frac{R_{ap} - R_p}{R_p} \right) \times 100 \qquad (1.1)$$

In this expression, R_{ap} and R_p represent the anti-parallel alignment resistance and parallel alignment resistance values of the multilayer, respectively. For most of the systems, TMR ratio is positive but it can also be negative depending on the combination of the electrode materials.

In MTJs, the transport of electrons is via tunnelling which is a purely quantum mechanical phenomenon. The basics of the effect will be given here briefly but it has been discussed thoroughly in [13-14]. Figure 1.4a shows the decay of the electron's wave-function while it is tunnelling through a potential barrier. Actually, most of the wave is reflected back from the barrier because electrons do not have sufficient energy to pass over the potential barrier. But, the probability of the electrons tunnelling through the potential barrier is not *zero* [15]. The amplitude of the wave-function is attenuated exponentially in the barrier.

Tunnelling current in metal/insulator/metal structures (energy band diagram is shown in Figure 1.4b) is given by

$$I_{l\to r}(V) = \int_{-\infty}^{+\infty} D_l(E)\cdot D_r(E+eV)\cdot |M|^2 \cdot f(E)\cdot [1-f(E+eV)]dE \qquad (1.2)$$

This expression describes the tunnelling current from the left electrode to the right electrode. In the equation, $D_l(E)$ represents the density of states at a given energy in the left electrode and $D_r(E+eV)$ is the density of states at the same energy in the right electrode when the bias voltage is V. $|M|^2$ is the square of the matrix element which is the tunnelling probability. $f(E)$ is the probability that the states in the left electrode are occupied and $[1-f(E+eV)]$ is the probability that the states in the

right electrode are empty where $f(E)$ is the Fermi-Dirac distribution function. The total current is given by $I_{l\to r} - I_{r\to l}$.

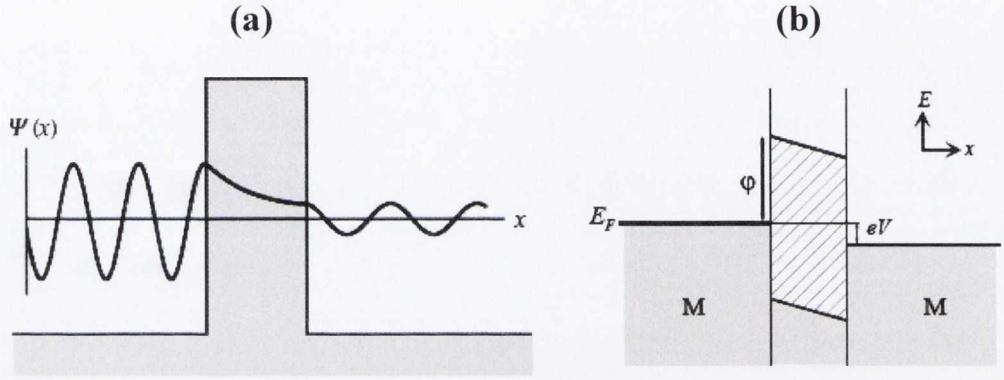

Figure 1. 4. (a) The decay of electron's wave-function within the tunnelling barrier and (b) the band diagram of a metal/insulator/metal structure.

The integrand of equation 1.2 depends on the barrier shape. The most simple barrier shape is a rectangular barrier, which assumes that the work functions of both electrodes into the barrier are the same. It deforms to trapezoidal shape when the bias is applied, but an asymmetry is found even in the experiments using same materials on either side of the barrier. This is related to differences in the quality of the two interfaces due to the fabrication. Therefore, it is very common to assume a trapezoidal barrier.

Simmons proposed a generalized formula for the electrical tunnelling between similar electrodes separated by a thin insulating film by solving the current equation [16]. He used Wentzel–Kramers–Brillouin (WKB) approximation to obtain

the matrix element $|M|^2$ for an arbitrary barrier of average height above the common Fermi level. His well-known result for a trapezoidal barrier is

$$J(V) = \frac{J_0}{d^2}\left(\overline{\varphi} - \frac{eV}{2}\right)\exp\left[-Ad\sqrt{\overline{\varphi} - \frac{eV}{2}}\right] - \frac{J_0}{d^2}\left(\overline{\varphi} + \frac{eV}{2}\right)\exp\left[-Ad\sqrt{\overline{\varphi} + \frac{eV}{2}}\right] \quad (1.3)$$

where $J(V)$ is the tunnel current density, $A = 4\pi\sqrt{2m_e^*}/h$ and $J_0 = e/2\pi h$ are constants, m_e^* is the effective mass of the electron, d is the barrier thickness, $\overline{\varphi}$ is the average barrier height above the Fermi level, and eV is the applied bias to the structure. Exponential dependence on the barrier thickness and the square root of barrier height can easily be observed from the equation. One important thing to mention about equation 1.3 is that the electrodes are assumed to be identical and the symmetry of electrons is not taken into account.

Brinkman *et al.* also calculated the tunnel current for a trapezoidal barrier numerically and found the conductance by direct differentiation of the calculated current with respect to voltage [17]. Their calculated conductance is

$$\frac{G(V)}{G(0)} = 1 - \left(\frac{A_0\Delta\varphi}{16\overline{\varphi}^{3/2}}\right)eV + \left(\frac{9}{128}\frac{A_0^2}{\overline{\varphi}}\right)(eV)^2 \quad (1.4)$$

where $G(0) = (3.16\times10^{10}\overline{\varphi}^{1/2}/d)\exp(-1.025d\overline{\varphi}^{1/2})$, $\overline{\varphi}$ is mean barrier height, $\Delta\varphi = \varphi_2 - \varphi_1$ (φ_1 and φ_2 are the barrier heights of electrodes), and $A_0 = 4(2m)^{1/2}d/3\hbar$ where d is the barrier thickness in Å. Equation 1.4 is accurate to roughly 10 % when the barrier thickness is greater than 10 Å and when $\Delta\varphi/\overline{\varphi}$ is less than 1 [17]. This expression can be used to fit the conductance vs. voltage graph to obtain average barrier height, $\Delta\varphi$ and the barrier thickness.

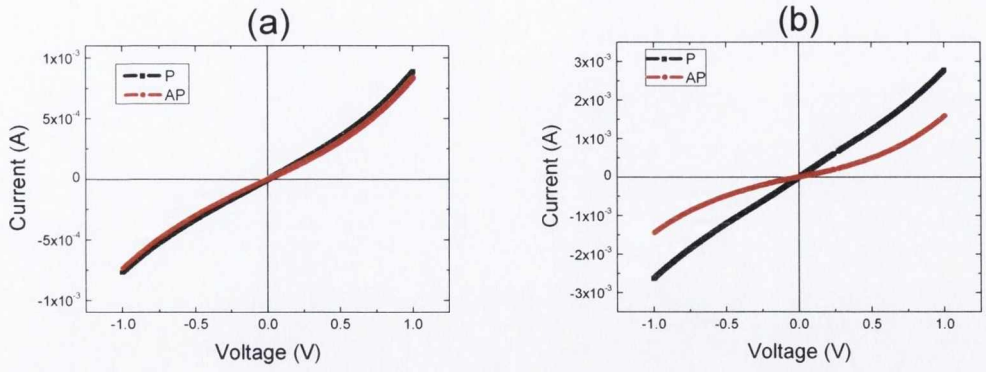

Figure 1. 5. I-V plots of MTJs with (a) amorphous AlO_x barrier (TMR ratio: 22 %) and (b) crystalline MgO barrier (TMR ratio: 250 %) for P and AP states.

Typical I-V curves of the MTJs with amorphous AlO_x and crystalline MgO barriers are shown in Figure 1.5a and Figure 1.5b, respectively. The nonlinear characteristic of the current with respect to bias voltage is clearly observed. For amorphous AlO_x barrier, the shape of the curve is identical for parallel (P) and antiparallel states (AP). However, for the crystalline MgO barrier, P state has an almost linear response due to coherent tunnelling which is a result of combining bcc CoFe (001) / MgO (001) / CoFe (001) structure which will be discussed later in the text.

The origin of TMR is from difference in the electronic band structure for spin up and spin down electrons. Since electrons preserve their spin orientation during tunnelling, they can only tunnel into the sub-band of the same spin orientation as illustrated in Figure 1.6. Thus, the tunnelling conductance is proportional to the product of the Fermi level density of states values of the two electrodes for the same spin orientation. A change from parallel to antiparallel configuration of two ferromagnetic layers will result in an exchange between the two spin sub-bands.

Jullière proposed a simple phenomenogical model in which the TMR effect is due to this spin-dependent electron tunnelling [18].

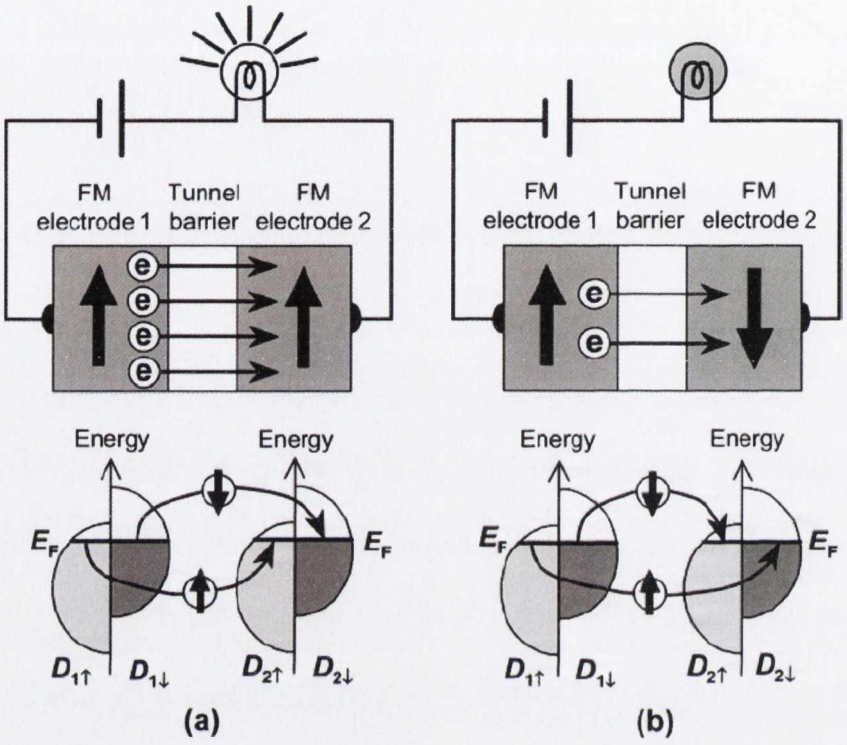

Figure 1. 6. Schematic illustration of the TMR effect in an MTJ. (*a*) Magnetisations in the two electrodes are aligned parallel (P state). (*b*) Magnetisations are aligned antiparallel (AP state) [19].

According to his model TMR ratio can be written as:

$$TMR \equiv \left(\frac{2P_1P_2}{1 - P_1P_2} \right) \times 100 \tag{1.5}$$

with $P_{1,2}$ denotes the spin polarizations of the ferromagnetic electrodes and it is given by

$$P_{1,2} \equiv \left(\frac{D_{1,2\uparrow} - D_{1,2\downarrow}}{D_{1,2\uparrow} + D_{1,2\downarrow}} \right) \tag{1.6}$$

where $D_{1,2\uparrow}$ and $D_{1,2\downarrow}$ are the densities of states (DOS) of the electrodes at the Fermi energy (E_F) for the majority-spin and minority-spin bands, respectively as shown in Figure 1.6. In Jullière's model spin polarization is an intrinsic property of an electrode material. Jullière's model assumes that tunnelling probabilities are equal for all the Bloch states in the electrodes. This assumption corresponds to a completely incoherent tunnelling. When an electrode material is normal metal, $P = 0$ and if the DOS of the electrode material is fully spin-polarized at E_F, $|P| = 1$ [19]. However, actual tunnelling spin polarization is found to be quite different than the ones obtained using equation 1.6 after the ground-breaking work of Tedrow and Meservey [20]. The quasi-particle states in thin superconducting Al films are split in a high magnetic field by the interaction of the field with the quasi-particle spins. This splitting allows the selection of tunnelling electrons of a particular spin direction. This method has been proven to be very effective in terms of determining the tunnelling spin polarization of ferromagnets. In their work, they were able to measure the tunnelling spin polarization of nickel films by measuring conductance of Al-Al_2O_3-Ni junctions in high magnetic fields at 0.4 K, where Al is superconducting [20]. They found a positive spin polarization of ~ 8 % for Ni. In later experiments, the values obtained for the spin polarization of Fe, Co, Ni and Gd were + 44, + 34, + 11 and + 4.3 %, respectively [21]. However, the polarization is found to be positive for all of 3d ferromagnetic metals, a result which had not been predicted. Stearns explained the problem with a very simple quantitative model in which the nearly

free-electron-like s-d hybridized bands are assumed to provide essentially all of the tunnelling current. The expression for spin polarization in her work is given by

$$P = \frac{k_F^{\uparrow} - k_F^{\downarrow}}{k_F^{\uparrow} + k_F^{\downarrow}}$$

where $k_F^{\uparrow}$ and $k_F^{\downarrow}$ are the Fermi wave vectors for spin up and spin down, respectively. The polarizations calculated from this equation agreed well with the experimentally measured polarizations [22]

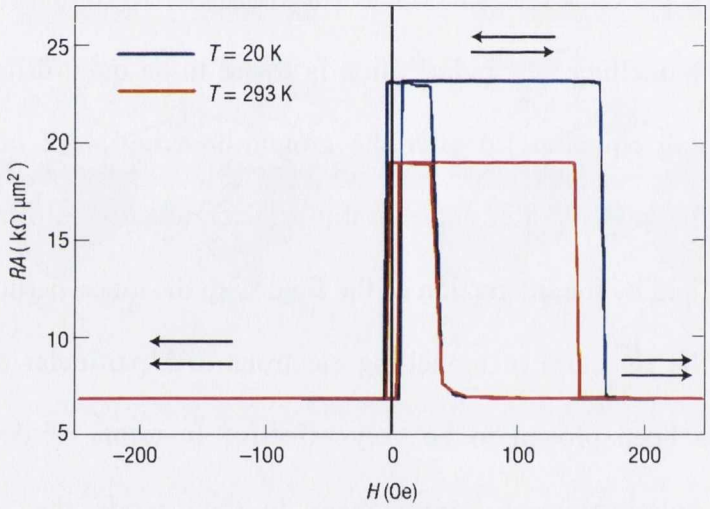

Figure 1. 7. Magnetoresistance curves of Fe (001) / MgO (001) / Fe (001) junctions (measured at a bias voltage of 10 mV) at T = 293 K and 20 K (MgO thickness t_{MgO} = 2.3 nm). Arrows indicate magnetisation configurations of the top and bottom Fe electrodes. The TMR ratio is 180 % at 293 K and 247 % at 20 K [23].

Jullière's model with the spin polarizations measured experimentally ($0 < P < 0.6$) yields a maximum MR ratio of about 100 % at low temperatures. A TMR ratio of about 70 % at RT is therefore close to the Jullière limit for the 3d-

ferromagnetic-alloy electrodes if a reduction in P due to thermal spin fluctuations at finite temperatures is taken into account. One way to obtain a MR ratio significantly higher than 70 % at RT is to use as electrodes special kinds of ferromagnetic materials called *half metals*, which have a full spin polarization ($|P| = 1$) and are therefore theoretically expected to give MTJs huge TMR ratios (up to infinity, according to Julliere's model). Some candidate half metals are CrO_2, Heusler alloys such as Co_2FeAl and Co_2MnSi, Fe_3O_4 and manganese perovskite oxides such as $La_{1-x}Sr_xMnO_3$. Very high MR ratios, above several hundred percent, have been obtained at low temperatures in $La_{1-x}Sr_xMnO_3$ / $SrTiO_3$ / $La_{1-x}Sr_xMnO_3$ MTJs [24] and Co_2MnSi / AlO_x / Co_2MnSi MTJs [25]. Recently, very high TMR ratios (> 300 %) have been observed at RT for half metal electrodes using MgO tunnel barrier [26-27].

The early experiments by Jullière on spin dependent tunnelling yielded a change of nearly 14 % at 4.2 K in the tunnel conductance at zero bias in Co/Ge-O/Fe junctions [18]. Later studies using barriers like NiO and Al_2O_3 demonstrated definite results for FM/I/FM tunnelling [28-31]. However, in these experiments, the change in the tunnel resistance was very small. In fact, it was not more than 1 % at RT. In 1995, Moodera *et al.* [32] and Miyazaki and Tezuka [33] both discovered high TMR ratio at room temperature in MTJs using amorphous aluminium oxide (AlO_x) tunnel barriers. Moodera's group used CoFe / AlO_x / Co junctions in their experiment and they achieved change in the resistance up to 11 % [32, 34]. Miyazaki and Tezuka investigated Fe / AlO_x / Fe structure and they found almost 20 % TMR ratio at RT [35]. The discovery of large TMR at room temperature accelerated the study of spin-dependent transport in magnetic thin films since then. In the last decade, the main

barrier material used was amorphous AlO_x due to its ease to form uniform and high quality tunnel barriers but the TMR values couldn't exceed 80 % at room temperature which limits practical applications [36-37].

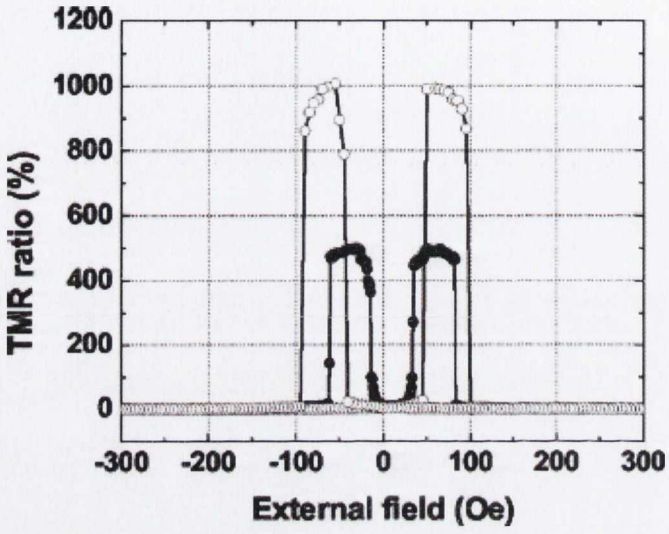

Figure 1. 8. TMR loops of an MTJ having 4 and 4.3 nm $(Co_{25}Fe_{75})_{80}B_{20}$ electrodes and a 2.1-nm-thick MgO annealed at 475 °C measured at RT (black circles) and 5 K (open circles) [38].

In 2004, giant tunnelling magnetoresistance values have been observed by implementing crystalline magnesium oxide (MgO) as a barrier layer in MTJs [23, 39]. Yuasa *et al.* fabricated epitaxial Fe (001) / MgO (001) / Fe (001) MTJs by molecular beam epitaxy. The TMR ratio of their junctions was 180 % at RT and 247 % at 20 K as shown in Figure 1.7 [23]. Independently, Parkin *et al.* also reported high TMR ratios using a combination of CoFe and Fe electrodes with highly crystalline MgO tunnel barrier and obtained TMR ratios exceeding 200 % at RT [39]. Recently, MTJs using MgO barriers and CoFeB electrodes with TMR ratios above 500 % at RT were reported [38, 40-41]. Figure 1.8 illustrates

magnetoresistance curves of a pseudo-spin valve type MgO based MTJ showing 500 % and 1010 % TMR ratios at RT and at 5 K, respectively [38].

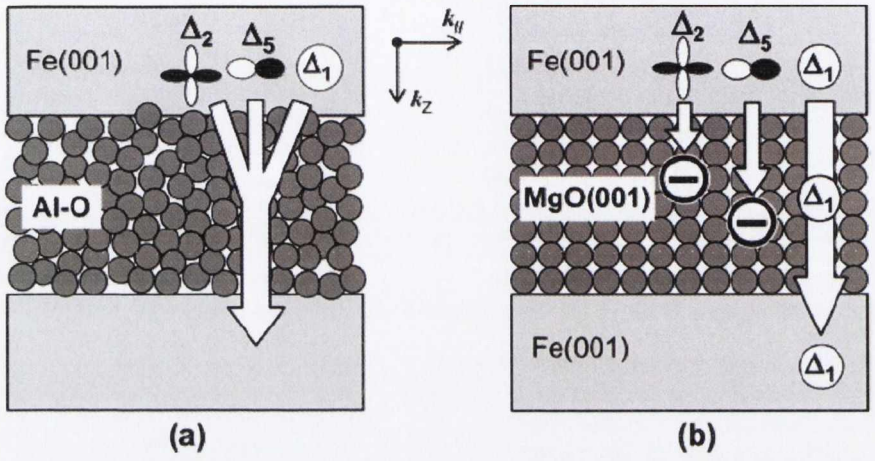

Figure 1. 9. Schematic illustrations of electron tunnelling through (*a*) an amorphous Al–O barrier and (*b*) a crystalline MgO(001) barrier [19].

1.3.1. Theory of coherent tunnelling through MgO (001) barrier

The enhancement of the TMR effect relies on the fact that coherent tunnelling occurs in MTJs with crystalline MgO (001) barriers. The possibility of growing (001) MgO on an amorphous CoFeB electrode has made these MTJs possible. The post annealing of these MTJs above 300 ^{o}C results in the crystallization of CoFeB in a (001) orientation, hence the very high TMR values were achieved. This effect was independently predicted by Butler *et al.* [42] and Mathon and Umerski [43] for a fully epitaxial Fe (001) / MgO (001) / Fe (001) MTJ. The large TMR ratio is due to a selection rule prohibiting the transition of the minority band Δ_5 wave function at transverse momentum $k_{//} = 0$ to the most slowly decaying Δ_1 wave function within

the MgO barrier. Subsequently Zhang and Butler further predicted even greater ratios in such junctions using Co or ordered CoFe electrodes instead of Fe [44].

Coherent tunnelling transport in epitaxial Fe (001) / MgO (001) / Fe (001) MTJ is illustrated schematically in Figure 1.9b. In the case of ideal coherent tunnelling, Fe Δ_1 states are theoretically expected to dominantly tunnel through the MgO (001) barrier by the following mechanism [42-43]. For the $k_{//} = 0$ direction ([001] direction in this case), in which the tunnelling probability is the highest, there are three kinds of evanescent states (tunnelling states) in the band gap of MgO (001): Δ_1, Δ_5 and $\Delta_{2'}$. It should be noted here that although conventional theories often assume tunnelling states to be plane waves, they actually have specific orbital symmetries. When the symmetries of tunnelling wave functions are conserved, Fe Δ_1 Bloch states couple with MgO Δ_1 evanescent states. Figure 1.10 shows the partial DOS (obtained by first-principle calculations) for the decaying evanescent states in a MgO barrier layer in the case of parallel magnetic alignment [42]. Of these states, the Δ_1 evanescent states have the slowest decay (i.e. the longest decay length). The dominant tunnelling channel for the parallel magnetic state is Fe $\Delta_1 \leftrightarrow$ MgO $\Delta_1 \leftrightarrow$ Fe Δ_1. Band dispersion of bcc Fe for the [001] ($k_{//} = 0$) direction is shown in Figure 1.11a. The *net* spin polarization of Fe is small because both majority-spin and minority-spin bands have many states at E_F, but the Fe Δ_1 band is fully spin-polarized at E_F ($P = 1$). A very large TMR effect in the epitaxial Fe (001) / MgO (001) / Fe (001) MTJ is therefore expected when Δ_1 electrons dominates tunnelling. It should also be noted that a small but finite tunnelling current flows even for antiparallel magnetic states.

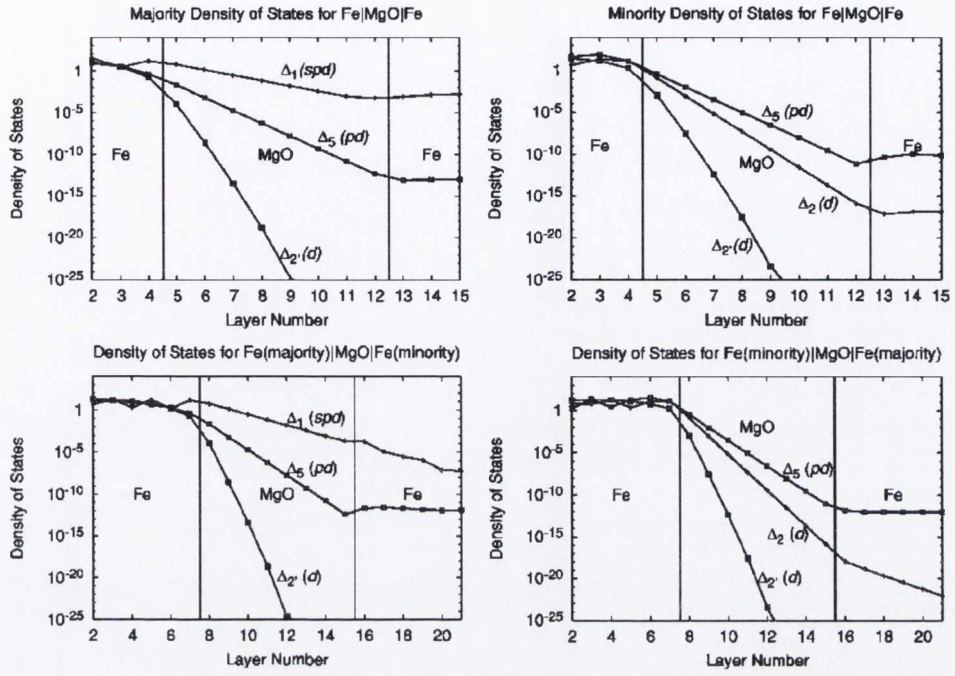

Figure 1. 10. Tunnelling DOS for $k_{//} = 0$ for Fe (100) / 8 MgO/ Fe (100). The four panels show the tunnelling DOS for majority (upper left) minority (upper right), and antiparallel alignment of the moments in the two electrodes (lower panels) [42].

For the majority-spin conductance in the parallel magnetic state (P state), tunnelling takes place dominantly at $k_{//} = 0$ because of the coherent tunnelling of majority-spin Δ_1 states. For the minority-spin conductance in the P state and the conductance in antiparallel magnetic state (AP state), spikes of tunnelling probability appear at finite $k_{//}$ points called *hot spots*. This *hot-spot tunnelling* is resonant tunnelling between interface resonant states [42-43]. Although a finite tunnelling current flows in the AP state, the tunnelling conductance in the P state is much larger than that in the AP state, making the MR ratio very high.

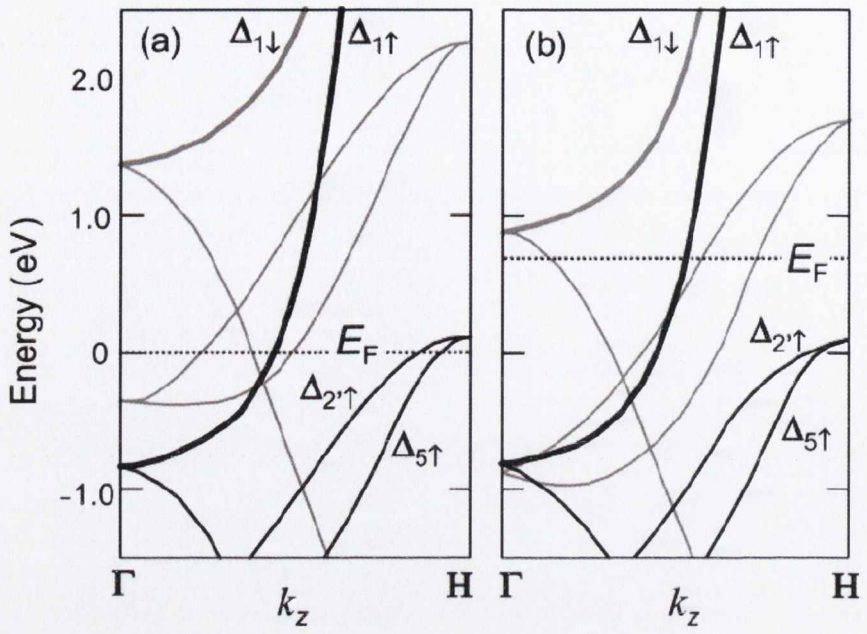

Figure 1. 11. (*a*) Band dispersion of bcc Fe in the [001] (Γ–H) direction [19]. (*b*) Band dispersion of bcc Co in the [001] (Γ-H) direction [45].

It should be noted that the Δ_1 Bloch states are highly spin-polarized not only in bcc Fe (001) but also in many other bcc ferromagnetic metals and alloys based on Fe and Co (e.g. bcc CoFe and some of the Heusler alloys). As an example, band dispersion of bcc Co (001) (a metastable structure) is shown in Figure 1.11b. The Δ_1 states in bcc Co, like those in bcc Fe, are fully spin-polarized at E_F. According to first-principle calculations, the TMR of a Co (001) / MgO (001) / Co (001) MTJ is even larger than that of an Fe (001) / MgO (001) / Fe (001) MTJ [44]. A very large TMR should be characteristic of MTJs with 3d-ferromagnetic alloy electrodes with bcc (001) structure based on Fe and Co.

Note also that very large TMR is theoretically expected not only for the MgO (001) barrier but also for other crystalline tunnel barriers such as ZnSe (001) [46] and

$SrTiO_3$ (001) [47]. However, large TMR has never been observed in MTJs with crystalline ZnSe (001) or $SrTiO_3$ (001) barriers because of experimental difficulties in fabricating high-quality MTJs without pin-holes and interdiffusion at the interfaces [19, 48-49].

The fabrication process of MTJ structures is not straightforward. Since the thicknesses of the films in these structures are about a few nanometers, their deposition process requires extreme care. Especially, growing an ultra thin, pinhole-free tunnel barrier with correct crystal texture is extremely difficult. Primarily, the bottom electrode should be very flat that is the surface RMS roughness should be less than 0.5 nm. In this case, the substrate choice is very important. Then on top of it, ultra thin (< 5 nm) barrier should be deposited with very high uniformity. The barrier layer should also be extremely flat to have good quality top electrode. The crystallinity of the electrodes is important in terms of their magnetic and electrical properties.

The interfaces between the barrier and the electrodes are critically important for the magnetic tunnel junctions. Magnetically dead layers should not be present at the interfaces. If so, these dead layers will reduce the device performance by decreasing the TMR value. Spin-polarized electrons should not lose their spin information while passing through interfaces. Therefore, choosing appropriate electrode and barrier is the key issue for the production of MTJs with high TMR ratios.

Successful demonstration of high TMR values in MTJs resulted in couple of industrial applications such as magnetic random access memory (MRAM) and MTJ based read heads in hard disks. Further applications like spin transfer torque RAM

(STT-RAM), spin torque diode, and spin torque oscillators are still under research and development. These will be discussed in the last section of this chapter.

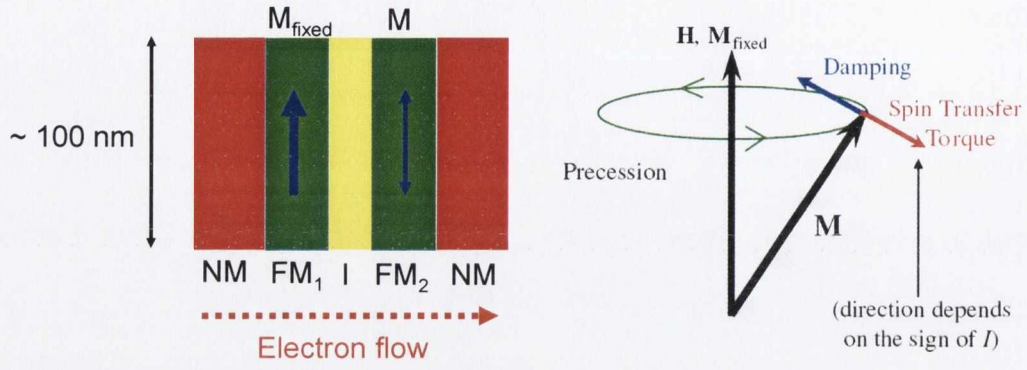

Figure 1. 12. Schematic indication of the magnetisation directions and the current flow through a nano-MTJ (left). Directions of damping and spin-torque vectors acting on the free layer magnetisation (right).

1.4. Spin transfer torque

Following the prediction of spin transfer torque (STT) due to spin polarized current in magnetic multilayers by Slonczewski [50] and Berger in 1996 [51], there has been considerable interest on the spin torque related effects in both spin valves and magnetic tunnel junctions due to their potential practical application. When a current flows through a ferromagnet it becomes spin polarized and hence carries angular momentum. The current remains polarized while passing through a spacer layer (normal metal for spin valves and insulator for MTJs) so that the current interacts with the magnetisation in the subsequent magnetic layers. The so-called spin current exerts a *spin-transfer torque* on the magnetisations in the structure due

to interaction between the conduction (or tunnelling) electron spin and the local magnetisation. Figure 1.12 illustrates the schematic of a nano-MTJ where electrons flow from the fixed layer to the free layer. They acquire spin polarization in the fixed layer and transfer their angular momentum to the free layer magnetisation via spin transfer torque.

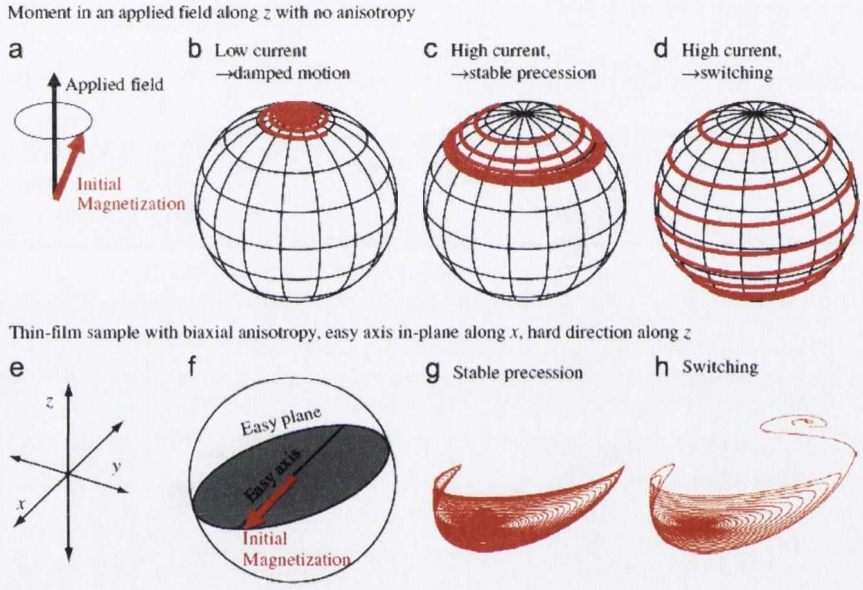

Figure 1. 13. Trajectories of spin-torque-driven dynamics for the magnetisation vector M. (a) Initial magnetic configuration for panels (b–d), with the free-layer magnetisation misaligned from z and magnetic anisotropy is zero. (b) Below a critical current, M spirals back toward z direction due to damping. (c) For currents larger than the critical value, M spirals away from z. The ultimate result can be either stable steady-state precession at large precession angle (c) or magnetic reversal (d). (e, f) Sample with a strong easy-plane anisotropy. For this geometry (g) shows steady-state precession and (h) shows magnetic reversal [52].

The direction of magnetisations and torque vectors are also shown in the same figure. Direction of the spin transfer torque depends on the sign of the current.

Depending on the strength of the current, this torque can lead to a stable precession by cancelling the damping torque (Figure 1.13c and Figure 1.13g) or a total magnetic reversal of the free layer magnetisation by overcoming the damping (Figure 1.13d and Figure 1.13h). It is important that the magnetisation vectors are not collinear otherwise the torque will be zero. This condition is generally satisfied because thermal fluctuations easily bring the magnetisations out of collinear geometry.

More interestingly, the temperature dependence of the magnetisation switching shows an intriguing relation between thermally activated magnetisation reversal and spin torque assisted magnetisation reversal in a long current pulse regime [53-57]. In the standard thermal activation process, the magnetisation reversal is determined by the classical Boltzmann factor exp $(-E_b/k_BT)$, where E_b is the energy barrier and T is the temperature. In the presence of the spin torque, it is difficult to define the energy barrier since the spin torque is a non-conservative force and there is no energy associated with the spin torque.

However, when the current density is smaller than the critical current density J_{c0} and the magnetic field is smaller than the coercive field, the Néel–Brown's formula $\tau = f_0^{-1} \exp(E_b / k_b T_{eff})$ (f_0 is the attempt frequency ~ 1 GHz) is still satisfied by introducing an effective temperature $T_{eff} = T(1 - J/J_{c0})^{-1}$ [58-59], though the above correction to the temperature breaks down at large currents since it is conceptually meaningless to have a negative effective temperature [60]. Furthermore, when $J > J_{c0}$ the precessional state is generated and the precessional state is neither at a local energy minimum nor a maximum. The thermal transition occurs between a static state and a precessional state [61].

1.4.1. Some theory of spin transfer torque

There are several different models to calculate the spin transfer effects, namely, models solving classical equations of motion for the magnetisation under the effect of spin current [62-66], models generalizing charge transport theory to take account of spin currents [67-69] and models based on quantum mechanical considerations of various parameters that are used by transport theories [50-51, 70-71].

A macrospin model treats a nanomagnet with the assumption that its internal magnetic degrees of freedom are frozen. The only relevant parameters are the total magnetic moment **m** and the magnetic anisotropy energy $U(\theta, \phi)$, where θ and ϕ are the polar-coordinate angles of **m**. The physical shape of the nanomagnet is relevant only in that its related shape demagnetisation energy contributes to the total anisotropy energy function $U(\theta, \phi)$.

The macrospin dynamics without the presence of a spin torque is well described by the classical Landau–Lifshitz–Gilbert (LLG) equation [72]

$$\left(\frac{1}{\gamma}\right)\frac{d\mathbf{m}}{dt} = \mathbf{m} \times \mathbf{H} - \left(\frac{\alpha}{\gamma m^2}\right)\mathbf{m} \times \frac{d\mathbf{m}}{dt} \tag{1.7}$$

Here **m** is the magnetic moment of the macrospin, $\gamma = g\mu_B / \hbar \approx 2\mu_B / \hbar$ is the gyromagnetic ratio, and α is the LLG damping coefficient. The first term in equation (1.7) describes the magnetic-field-induced torque on a magnetic moment **m**. The second term describes damping.

When a spin-polarized current passes through a ferromagnetic electrode that is **m**, **m** will attempt to repolarise the current in the direction of its magnetisation, $\mathbf{n}_m$.

In the process, some of the angular momentum from the electron spins will be absorbed by **m**. This exerts a net torque on **m**. For a nanomagnet **m** within which magnetisation is uniform, the transverse component of spin torque is [50]

$$\Gamma = g(\mathbf{n}_m, \mathbf{n}_s)\left[\frac{\hbar}{2e}\right]\left(\frac{\eta I}{m^2}\right)\mathbf{m}\times(\mathbf{m}\times\mathbf{n}_s) \qquad (1.8)$$

where $\mathbf{n}_m$ is the unit vector direction of **m**, $\mathbf{n}_s$ is the direction of spin polarization of the incoming current, and $\eta = (I_\uparrow - I_\downarrow)/(I_\uparrow + I_\downarrow)$ is the spin-polarization factor, where $I_\uparrow$ and $I_\downarrow$ are the majority and minority spin-polarized currents with their polarization axis $\mathbf{n}_s$ defined by the polarizing magnet (FM_1 in Figure 1.12). $g(\mathbf{n}_m, \mathbf{n}_s)$ is a numerical prefactor that describes the angular dependence of the efficiency of spin-angular momentum transfer, originating from the dependence of net spin polarization of the current on the relative orientation of the two ferromagnets. Because the net spin polarization depends on the exact arrangements of the electrodes, so does $g(\mathbf{n}_m, \mathbf{n}_s)$ [50, 69, 73]. For all-metal spin valves, the detailed angular dependence of $g(\mathbf{n}_m, \mathbf{n}_s)$ is model dependent, and is microscopically never an angle-independent quantity. Its macroscopic form relates to the angular dependence of magnetoresistance. In addition, there is an additional contribution of a perpendicular torque of the form $\mathbf{m}\times\mathbf{n}_s$ and it is calculated to be typically 1 – 3% of the in-plane component.

The case of a constant $g(\mathbf{n}_m, \mathbf{n}_s) \equiv 1$ describes a spin current whose polarization is independent of the relative angle, and the macrospin simply redirects the spin-current polarization direction, and in the process completely absorbs its transverse angular momentum. For simplicity of discussion, on a semi quantitative level, a constant $g(\mathbf{n}_m, \mathbf{n}_s)$ is assumed, and use equation (1.8) as the basic interaction

that enters the magnetodynamics equation for the motion of the macrospin. The LLG equation [72] with the spin-torque term therefore is

$$\left(\frac{1}{\gamma}\right)\frac{d\mathbf{m}}{dt} = \mathbf{m}\times\left[\mu_0\mathbf{H} - (\alpha/m)\mathbf{m}\times\left(\mu_0\mathbf{H} + \frac{\eta\hbar I}{2em\alpha}\mathbf{n}_s\right)\right] \tag{1.9}$$

For simple geometries and under a macrospin approximation, equation (1.9) can be linearized and solved for its stability boundary. For a thin, free-layer nanomagnet in a collinear geometry, with its uniaxial anisotropy field's easy axis aligned with that of the field applied in the film plane, and the easy-plane anisotropy sharing its easy plane with the film plane, this gives a stability threshold current I_c of [50, 64, 74]

$$I_c = \left(\frac{2e}{\hbar}\right)\left(\frac{\alpha}{\eta}\right)\mu_0 M_s V\left(H + H_k + \frac{M_s}{2}\right) \tag{1.10}$$

Here α is the LLG damping coefficient, M_s is the saturation magnetisation of the free layer (FM_2) and V is the volume of the free layer. H_k is the uniaxial anisotropy field. Equation (1.10) gives a current threshold, above which the *linearized* LLG equation becomes unstable over time, and a net gain of precession cone angle results. While comparing with experimental results, however, effects of large cone-angle precession often need to be carefully taken into account, since the development of an initial cone-angle increase as dictated by a linear stability threshold may not necessarily lead to complete magnetic reversal [64]. Although in many simple geometries, such as systems with uniaxial-only anisotropy or thin-film nanomagnets with a strong easy-plane anisotropy due to demagnetisation and a moderate in-plane uniaxial anisotropy, oftentimes the linear stability threshold does lead to the reversal of the magnetic moment [75].

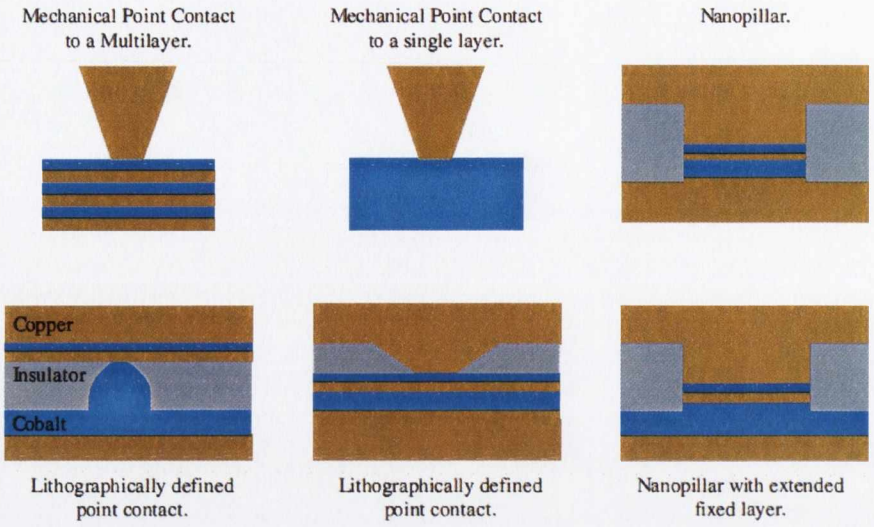

Figure 1. 14. The schematics of the experimental geometries [52].

1.4.2. Spin transfer torque experiments

Since the prediction of the effect in 1996, spin-transfer-induced magnetisation dynamics have been observed in several laboratories [53, 74, 76-85]. These observations have been made in different device geometries, some of those are shown in Figure 1.14, including mechanical point contacts [76-77], lithographically defined point contacts [77-78], electrochemically grown nanowires [80], manganite junctions [74], lithographically defined nanopillars [53, 81], tunnel junctions [82-84], and semiconductor structures [85]. These devices all share two characteristics, magnetoresistive read out of the magnetic state and small cross-sectional area (~ 100 × 200 nm^2).

Typical spin transfer torque magnetisation switching measurements for a spin valve (Co/Cu/Co) and an MgO based magnetic tunnel junction are shown in Figure

1.15 The critical current density for a spin valve is around 1×10^8 A/cm^2 [81] and it is around 6×10^6 A/cm^2 [86] for the MTJ.

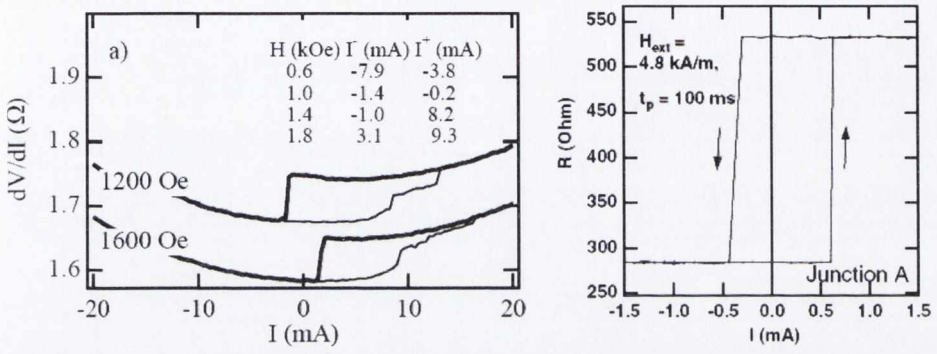

Figure 1. 15. Spin transfer torque switching measurements on a spin valve [81] (left) and an MgO based magnetic tunnel junction [86] (right) (10000 Oe = 80 kAm^{-1}).

Spin torque related effects were mainly observed in spin valves until 2004 but recently spin transfer torque switching has also been demonstrated in magnetic tunnel junctions with Al_2O_3 [83, 87] and MgO [83, 88] barriers. The switching current density is the main parameter to consider for achieving this phenomenon. Equation 1.11 obtained by modifying equation (1.10) is an expression for J_c, the critical current density needed to induce spin transfer reversal [89] with the magnetisation of the layers in the film plane,

$$J_c = \left(\frac{2e}{\hbar}\right)\left(\frac{\alpha}{\eta}\right)\mu_0 M_s t\left(H + H_k + \frac{M_s}{2}\right) \tag{1.11}$$

where H is the field applied along the easy axis (also the uniaxial anisotropy direction including the dipole field from the reference layer), M_s and t are the saturation magnetisation and the thickness of the free layer respectively, α is the

Gilbert damping coefficient, and H_k is the in-plane anisotropy field. The spin transfer efficiency, η, is a function of the current polarity, polarization, and the relative angle between the free and pinned layer. An interesting feature of spin-transfer induced switching is that the switching speed depends on the duration and amplitude of the current pulse. For room temperature operation, the J_c of the equation 1.11 corresponds to switching times in the 5 - 20 ns range for a typical free layer. Thermal excitations, however, will allow reversal at currents densities well below J_c [90].

At a finite temperature, thermal agitation plays an important role in reducing the switching current at long current pulses,

$$J_c = J_{c0}\left(1 - \frac{k_B T}{KV}\ln\left[\frac{\tau_p}{\tau_0}\right]\right) \tag{1.12}$$

where τ_0 is the relaxation time (~ 1 ns) and τ_p is the current pulse width. From equation (1.11), one can estimate the critical current density J_{c0} by extrapolating the experimentally observed switching current density J_c at $\tau_p = \tau_0$ by measuring the pulse width dependence of the critical current density. This equation also allows us to obtain thermal stability constant (Δ) of the device. Thermal stability constant is given by

$$\Delta = \frac{E_b}{k_B T} = \frac{KV}{k_B T} \tag{1.13}$$

The slope of a J_c vs. ln (τ_p/τ_0) graph is $-J_{c0}/\Delta$ according to equation (1.12). Here, it is possible to calculate the thermal stability constant which is very important for practical application of spin torque devices. In general, Δ should be over 40 for reliable operation of a device for at least 10 years. This value depends on the operation temperature of such a device and can vary accordingly.

1.4.3. Reduction of critical current density

The main concern about the spin transfer torque switching is the high current densities required for magnetic reversal which is on the order of 6×10^6 A/cm^2 for a typical MTJ. This value is too high for a practical application because the highest amount of current that the smallest transistor (~ 45 nm) can carry is around 5×10^5 A/cm^2. Therefore, the switching current density should be reduced. There are a couple parameters one can play to reduce the current density as can be seen from equation 1.11. First of which is the saturation magnetisation (M_s) of the free layer, that is critical current density quadratically scales with the saturation magnetisation. The M_s can easily be decreased with low moment magnetic materials such as CoFeB, CoFeCrB, CoFeSiB and etc. Besides reducing the M_s, the thickness of the free layer can also be reduced which will also decrease the critical current density.

The other coefficients like spin transfer efficiency and the damping constant can also be increased and reduced respectively to have lower critical current values. As stated above, spin transfer efficiency depends on the current polarity, polarization, and the relative angle between the free and pinned layer. There is a lot to play with spin transfer efficiency by carefully engineering the free layer material and multilayer device structure. For example, it is possible to use ferromagnets with high spin polarization such as half metals (Heusler alloys, CrO_2 and Fe_3O_4) which have spin polarization of 1. Another method would be using a dual barrier MTJ structure where the two pinned layers are anti-parallel to each other. It has been predicted [91] and demonstrated [92] that it is possible to increase spin transfer efficiency by a factor of two or higher. On the other hand, the damping coefficient is

more difficult to control and there is no theoretical understanding but it is found that during the growth of magnetic thin films, surface oxides and other effects increase the damping coefficient considerably [93]. Therefore, it should be kept as low as possible by optimization of the growth and fabrication processes.

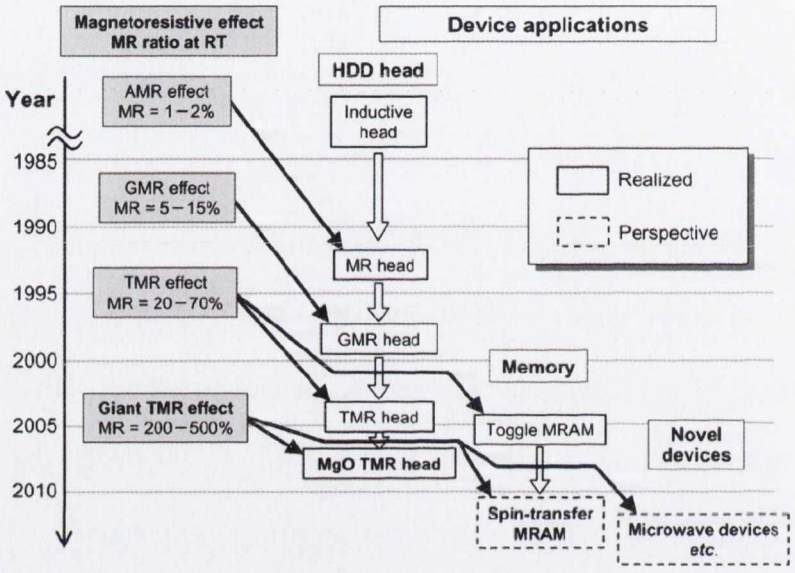

Figure 1. 16. History and future prospects of magnetoresistive effects, MR ratios at room temperature and applications of MR effects in spintronic devices [19].

1.5. Applications

The rapid advancements in spintronics especially in magnetic tunnel junctions in recent years sparked a very intense interest from industrial companies looking for the possible applications. From the device applications perspective, the history of spintronics is the history of magnetoresistance at RT (Figure 1.16). GMR

spin-valve devices have MR ratios of 5 – 15 % at RT and have been extensively used in the read heads of computer hard disks (HDD) since 1997. AlO_x based MTJs show MR ratios of 20 – 70 % at RT and have been used both in HDD read heads and in first generation magnetic random access memory (MRAM) cells. On the other hand, giant TMR MgO-based MTJs have MR ratios of 200 – 600 % at RT and are being used as HDD read heads since 2006. It is possible to see other types of products such as spin-transfer MRAM and novel microwave devices in the near future as illustrated in Figure 1.16.

1.5.1. Spin transfer torque magnetic random access memory (STT-MRAM)

The use of spin transfer torque magnetisation reversal (STS) is critical for the scaling of MRAM. The problem with conventional MRAM is the increase in the write current to generate strong enough field to write the bit as the bit size get smaller. Thus, the drive transistor has to be large enough to supply enough current. Prototype spin-transfer MRAM cells based on the giant TMR effect and STS in MgO-based MTJs have been developed [94]. The 4 Kbit spin-transfer MRAM developed by Sony Corp., for example, (shown in Figure 1.17) provides reliable read-out and write operations [94]. At the present stage, the intrinsic critical current density J_{c0}, or switching pulse-current density when the pulse duration is 1 ns is about 2×10^6 A/cm^2 [83, 94] and is not small enough for high-density MRAM. If J_{c0} is reduced to about 5×10^5 A/cm^2, it should be possible to develop Gbit-scale spin-transfer torque MRAM.

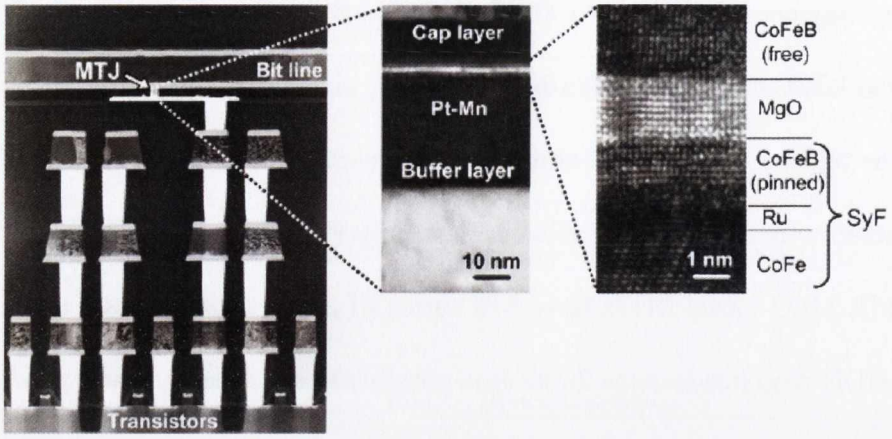

Figure 1. 17. Cross-sectional TEM images of a 4 Kbit spin-transfer torque MRAM using CoFeB / MgO / CoFeB MTJs [94].

1.5.2. Microwave oscillators

The microwave emission occurs when a dc current flows through a nano-scale magnetoresistive device. A spin-transfer torque acting on the free-layer magnetic moment can induce a steady precession of the free-layer moment at an FMR frequency (GHz). The steady precession of the free-layer moment in the magnetoresistive device induces an ac current or ac voltage at a FMR frequency (i.e. a microwave frequency). This microwave emission was first demonstrated using a CPP spin valve device with a GMR ratio of about 1 % at RT [95]. The microwave power from a CPP spin valve device, however, is only of the order of nanowatts and is too small for practical application. However, MgO-based MTJs with giant MR ratios are potentially able to achieve high-power microwaves because the microwave power is theoretically proportional to the square of the MR ratio. It was recently

reported that microwave emission of the order of microwatts is possible from nano-scale CoFeB / MgO / CoFeB MTJ with a TMR ratio of about 100 % [96]. Spin-torque-induced microwave emission based on MgO-based MTJs is expected to be the third major application of spintronics technology.

1.6. References

1. Bardeen, J. and W.H. Brattain, *"The Transistor, A Semi-Conductor Triode"*, Physical Review. **74**, 230, (1948).
2. Baibich, M.N., *et al.*, *"Giant Magnetoresistance of (001)Fe/(001)Cr Magnetic Superlattices"*, Physical Review Letters. **61**, 2472, (1988).
3. Binasch, G., *et al.*, *"Enhanced magnetoresistance in layered magnetic structures with antiferromagnetic interlayer exchange"*, Physical Review B. **39**, 4828, (1989).
4. Kapser, K. and J. Sterling. *Integrated GMR based Wheel Speed Sensor for Automotive Applications*. in *Sensors, 2007 IEEE*. 2007.
5. Loureiro, J., *et al.*, *"Magnetoresistive Detection of Magnetic Beads Flowing at High Speed in Microfluidic Channels"*, Magnetics, IEEE Transactions on. **45**, 4873, (2009).
6. Meiklejohn, W.H., *"Exchange Anisotropy - A Review"*, Journal of Applied Physics. **33**, 1328, (1962).
7. Meiklejohn, W.H. and C.P. Bean, *"A new magnetic anisotropy"*, Magnetics, IEEE Transactions on. **37**, 3866, (2001).

8. Malozemoff, A.P., *"Anisotropic magnetoresistance of amorphous and concentrated polycrystalline iron alloys"*, Physical Review B. **32**, 6080, (1985).

9. McGuire, T. and R. Potter, *"Anisotropic magnetoresistance in ferromagnetic 3d alloys"*, Magnetics, IEEE Transactions on. **11**, 1018, (1975).

10. Smit, J., *"Magnetoresistance of ferromagnetic metals and alloys at low temperatures"*, Physica. **17**, 612, (1951).

11. Valet, T. and A. Fert, *"Theory of the perpendicular magnetoresistance in magnetic multilayers"*, Physical Review B. **48**, 7099, (1993).

12. Parkin, S.S.P., *"Origin of enhanced magnetoresistance of magnetic multilayers: Spin-dependent scattering from magnetic interface states"*, Physical Review Letters. **71**, 1641, (1993).

13. Duke, C.B., *Tunneling in Solids*. 1969, New York: Academic Press.

14. Wolf, E.L., *Principles of Electron Tunneling Spectroscopy*. 1985, London: Oxford University Press.

15. Fisher, J.C. and I. Giaever, *"Tunneling Through Thin Insulating Layers"*, Journal of Applied Physics. **32**, 172, (1961).

16. Simmons, J.G., *"Generalized Formula for the Electric Tunnel Effect between Similar Electrodes Separated by a Thin Insulating Film"*, Journal of Applied Physics. **34**, 1793, (1963).

17. Brinkman, W.F., R.C. Dynes, and J.M. Rowell, *"Tunneling Conductance of Asymmetrical Barriers"*, Journal of Applied Physics. **41**, 1915, (1970).

18. Julliere, M., *"Tunneling between ferromagnetic films"*, Physics Letters A. **54**, 225, (1975).

19. Yuasa, S. and D.D. Djayaprawira, *"Giant tunnel magnetoresistance in magnetic tunnel junctions with a crystalline MgO (001) barrier"*, Journal of Physics D: Applied Physics. **40**, R337, (2007).

20. Tedrow, P.M. and R. Meservey, *"Spin-dependent tunneling into ferromagnetic nickel"*, Physical Review Letters. **26**, 192, (1971).

21. Tedrow, P.M. and R. Meservey, *"Spin Polarization of Electrons Tunneling from Films of Fe, Co, Ni, and Gd"*, Physical Review B. **7**, 318, (1973).

22. Stearns, B.M., *"Simple explanation of tunneling spin-polarization of Fe, Co, Ni and its alloys"*, Journal of Magnetism and Magnetic Materials. **5**, 167, (1977).

23. Yuasa, S., *et al.*, *"Giant room-temperature magnetoresistance in single-crystal Fe/MgO/Fe magnetic tunnel junctions"*, Nature Materials. **3**, 868, (2004).

24. Bowen, M., *et al.*, *"Nearly total spin polarization in $La_{2/3}Sr_{1/3}MnO_3$ from tunneling experiments"*, Applied Physics Letters. **82**, 233, (2003).

25. Sakuraba, Y., *et al.*, *"Giant tunneling magnetoresistance in Co_2MnSi/Al-O/Co_2MnSi magnetic tunnel junctions"*, Applied Physics Letters. **88**, 192508, (2006).

26. Wang, W., *et al.*, *"Giant tunneling magnetoresistance up to 330% at room temperature in sputter deposited Co_2FeAl/MgO/CoFe magnetic tunnel junctions"*, Applied Physics Letters. **95**, 182502, (2009).

27. Wang, W., *et al.*, *"Coherent tunneling and giant tunneling magnetoresistance in Co_2FeAl/MgO/CoFe magnetic tunneling junctions"*, Physical Review B. **81**, 140402, (2010).

28. Maekawa, S. and U. Gafvert, *"Electron tunneling between ferromagnetic films"*, Magnetics, IEEE Transactions on. **18**, 707, (1982).

29. Miyazaki, T., T. Yaoi, and S. Ishio, *"Large magnetoresistance effect in $_{82}$Ni-Fe/Al-Al_2O_3/Co magnetic tunneling junction"*, Journal of Magnetism and Magnetic Materials. **98**, L7, (1991).

30. Nowak, J. and J. Rauluszkiewicz, *"Spin dependent electron tunneling between ferromagnetic films"*, Journal of Magnetism and Magnetic Materials. **109**, 79, (1992).

31. LeClair, P., J.S. Moodera, and R. Meservey, *"Ferromagnetic-ferromagnetic tunneling and the spin filter effect"*, Journal of Applied Physics. **76**, 6546, (1994).

32. Moodera, J.S., *et al.*, *"Large magnetoresistance at room temperature in ferromagnetic thin film tunnel junctions"*, Physical Review Letters. **74**, 3273, (1995).

33. Miyazaki, T. and N. Tezuka, *"Giant magnetic tunneling effect in Fe/Al_2O_3/Fe junction"*, Journal of Magnetism and Magnetic Materials. **139**, L231, (1995).

34. Moodera, J.S., *et al.*, *"Large Magnetoresistance at Room Temperature in Ferromagnetic Thin Film Tunnel Junctions"*, Physical Review Letters. **74**, 3273, (1995).

35. Miyazaki, T. and N. Tezuka, *"Spin polarized tunneling in ferromagnet/insulator/ferromagnet junctions"*, Journal of Magnetism and Magnetic Materials. **151**, 403, (1995).

36. Gao, L., *et al.*, *"Increased Tunneling Magnetoresistance Using Normally bcc CoFe Alloy Electrodes Made Amorphous without Glass Forming Additives"*, Physical Review Letters. **102**, 247205, (2009).

37. Wang, D., *et al.*, *"70% TMR at room temperature for SDT sandwich junctions with CoFeB as free and reference Layers"*, Magnetics, IEEE Transactions on. **40**, 2269, (2004).

38. Lee, Y.M., *et al.*, *"Effect of electrode composition on the tunnel magnetoresistance of pseudo-spin-valve magnetic tunnel junction with a MgO tunnel barrier"*, Applied Physics Letters. **90**, 212507, (2007).

39. Parkin, S.S.P., *et al.*, *"Giant tunnelling magnetoresistance at room temperature with MgO (100) tunnel barriers"*, Nature Materials. **3**, 862, (2004).

40. Ikeda, S., *et al.*, *"Tunnel magnetoresistance of 604% at 300 K by suppression of Ta diffusion in CoFeB/MgO/CoFeB pseudo-spin-valves annealed at high temperature"*, Applied Physics Letters. **93**, 082508, (2008).

41. Jiang, L., *et al.*, *"Large Tunnel Magnetoresistance of 1056% at Room Temperature in MgO Based Double Barrier Magnetic Tunnel Junction"*, Applied Physics Express. **2**, 083002, (2009).

42. Butler, W.H., *et al.*, *"Spin-dependent tunneling conductance of Fe|MgO|Fe sandwiches"*, Physical Review B. **63**, 054416, (2001).

43. Mathon, J. and A. Umerski, *"Theory of tunneling magnetoresistance of an epitaxial Fe/MgO/Fe(001) junction"*, Physical Review B - Condensed Matter and Materials Physics. **63**, 2204031, (2001).

44. Zhang, X.G. and W.H. Butler, *"Large magnetoresistance in bcc Co/MgO/Co and FeCo/MgO/FeCo tunnel junctions"*, Physical Review B. **70**, 172407, (2004).

45. Bagayoko, D., A. Ziegler, and J. Callaway, *"Band structure of bcc cobalt"*, Physical Review B. **27**, 7046, (1983).

46. Mavropoulos, P., N. Papanikolaou, and P.H. Dederichs, *"Complex Band Structure and Tunneling through Ferromagnet /Insulator /Ferromagnet Junctions"*, Physical Review Letters. **85**, 1088, (2000).

47. Wulfhekel, W., *et al.*, *"Single-crystal magnetotunnel junctions"*, Applied Physics Letters. **78**, 509, (2001).

48. Oguz, K. and J.M.D. Coey, *"Room-temperature magnetoresistance in CoFeB/STO/CoFeB magnetic tunnel junctions"*, Journal of Magnetism and Magnetic Materials. **321**, 1009, (2009).

49. Moubah, R., *et al.*, *"Effect of interface bonding on the transport properties in $CoFe_2/SrTiO_3/CoFe_2/NiFe$ magnetic tunnel junctions"*, Physical Review B. **82**, 024415, (2010).

50. Slonczewski, J.C., *"Current-driven excitation of magnetic multilayers"*, Journal of Magnetism and Magnetic Materials. **159**, L1, (1996).

51. Berger, L., *"Emission of spin waves by a magnetic multilayer traversed by a current"*, Physical Review B. **54**, 9353, (1996).

52. Ralph, D.C. and M.D. Stiles, *"Spin transfer torques"*, Journal of Magnetism and Magnetic Materials. **320**, 1190, (2008).

53. Urazhdin, S., *et al.*, *"Current-Driven Magnetic Excitations in Permalloy-Based Multilayer Nanopillars"*, Physical Review Letters. **91**, 146803, (2003).

54. Koch, R.H., J.A. Katine, and J.Z. Sun, *"Time-Resolved Reversal of Spin-Transfer Switching in a Nanomagnet"*, Physical Review Letters. **92**, 088302, (2004).

55. Myers, E.B., *et al.*, *"Thermally Activated Magnetic Reversal Induced by a Spin-Polarized Current"*, Physical Review Letters. **89**, 196801, (2002).

56. Fabian, A., *et al.*, *"Current-Induced Two-Level Fluctuations in Pseudo-Spin-Valve (Co/Cu/Co) Nanostructures"*, Physical Review Letters. **91**, 257209, (2003).

57. Pufall, M.R., *et al.*, *"Large-angle, gigahertz-rate random telegraph switching induced by spin-momentum transfer"*, Physical Review B. **69**, 214409, (2004).

58. Li, Z. and S. Zhang, *"Thermally assisted magnetization reversal in the presence of a spin-transfer torque"*, Physical Review B. **69**, 134416, (2004).

59. Apalkov, D.M. and P.B. Visscher, *"Spin-torque switching: Fokker-Planck rate calculation"*, Physical Review B. **72**, 180405, (2005).

60. Diao, Z. and et al., *"Spin-transfer torque switching in magnetic tunnel junctions and spin-transfer torque random access memory"*, Journal of Physics: Condensed Matter. **19**, 165209, (2007).

61. Li, Z., J. He, and S. Zhang, *"Stability of precessional states induced by spin-current"*, Physical Review B. **72**, 212411, (2005).

62. Bazaliy, Y.B., B.A. Jones, and S.-C. Zhang, *"Modification of the Landau-Lifshitz equation in the presence of a spin-polarized current in colossal- and giant-magnetoresistive materials"*, Physical Review B. **57**, R3213, (1998).

63. Bazaliy, Y.B., B.A. Jones, and S.C. Zhang, *"Towards metallic magnetic memory: How to interpret experimental results on magnetic switching induced by spin-polarized currents"*, Journal of Applied Physics. **89**, 6793, (2001).

64. Sun, J.Z., *"Spin-current interaction with a monodomain magnetic body: A model study"*, Physical Review B. **62**, 570, (2000).

65. Miltat, J., *et al.*, *"Spin transfer into an inhomogeneous magnetization distribution"*, Journal of Applied Physics. **89**, 6982, (2001).

66. Zhang, S. and P.M. Levy, *"Time dependence of spin accumulation and magnetoresistance in magnetic multilayers"*, Physical Review B. **65**, 052409, (2002).

67. Wegrowe, J.E., *"Thermokinetic approach of the generalized Landau-Lifshitz-Gilbert equation with spin-polarized current"*, Physical Review B. **62**, 1067, (2000).

68. Brataas, A., Y.V. Nazarov, and G.E.W. Bauer, *"Finite-Element Theory of Transport in Ferromagnet-Normal Metal Systems"*, Physical Review Letters. **84**, 2481, (2000).

69. Stiles, M.D. and A. Zangwill, *"Anatomy of spin-transfer torque"*, Physical Review B. **66**, 014407, (2002).

70. Berger, L., *"Generation of dc voltages by a magnetic multilayer undergoing ferromagnetic resonance"*, Physical Review B. **59**, 11465, (1999).

71. Xia, K., *et al.*, *"Spin torques in ferromagnetic/normal-metal structures"*, Physical Review B. **65**, 220401, (2002).

72. Lifshitz E. M. and P.L. P., *Statistical Physics Part 2*. 1980, Oxford: Reed Educational and Professional Publishing Ltd.

73. Waintal, X., *et al.*, *"Role of spin-dependent interface scattering in generating current-induced torques in magnetic multilayers"*, Physical Review B. **62**, 12317, (2000).

74. Sun, J.Z., *"Current-driven magnetic switching in manganite trilayer junctions"*, Journal of Magnetism and Magnetic Materials. **202**, 157, (1999).

75. Kronmuller H. and S. Parkin, *Handbook of Magnetism and Advanced Magnetic Materials*. Vol. 5. 2007, West Sussex: John Wiley & Sons Ltd.

76. Tsoi, M., *et al.*, *"Excitation of a Magnetic Multilayer by an Electric Current"*, Physical Review Letters. **80**, 4281, (1998).

77. Myers, E.B., *et al.*, *"Current-Induced Switching of Domains in Magnetic Multilayer Devices"*, Science. **285**, 867, (1999).

78. Ji, Y., C.L. Chien, and M.D. Stiles, *"Current-Induced Spin-Wave Excitations in a Single Ferromagnetic Layer"*, Physical Review Letters. **90**, 106601, (2003).

79. Rippard, W.H., M.R. Pufall, and T.J. Silva, *"Quantitative studies of spin-momentum-transfer-induced excitations in Co/Cu multilayer films using point-contact spectroscopy"*, Applied Physics Letters. **82**, 1260, (2003).

80. Kelly, D., *et al.*, *"Spin-polarized current-induced magnetization reversal in single nanowires"*, Physical Review B. **68**, 134425, (2003).

81. Katine, J.A., *et al.*, *"Current-Driven Magnetization Reversal and Spin-Wave Excitations in Co /Cu /Co Pillars"*, Physical Review Letters. **84**, 3149, (2000).

82. Liu, Y., *et al.*, *"Current-induced switching in low resistance magnetic tunnel junctions"*, Journal of Applied Physics. **93**, 8385, (2003).

83. Diao, Z., *et al.*, *"Spin transfer switching and spin polarization in magnetic tunnel junctions with MgO and AlO_x barriers"*, Applied Physics Letters. **87**, 232502, (2005).

84. Kubota, H., *et al.*, *"Quantitative measurement of voltage dependence of spin-transfer torque in MgO-based magnetic tunnel junctions"*, Nature Physics. **4**, 37, (2008).

85. Moriya, R., *et al.*, *"Current-Induced Magnetization Reversal in a (Ga,Mn)As-Based Magnetic Tunnel Junction"*, Japanese Journal of Applied Physics. **43**, L825, (2004).

86. Kubota, H., *et al.*, *"Evaluation of Spin-Transfer Switching in CoFeB/MgO/CoFeB Magnetic Tunnel Junctions"*, Japanese Journal of Applied Physics. **44**, L1237, (2005).

87. Huai, Y., *et al.*, *"Observation of spin-transfer switching in deep submicron-sized and low-resistance magnetic tunnel junctions"*, Applied Physics Letters. **84**, 3118, (2004).

88. Hayakawa, J., *et al.*, *"Current-Driven Magnetization Switching in CoFeB/MgO/CoFeB Magnetic Tunnel Junctions"*, Japanese Journal of Applied Physics. **44**, L1267, (2005).

89. Sun, J.Z., *"Spin angular momentum transfer in current-perpendicular nanomagnetic junctions"*, IBM Journal of Research and Development. **50**, 81, (2006).

90. Katine, J.A. and E.E. Fullerton, *"Device implications of spin-transfer torques"*, Journal of Magnetism and Magnetic Materials. **320**, 1217, (2008).

91. Berger, L., *"Multilayer configuration for experiments of spin precession induced by a dc current"*, Journal of Applied Physics. **93**, 7693, (2003).

92. Diao, Z., *et al.*, *"Spin transfer switching in dual MgO magnetic tunnel junctions"*, Applied Physics Letters. **90**, 132508, (2007).

93. Emley, N.C., *et al.*, *"Time-Resolved Spin-Torque Switching and Enhanced Damping in Permalloy/Cu/Permalloy Spin-Valve Nanopillars"*, Physical Review Letters. **96**, 247204, (2006).

94. Hosomi, M., *et al. A novel nonvolatile memory with spin torque transfer magnetization switching: spin-ram.* in *Electron Devices Meeting, 2005. IEDM Technical Digest. IEEE International*. 2005.

95. Tulapurkar, A.A., *et al.*, *"Spin-torque diode effect in magnetic tunnel junctions"*, Nature. **438**, 339, (2005).

96. Deac, A.M., *et al.*, *"Bias-driven high-power microwave emission from MgO-based tunnel magnetoresistance devices"*, Nature Physics. **4**, 803, (2008).

Chapter 2

Experimental Methods

This chapter describes the experimental methods used for the deposition and characterization of thin film devices. These devices include magnetic tunnel junctions and spin valves. Thin films were deposited by magnetron sputtering and e-beam evaporation which are described in detail in this chapter. Films and multilayer stacks were characterized using several analysis techniques like X-ray diffraction, X-ray reflection, Energy dispersive x-rays, SQUID magnetometer, transmission electron microscope, and magneto-transport measurements.

2.1. Thin film deposition

2.1.1. Sputtering

Sputtering is one of the widely used physical vapour deposition techniques. This method is applicable both in industry and in the research laboratories. The advantages of sputtering can be stated as moderately low cost, high deposition rate, reproducibility and large area fabrication ability. In this method, the atoms/molecules

of a target are essentially ejected towards a substrate through momentum transfer by bombarding the target with energetic ions. In the following sections, the sputter deposition process is described in more detail.

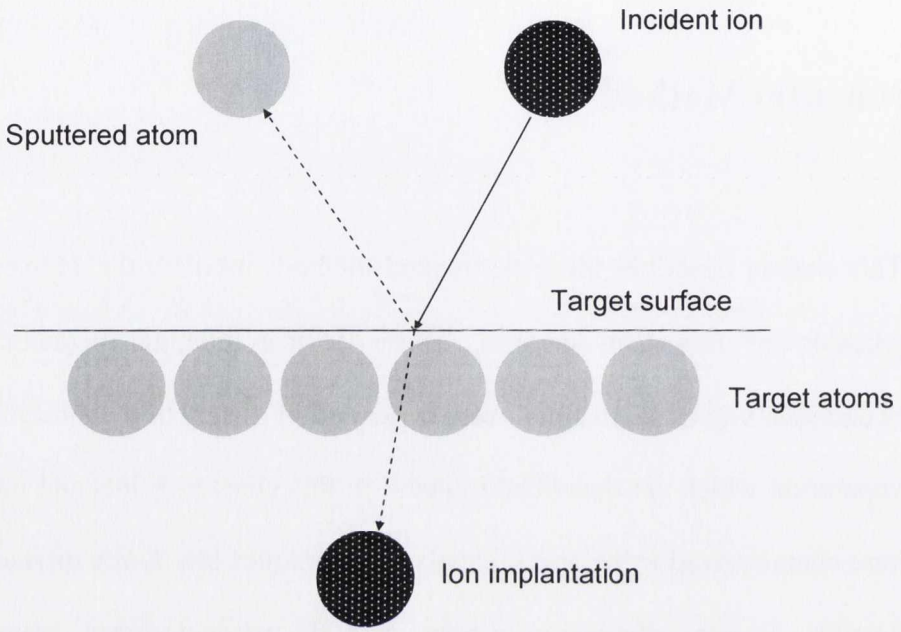

Figure 2. 1. Basic schematic of the sputtering process.

2.1.1.1. Basics

The details of the sputtering processes are rather complex, but the basic principles are straightforward [1]: a target material is bombarded by accelerated ions, resulting in ejection (sputtering) of atoms/molecules from the target (Figure 2.1). These atoms/molecules deposit onto the substrate and a film is formed. In thin film deposition, the source of the energetic ions is usually a low-pressure *glow discharge* or *plasma* (see next section), which is ignited and sustained between the target

(cathode) and the substrate (anode) using a noble gas such as Argon (typically at a pressure of 1-100 mTorr). A basic sputtering system is illustrated in Figure 2.2.

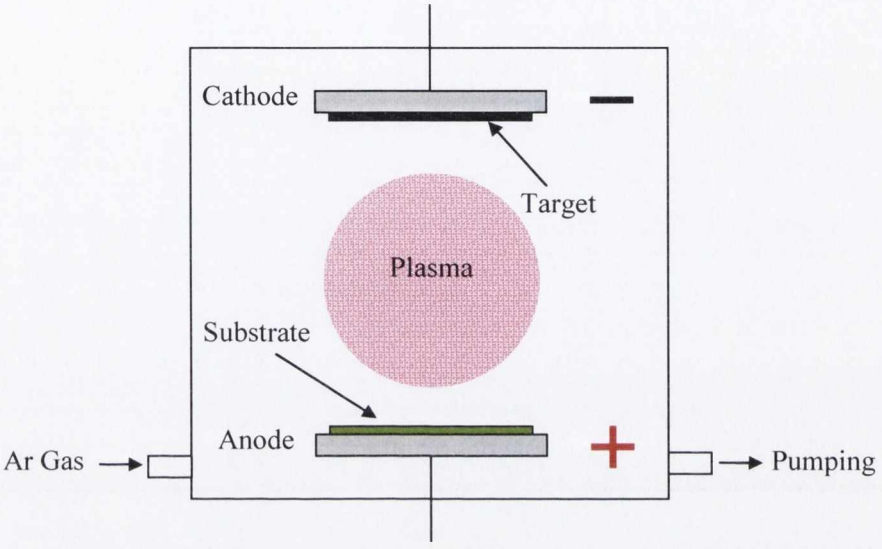

Figure 2. 2. Simple schematic of a glow discharge (basic sputtering) system.

As a high negative potential is maintained at the target, positive ions are accelerated from the plasma onto the target, causing sputtering. Two deposition parameters, both of which depend on the specific combination of process gas and target material, are critically important for the efficiency of the sputtering deposition process. These are the *sputter yield* and the *secondary electron yield*, i.e., the number of sputtered atoms and secondary electrons, respectively, which are produced per bombarding gas ion. The sputter yield e.g., the efficiency of momentum transfer, depends on the cross section of the collision, the binding energy of the target atoms, and the kinetic energy of the incoming ions. Sputter yield is denoted with, S, and is given by

$$S = \frac{N_{EmittedParticles}}{N_{IncidentIon}} \tag{2.1}$$

In Table 2.1, sputter yields of selected materials as a function of ion energy are summarized. The yield is dramatically different for different elements. This is basically due to the difference on the nature of the bonds between the atoms of a specific element. It is much smaller for heavy elements and oxide materials. A number of studies revealed that the crystal structure of the target considerably affects the sputter yield. Non-uniform angular dependencies of the sputter yield are also reported by Elich *et al.* for single crystal targets while it shows a uniform character for polycrystalline targets [2].

Table 2. 1. Sputter yields of some materials for Ar^+ ion bombardment as a function of ion energy [3].

Material	300 eV	500 eV	1000 eV
Au	1.10	1.70	2.50
B	0.20	0.60	1.10
Cr	0.80	1.10	1.90
Cu	1.50	1.90	2.90
Fe (Co & Ni)	0.70	1.00	1.70
Si	0.30	0.70	1.00
Ta	0.30	0.50	0.90
Ti	0.30	0.50	0.70

The secondary electron yield is strongly dependent on the work function of the target material, i.e., high yield is achieved with low work function. At constant power, a higher electron yield results in a higher current drawn and, thus, lower discharge voltage and sputter yield. A higher yield also means a larger electronic fraction of the current and, hence, a lower sputter rate and ionic current. Therefore, a high secondary electron yield generally decreases the sputter efficiency.

2.1.1.2. The plasma

Plasma is described as a partially ionized, but macroscopically neutral, gas containing neutrals, ions, and electrons, with high enough concentrations of charged particles for significant Coulomb interaction to occur [4]. Another characteristic is a positive potential of the plasma (the plasma potential) relative to any surface in contact with it. This potential difference is caused by the higher velocities of the electrons in the plasma compared to the ions, resulting in an initial negative charge build-up on the surface. The negative charge then tends to repel electrons and attract positive ions from the plasma until equilibrium is reached at a certain negative potential, relative to the plasma potential. The region between the plasma and an adjacent surface, over which the potential changes, is called the *sheath*.

Sputtering plasma is sustained by applying a high (a few hundred volts) negative voltage to the target, which causes ions in the plasma to be accelerated over the sheath toward the target [1]. The resulting collisions give rise to sputtering of target atoms and emission of secondary electrons. The electrons are accelerated toward the anode to ionize (by direct impact) more gas atoms, which bombard the

target and produce more sputtered atoms and secondary electrons. When equilibrium is reached, a steady-state discharge is sustained and the ejected target atoms/molecules are deposited on the substrate and on the chamber walls also.

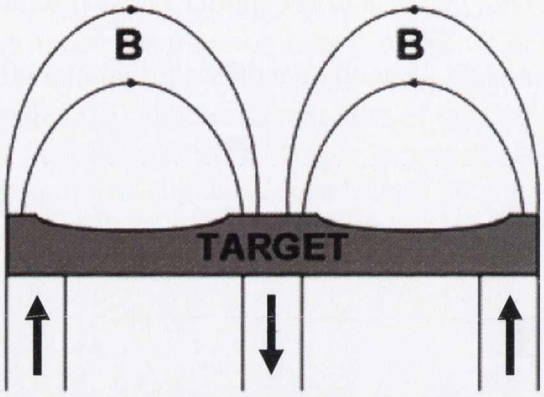

Figure 2. 3. Schematic view of the magnetron cross-section and the erosion area formed on the target.

2.1.1.3. Magnetron sputtering

Practically, all sputtering tools today use *magnetrons*. The basic principle is to place permanent magnets behind the target to create a magnetic field between the outer and inner parts of the target, as schematically shown in Figure 2.3. The electrons involved in the sputtering process are trapped in this field close to the target, where they increase the rate of ionization by an order of magnitude, thus the sputter rate. This can increase the deposition rate by an order of magnitude compared to non-magnetron sputtering. It also enables the use of lower pressures, which gives a more directional and energetic deposition flux due to less scattering of sputtered

species. There is one drawback of magnetron sputtering which is a non-uniform consumption of the target because sputtering is focused in the area of highest electron density (the *erosion area*), i.e., where the magnetic field is parallel to the target surface. This can be improved by balancing the magnetic field on the surface of the target. The nature of the target materials also affects the erosion region. For instance, magnetic targets require different thickness and magnet configuration because the flux tends to pass through the ferromagnet instead of creating a stray field above it. Generally, $B_mA_m > 2\pi rtB_t$ where B_m and B_t are the saturation flux density of the permanent magnet and the ferromagnetic target, respectively. A_m is the magnet cross-section, r and t are the radius and the thickness of the target.

2.1.1.4. Radio frequency sputtering

Radio frequency (RF) power is commonly used to deposit insulating materials, which can be coupled through any target material, conducting or not. At these high frequencies, -the most common frequency is 13.56 MHz which is reserved for this purpose by the Federal Communications Commission and similar authorities- the relatively heavy ions can not follow the oscillations, while the electrons can easily oscillate with the current [1]. Therefore, they gain enough energy from the RF field to ionize the sputtering gas, reducing the need for secondary electrons to sustain the plasma and enabling lower operating pressures compared to DC sputtering. The RF sputtering process is based on the fact that there is a *self-biasing* of the target to a negative potential of typically a few hundred volts. Due to this bias, the resulting sputtering process is quite similar to the case of DC sputtering. The self-bias is, in

analogy with the plasma potential, explained by the much higher mobility of the electrons compared to the ions.

During a positive half-cycle of the oscillating RF voltage, a large negative (electron) current will be drawn on to the target, but during the following negative half-cycle only a small positive (ion) current flows, due to the low mobility of the ions. Therefore, initially a net negative current is drawn into the target. Since no charge can be transferred through the capacitively coupled target, a negative potential (the target self-bias) builds up until no net current flows. On the other hand, a matching circuit should also be used for RF sputtering to operate more efficiently because of the impedance difference between the chamber and the power supply. One of the common impedance matching circuits can be seen in Figure 2.4.

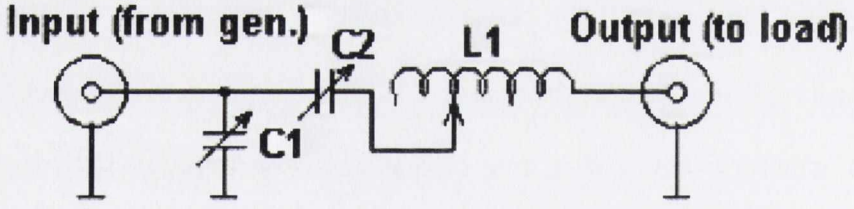

Figure 2. 4. Typical impedance matching circuit for RF sputtering

2.1.2. Evaporation

Evaporation is a very simple and inexpensive way of depositing thin film materials and it has been widely used in industry for several different coatings. The metal layers in early semiconductor technologies were also deposited by evaporation.

But, recently it has been replaced by sputtering due to two main reasons. The first is the poor cover surface topology often called step coverage which is much better in sputtering. The second is the difficulty in producing well-controlled alloys.

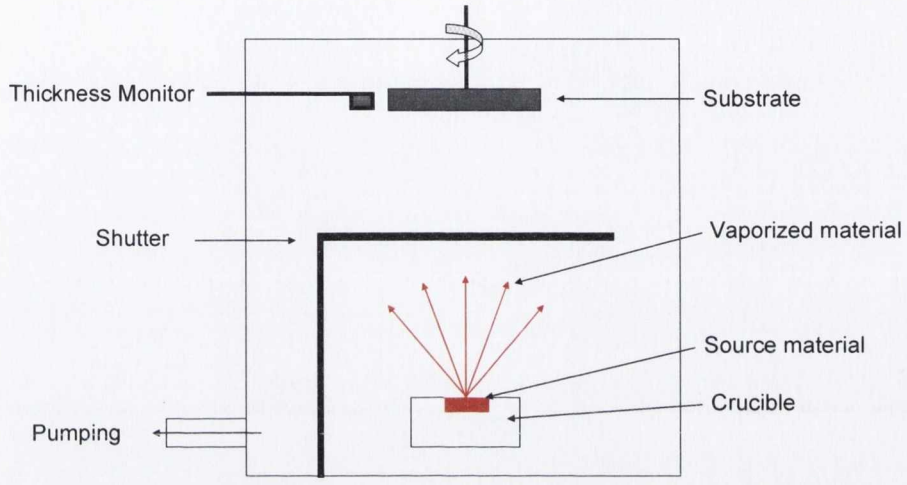

Figure 2. 5. Schematic of a simple high vacuum evaporation system.

Figure 2.5 shows a simple high vacuum evaporation system. Samples are loaded into a high vacuum chamber that is pumped by a turbo molecular pump or a cryo-pump. The source material is loaded into a heated container called the crucible. The crucible can be heated with three common methods: resistive heating, electron beam heating and inductive heating. First two are the most common evaporation methods and these will be briefly described in the following sections. After heating the source, it gives off vapour. When the shutter is open, the atoms of the vapour travel across the chamber in a straight line and deposit on the sample/wafer surface forming a thin film. In order to have sufficient mean free path, chamber pressure should be adequately low ($< 10^{-3}$ Torr). The mean free path of the atomic species in thermal equilibrium is determined by the pressure. The kinetic theory of gases leads

to a handy numerical relation $\lambda \equiv 6/P$ at room temperature, where λ is the mean free path of the atom in millimetres, and P is the pressure in pascals [5]. The thickness of the films is controlled by a thickness monitor adjacent to the sample holder.

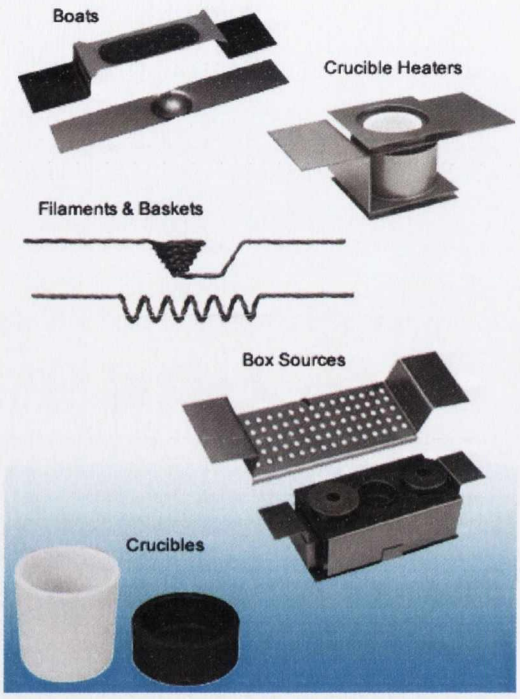

Figure 2. 6. Different types of crucibles for evaporation.

2.1.2.1. Thermal evaporation

A resistively heated system is the simplest type of source and often referred to as thermal evaporation. In the simple case, two high current feed-throughs are used to supply current to a solid crucible (boat) made of tungsten or molybdenum. Different types of crucibles can be used depending on the purpose (Figure 2.6). The source material is placed in the boat and it is heated by passing high current through

it using a low voltage dc power supply. As the temperature is raised, material goes through the solid, liquid and gas phases. At every temperature, there exists an equilibrium pressure of vapour above the solid or liquid material. When the sample is below the melting temperature this process is called *sublimation*. When the sample is molten it is called *evaporation*. In order to have reasonable deposition rate, the material has to be in the molten state. The deposition rate is directly proportional to the vapour pressure of the sample at certain temperature (Figure 2.7). Typical vapour pressure should be > 10^{-3} Torr to achieve reasonable deposition rate.

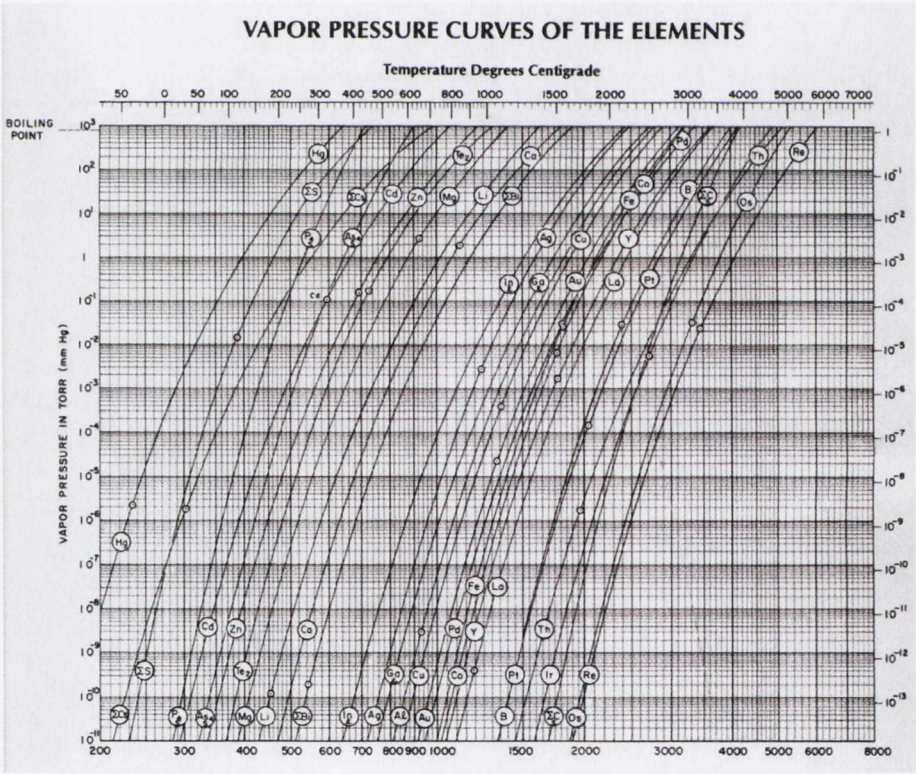

Figure 2. 7. Vapour pressure curves for some commonly evaporated materials.

2.1.2.2. Electron beam (e-beam) evaporation

The only difference between thermal evaporation and e-beam evaporation is the way to heat the source material. In this case, source material is heated by bombardment of highly energetic electrons. Electrons are created by heating a tungsten filament located under the crucible (to avoid exposure of substrate to e-beam) and electrons are accelerated by high voltage (~ 5 kV) applied on the accelerating electrodes. Then electrons are bent towards the source in the crucible using bending magnets. A typical e-beam evaporation source is illustrated in Figure 2.8.

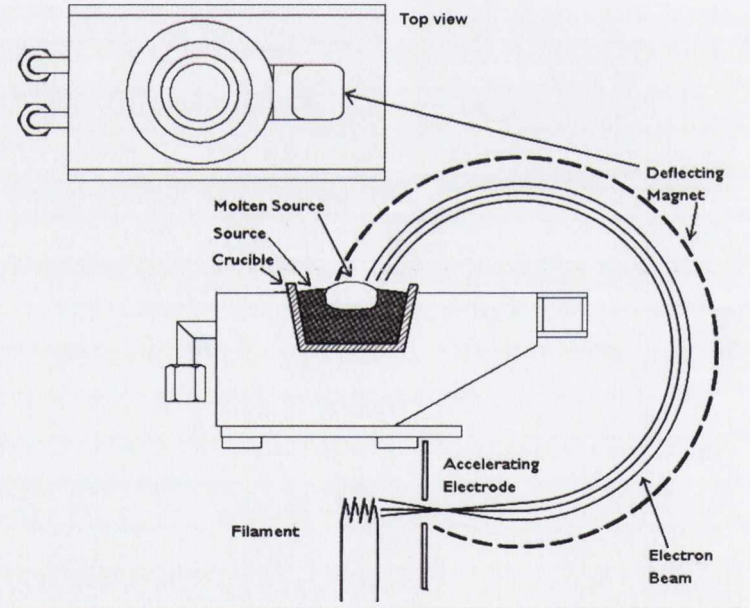

Figure 2. 8. Schematic of a typical e-beam evaporation source.

E-beam evaporation systems can have several pockets with a different source material in each to deposit multilayers. Typical evaporation pressure is around 10^{-6} - 10^{-7} Torr. This method also allows evaporating insulating materials by heating them locally which is high enough to start sublimation.

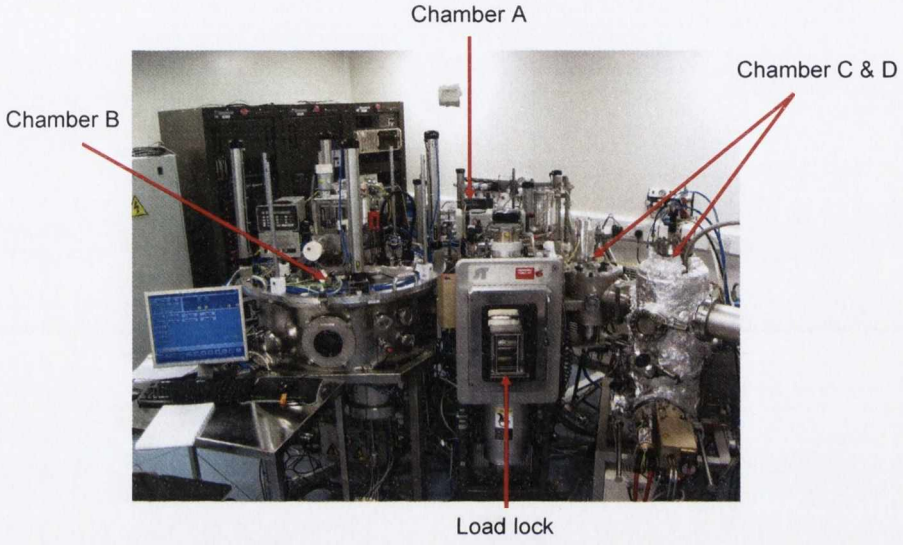

Figure 2. 9. The photograph of our Shamrock magnetron sputtering/evaporation cluster deposition tool.

2.2. Thin film deposition systems

The metal film depositions in this study were all carried out in our high vacuum magnetron sputtering/evaporation cluster tool located in the CRANN Class 10000 clean room. The overall system consists of three interconnected deposition chambers (A, B and D). Figure 2.9 illustrates the entire tool and Figure 2.10 schematically describes the layout of the deposition chambers, transfer chambers and

the load lock. Chamber A is a high vacuum Shamrock sputtering machine, Chamber B is a Plassys MP900 sputter deposition system and Chamber D is a custom-built ultra high vacuum (UHV) e-beam evaporation/sputter deposition system. Further details are given in the following sections.

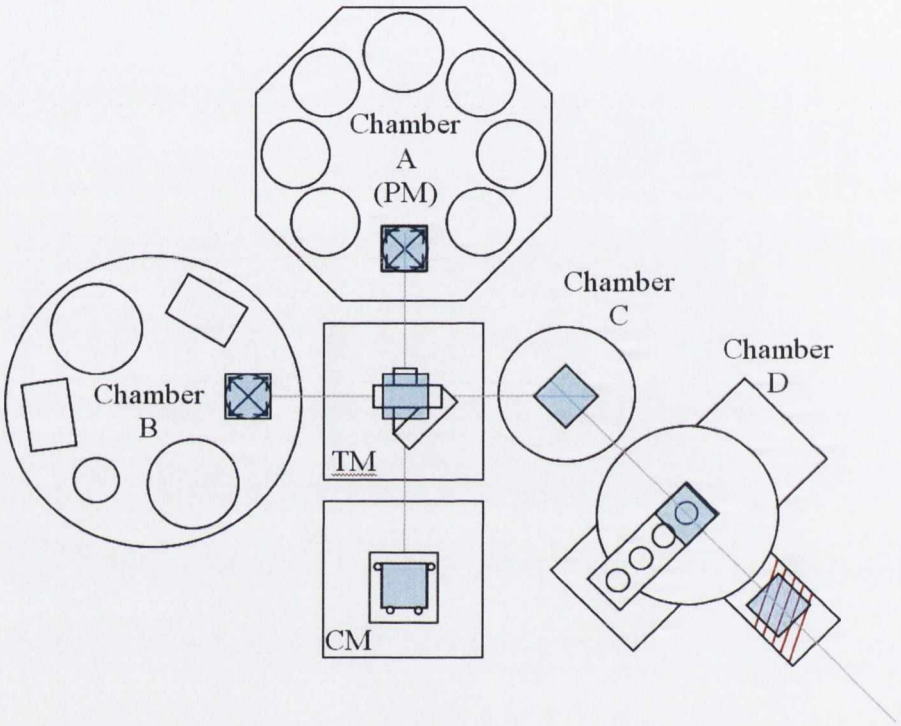

Figure 2. 10. Layout of three deposition chambers (A, B and D), transfer chambers (TM and Chamber C) and the load lock (CM).

2.2.1. Shamrock sputtering system (Chamber A)

The Shamrock is originally designed and used for the production of AMR and GMR sensors at Seagate. It was purchased by the CINSE group in June 2002. The system incorporates three interconnected high vacuum chambers which are

process module (PM) also called Chamber A, transfer module (TM) and the cassette module (CM), load lock, as can be seen in Figure 2.11a.

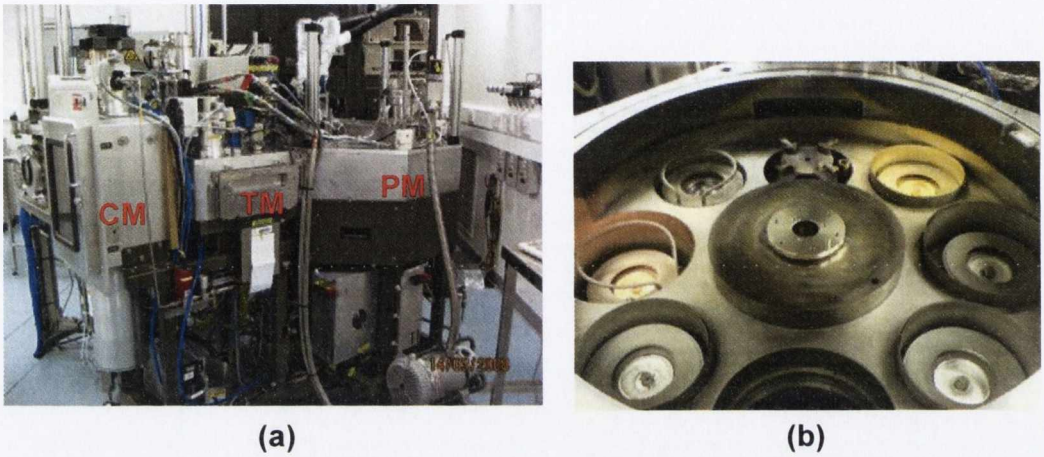

Figure 2. 11. (a) Chamber A picture indicating CM, TM, and PM (b) inside view of the process module showing six sputter guns and the ion gun, at the front.

The process module is a high vacuum magnetron sputtering chamber equipped with six three inch Series III magnetron guns and an ion milling gun inside as shown in Figure 2.11b. The system is capable of processing both four and six inch wafers. The deposition is fully automated and computer controlled. 4 wafers can be processed at the same time. The chamber is pumped by a Varian turbo molecular pump and Oxford water pump. It can reach base pressure of $< 8 \times 10^{-8}$ Torr. Typical deposition pressure is $1 - 5 \times 10^{-3}$ Torr.

All six magnetrons can operate in DC mode. Six 1.5 kW (Advanced Energy-MDX 1.5K) power supplies control the cathode bias and two power supplies control the anode bias on guns 1-3, 4-6 respectively. It is not essential to apply anode bias but it can be helpful to increase the deposition rate. Guns 5 and 6 can also work in

RF mode (two Dresslar Cesar 300W RF supplies & matching networks). A pulsed DC supply can be used on gun 2 & 6. There is also an ion mill for substrate pre-cleaning or ion etching. Targets are cup-shaped and 3" in diameter with different designs for magnetic and non-magnetic materials.

Table 2. 2. List of different MTJ stacks used in this study

MTJ Type	Multilayer stack
Single-Simple bottom pinned	SiO_2/Ta (5)/Ru (30)/Ta (5)/$Ni_{80}Fe_{20}$ (5)/$Ir_{22}Mn_{78}$ (10)/$Co_{40}Fe_{40}B_{20}$ (3)/MgO (t)/ $Co_{40}Fe_{40}B_{20}$ (3)/Ta (5)/Ru (5)
Single-bottom pinned with SAF	SiO_2/Ta (5)/Ru (30)/Ta (5)/$Ni_{80}Fe_{20}$ (5)/$Ir_{22}Mn_{78}$ (10)/$Co_{90}Fe_{10}$ (2.5)/Ru (0.9)/ $Co_{40}Fe_{40}B_{20}$ (3)/MgO (t)/ $Co_{40}Fe_{40}B_{20}$ (3)/Ta (5)/Ru (5)
Single-simple top pinned	SiO_2/Ta (5)/Ru (30)/Ta (5)/ $Co_{40}Fe_{40}B_{20}$ (3)/MgO (t)/ $Co_{40}Fe_{40}B_{20}$ (3)/$Ir_{22}Mn_{78}$ (10)/Ta (5)/Ru (5)
Single–top pinned with SAF	SiO_2/Ta (5)/Ru (30)/Ta (5)/ $Co_{40}Fe_{40}B_{20}$ (3)/MgO (t)/ $Co_{40}Fe_{40}B_{20}$ (3)/Ru (0.9)/$Co_{90}Fe_{10}$ (2.5)/$Ir_{22}Mn_{78}$ (10)/Ta (5)/Ru (5)
Double	SiO_2/Ta (5)/Ru (30)/Ta (5)/$Ni_{80}Fe_{20}$ (5)/$Ir_{22}Mn_{78}$ (10)/$Co_{90}Fe_{10}$ (2.5)/Ru (0.9)/ $Co_{40}Fe_{40}B_{20}$ (3)/MgO (t)/ $Co_{40}Fe_{40}B_{20}$ (2)/MgO (t)/ $Co_{40}Fe_{40}B_{20}$ (3)/ $Ir_{22}Mn_{78}$ (10)/Ta (5)/Ru (5)

Table 2. 3. Typical deposition parameters for some of the materials used in this study.

Material	Deposition Chamber	Power (W)	Ar Flow (sccm)	Pressure (10^{-3} Torr)	Growth Rate (nm/s)
Ta	A	100	40	2.0	0.01
Ru	A	100	25	1.4	0.016
$Ni_{80}Fe_{20}$	A	100	25	1.4	0.01
$Ir_{22}Mn_{78}$	A	100	25	1.4	0.02
$Co_{90}Fe_{10}$	A	100	25	1.4	0.01
$Co_{40}Fe_{40}B_{20}$	A/B/D	100/33/30	25/20/25	1.4/4.7/1.0	0.009
MgO (e-beam)	D	-	-		0.03
MgO (sputter)	B	100	15	4.0	0.017

A motorized turntable with rotating planets sits above the S-Guns. Each planet is equipped with permanent magnets which produce a field of 5 mT. Applying a magnetic field during growth predetermines the easy axis of the free layer and helps in achieving proper exchange bias. As the turntable rotates about a central axis, each planet also rotates about its own axis resulting in a planetary–type motion. This design enables uniform deposition up to 6" wafers from only 3" targets. In practice, we use the Shamrock with 4" wafers. In addition, the planetary motion allocates time for the cooling of the substrate during growth which results in smoother films.

This chamber was used to deposit the most of the metal layers in the MTJ stacks listed in Table 2.2. It is also used to deposit the top contact layers (Ta/Cu) for the micro/nano fabrication of MTJ devices described in Chapter 3.

2.2.2. Plassys MP900 sputtering system (Chamber B)

Chamber B is originally designed by Plassys. The chamber includes an ion gun and a total of eight sputtering guns forming two clusters with three guns each and two Target Facing Target (TFT) guns, as illustrated in Figure 2.12. The cluster guns are equipped with three 0.5 kW DC power supplies (Advanced Energy-MDX 500) which can be subsequently used for both clusters. TFT guns are powered with a 300W RF power supply (Huttinger PFG 300 RF) with a matching circuit. The system has the capability of heating the substrate up to 750 ^{o}C in both vacuum and an oxygen environment. The typical base pressure of the system is $< 3 \times 10^{-8}$ Torr achieved by Turbo Molecular Pump and a CTI water pump. The partial pressure of water vapour is $< 3 \times 10^{-9}$ Torr. This is critical for the deposition of high quality MgO layers.

The system was designed for oxide deposition and alloy co-sputtering. At present, TFT targets are used to grow high quality oxide materials including MgO, Al_2O_3, $SrTiO_3$, $BaTiO_3$, $PbTiO_3$, SiO_2, and etc. Cluster guns are used to deposit CoFeB, CoFeCrB, CoNiCrB and CoFeNiB alloys using co-sputtering. To achieve the right composition of the alloy films, the growth rates of the individual targets were carefully adjusted by varying the gun power. In addition to these, the entire MTJ

stack can be deposited in chamber B by making use of the both clusters (metal depositions) and TFTs (barrier layer).

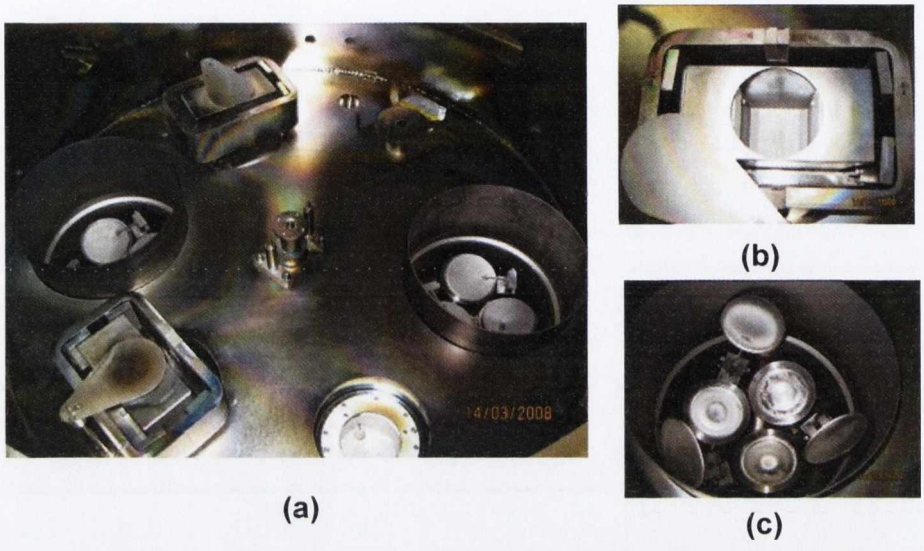

Figure 2. 12. (a) Inside view of Chamber B (b) TFT sputter gun (c) Cluster guns.

2.2.3. UHV e-beam evaporation / sputtering system (Chamber D)

Chamber D is an ultra high vacuum system consists of a linear electron beam evaporation system, a 2" magnetron sputter gun and an annealing furnace (Figure 2.13). This chamber can achieve $2x10^{-10}$ Torr base pressure with the help of a CTI cryo-pump which is critical for high quality thin films and it is connected to other deposition chambers via a transfer chamber (Chamber C). There are four evaporation pockets which are used to evaporate primarily MgO, Fe, Au and Cr. The sputter gun is an AJA low pressure sputter gun equipped with a local gas injection ring which allows low pressure operation. It is connected to a 0.5 kW DC power supply

(Advanced Energy MDX 500). This gun is mainly used to deposit CoFeB films for the MTJ stacks. The system has an in-situ heating furnace achieving temperatures up to 500 ^{o}C used for post-annealing. The robotic computer controlled substrate holder also allows us to flip the wafer upside down thus it is possible to deposit on both sides of a substrate / wafer or membrane.

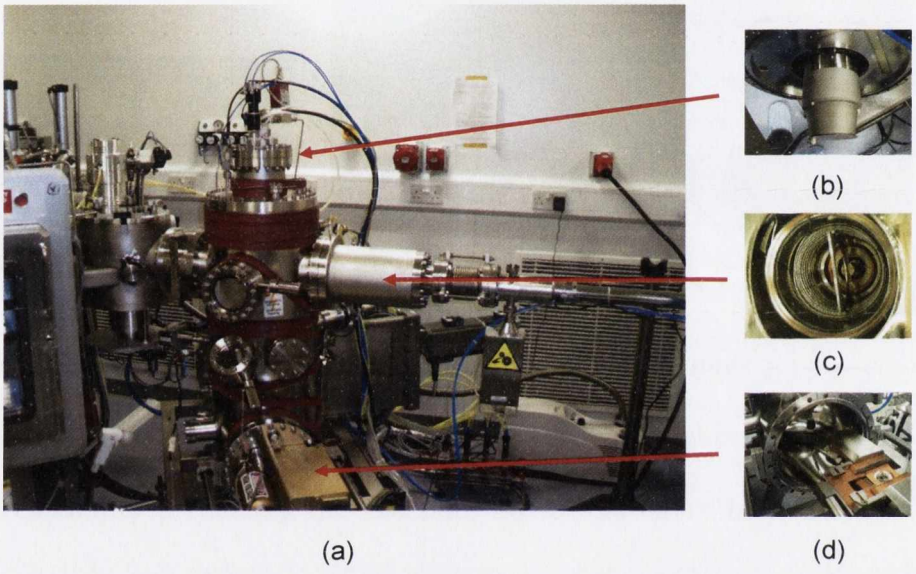

Figure 2. 13. (a) Image of our UHV evaporation / sputtering system showing (b) sputter gun, (c) annealing furnace, and (d) linear e-beam evaporation system.

2.3. Structural characterization

Structural characterizations of thin films are performed by X-ray diffraction, X-ray reflectivity and transmission electron microscopy. Composition analysis of alloy materials is performed by energy dispersive X-ray measurements. These methods are described briefly in the following sections.

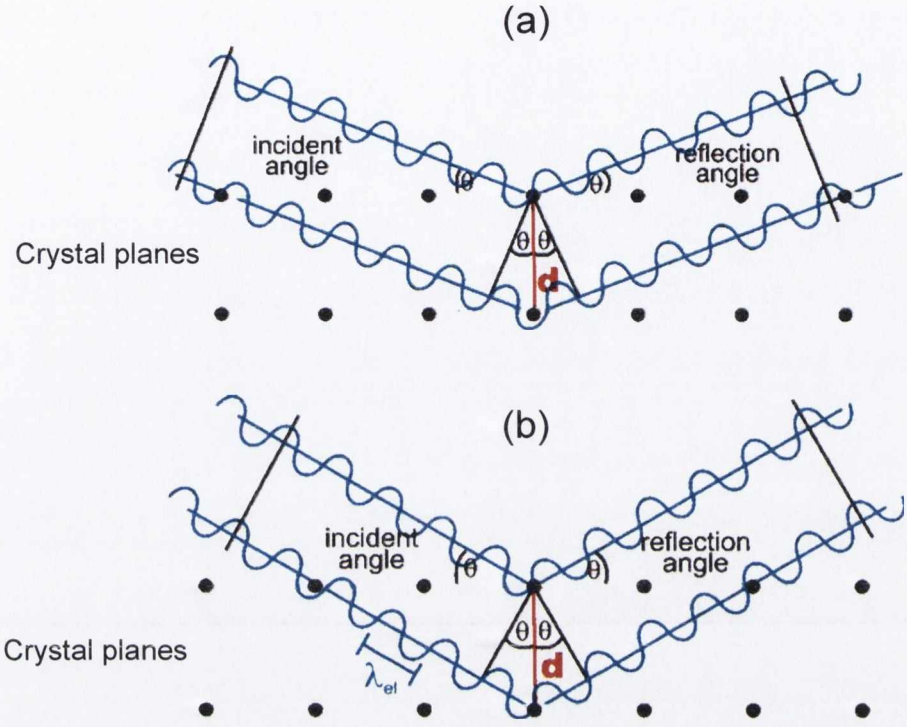

Figure 2. 14. Schematic of diffraction of X-rays from crystal planes due to Bragg's law. (a) destructive and (b) constructive.

2.3.1. X-ray diffraction

X-ray diffraction (XRD) is the standard technique for crystal structure determination. In this technique, the diffraction of the X-rays occurs within the sample according to the Bragg's Law;

$$m\lambda = 2d\sin\theta \tag{2.2}$$

where λ is the X-ray wavelength, d is the layer separation, m is the diffraction order and θ is the angle of incidence with the sample surface. The interference of the re-emitted waves from crystal planes is constructive when the phase shift is a multiple

of 2π (Figure 2.14). Depending on the intensity, the position and the width of the diffraction peaks, the type and the quality of the crystal structure of the samples are determined.

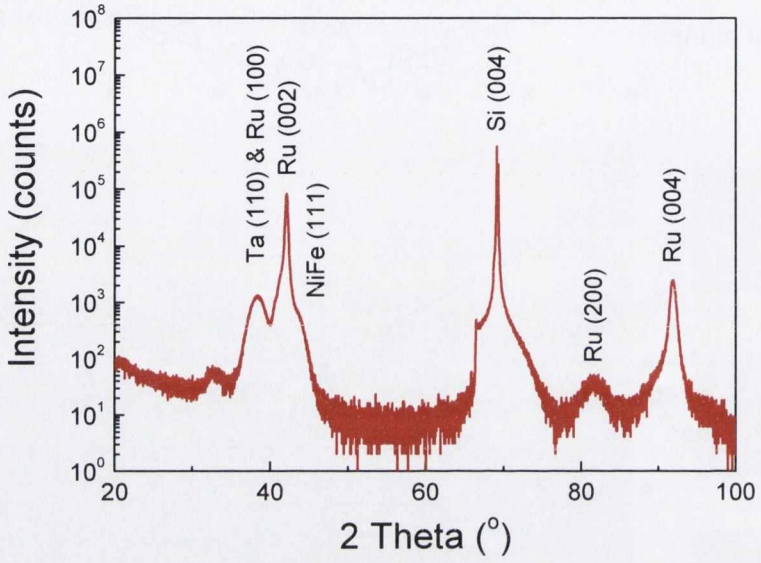

Figure 2. 15. Typical X-ray diffraction spectrum of a magnetic tunnel junction. There are several peaks at different angles which are coming from different layers in the stack. In general, the thickest film gives the highest intensity peak.

The crystal structure of a sample is determined by analyzing the observed diffraction peaks. All of the planes do not result in a diffraction peak in an XRD pattern. The crystal structure determines which diffraction peaks can be observed in the spectrum. For instance, $(h^2+k^2+l^2)$ should be even for BCC structures i.e., (110), (200), (211) planes give a diffraction peak in the XRD pattern. A typical XRD diffraction pattern is illustrated in Figure 2.15, plotted on a logarithmic intensity scale. All of the known crystal structures give different diffraction patterns. The

positions of the peaks are given by the unit cell (lattice) parameters and the intensity depends on the structure factor, which depends on the structure of the unit cell. A comparison of the position and the intensity of the observed peaks with the known systems enables to determine the crystal structure of an unknown sample.

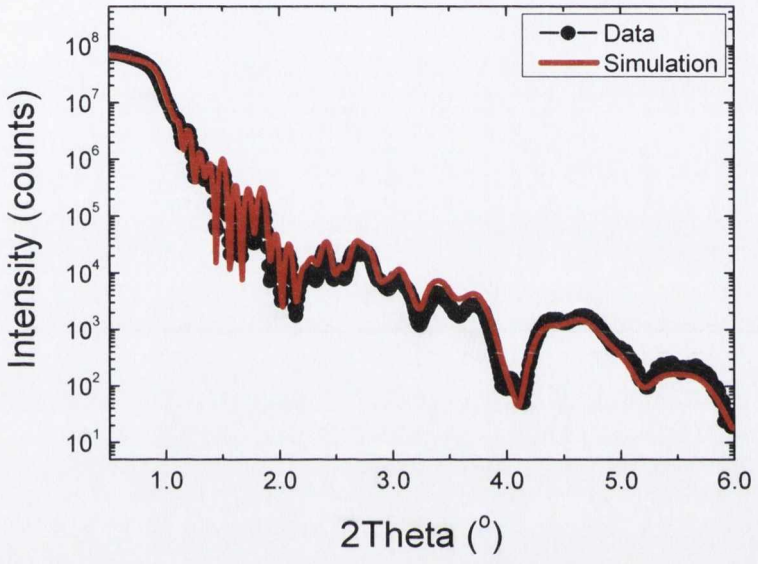

Figure 2. 16. Example of an XRR measurement and simulation of SiO_2 / Ta (5) / CoFeB (5) / MgO (20) / FePt (40) / Pt (2). Numbers in parentheses are the layer thicknesses in nm. Superimposed oscillations come from interference from different layers in the multilayer sample.

2.3.2. X-ray reflectivity

X-ray reflectivity (XRR) is a technique used to measure the thickness and roughness of the thin films. When X-rays are incident onto a material's flat surface at grazing angles of incidence, total reflection will occur at or below a certain angle,

θ_c. This angle is called the critical angle. It is material specific and is related to the density. The higher the incident X-ray angle relative to the critical angle, the deeper the X-rays penetrate into the material. If a material whose surface is ideally flat, the reflectivity abruptly decreases at angles above θ_c. If the surface is rough it can cause a more drastic decrease in reflectivity.

When X-rays are incident on a thin film at grazing angles of incidence ($0 < \theta < 10^o$), reflected X-rays from the interface between the substrate and the thin film as well as from the free surface of the film will interfere with each other either constructively or destructively. The result is the oscillations in reflected intensity as a function of incident angle as shown in Figure 2.16.

The positions of the maxima of reflected intensity are related to the thickness of the film according to modified Bragg's law;

$$m\lambda = 2t\sqrt{\sin^2\theta - 2\delta} \tag{2.3}$$

where t is the film thickness, m=1, 2, 3, δ = dispersive part of refractive index of sample. A more rigorous approach is needed to incorporate the effect of roughness which will not be discussed here. Simple fitting of the oscillations results in a quick measurement of the thickness of the film. Surface roughness can be deduced by fitting the amplitude.

In this study, our X-ray diffractometer (Phillips X'Pert Pro) operating with Cu-K^{α} (1.54056 Å) radiation with a Ni filter adjusted to 40 kV and 40 mA was used to determine the crystal quality and the thickness of the films. The films were properly aligned in the beam by adjusting the height and the position of the sample. Two types of X-ray detectors were used for diffraction and reflection measurements. For diffraction experiments, a Phillips X'cellerator detector was used for $20^o < 2\theta <$

100°. For XRR measurements, PRS/PASS detector was used which is equipped with a beam attenuator for $0.2^{\circ} < 2\theta < 6^{\circ}$. Measured XRR curves were fitted using the Phillips Wingixa software. Thickness and roughness values were obtained from these fits.

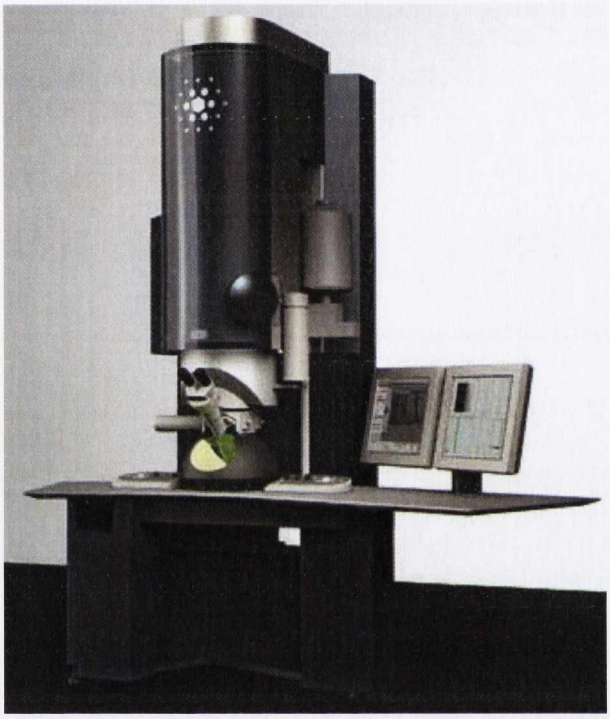

Figure 2. 17. Image of CRANN FEI Titan transmission electron microscope.

2.3.3. Transmission electron microscopy

Transmission electron microscope (TEM) is used to analyze the cross-section of plane and patterned magnetic tunnel junctions. It is critical to understand the crystal structure of CoFeB/MgO interfaces in MgO based MTJs. For this purpose, the FEI Titan S/TEM located in CRANN Advanced Microscopy Laboratory is

mainly used (Figure 2.17). The tool is operated at 300 kV to obtain high resolution TEM micrographs. The imaging resolution is in sub-nm range. The system also has detectors for elemental analysis: The first one is the energy dispersive X-ray (EDX) detector and the second one is the Gatan Tridiem Energy Filtering (EFTEM) system for Electron Energy Loss Spectroscopy (EELS).

2.3.4. Elemental analysis

Energy dispersive X-ray measurements are performed to analyze the composition of alloy films prepared in this study (CoFeB, CoFeCrB, CoNiCrB and CoFeNiB). In an EDX measurement, high energy electrons are incident on the sample and incident electrons excite the atoms of the sample to higher energy states. When the atom relaxes back, it emits characteristic X-rays during the transitions of electrons from excited states to the ground states. The energy spectrum of these X-rays carries the signatures of different elements present in the sample. For this measurement, the Bruker EDX detector installed on CRANN FEI Strata 265 dual beam scanning electron/ion microscope was used. The EDX spectrum was obtained using 15 kV electrons on a sample area of $5 \times 5\ \mu m^2$. 50 nm films were sufficiently thick to obtain a reasonable signal to noise ratio.

2.4. Magnetic characterization

2.4.1. Superconducting Quantum Interference Device (SQUID) magnetometer

A Quantum Design Magnetic Property Measurement System (MPMS XL5) was used to characterize the magnetic properties of thin films (Figure 2.18). A superconducting quantum interference device (SQUID) detection system is integrated with a temperature control unit, a high field superconducting magnet and the computer operating system. Liquid helium is used for cooling of the superconducting components as well as for low temperature measurements. The ultrahigh sensitivity of the magnetometer makes it ideal for thin film measurements where the signals are too weak for detection with a vibrating sample magnetometer. Measurements can be made between 1.9 and 800 K in a field of up to 5 T, with a sensitivity of 10^{-11} Am^2. For the measurements, plane samples are diced into 5 × 5 mm^2 pieces and installed into system by mounting them in a plastic straw.

2.4.2. Spin valve test structures

A very simple way of testing the quality of exchange bias in magnetic tunnel junctions has been developed. In this method, a spin valve with the same stack of an MTJ replacing tunnel barrier with copper is deposited and the magneto-resistance of the spin valve is measured in the current in-plane geometry using 4-point probe

technique. This gave us the opportunity to evaluate quickly the magnetic structure of the stacks, before patterning them.

Figure 2. 18. Our Quantum Design SQUID magnetometer (MPMS XL5).

2.5. Magneto-transport measurements

2.5.1. Magneto-resistance measurements

Magneto-resistance (MR) measurements were carried out on the patterned and un-patterned samples using the standard four-point probe technique by a computer-controlled set-up using a Keithley 2400 source meter (RT rig, shown in Figure 2.19). The field is generated by an electromagnet driven by a Kepco 10 amp

bi-polar power supply. The maximum field attainable using this power supply is 180 mT. The field is applied parallel to the easy axis of the sample and is measured by reading out the voltage from a Hall sensor attached to one of the pole pieces of the magnet. The sample was connected to the Keithley using BNC connectors contacted to the sample by hard contacts using indium. For MR measurements of MTJs, a constant DC voltage of 5 mV is applied and the current is measured simultaneously while sweeping the magnetic field. The resistance is obtained by dividing the voltage to the measured current. TMR ratios of the junctions are calculated from the parallel and anti-parallel resistance values.

2.5.2. Spin transfer torque switching measurements

Spin transfer torque switching experiments were also carried out using the RT rig (Figure 2.19). To obtain current reversal curves, first magnetoresistance of the sample was measured. The offset field on the free layer due to coupling is identified by minor loop measurements. This offset field was applied to the substrate to cancel the coupling between free and pinned layers during the current sweep measurements. For the current sweep measurement, MTJ was set to antiparallel state by sweeping the field from high field. Then, to see antiparallel to parallel switch, DC current was swept from negative to positive while measuring the voltage drop simultaneously. The current direction was reversed to obtain switching from parallel to antiparallel state. The electrons were flowing from pinned layer to free layer for the positive current. Similar measurement was performed for different pulse widths using Keithley's pulse option. The pulse widths were between 1 ms and 1 s.

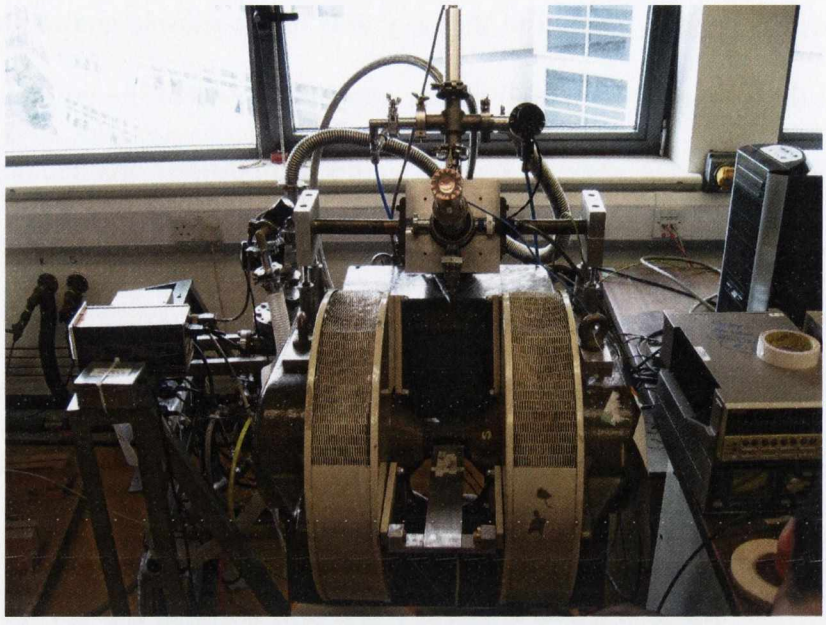

Figure 2. 19. Image of RT rig which is used to measure DC magnetoresistance and STT measurements.

2.5.3. Magnetic annealing

The importance of magnetic annealing is two fold: The primary reason is to set the exchange bias in magnetic tunnel junctions/spin valves, the secondary reason is to promote the required crystallization process of CoFeB layer in our MTJs, which is essential to get very high TMR ratios. Figure 2.20 shows the setup for the magnetic annealing furnace. The annealing furnace is essentially a quartz tube with a resistive heater wrapped around the outside. The tube is pumped by a turbo molecular pump to high vacuum of 10^{-6} Torr. A sample holder was designed to fit into the quartz tube such that samples are placed at the centre of the magnetic field.

The annealing furnace is fixed inside a permanent magnet which has 0.8 T magnetic field. Maximum sample size is 30 × 30 mm^2. It is possible to anneal three samples at the same time.

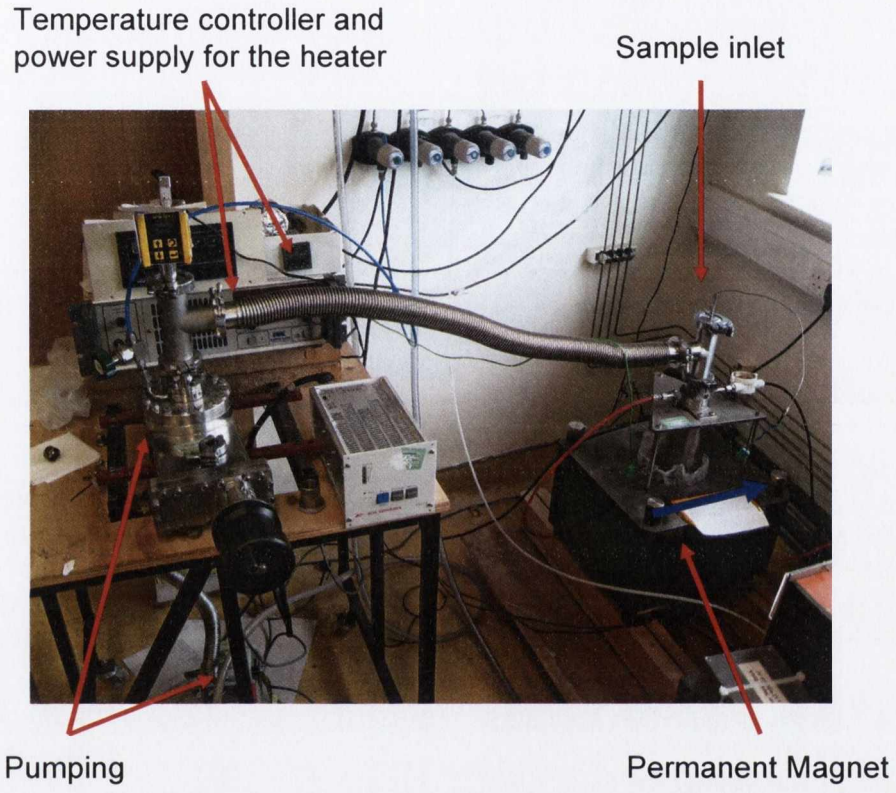

Figure 2. 20. Custom-built high vacuum magnetic annealing furnace. Blue arrow shows the direction of magnetic field created by the permanent magnet.

Samples are inserted with their easy axis aligned with the field, parallel to the bore axis. The easy axis was defined by the direction of the magnetic field applied during sputter deposition in chamber A. Temperature is monitored and controlled using a Eurotherm 2416 temperature controller and a thermocouple fixed on the sample holder. Furnace is capable of annealing samples up to 500 °C. Water is

circulated continuously during process to prevent permanent magnet from overheating.

2.6. References

1. Ohring, M., *Materials Science of Thin Films: Deposition & Structure*. Second ed. 2002, San Diego: Academic Press.
2. Elich, J.J.P., H.E. Roosendaal, and D. Onderdelinden, *"Precision measurements on the angular and temperature dependence of sputtering"*, Radiation Effects. **14**, 93 (1972).
3. Seshan, K., *Handbook of Thin-Film Deposition Processes and Techniques*. Second ed. 2002, New York: Noyes Publications / William Andrew Publishing.
4. Chapman, B., *Glow Discharge Processes: Sputtering and Plasma Etching*. 1980: John Wiley & Sons, Inc.
5. Coey, J.M.D., *Magnetism and Magnetic Materials*. 2009: Cambridge University Press.

Chapter 3

Device Development

The micro-fabrication and nano-fabrication processes used in this work are discussed in detail. The chapter is divided into three sections. The first section discusses the microfabrication process with the following order: (1) Basics of photolithography, (2) Argon ion milling and (3) Lift-off. The second section describes nano-fabrication with a focus on the details of e-beam lithography. The last section is about the micro and nano fabrication procedures used in the realization of magnetic tunnel junction devices in the micro and nano scale.

3.1. Micro-fabrication process

3.1.1. Photolithography

3.1.1.1. Basics

Photo-lithography is a manufacturing process for producing highly accurate and microscopic features on a substrate by using a photo-sensitive material which is called photoresist. This process is often called as micro-lithography (or micro-fabrication) within the semiconductor community. The patterns created are identical copies of a master pattern on a photomask. These masks are generally made of a patterned thin layer of chromium on a transparent glass [1]. Masks should be transparent to the wavelength that is being used for the exposure. Typical source wavelengths are 436 nm for g-line, 405nm for h-line and 365 nm for i-line. The lines have been named according to their energy [2]. Figure 3.1 shows the spectra for a mercury arc lamp which are the main light sources that are used in photolithography. The highest intensity peaks are being used as ultraviolet (UV) sources of present mask aligners.

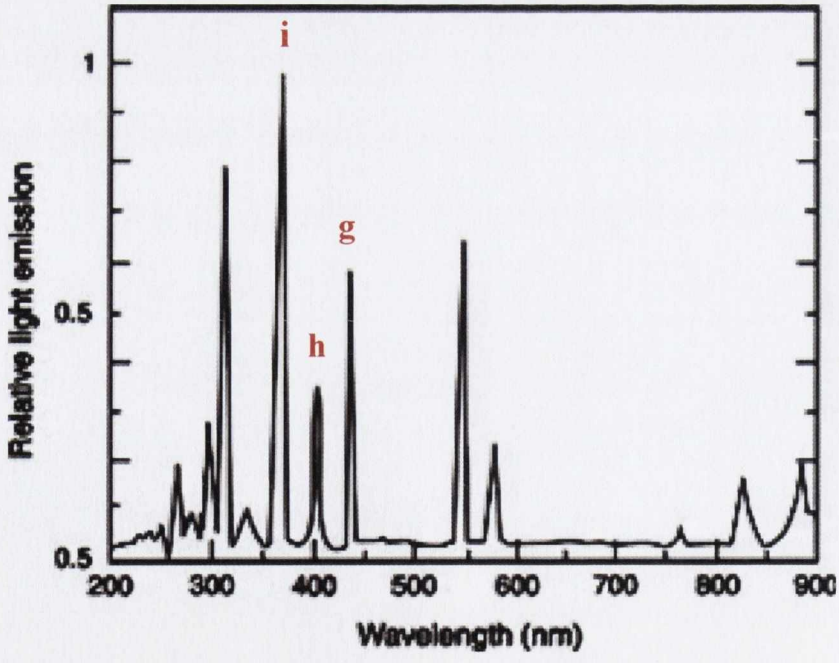

Figure 3. 1. Line emission spectra for mercury arc lamp indicating the emission lines.

It is possible to create different type of structures using photo-lithography. For instance, a uniform coating of a thin film multilayer can be etched to create strips/mesas or trenches for transport measurement can be created in the photoresist to deposit contact layers on a chip. Photolithography is heavily used in the semiconductor industry, hence it advances very rapidly driven by the need to miniaturize semiconductor elements like transistors and memory bits within a chip. Miniaturization has been the main driving force of the whole semiconductor technology since the discovery of the transistor back in 1947 [3].

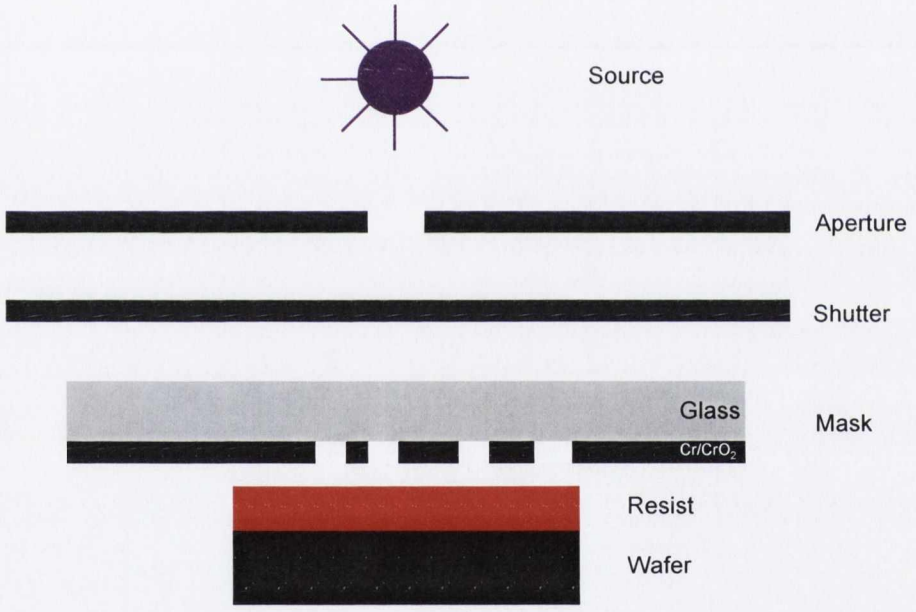

Figure 3. 2. Schematic of a basic lithographic exposure system.

Figure 3.2 shows a schematic of a simple system for photolithography. The optical source at the very top is used to shine light on the photoresist-coated wafer through a mask. The image on the mask is transferred to wafer via exposure of the resist. Depending on the resist type, either the exposed (positive resist) or the

unexposed (negative resist) area dissolves in an alkaline based chemical solution called developer. This process is called developing.

The tool used to perform photolithography is the *mask aligner*. They are called aligners because they have a dual purpose. Firstly, they have to reproduce the image of the particular pattern onto the substrate and secondly they must align that pattern to the previous one. A device production process can involve several lithography steps. Therefore, alignment is critical for reproducibility. The tools discussed in this section are all using optical sources. The energy of the exposing radiation can be in visible, UV, deep UV or extreme UV region of the optical spectrum.

The resolution of lithography is described as the minimum feature that can be exposed. There are several parameters that affect the resolution such as exposure system, photoresist, substrate, mask and the operator. The most important ones are the exposure system and the photoresist. The resolution of the exposure system depends on the quality of the optics and the wavelength of the source. Photoresist will be described in detail in the next section.

3.1.1.2. The photoresist

The resolution of the photolithography depends on several parameters. The most important one is the photoresist that is being used in the process. Photoresists can be simply categorized into two depending on the polarity. After exposure to light, exposed areas of positive photoresist dissolve in the developer but in the case

of negative resist, the unexposed areas dissolve in the developer while exposed areas remain.

A photoresist is a solution which includes a resin, base material and a photoactive compound (PAC) [2]. In positive resists, PAC acts as an inhibitor before exposure, slowing the dissolution rate of the resist in developer. After exposure, the PAC becomes sensitizer due to a chemical process and increases the dissolution rate of the resist. Ideally, the inhibitor should prevent any dissolution of the photoresist. Opposite effects happen in the case of a negative resist.

The most important metrics for the performance of a resist are sensitivity and the resolution. Sensitivity is the amount of light energy that is needed to start the chemical process described above. It is generally given in mJ/cm^2. The more sensitive a resist is, the faster the chemical process will be, since for a given intensity, the exposure time will decrease. As mentioned earlier, the resolution is the minimum feature that can be created. The resolution is given by the exposure tool and the nature of the resist. Practically, the resolution of the resist is given by the size of the polymer molecule used in the resist.

Most negative resist works by cross-polymerization, a process in which the large resin molecules attach to each other to become less soluble. A typical negative resist is an azide-sensitized rubber such as cyclized polyisoprene. Negative photoresists have very high photospeeds and adhere well to the wafer without pre-treatment. The primary disadvantage of these resists is swelling which is broadening of the linewidth during development phase. A developing after bake will typically cause the lines to return to their original dimensions.

3.1.1.2.1. Shipley S1813-G2 positive photoresist

S1800 is a high-resolution positive resist designed for g-line exposure. It is commonly used in research laboratories all over the world. The resolution of this resist is well below 1 μm as shown in Figure 3.3. It has very good adhesion and coating uniformity. Different viscosities are available for different resist thickness requirements (0.5 μm - 3 μm see Appendix). Sensitivity of the resist is 90-150 mJ/cm^2. In general, wafer primer is not needed for this resist. It was heavily used in our micro and nano-fabrication of magnetic tunnel junction devices. The process recipe is given in section 3.3.1. It can be removed using either Acetone or Microposit 1165 remover (N-methyl-2-pyrrolidone).

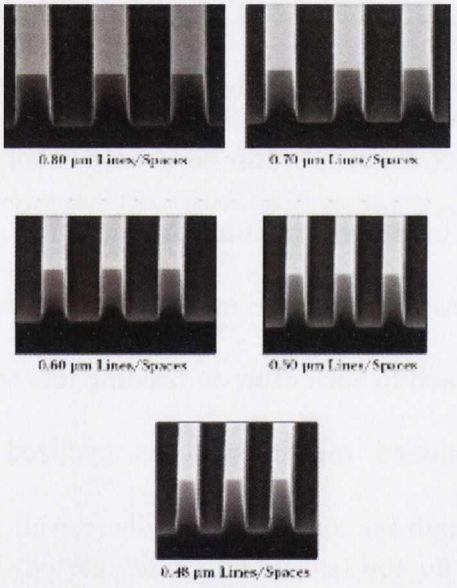

Figure 3. 3. Sub-micron lines fabricated on S1800 G2 series photoresist.

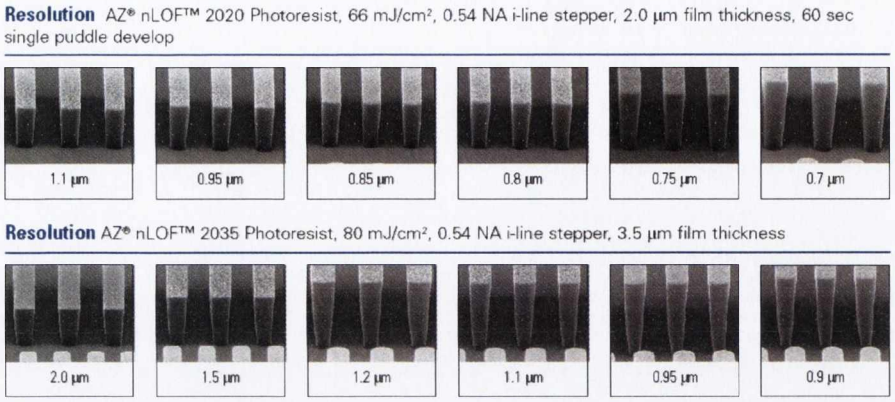

Figure 3. 4. Different size lines and spaces exposed using AZ nLOF series photoresist [4].

3.1.1.2.2. AZ nLOF 2070 negative photoresist

AZ nLOF is an image reversal (negative) resist designed for standard lift-off application with a simplified process to get a suitable lift-off profile. It is an i-line photoresist. The nLOF 2000 series photoresists work well in both surfactant and non-surfactant containing tetramethylammonium hydroxide (TMAH) developers using standard conditions. These photoresists can be used for coating thicknesses beyond 7.0 µm (see Appendix), achieving aspect ratios of up to 4:1. The resolution of the resist is not as good as S1813 positive resist but lines as small as 0.7 µm can be exposed as shown in Figure 3.4. The sensitivity of the resist is < 100 mJ/cm^2 which is comparable to S1813. The main advantage of this resist is the lift-off performance. It is critical especially in magnetic tunnel junction fabrication which requires insulation layer deposition (in general SiO_2 or AlO_x). It is well known that lift-off of oxide materials is more difficult compared to metals. Therefore, much effort has to be spent on the lift-off process. This resist can be easily removed using Microposit

1165 remover (N-methyl-2-pyrrolidone). This resist was also used in our microfabrication process. The process recipe can be found in section 3.3.1.

3.1.1.3. The mask aligner

The simplest type of aligner is a contact printer. In contact printing, the resist coated sample is pressed against the mask during exposure. This type of aligners is advantageous because reasonably high resolution can be achieved with inexpensive aligners. This is ideal for research laboratories therefore it is popular in academia rather than the industry. Figure 3.5 shows a Karl Suss MJB3 contact exposure system used in our lab.

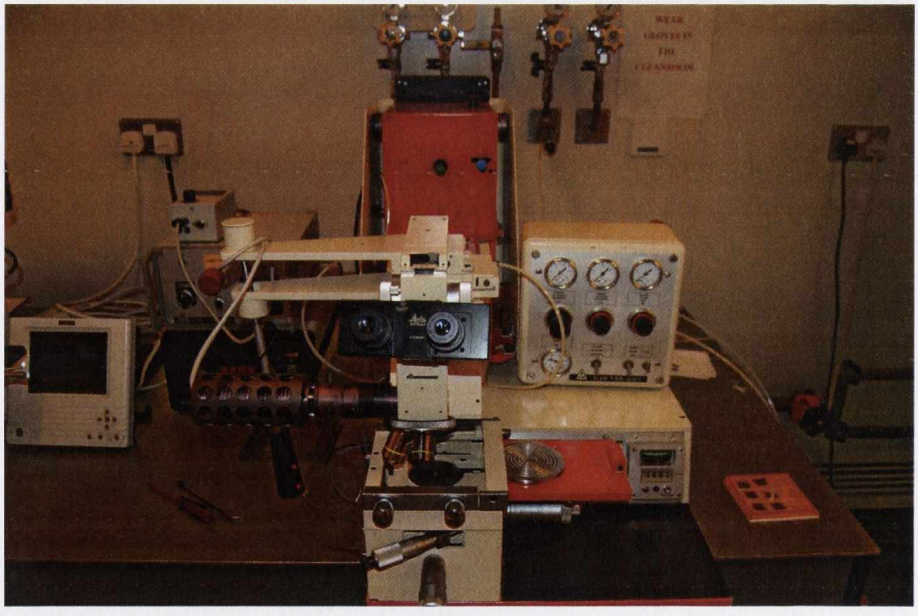

Figure 3. 5. Image of a Karl Suss MJB-3 mask aligner.

Operation is very simple: the mask is held chrome side down in a frame just below the microscope objectives. The resist coated sample/wafer is mounted on a moveable sample holder. Micropositioners are used the move the sample with respect to the mask. In general there are three micropositioners for x, y and θ (substrate rotation). It is common to use vacuum to keep the sample fixed on the holder. Once the sample is aligned to the mask, sample is pushed against the mask with mechanical pressure, N_2 flow or vacuum to obtain contact. Once the contact is obtained, the microscope and the lamp assembly moves forward and the shutter opens to start exposure. The exposure dose is controlled by time with a fixed light intensity.

The contact between the mask and the sample is a critical parameter to have high resolution in this type of exposure system. The best contact is achieved using the vacuum contact method where the sample chamber is pumped via a mechanical pump. The gap between the mask and the sample causes diffraction effects, hence the feature size increases. But, a perfect contact can never be achieved because neither the sample nor the mask is ever perfectly flat. Resist thickness uniformity also affects the overall resolution of the exposure. Non-uniform thickness along the sample will result in contact difference hence change the resolution. The resolution of common systems is around 0.5 μm.

The main disadvantage of contact exposure systems is the defect generation due to contact between the resist-coated sample and the mask. Defects can be generated both on the substrate and the mask on every contact cycle. Therefore, contact systems are not used in the semiconductor industry. To overcome these problems, proximity printing is developed. In this type of tool, mask floats on the

surface of the sample using a cushion of nitrogen gas and the gap can be controlled by adjusting nitrogen flow. This overcomes the defect creation due to absence of contact but the problem with proximity printing is the reduction in the resolution. In order to increase the resolution, projection type exposure systems are developed. Projection aligners are most widely used exposure tools for manufacturing of integrated circuits. Details of projection aligners won't be discussed in this thesis.

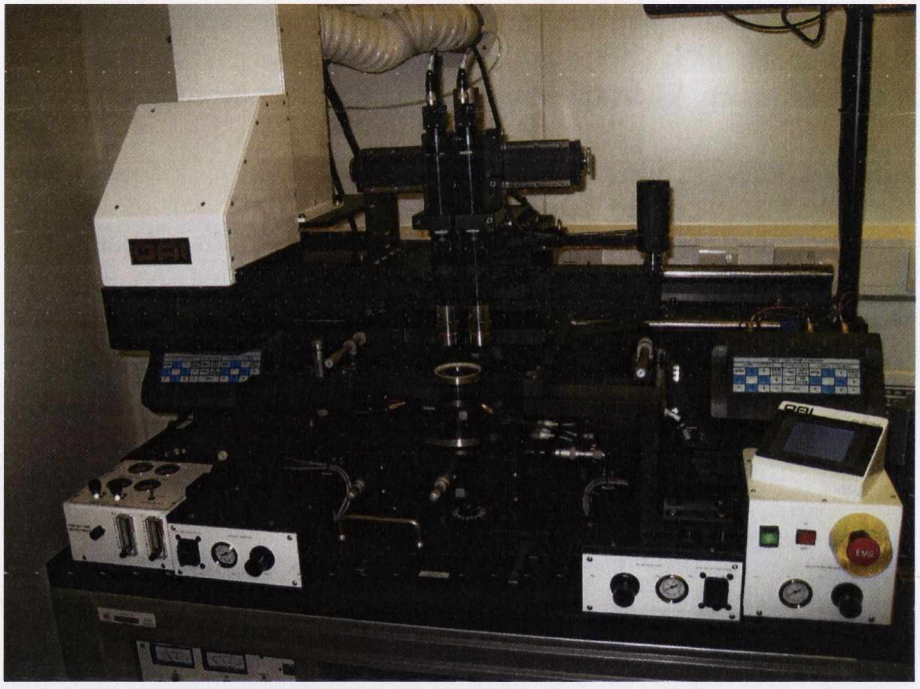

Figure 3. 6. Picture of the OAI UV mask aligner.

3.1.1.3.1. OAI mask aligner

In this study, OAI Model 800 CE mask aligner is used to perform photolithography, see Figure 3.6. It is a typical contact printing tool. It is capable of

doing back-side and front-side alignment and exposure with a nano-imprint option. It is possible to expose up to 6″ wafers. The exposure wavelength can be altered to near UV (365 nm) or deep UV (220-260 nm) with the replacement of mirrors. The exposure is performed at a constant intensity of ~ 20 mW/cm^2. There are three exposure modes: soft contact, hard contact and the vacuum contact. Best resolution of < 1 μm can be obtained by vacuum contact with careful optimization of exposure dose and development time of particular resist. The tool is located in the CRANN Class 100 clean room.

3.1.1.4. The optical mask

Photolithography masks are made of UV transparent glasses which are coated with Cr/CrO_2 thin film. It is important to consider the type of glass out of which the mask is made: the *thermal expansion* of the glass and its *transmission* at the exposure wavelength have to be considered. Typical glass materials are soda-lime, borosilicate and quartz (fused glass). All of these three materials have different thermal and transmission coefficients. For example; soda-lime glass has a thermal expansion coefficient of 9.3 ppm/°C which means a 5 inch mask will expand ~ 1.2 μm per °C. Borosilicate and quartz have much lower thermal expansion coefficients. On the other hand, soda-lime glass and borosilicate starts to absorb strongly at wavelengths below 350 nm, hence quartz is used for wavelengths lower than the i-line.

Figure 3. 7. Image of Heidelberg DWL 66 direct writing system.

Masks are designed using softwares like Autocad or Layout editor and can be fabricated using either e-beam lithography or direct laser beam writer systems like the Heidelberg DWL 66 direct writing system (Figure 3.7). The Heidelberg system is equipped with a laser interferometer stage with an alignment accuracy of 10 nm. The minimum feature size is 0.6 μm. In this study, The Heidelberg system was used to make UV masks for MTJ fabrication. Figure 3.8a shows an MTJ mask design created using Layout editor. Different lithography masks can be designed in a same file by overlaying different layers to align them properly. One of the completed MTJ mask is shown in Figure 3.8b. The dark areas on the mask are the Cr / CrO coated regions

which will block the UV light during exposure. Soda-lime glass coated with CrO (8) / Cr (62) / CrO (30) was used to make masks. Numbers in parenthesis indicate the thickness of the coating in nm.

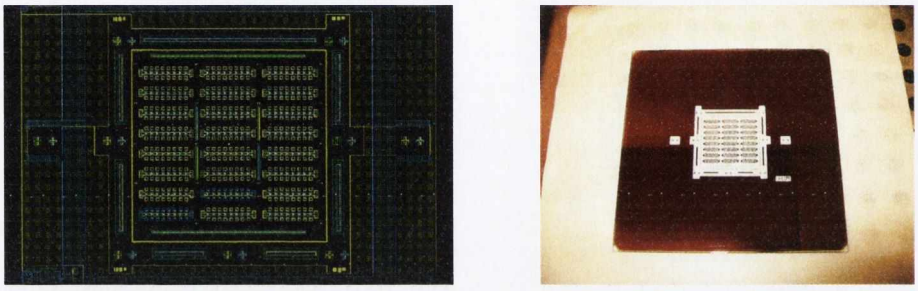

(a) (b)

Figure 3. 8. (a) Capture from MTJ mask design (b) Image of a completed MTJ mask

3.1.2. Ion milling

Ion milling or ion beam etching is very similar to sputtering in which the target atoms are ejected when a highly energetic noble gas ion hits the surface. The only difference from sputtering is that the noble gas ions are created in an ion gun and accelerated towards the sample surface. It is a strictly mechanical process, sometimes called the micromechanical analogy of sandblasting. Ion milling has two main advantages: directionality and applicability. The directionality is a due to the fact that ions in the beam are accelerated by a strong electric field and the chamber pressure is low enough to minimize the atomic collisions. Anisotropic etching is practically possible for any material since it is a chemistry-independent process. The

second advantage of ion milling is that it can be used to etch wide range of materials even if there are no volatile etch products.

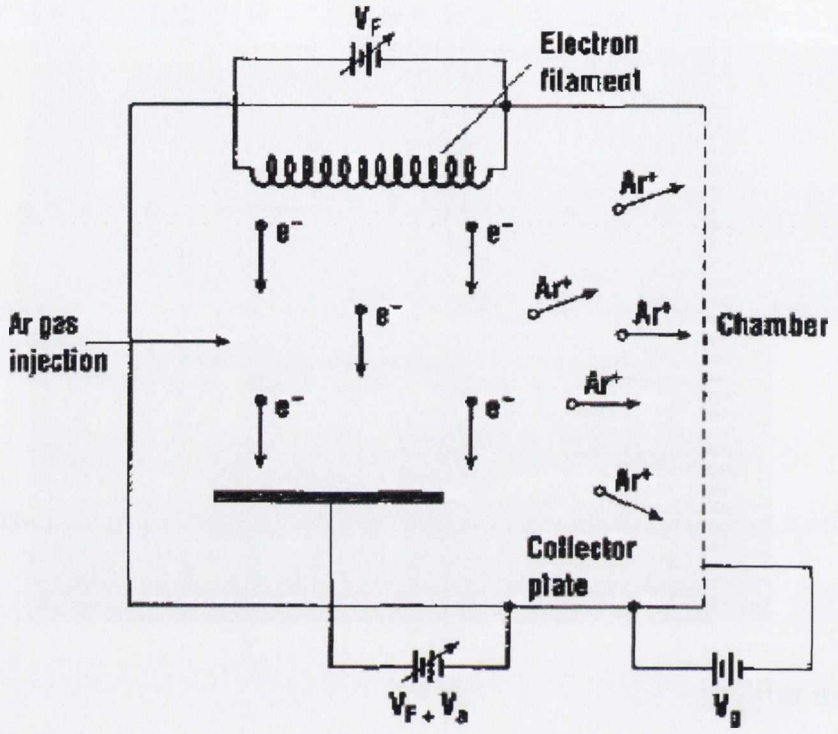

Figure 3. 9. Schematic of the Kaufman type ion source [5].

There are different types of sources for ion milling. The most popular one is the Kaufman source [5] which is shown in Figure 3.9. This source has a filament to create electrons by heating the filament with an applied potential (V_F). Electrons emitted from the filament and are accelerated towards the anode which is kept at a positive potential. The anode potential V_a must be large (~40 V) enough so that accelerated electrons have sufficient energy to ionize the neutral gas atoms. In order to sustain a stable plasma, the source is held around 10^{-3} Torr pressure. One side of the ion source has a grid which is made of tungsten or carbon. The grid is held at a

potential V_g which accelerates the ions towards the substrate. Typical accelerating potentials are 500 V to 1000 V. To increase ion density, a magnetic field is also applied to the source. The field strength is around 10 mT. This field changes the trajectory of electrons accelerated towards the anode hence the number of collisions with noble gas atoms increases roughly by a factor of 10. This in return increases the ion density. Typical Kaufman sources can produce ion current density of 1 mA/cm^2.

Other widely used type of ion source is the electron cyclotron resonance (ECR) controlled plasma reactor (COPRA) in which the ion current density, ion energy and the degree of ionization can be controlled independently of each other [6]. The COPRA is flamentless single turn inductively coupled RF (13.6 MHz) discharge with a superimposed static transverse magnetic field. The ion energy can be varied by applying an RF bias voltage to an electrode placed behind the plasma ball. The plasma is typically ignited by the creation of a pressure pulse. The process gas is fed directly into the excitation cavity of the plasma source. Resonant excitation of the plasma (by Electron Cyclotron Wave Resonance) is achieved by applying a weak DC transverse magnetic field (~ 2 mT) generated by means of a series of built-in Helmholtz coils. The strength of the magnetic field is controlled by an auxiliary power supply. The COPRA type sources typically operate within a pressure range of approximately 0.3 to 3 $\times$ 10^{-3} Torr. The advantages of COPRA ion source are low pressure operation, high plasma density (1 $\times$ 10^{12} cm^3), high ion current density (3 mA/cm^2), and longer life time.

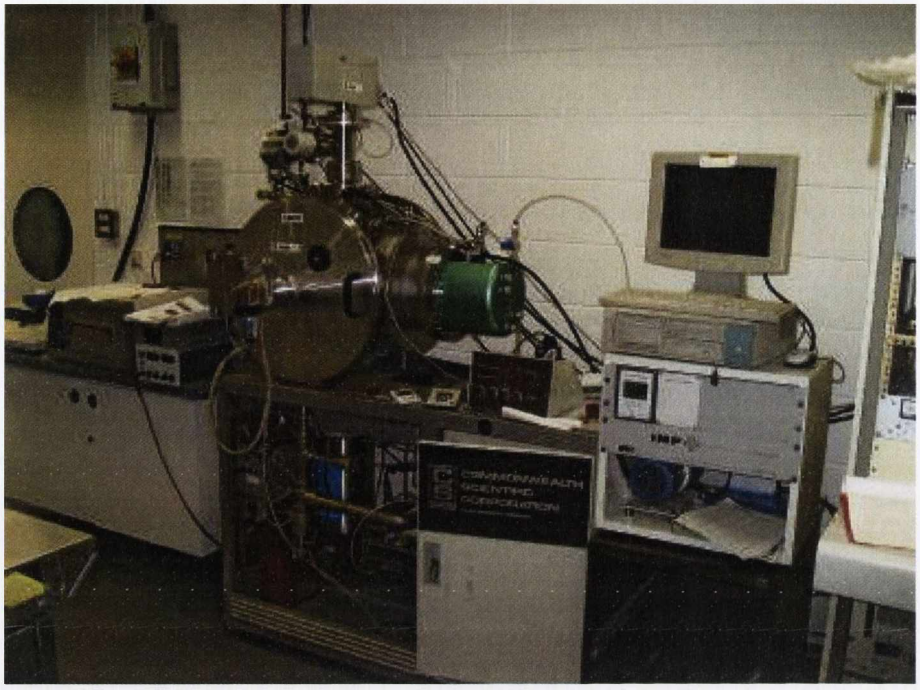

Figure 3. 10. Millatron ion milling system with an end point detector.

3.1.2.1. Millatron Ion Milling Tool

The Millatron ion milling system (Figure 3.10) consists of a vacuum chamber with a rotational water-cooled sample stage and end-point detector, a CCR Technology COPRA DN250 plasma beam source with an RF power supply (max 1.2 kW), a DC supply which controls the magnet (Helmholtz coils) in the ion gun and a mass flow controller (MFC) which supplies high purity (6N) Ar into the system. The base pressure of the system is typically 2×10^{-7} Torr achieved with a cryogenic pump. The operating pressure is in general $0.5 - 1.0 \times 10^{-4}$ Torr. RF power of 300 - 400 W is used with a magnet current of 2.5 A. The water cooled sample is rotated during milling and can be tilted 0 - 90° with respect to the ion beam.

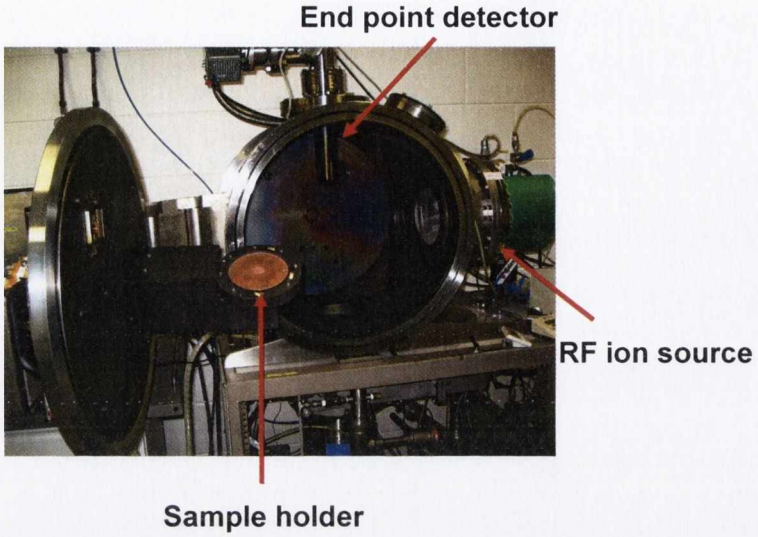

Figure 3. 11. Inside view of Millatron ion milling system indicating the end point detector, substrate holder and ion source.

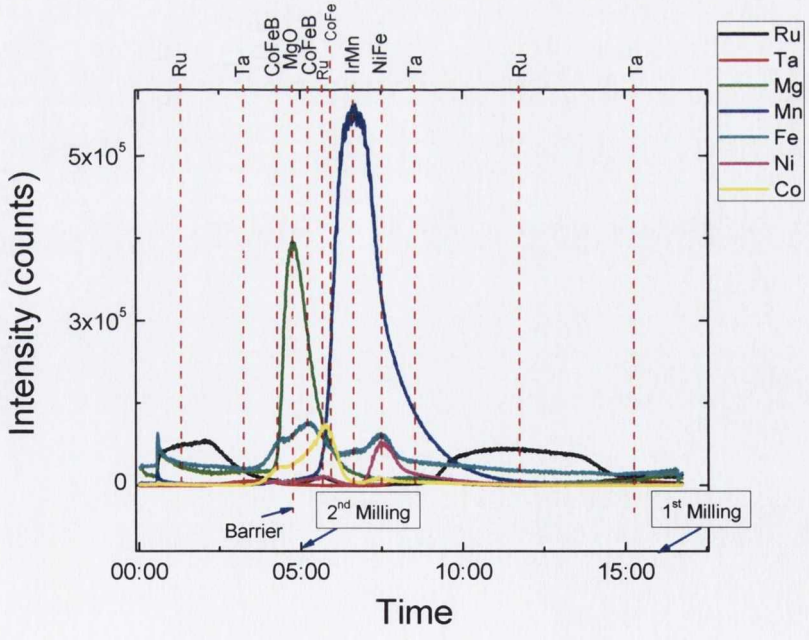

Figure 3. 12. Typical EPD scan taken during ion milling of an MTJ sample indicating individual layers and the stopping points for the 1st and 2nd milling.

One of the most important issues in ion milling process is how to precisely control it, stopping the milling process at certain layers in the multi-layer stacks. In the case of MgO-based MTJs, it is critical to stop the milling below MgO layer. For this purpose, a highly sensitive Hiden end-point detection (EPD) system was used, as shown in Figure 3.11.

The Hiden EPD consists of ion milling probe, radio frequency head with an amplifier and PC running MASsoft. The ion milling probe contains an energy filter, a quadrupole mass spectrometer and a secondary electron multiplier detector. Any ions entering the quadrupole field experience potential differences deflecting them from their original trajectory. The extent of deflection of any ion entering the field is related to its mass: charge (m/e) ratio. At each interval on the RF scan only one m/e ratio resonates with the field allowing the ion to pass along the z-axis. All other species are deflected and neutralized by impact upon the rods of the quadrupole. The ion signal then collected and displayed by the MASsoft. Using the software, a certain end-point of the ion milling process can be easily set. Typical scan during milling is illustrated in Figure 3.12.

3.1.3. Lift-off

Lift-off is an alternative technique to etching processes like ion milling and reactive ion etching. It is used if the material is sensitive to etch damage. In order to obtain good lift-off result, it is critical to have high aspect ratio resist. There are several resists which are designed for lift-off. Alternatively, undercut can be created in the resist which considerably improves the performance of lift off. This can be

achieved by dipping resist coated wafer into chlorobenzene or similar compounds [7-9] after soft bake. The soak process reduces the dissolution rate of upper surface of the resist. After development, a ledge appears like in Figure 3.13.

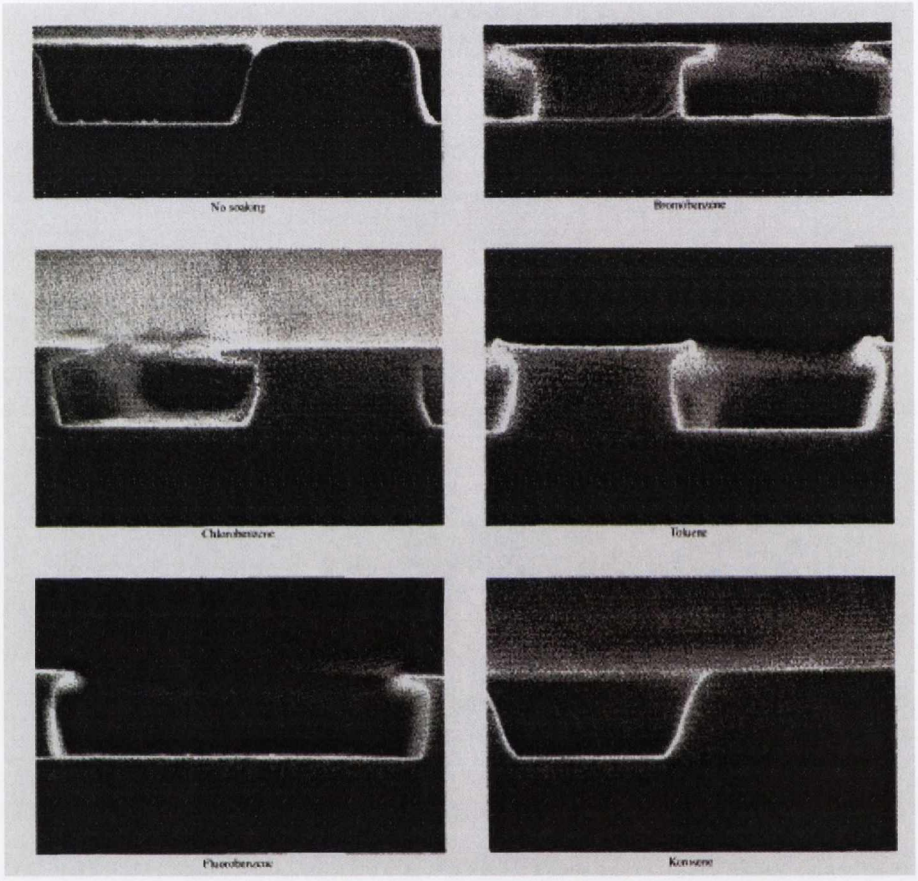

Figure 3. 13. Lift off profiles after several resist treatments [7].

The lift-off process is used in steps of our MTJ fabrication where we deposit SiO_2 for insulation or a Ta / Cu bilayer for contact (see sections 3.3.1 and 3.3.2). AZ nLOF 2070 negative photoresist was used in our process. The thickness of the resist is more than 2 μm with a reasonable undercut, hence lift off is relatively easy compared to S1813. For effective lift off, Microposit 1165 remover (N-methyl-2-

pyrrolidone) is used and sample is kept in remover at 80 °C in ultrasonic bath for approximately 1 hour. It was possible to improve lift-off process using SiO evaporation which results in less conformal coating around the edges of the photoresist.

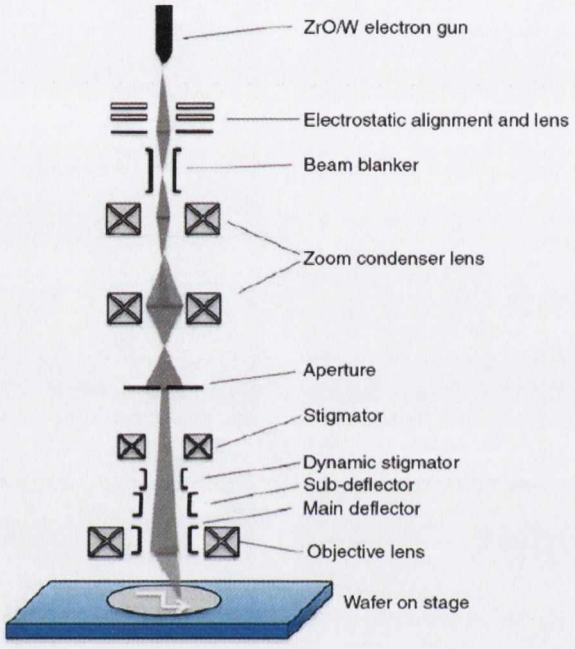

Figure 3. 14. Schematic of a modern electron column [10].

3.2. Nano-fabrication process

3.2.1. Basics of electron beam lithography (EBL)

Electron beam lithography is an essential method to create sub-micron features which became very important with the emergence of nanotechnology. It is a precise and high-resolution direct write method. The advantage of EBL over photon based lithography systems are: higher resolution, lower diffraction effects and direct transfer of pattern from a data file.

The essential element of an EBL system is the electron column which is similar to the ones in scanning electron microscopes. The schematic of a modern EBL system is shown in Figure 3.14. Electrons are readily focused and steered using magnetic and electric fields due to their high charge to mass ratio. Therefore, electron columns use magnetic and electrostatic lenses. Another important point is that, since electrons are charged and very light particles, they interact with gas atoms. Therefore, the entire electron column has to be kept under high vacuum to reduce the effect of scattering which will disturb the focus of the electron beam.

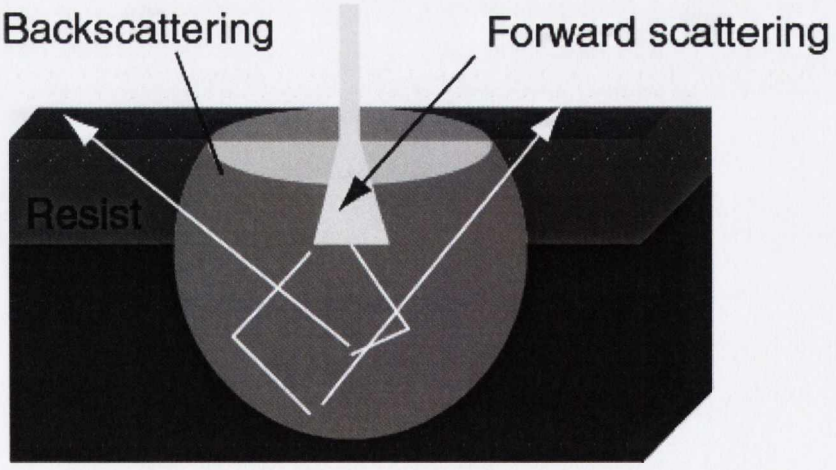

Figure 3. 15. Illustration of interaction volume of electrons in the resist and substrate [10].

The resolution of an EBL system mainly depends on the alignment quality of the electron column and the accelerating voltage that is being used. The alignment quality determines the minimum electron beam spot size achieved. It should be as small as possible because it basically determines the minimum feature that can be exposed. On the other hand, the accelerating voltage affects the interaction of the electrons with the resist. It is well known that electrons have certain interaction volume when they enter the resist (Figure 3.15). Shape of the interaction volume strongly depends on the energy of the electrons as shown in Figure 3.16. In the case of low voltage (10 kV), lateral dimension of the interaction region can be as large as 200 nm for an electron beam diameter of 10 nm. It can be dramatically reduced to 12 nm when high voltage (100 kV) is used. The effect of electron energy is clearly observed in Figure 3.16.

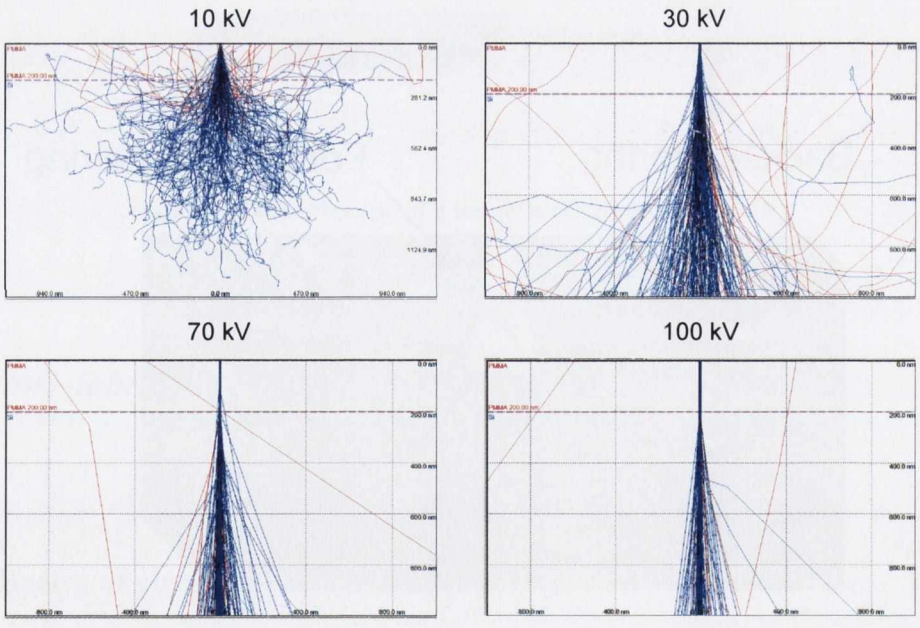

Figure 3. 16. Monte Carlo simulations of electron penetration in a 200 nm PMMA resist on a Si wafer calculated for different electron energies (Casino v 2.42 [11]).

Resolution of EBL depends on not only the exposure tool but also the e-beam resist that is used. There are several high resolution positive and negative e-beam resists. Table 3.1 summarizes properties of some common e-beam resists. PMMA (Poly-methyl methacrylate) and HSQ (Hydrogen silsesquioxane) are the e-beam resists which have the highest resolution. PMMA is a positive resist with low sensitivity but sub 10 nm resolution has been reported [12]. Similarly, HSQ is the highest resolution negative resist. Sub 10 nm lines were also demonstrated using thin HSQ resist [13]. TOK TGMR-EN103PE is a chemically amplified negative e-beam resist that has high resolution with high sensitivity (30-80 $\mu C/cm^2$).

Table 3. 1 Properties of common ebeam resists

Resist	Tone	Resolution	Etch Resistance	Sensitivity ($\mu C/cm^2$ at 30 kV)
PMMA	**Positive**	Very high	Poor	200 - 400
ZEP 520	**Positive**	Very high	Good	100 - 200
UV-5	**Positive**	High	Good	10 - 20
HSQ	Negative	Very high	Good	300 - 700
TOK-TGMR-EN103PE	Negative	High	Good	30 - 80
SAL 601	Negative	High	Moderate	5 - 15

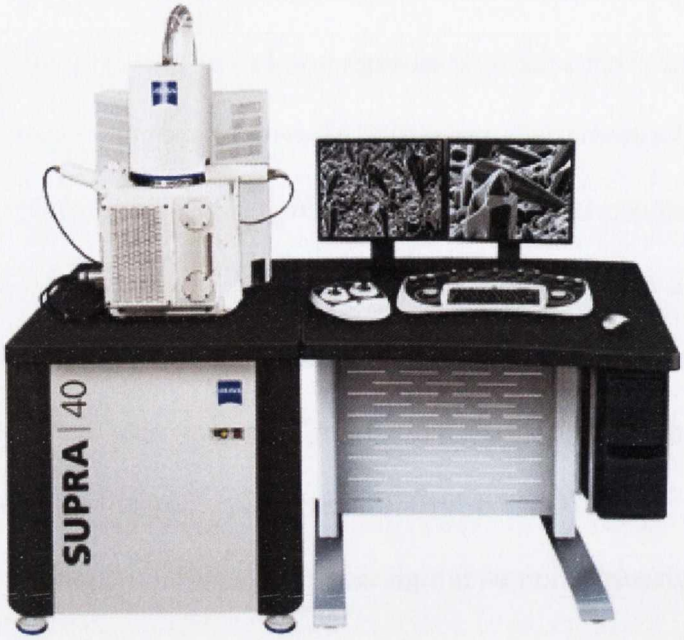

Figure 3. 17. Image of Zeiss SUPRA 40 scanning electron microscope.

3.2.2. Carl Zeiss SUPRA 40 scanning electron microscope for EBL

The Carl Zeiss Supra 40 is a general purpose ultra high resolution field emission- scanning electron microscope (SEM) based on the unique GEMINI® technology equipped with Raith Elphy Quantum software to facilitate e-beam lithography (Figure 3.17). The microscope can operate over a wide voltage range 0.02 - 30 kV. It has both conventional and in-lens imaging detectors to obtain high quality images. Imaging resolution is better than 5 nm. Most of the EBL in this study is performed using this microscope which is located in the Advanced Microscopy Laboratory (AML) of CRANN. An accelerating voltage of 30 kV was used to obtain the highest resolution. The e-beam current was 16 and 20 pA using 7.5 μm and 10

μm apertures, respectively. A working distance of 4 mm was used while having 100 × 100 μm^2 write field. The exposure step size was kept at 6 nm for all exposures. Dose was adjusted by varying the exposure dwell time.

3.2.3. TOK TGMR-EN103 PE Negative e-beam resist

TGMR-EN103 is a high resolution and high sensitivity negative e-beam resist as mentioned in the previous sections. It has very good dry etch resistance with reasonable contrast. This resist can be coated in the thickness range of 100 - 700 nm (see Appendix) by using different viscosities like 2.5 cp or 3.6 cp. It is a chemically amplified resist; therefore it is very sensitive to baking and development time and temperature. The sensitivity of the resist is 20 - 80 $\mu C/cm^2$. Features down to 30 nm has been demonstrated [14]. The shelf life of the resist is relatively short, 6 months, if it is refrigerated. This negative resist has been extensively used in our nanofabrication process, details can be found in section 3.3.2.

3.3. Device integration

3.3.1. Micron scale device fabrication procedure

The fabricated MTJs are patterned into micron-sized junctions to carry out transport and magnetoresistance measurements via the conventional four-point probe

technique. Micron scale MTJs were mainly used for MTJs with thick (2 - 3 nm) MgO barrier layer. Microfabrication is achieved by a combination of UV-lithography, Ar^+ ion milling and lift-off. UV-lithography is performed in the CRANN Class-100 clean room using the OAI 800 CE (wavelength 365 nm) mask aligner as mentioned in section 3.1.1.3.1. MTJ junction size can be as small as 4 × 4 μm^2. Figure 3.18 shows the SEM micrograph of a negative resist pillar which was exposed with nominal size of 4 × 4 μm^2. The corners of the pillar are not well defined and the actual size is larger than 5 × 5 μm^2. This is mainly due to a low contact pressure during exposure of the resist. MTJs can be produced with different aspect ratios such as 1:1 and 1:3. The biggest junction size is 50 × 150 μm^2.

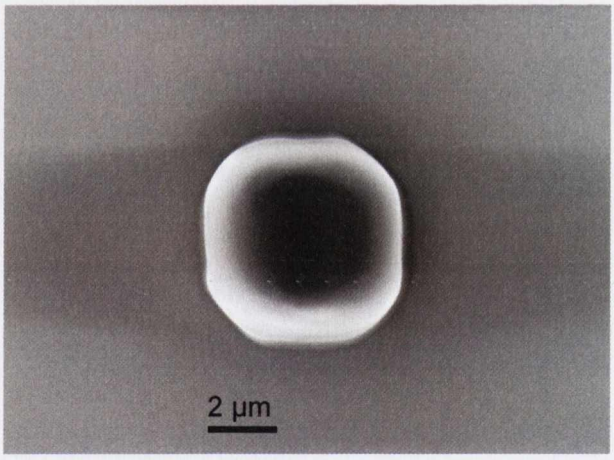

Figure 3. 18. SEM micrograph of a resist pillar with nominal size of 4 × 4 μm^2 taken during the second step of the MTJ microfabrication.

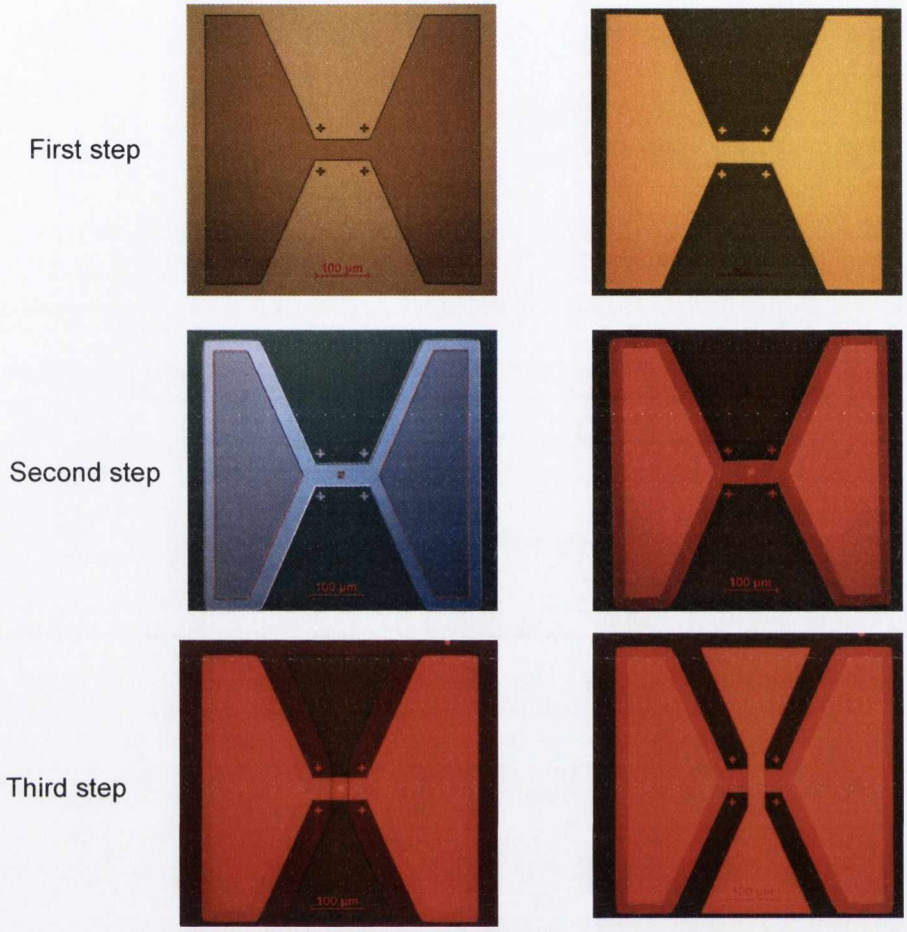

Figure 3. 19. Optical images of the entire microfabrication process indicating exposure (left images) and after lift-off (right images) for three steps. First step: bottom contact patterning, Second step: junction definition, Third step: top contact patterning.

Figure 3.19 illustrates the optical images of the microfabrication steps. The complete microfabrication process is composed of three main steps and those are as follows;

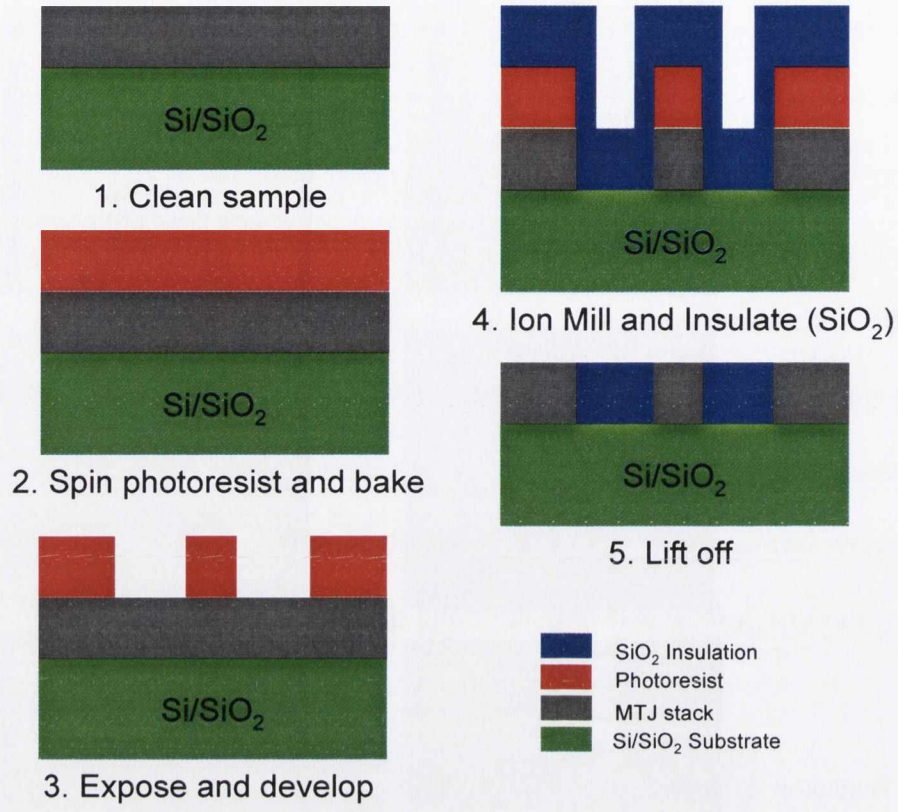

Figure 3. 20. First step of photo-lithography process.

(1) Bottom contact patterning (Figure 3.20) ;

a. Shipley 1813 positive photoresist is spun on the full MTJ stack (Spinning parameters: 5000 rpm (~1.2 μm) for 45 s).

b. Resist is pre-baked at 115 ^{o}C for 2 mins.

c. Photoresist is exposed for 5.5 s (~80 mJ/cm^2) with MTJ-1 mask using the OAI mask aligner.

d. Photoresist is developed in MF 319 developer for 40 - 60 s.

e. Samples are loaded into our Millatron ion milling system and etched at 45° down to the SiO_2 substrate (approx. 25 mins at 400 W RF power).

f. 70 nm of SiO_2/SiO is deposited.

g. Lift-off of the photoresist/SiO_2 is performed in Microposit 1165 remover (N-methyl-2-pyrrolidone) using an ultrasonic bath at 80 °C for 30 mins.

(2) Junction area definition (Figure 3.21);

a. AZ-nLOF 2070 negative photoresist is spun on the sample (Spinning parameters: 3000 rpm (~ 2 μm) for 45 s).

b. Resist is pre-baked at 115 °C for 1 min.

c. Photoresist exposed for 5.5 s (~ 80 mJ/cm^2) with MTJ-2 mask using the OAI mask aligner.

d. Resist is post-baked at 115 °C for 1 min.

e. Photoresist is developed in MF 319 developer for 40 - 60 s.

f. Samples then are loaded into our Millatron Ion Milling system and etched at 75° down to bottom FM electrode (approx. 10 mins at 400 W RF power).

g. SiO_2 (or SiO) (~ 50 nm) is sputtered (evaporated) on the etched samples in order to insulate the top and bottom contact.

h. Lift-off of the photoresist/insulation is performed in Microposit 1165 remover (N-methyl-2-pyrrolidone) using ultrasonic bath at 80 °C for 1 hour.

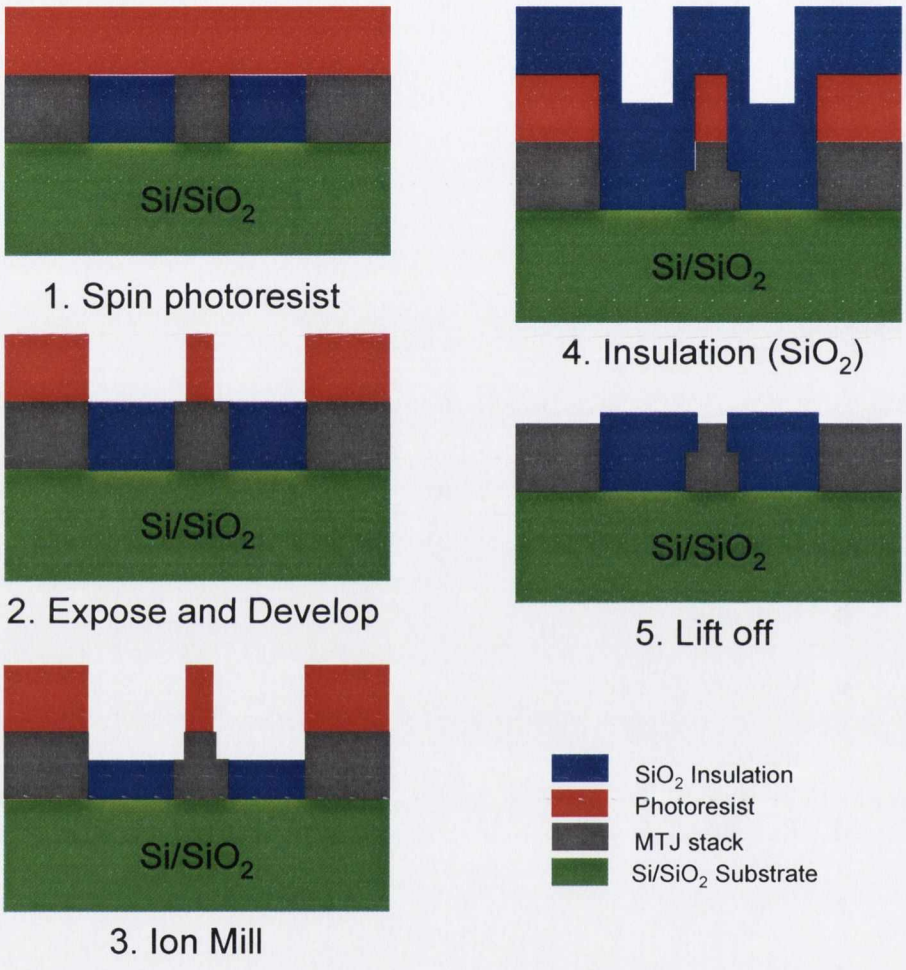

Figure 3. 21. Second step of photo-lithography process.

(3) Top contact patterning (Figure 3.22);

a. Shipley 1813 positive photoresist is spun on sample (Spinning parameters: 5000 rpm (~ 1.2 μm) for 45 s).

b. Resist is pre-baked at 115 °C for 2 mins.

c. Photoresist exposed for 5.5 s by using MTJ-3 mask using the OAI mask aligner.

d. Photoresist is developed in MF 319 developer for 40 - 60 s.

e. Ta (5 nm)/Cu (50 nm) bilayer is sputtered as top contact on the resist defined areas.

f. Lift off is performed in acetone in the ultrasonic bath.

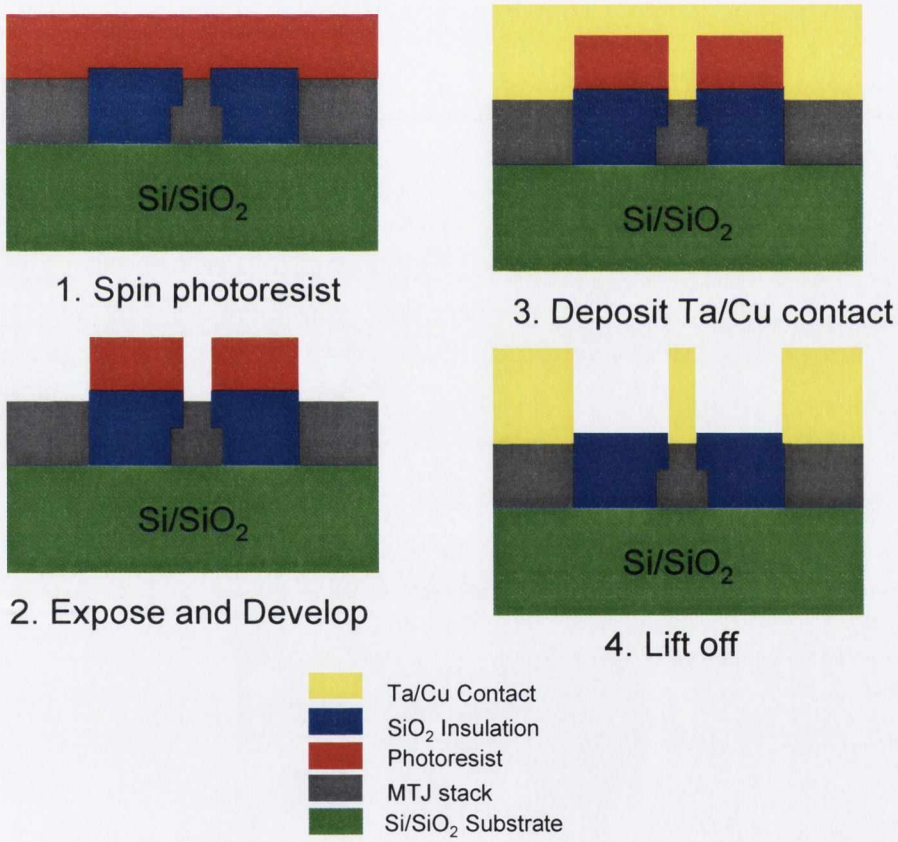

Figure 3. 22. Third step of photo-lithography process.

3.3.2. Nano scale device fabrication procedure

MTJs with thin MgO (~ 1 nm) barrier were patterned into sub-micron junctions (nanopillars) by the combination of UV-lithography, E-Beam lithography (EBL) and Ar^+ Ion Milling to perform spin transfer torque measurements. The entire process simply includes two UV steps for bottom and top contact patterning and a single EBL step is used to obtain nanopillars. Nano-fabrication process is identical to micro-fabrication except the nanopillar defining step.

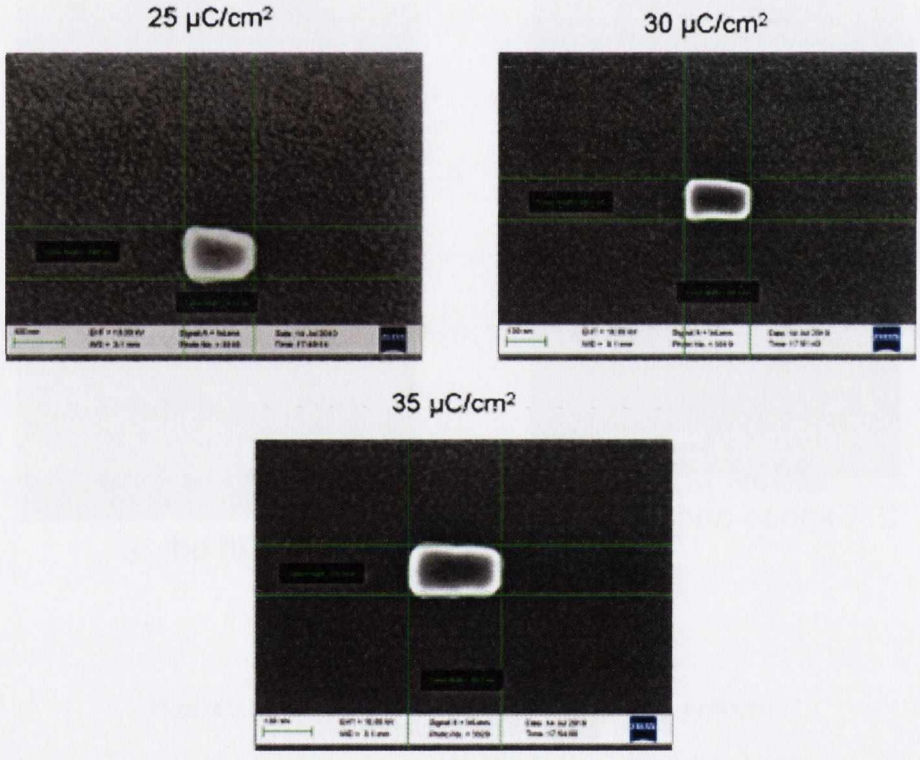

Figure 3. 23. SEM images of 100 × 200 nm² rectangular nanopillars exposed at different exposure doses.

3.3.2.1. Optimization of TOK TGMR e-beam resist

Typically, 100 × 200 nm^2 rectangular nanopillars (shown in Figure 3.23) were fabricated. Optimum parameters are found by careful optimization of exposure dose for a given accelerating voltage of electrons (30 kV). Figure 3.23 shows the effect of dose on the nanopillar size for 100 × 200 nm^2 pillar exposure. For 25 $\mu C/cm^2$, the shape of the pillar is not very good and dimensions are 106 × 142 nm^2. As the dose increases the shape of the pillar gets better and the dimensions approach the designed values. It is found that 35 $\mu C/cm^2$ is the best dose for a 100 × 200 nm^2 for a rectangular nanopillar. Exposure dose depends on the accelerating voltage of the electrons due to the fact that the interaction volume of the electrons changes with energy. In general, dose has to be increased with increasing electron energy.

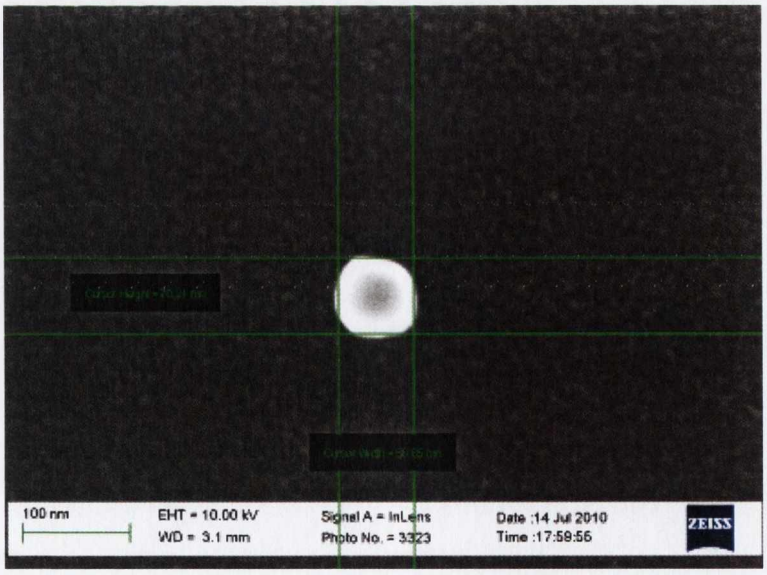

Figure 3. 24. Smallest nanopillar exposed using TOK TGMR negative resist (70 × 70 nm^2)

The smallest nanopillar fabricated is shown in Figure 3.24 and the size of the nanopillar is 70 × 70 nm^2. Pillar size can be further reduced by reducing the resist thickness but lift-off will be almost impossible. It has to be replaced by a chemical mechanical polishing step.

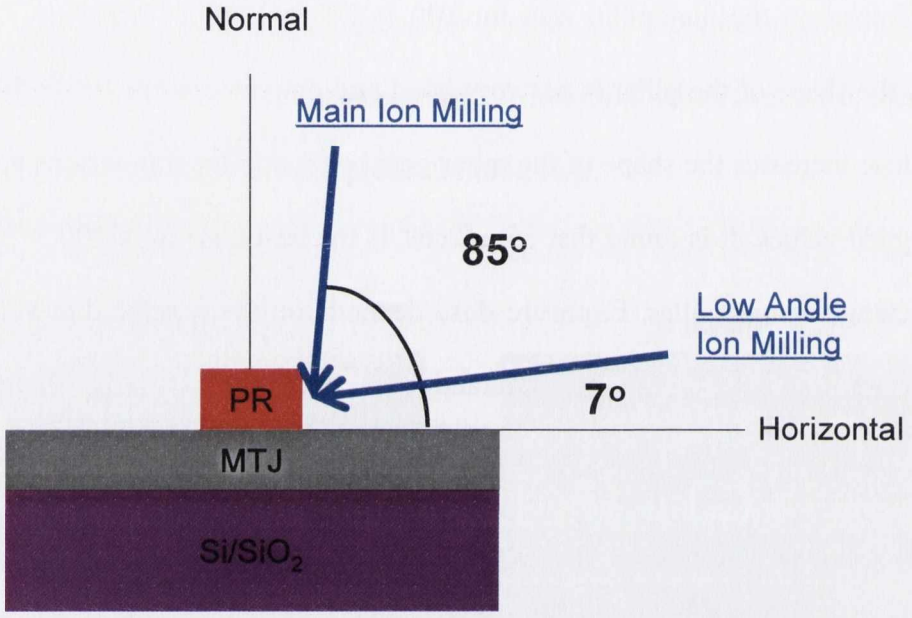

Figure 3. 25. Schematic description of main and low angle Ar ion milling.

3.3.2.2. The effect of low angle ion milling

The nanopillar profile and sidewall deposition are very important drawbacks of Ar^+ ion milling and they have significant effects on the spin transfer torque magnetisation reversal because these affect the switching behaviour of the free layer. Therefore, we investigated two-step ion milling: 85° main milling + 7° low angle milling (shown schematically in Figure 3.25). The main milling takes 7 - 10 mins

depending on the cap layer thickness and milling rate. Figure 3.26 shows cross-section HR-TEM micrographs of nanopillars fabricated using additional low angle milling. Figure 3.26a has only 1 min of low angle milling and the edges of the pillar are not sharp. However, if we increase the time of the low angle milling up to 3 mins, the pillar edge profile significantly improves and becomes much sharper, see Figure 3.26b.

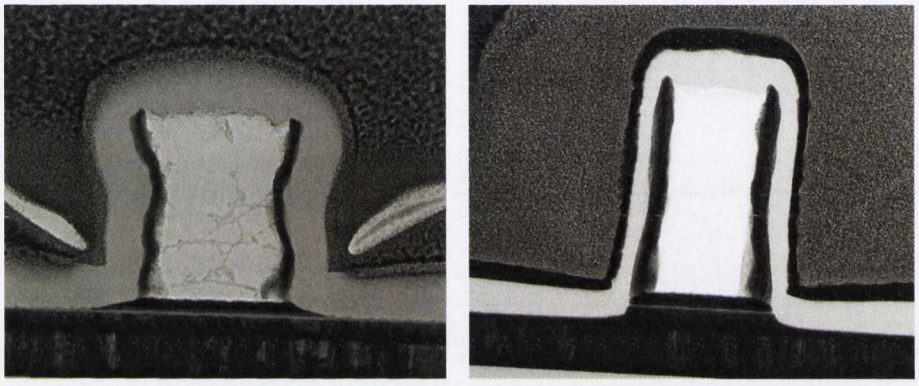

(a) (b)

Figure 3. 26. The effect of low angle (7^{0}) ion milling (a) short time (1 min) (b) long time (3 mins).

The nanofabrication process is as follows;

(1) Bottom contact patterning is the same with microfabrication process (see previous section

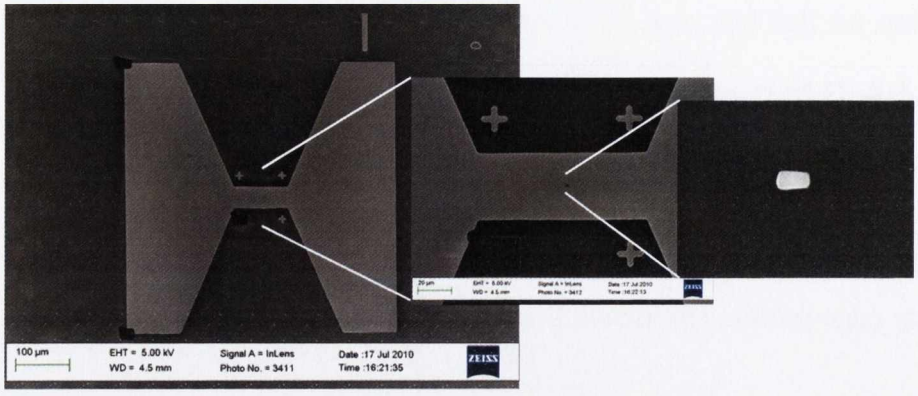

Figure 3. 27. SEM micrographs of pillar position on the bottom contact strip.

(2) Nanopillar definition by EBL:

a. HMDS:IPA mixture is spun on the cleaned sample (Spinning parameters: 4000 rpm for 45 s)

b. Sample is baked at 110 ^{o}C for 120 s.

c. TOK-TGMR-EN103 PE negative e-beam resist is spun on the sample (Spinning parameters: 2000 rpm (~ 350 nm) for 45 s).

d. Resist is pre-baked at 110 ^{o}C for 90 s.

e. Exposure is performed using Zeiss SUPRA 40 SEM system (30 kV, Spotsize: 1, Beam current: ~ 16 - 20 pA, Dose: 20 - 80 µC/cm^2). First beam is focussed on an alignment cross which is 40 µm away from the exposure area. Then, pillar is exposed at the centre of the bottom contact strip as shown in Figure 3.27.

f. Resist is post-exposure baked at 120 ^{o}C for 90 s.

g. EBL resist is developed in NMD (TMAH 2.39 %) developer for 60 s by puddling.

h. Samples then are loaded into our Millatron Ion Milling system and etched at 85° down to the bottom FM electrode (approx. 10 mins at 400 W RF power). Extra low angle sidewall cleaning is performed at 7 - 10° for 1 - 3 mins (half time of the main ion milling).

i. SiO_2 (or SiO) (~ 40 nm) is sputtered (evaporated) on the etched samples in order to provide insulation of the top and bottom contacts.

j. Lift-off for the EBL resist/insulator is performed in Microposit 1165 remover (N-methyl-2-pyrrolidone) using ultrasonic bath at 80 °C for 4 - 6 hours (shorter for SiO ~ 2 hours).

(3) Top contact patterning is also identical to the one used for the microfabrication (see previous section).

3.4. References

1. Sheats, J.R. and B.W. Smith, *Microlithography: science and technology*. 1998, New York: MARCEL DEKKER, INC.
2. Campbell, S.A., *The Science and Engineering of Microelectronic Fabrication*. Second ed. 2001, New York: Oxford University Press.
3. Bardeen, J. and W.H. Brattain, *"The Transistor, A Semi-Conductor Triode"*, Physical Review. **74**, 230, (1948).
4. Microchem. *http://www.microchemicals.net/photoresist/photoresist_az_nlof_2070_eng.htm*. 2010.

5. Kaufman, H.R., *"Technology of ion beam sources used in sputtering"*, Journal of Vacuum Science and Technology. **15**, 272, (1978).

6. Weiler, M., *et al.*, *"Deposition of tetrahedral hydrogenated amorphous carbon using a novel electron cyclotron wave resonance reactor"*, Applied Physics Letters. **72**, 1314, (1998).

7. Hatzakis, M., B.J. Canavello, and J.M. Shaw, *"Single-Step Optical Lift-Off Process"*, IBM Journal of Research and Development. **24**, 452, (1980).

8. Fathimulla, A., *"Single-step lift-off process using chlorobenzene soak on AZ4000 resists"*, Journal of Vacuum Science & Technology B: Microelectronics and Nanometer Structures. **3**, 25, (1985).

9. Collins, G.G. and C.W. Halsted, *"Process Control of the Chlorobenzene Single-Step Liftoff Process with a Diazo-Type Resist"*, IBM Journal of Research and Development. **26**, 596, (1982).

10. Wiederrecht, G.P., *Handbook of Nanofabrication*. First ed. 2010, Amsterdam: Elsevier B.V.

11. Drouin, D. *CASINO V2.42 - A Fast and Easy-to-use Modeling Tool for Scanning Electron Microscopy and Microanalysis Users*. 2010; Available from: http://www.gel.usherbrooke.ca/casino/index.html.

12. Hu, W., *et al.*, *"Sub-10 nm electron beam lithography using cold development of poly(methylmethacrylate)"*, Journal of Vacuum Science & Technology B: Microelectronics and Nanometer Structures. **22**, 1711, (2004).

13. Baek, I.-B., *et al. Electron beam lithography patterning of sub-10 nm line using hydrogen silsesquioxane for nanoscale device applications*. 2005: AVS.

14. Pauliac-Vaujour, S., *et al.*, *"Improvement of high resolution lithography by using amorphous carbon hard mask"*, Microelectronic Engineering. **85**, 800, (2008).

Chapter 4

Magnetic Tunnel Junctions

Magnetic tunnel junctions (MTJ) with different barrier materials were fabricated and characterized in order to understand the basic physics of these structures and to explore the possible applications. In this section, the results on the dead layer formation in ultra-thin CoFeB films is given first and the following sections include AlO_x and $SrTiO_3$ (STO) based MTJs and finally the work on MgO based MTJs with high magnetoresistance.

4.1. Magnetic dead layers

Ultra-thin ferromagnetic films are becoming increasingly important, as they are key constituents of the film stacks used in magnetic sensors and memory elements. The magnetic tunnel junction (MTJ) is a widely-used device of this type and high tunnelling magneto-resistance (TMR) values are critical for high-performance MTJ devices. Recently, very high TMR (~ 250 % at room temperature) MTJs have been fabricated with MgO barriers using amorphous CoFeB alloy electrodes in several laboratories worldwide including our own [1-7]. It is the

possibility of sputtering (001) oriented magnesium oxide (MgO) barriers on top of amorphous CoFeB films and of depositing amorphous CoFeB layers on top of MgO that has made these devices possible. Annealing such a stack at temperatures higher than 300 °C leads to the coherent crystallization of a few monolayers of bcc-Co-Fe on the MgO, which results in the large TMR due to selective tunnelling of spin polarized electrons of different symmetry. Therefore, it is of interest to characterize the magnetic behaviour of ultra-thin sputtered CoFeB films that are only a few monolayers thick.

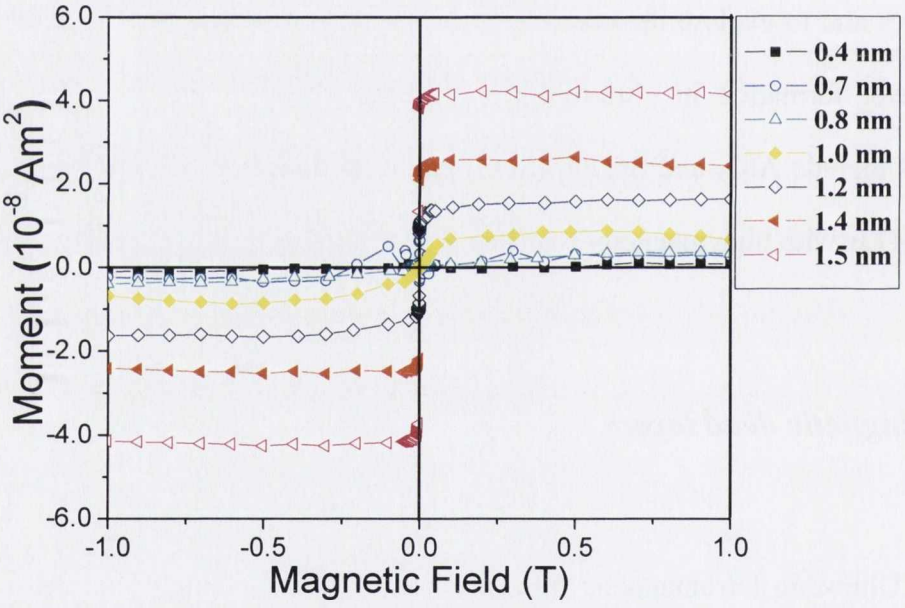

Figure 4. 1. Magnetisations of ultrathin CoFeB films deposited on MgO substrates after correction for the diamagnetism of the silicon substrate measured at RT.

There have been several previous studies of various (NiFe, CoFe, Fe and etc.) ultra-thin ferromagnetic films produced by sputtering and other methods which indicate the existence of magnetic dead layers in films that are only a few

monolayers thick [8-10]. However, there is little information on CoFeB films in the literature. It has been shown by Wang *et al.* that the thickness of the film and its interfaces significantly affect the magnetic properties of the $Co_{60}Fe_{20}B_{20}$ films, depending on the capping and seed layer materials. Films on ruthenium (Ru) and tantalum (Ta) seed layers have been studied [8]. $Co_{40}Fe_{40}B_{20}$ is one of the best alloy compositions for tunnel junctions. Films are in general grown underneath and on top of the MgO barrier. A series of Co-Fe-B films with thicknesses ranging from 0.4 nm - 6.0 nm were grown on Si (001) / SiO_2 (500 nm) and Si (001) / SiO_2 (500nm) / MgO (3 nm) substrates and all samples were capped with a Ta layer. Additional films were grown on Si (001) / SiO_2 (500nm) / Ta (5 nm) buffer layers as a reference.

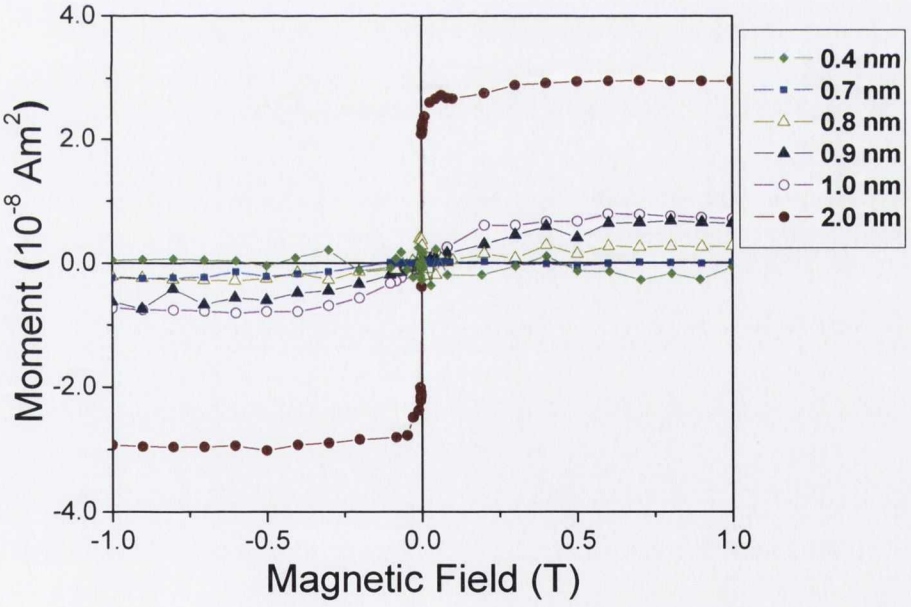

Figure 4. 2. Magnetisations of ultrathin CoFeB films deposited on SiO_2 substrates after correction for the diamagnetism of the silicon substrate measured at RT.

The magnetisation curves of as-deposited amorphous CoFeB films on MgO and SiO_2 are shown in Figure 4.1 and Figure 4.2, respectively. Films are found to be totally amorphous according to X-ray diffraction pattern of a thick CoFeB film deposited on SiO_2 as shown in Figure 4.3. All of the observed peaks belong to Si substrate. Possible $Co_{50}Fe_{50}$ related peaks are indicated with black lines on the spectrum.

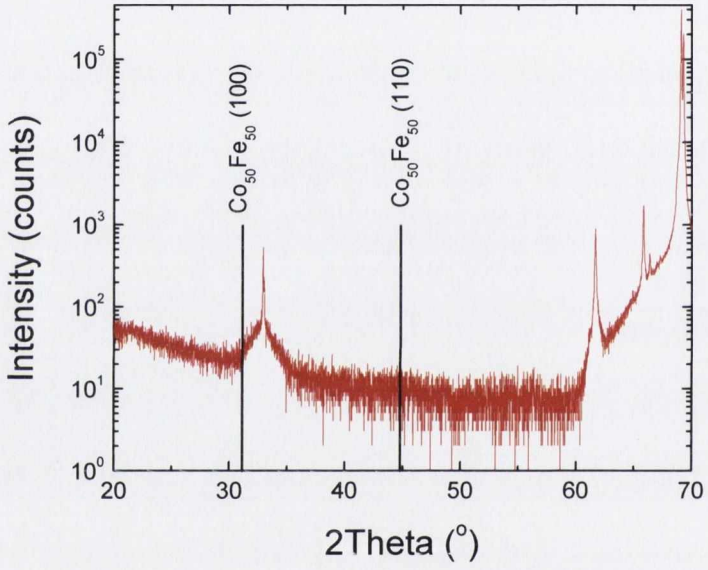

Figure 4. 3. X-ray diffraction pattern for a 30 nm thick CoFeB film grown on SiO_2.

The magnetic signal of the CoFeB is superimposed on the strong background signal of the silicon substrate for which $\chi = -1.47 \times 10^{-9}$ m^3 kg^{-1}. Figure 4.1 and Figure 4.2 illustrate the magnetisation curves after correction for the diamagnetic background. It must be remembered that the mass of the substrate is typically one thousand times greater than that of the film so the data reduction is performed by correcting the diamagnetic signal from the slope from 0.6 – 1.0 T. A magnetic

moment is still present even for the 0.6 nm CoFeB film on MgO seed layers but it is lost for the films less than 0.8 nm thick on SiO_2 substrates.

The magnetisation of the films was deduced by extrapolation of the data in the 0.6 T - 1.0 T range to B = 0. Figure 4.5 plots this quantity versus the film thickness for the films on three different substrates. The plot in Figure 4.5a, for the films on MgO, extrapolates to ~ 0.2 nm. We infer from the data that any dead layer formed is less than 0.2 nm thick and it originates from the Ta interface. The slope of the graph gives a magnetisation for amorphous $Co_{40}Fe_{40}B_{20}$, M = 0.78 MAm^{-1} which is found as the ratio of the slope and the area. The shape of the curve suggests that the ultra-thin films become granular in nature, and they behave superparamagnetically when the film is thinner than about 1.0 nm. These separated grains form a continuous ferromagnetic film when films are thicker than 1.0 nm.

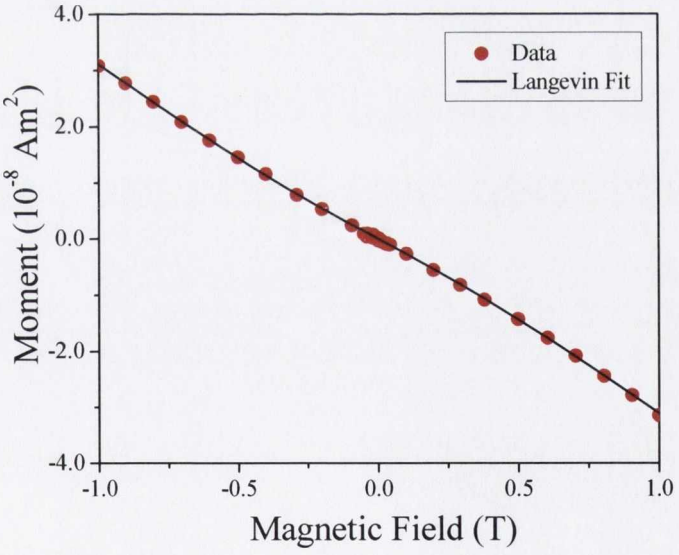

Figure 4. 4. Langevin fit to the uncorrected magnetisation data for the 0.8 nm CoFeB film on MgO buffer layer.

The size of the superparamagnetic particles is deduced by fitting the uncorrected magnetisation data to a Langevin function $M/M_s \sim (\coth x - 1/x)$, where $x = mB/k_BT$. Here, m is the magnetic moment of the grain, in Am^2 and k_B is Boltzmann constant. The Langevin function fit for the 0.8 nm film on MgO is illustrated in Figure 4.4. Assuming the nominal thickness, the average lateral dimensions of a grain are found to be 12.7 nm for the 1.0 nm film and 5.1 nm for the 0.8 nm film.

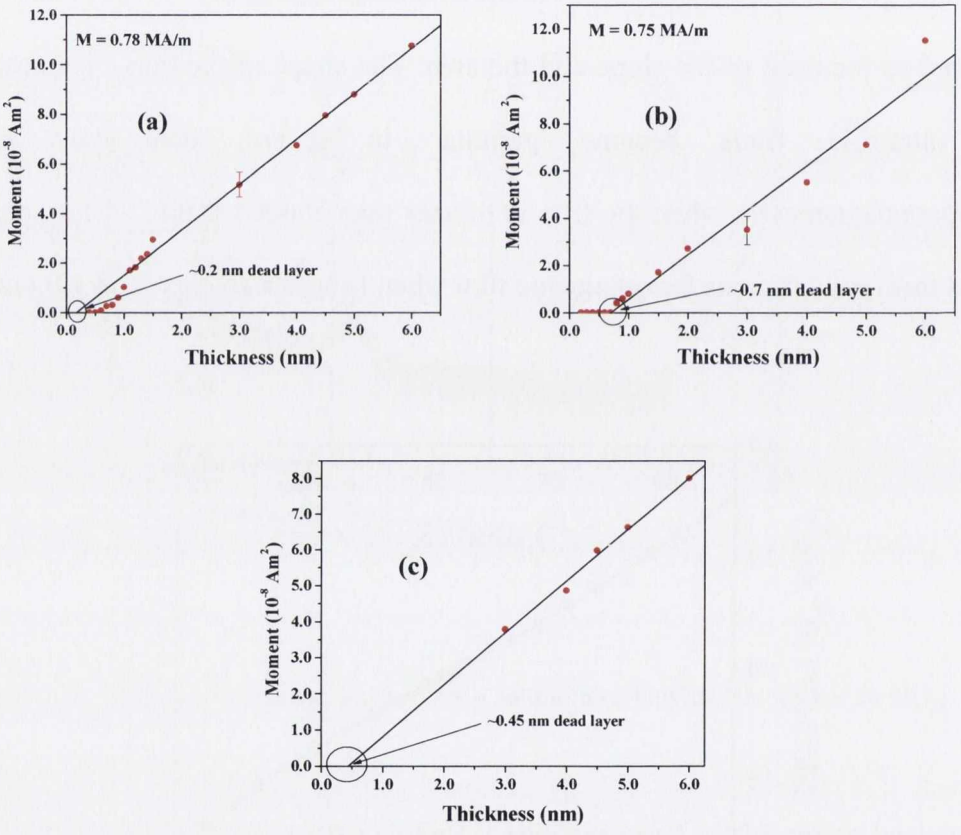

Figure 4. 5. Plot of the extrapolated magnetic moment vs. thickness of thin films of CoFeB with dimensions 5 × 5 mm^2 deposited on (a) MgO, (b) SiO_2 and (c) Ta buffer layers.

The behaviour of the films grown on SiO_2 is different as illustrated in Figure 4.5b. The data do not extrapolate to the origin, suggesting the presence of a true dead layer, instead of one that is simply discontinuous. The magnetisation deduced from the slope in Figure 4.5b is 0.75 MAm^{-1}. A nonmagnetic interdiffused layer, a few monolayers thick (0.7 nm), is indicated. The nature of the interdiffused layer is unknown but can be identified by X-ray photoemission spectroscopy. The interfacial dead layer forms only in SiO_2 samples. The same capping layer (Ta) was used in all cases. This indicates that the effect mainly arises from SiO_2-CoFeB interface rather than the CoFeB-Ta interface. To check the influence of Ta, we deposited a series of films on Ta seed layers, with a Ta cap layer. Figure 4.5c illustrates the moment vs. thickness for these films. The extrapolated dead layer thickness for the Ta interfaces is 0.45 ± 0.1 nm, or ~ 0.2 nm per interface. In our case, the effect of a Ta cap is to produce 0.2 nm dead layer at the upper surface which is consistent with the observed behaviour for MgO and SiO_2 samples. Therefore, the dead layer formed at SiO_2 interface is 0.5 ± 0.1 nm thick.

Figure 4.6 illustrates the difference between the SiO_2 and MgO cases schematically. In the SiO_2 case, there is a dead layer forming at the SiO_2/CoFeB interface whereas MgO has a cleaner CoFeB interface and only dead layer is formed due to Ta cap layer. The contribution of tantalum is found to be ~ 0.2 nm. It is very critical to have clean tunnel barrier/electrode interfaces for the performance of magnetic tunnel junctions.

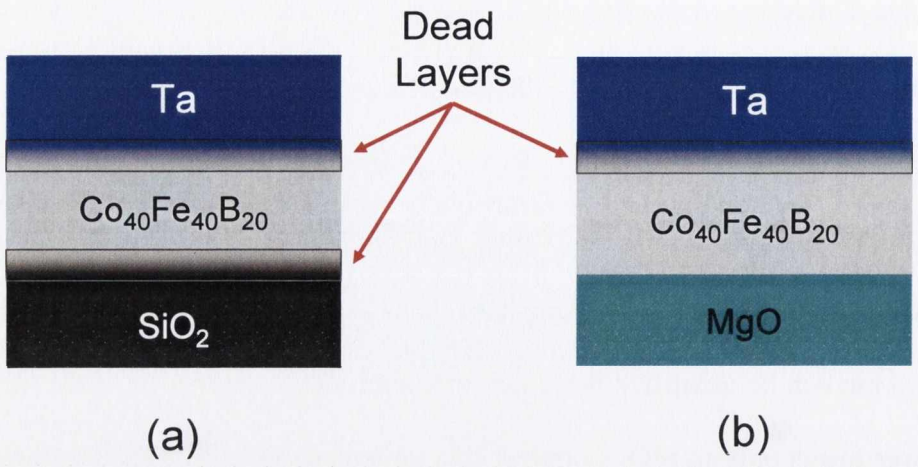

Figure 4. 6. Schematic representation of dead layers at the interfaces of CoFeB on (a) SiO_2 and (b) MgO.

The granular nature of the CoFeB films can be exploited when it is used as a free layer in a magnetic tunnel junction. Instead of switching abruptly when the field crosses zero, the magnetisation of the superparamagnetic grains is progressively aligned. This leads to a linear response of the magnetoresistance over an extended field range, which can be tuned by choosing the grain size of the free layer [9]. This can be helpful for producing a working magnetic sensor.

4.2. AlO_x based magnetic tunnel junctions

The AlO_x based MTJs are investigated to understand the basics of magnetic tunnel junctions. First high TMR AlO_x based MTJ was reported by Moodera *et al.* and Miyazaki *et al.* in 1995 [10-11]. Plasma oxidation of aluminum was a common method to produce AlO_x barrier. The AlO_x film is in general amorphous with a

uniform surface coverage. Our AlO_x MTJ stack is illustrated in Figure 4.7. All samples are deposited by magnetron sputtering at room temperature on thermally oxidized Si (001) wafers. AlO_x barrier layer (2.5 nm) is deposited from a stochiometric ceramic Al_2O_3 target by RF sputtering using the TFT gun. MTJs are then patterned into micron-scaled devices by UV-lithography and ion milling. In the stack, simple IrMn bottom pinning is used and ~ 40 mT exchange bias field was obtained after annealing. MTJs didn't show proper magnetic alignment in the as-grown state due to the lack of exchange anisotropy (Figure 4.8a), thus the TMR ratio is around 4 %. However, the magnetic structure improves after vacuum annealing at various temperatures under magnetic field of 0.8 T for 40 mins as shown in Figure 4.8b. This allows the stable antiparallel and parallel alignments of electrodes for the MTJ, hence higher TMR ratios.

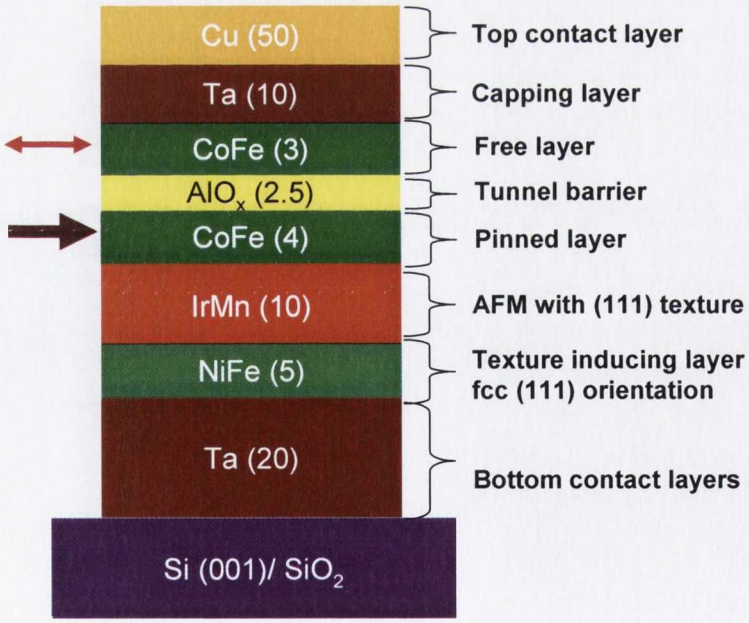

Figure 4. 7. Schematic of the MTJ stack of AlO_x based MTJs (numbers in parenthesis show the layer thicknesses in nm).

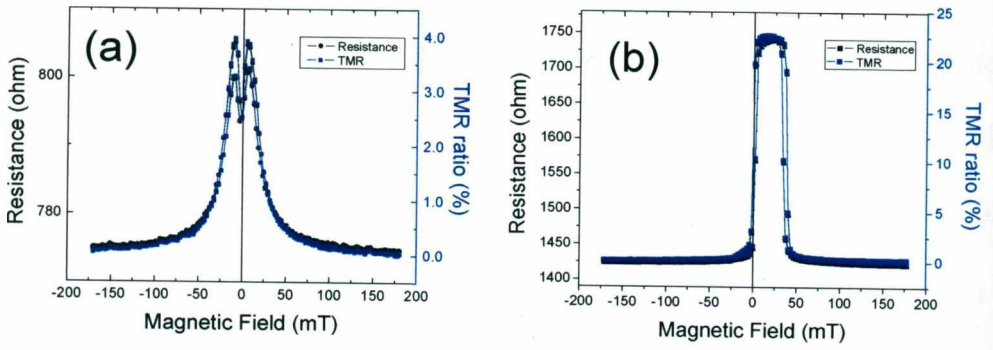

Figure 4. 8. Resistance and TMR vs. magnetic field plot of an AlO_x MTJ for the as-grown (a) and sample annealed at 250 °C (b). Measurements were performed at room temperature. Junction size was 30 × 30 μm^2.

Figure 4.9 summarizes the room temperature measurements of the current, TMR ratio and conductance vs. applied bias for an AlO_x MTJ junction which is deposited with pure Argon and annealed at 250 °C. The I-V curve (Figure 4.9a) shows a typical tunnelling behaviour indicating the quality of AlO_x barrier which is uniform and pinhole-free. The TMR ratio shows an asymmetric bias dependence (Figure 4.9b). This shows that the top and bottom interfaces are not identical even though the electrodes are the same. At negative bias (reflects the bottom CoFe/AlO_x interface), TMR ratio decreases faster compared to the positive bias. The crystal quality of bottom CoFe layer seems to be worse that the top one and causing higher spin flip scattering for higher energy of electrons. This might be due to Mn diffusion from IrMn into CoFe during annealing. Similar asymmetry is observed in conductance vs. bias voltage graphs obtained from DC I-V measurements as shown in Figure 4.9c. But, conductance has simple a parabolic shape which is expected from an amorphous tunnel barrier.

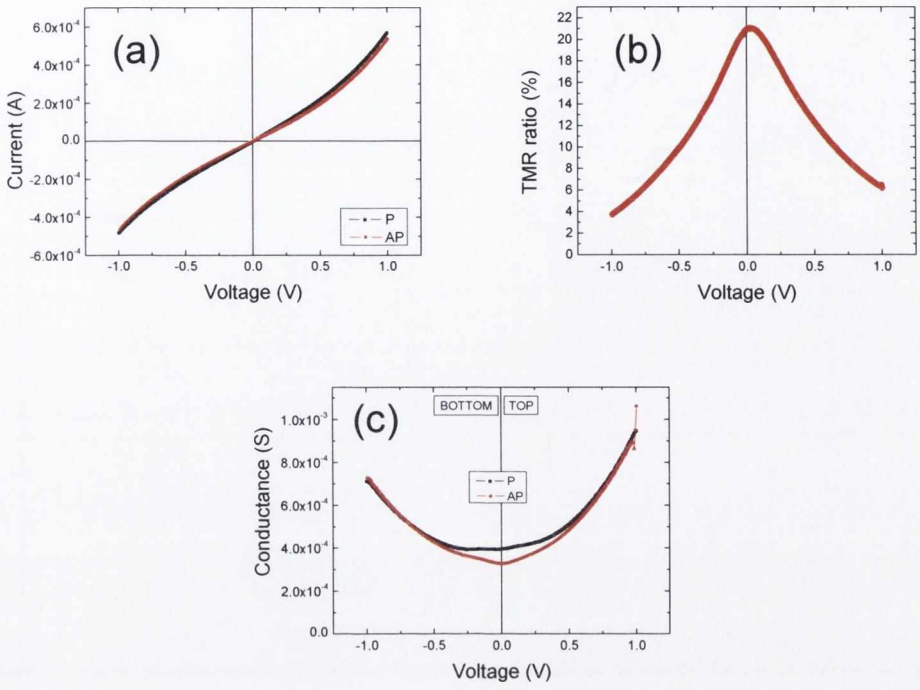

Figure 4. 9. (a) Current-voltage curves for P and AP states (b) TMR ratio vs. bias voltage graph, and (c) conductance vs. bias plots (P and AP state) of an AlO_x MTJ deposited with pure Argon and annealed at 250 °C.

AlO_x based MTJs generally suffer from oxygen deficiency when the AlO_x barrier is sputtered from a ceramic target due to dissociation of Al_2O_3 during sputtering. Therefore, the effect of O_2 insertion during AlO_x growth was investigated in these MTJs. In addition, annealing temperature dependence was also investigated in order to find optimum temperature for this type of stack. Figure 4.10a shows the effect of annealing temperature on TMR values. Room temperature TMR ratios exceeding 20 % are observed for the devices with AlO_x barrier sputtered with pure Argon. TMR values seem independent of the annealing temperature. This indicates that the spin polarization of CoFe electrodes does not change with different

annealing temperatures. The optimum annealing temperature is found to be > 175 °C which is sufficient to set the exchange bias.

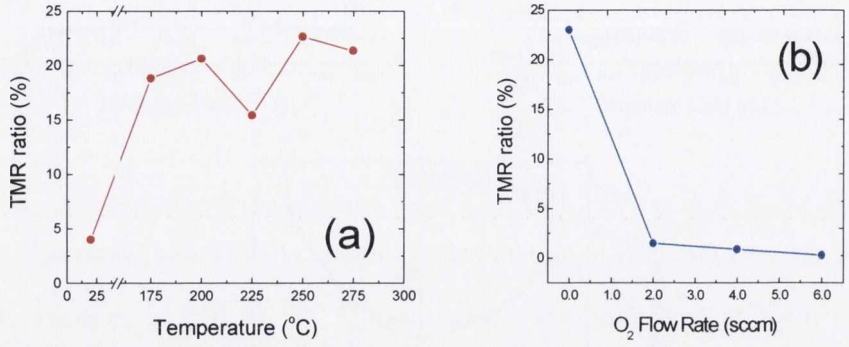

Figure 4. 10. (a) Annealing temperature dependence and (b) the effect of oxygen insertion on TMR values for the samples annealed at 250 °C.

The effect of oxygen insertion on the TMR ratio is illustrated in Figure 4.10b. The oxygen insertion dramatically decreased the TMR values from 23 % to 1 - 2 % with increasing oxygen content in the mix at room temperature. As the oxygen partial pressure is increased, the effect becomes more pronounced. TMR ratio is almost annihilated at 6 sccm of oxygen. The degradation of TMR is due to the oxidation of bottom ferromagnetic electrode during barrier deposition. The oxidation of the electrode causes formation of magnetic dead layers at the barrier electrode interface [12] and it is very well known that magnetic dead layers reduce the spin polarization of electrons transmitted through it due to increased spin flip scattering. Hence, TMR value of the MTJ decreases with increasing dead layer thickness.

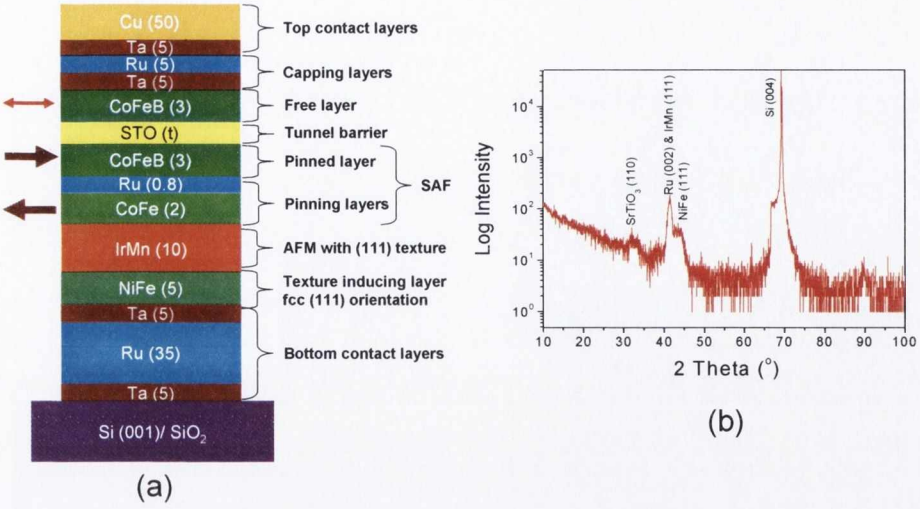

Figure 4. 11. (a) Schematic of the STO MTJ stack and (b) XRD pattern of 100 nm STO on full bottom stack of the MTJ.

4.3. $SrTiO_3$ based magnetic tunnel junctions

$SrTiO_3$ is a very interesting barrier material which might give giant TMR values if deposited in a crystalline fashion. Furthermore, it has very high dielectric constant (90 - 240) which is important to realize very thin barrier layers with good insulation properties [13]. Theoretical calculations predicted above 1000 % TMR for fully epitaxial Co (001) / STO (001) / Co (001) magnetic tunnel junctions [14]. Therefore, we investigated the possibility of realizing similar structure with CoFeB electrodes.

The STO based MTJs are prepared on thermally oxidized Si (001) substrates by sputtering at room temperature. The STO MTJ structure, bottom-pinned with IrMn and with a synthetic antiferromagnet as the pinning layer (Figure 4.11a), consisted of Si (001) / SiO_2 (substrate) / Ta (5) / Ru (35) / Ta (5) / $Ni_{81}Fe_{19}$ (5) /

$Ir_{22}Mn_{78}$ (10) / $Co_{90}Fe_{10}$ (2) / Ru (0.8) / $Co_{40}Fe_{40}B_{20}$ (3) / STO (t) / $Co_{40}Fe_{40}B_{20}$ (3) / Ta (5) / Ru (5) where the numbers in parenthesis are the layer thicknesses in nm. The thickness of the STO barrier was varied from 1.0 nm to 2.5 nm.

First, the crystal structure of STO layer was investigated by growing a very thick (100 nm) STO film on top of the bottom stack of the MTJ. The X-ray diffraction pattern reveals that the STO barrier is poorly crystalline, with only a very broad and low intensity (110) peak at 32.1° as shown in Figure 4.11b. In the XRD pattern, no CoFe related peaks are present, indicating that the CoFeB layer is amorphous. However, good (111) texture for IrMn and NiFe has been observed, which is essential to obtain high exchange bias fields in the stack.

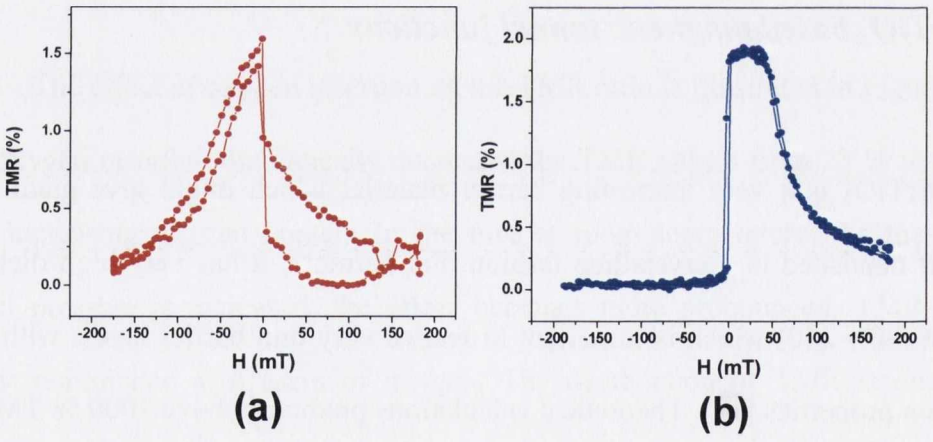

Figure 4. 12. Room temperature magnetoresistance curve of CoFeB / STO / CoFeB MTJ for the as-grown (a) and annealed at 325 °C (b) samples which have 2.5 nm STO barriers.

Room-temperature magnetoresistance curves of the as-grown and annealed samples with 2.5 nm STO barriers are shown in Figure 4.12a and Figure 4.12b, respectively. The TMR value of the as-grown sample is found to be 1.6 % without

having proper antiparallel magnetic alignment of the magnetisation of the electrodes. However, annealing at 325 °C improved the magnetic structure and the TMR value to just 2.0 %. A contributing factor to the low TMR ratio is the crystallization process of the CoFeB electrode. Due to the absence of the desired (001) orientation in the STO barrier, CoFeB electrodes crystallize in a random fashion which does not result in the correct band structure matching between Co and STO layers.

No TMR has been observed for the samples which have STO barriers thinner than 2.5 nm, mainly due to the high conductivity (almost metallic) of the STO layer. The 24 × 48 μm^2 junction with an STO barrier has a resistance of 4 Ω; similar junction with an MgO barrier giving 200 % TMR has a resistance of 4 kΩ. The low resistance-area (RA) values (~10^4 $\Omega\mu m^2$ for the junctions with 2.5 nm STO barriers) are attributed to the lack of oxygen stochiometry in the STO barrier due to the growth conditions. Usually, STO is grown in oxygen–argon mixed plasma to provide sufficient oxygen during growth using high substrate temperature [15] or by pulsed lased deposition in oxygen atmosphere [16], whereas we have had to use only argon during sputtering of STO to prevent oxidizing the bottom CoFeB electrode which has been observed in AlO_x based MTJs.

4.4. MgO based magnetic tunnel junctions

Magnesium oxide (MgO) based magnetic tunnel junctions are the main focus of spintronics nowadays due to their high TMR values. One can achieve TMR ratios exceeding 200 % at room temperature with a crystalline (001) MgO barrier using bcc CoFe, Fe, Co or CoFeB electrodes. Therefore, MgO MTJs was investigated in this

study utilizing CoFeB, CoFeCrB and CoNiCrB amorphous electrodes. In our lab, it is possible to deposit MgO by two different methods: The first one is RF sputtering with TFT guns and the second one is e-beam evaporation. Both of the methods were used to deposit MTJs in this work and they will be described in the following sections of this chapter.

4.4.1. RF sputtered MgO MTJs

RF sputtering of magnesium oxide from a sintered target is the common method for MgO deposition in literature. The highest TMR ratios are obtained using this method by several research groups, including our own. In our case, we use a special type of sputter gun which has target-facing-target geometry. With this gun, it is possible to realize very low deposition rates for MgO. Several optimization processes have been applied to the MTJs to obtain high TMR ratios. These are *the effect of pinning structure*, *MgO and CoFeB sputtering pressure optimization*, *the effect of MgO deposition temperature, the change of target-sample distance for MgO deposition*, and *the effect of MgO thickness*. It is a long process to find the optimum conditions with so many variables.

4.4.1.1. The effect of pinning structure

The pinning structure has a serious impact on the performance of an MgO based MTJ. Three types of pinning structures for single barrier MTJs have been

investigated in this study. First one is the simple bottom pinning structure, second one is the simple top pinning structure and the last one is the bottom pinning with a synthetic antiferromagnetic layer, as shown in Figure 4.13 (a), (b) and (c), respectively.

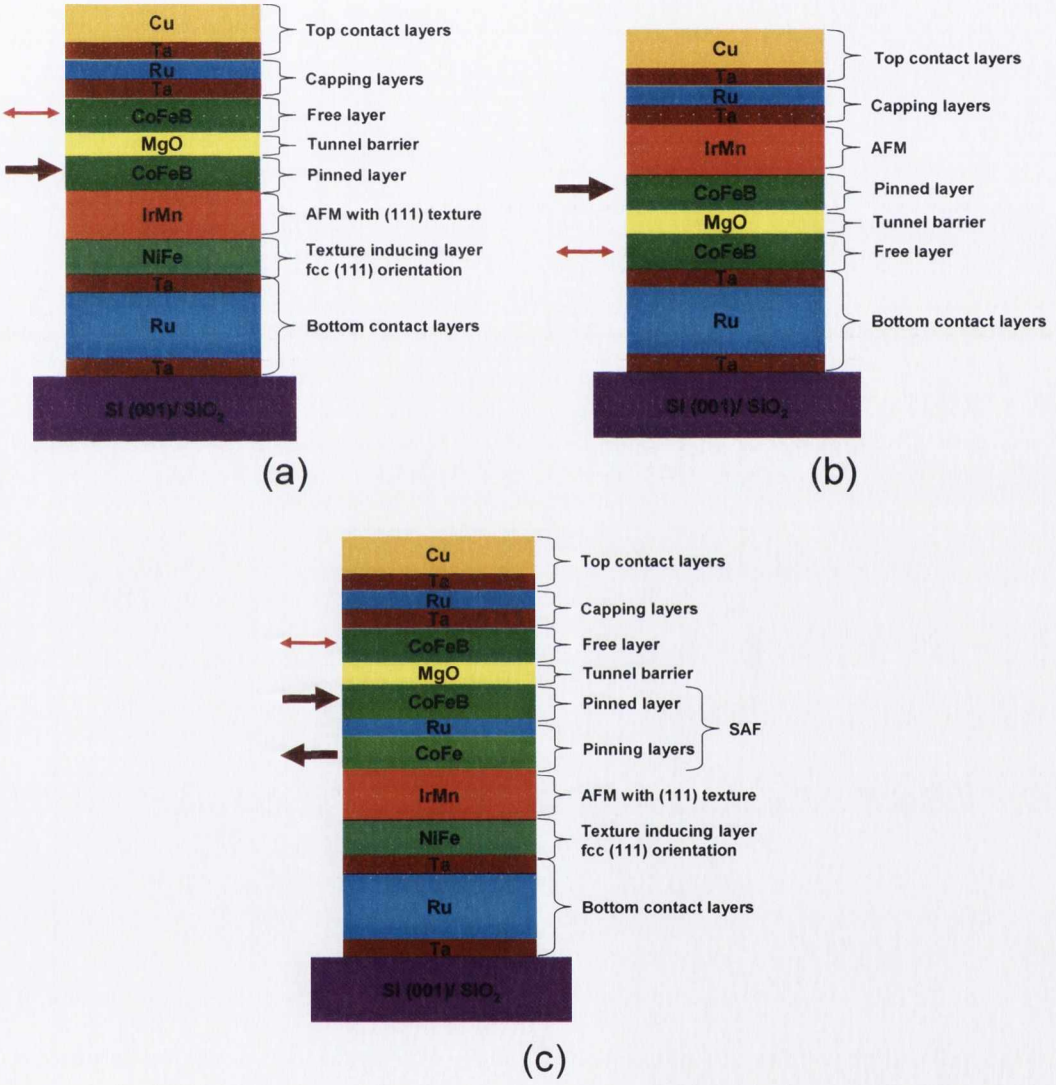

Figure 4. 13. Schematics of different pinning structures: (a) simple bottom pinning (b) simple top pinning and (c) bottom pinning with a synthetic antiferromagnet (SAF). Arrows indicate the magnetisation directions of free and pinned layers.

All of these structures are commonly used in the literature. Deposition and cost-wise, the simpler is the better. However, the annealing stability of these structures is quite different. Exchange bias in simple bottom and top pinning structures are easily destroyed at elevated annealing temperatures. For MgO based MTJs, samples require > 300 °C annealing step in order to have high TMR ratios. Therefore, pinning layers must withstand these temperatures.

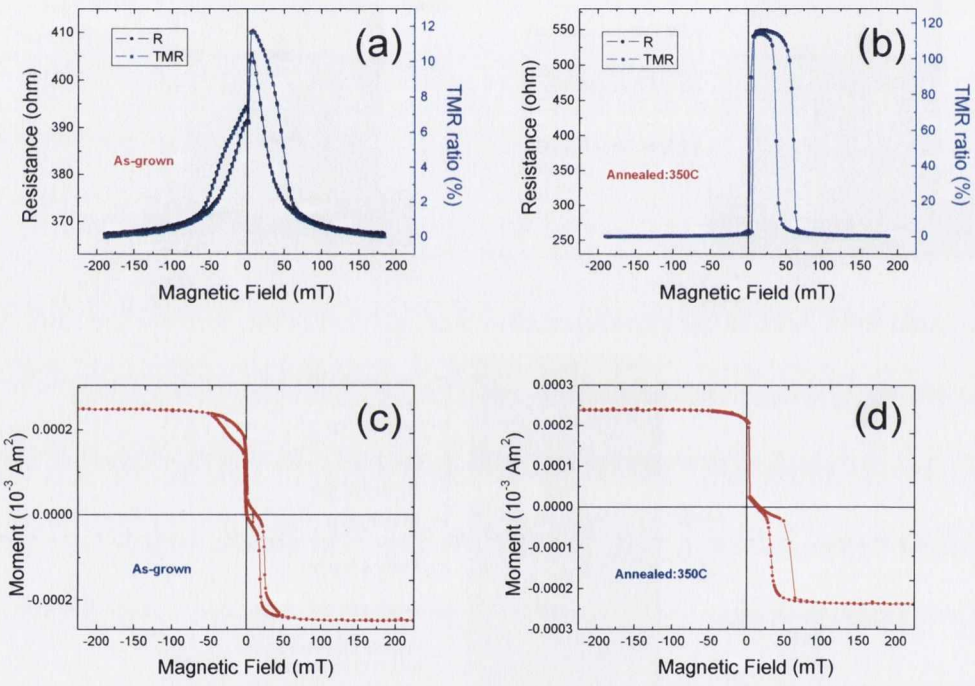

Figure 4. 14. Magnetoresistance and magnetic moment measurements of as-grown (a and c) and annealed (b and d) samples of a simple bottom pinned MgO MTJ. Annealing temperature is 350 °C.

Figure 4.14 summarizes the room temperature magnetoresistance and magnetisation measurements for a simple bottom pinned MTJ stack. In the as-grown state, the exchange bias is not properly set and CoFeB is amorphous, thus TMR ratio

is low (~ 12 %) (Figure 4.14a). After annealing, the exchange bias field of > 50 mT is obtained due to crystallization of IrMn with fcc (111) texture. TMR ratio has also increased to > 110 % which is due to crystallization of CoFeB during annealing, as shown in Figure 4.14b. Magnetisation measurements confirm the effect of annealing (Figure 4.14c and Figure 4.14d).

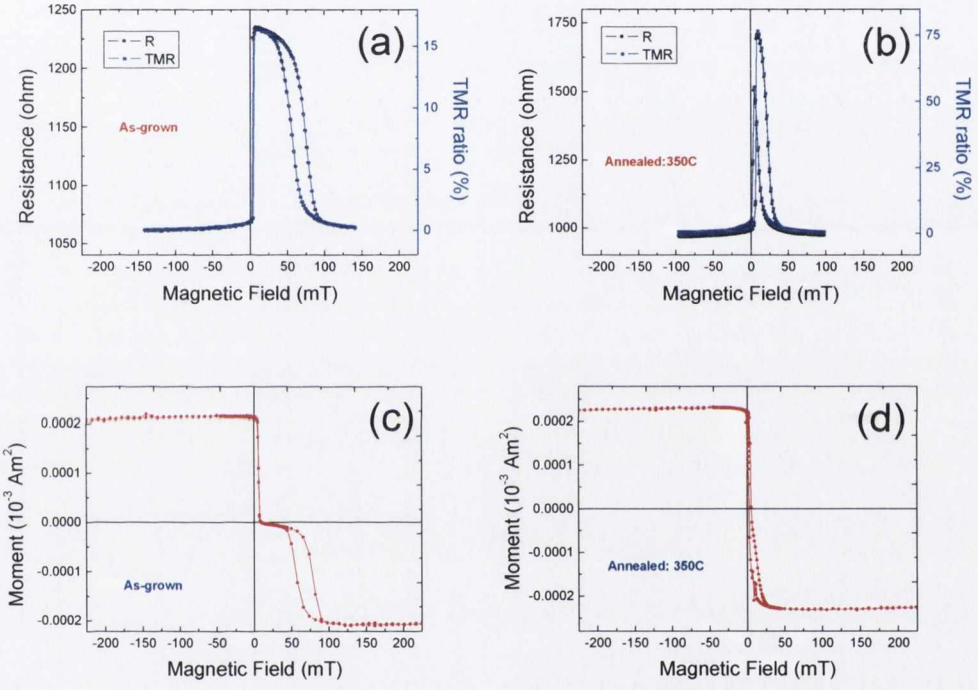

Figure 4. 15. Magnetoresistance and magnetic moment measurements of as-grown (a and c) and annealed (b and d) samples of a simple top pinned MgO MTJ.

In the case of a simple top pinned structure, there is good exchange bias in the as-grown state (> 70 mT) and the TMR ratio (16 %) is also higher compared to the simple bottom pinned structure, as shown in Figure 4.15a and Figure 4.15c. This is due to proper alignment of magnetisations of free and pinned layers in both

antiparallel and parallel states. The exchange bias in top pinned structures does not require annealing if there is a magnetic field sufficient to saturate the ferromagnet during antiferromagnetic layer deposition. The TMR ratio in the as-grown state is still low because CoFeB is amorphous. It increases rapidly to over 75 % by annealing at 350 ^{o}C but the exchange bias field decreases to less than 20 mT, hence stable antiparallel state can not be observed (Figure 4.15b and Figure 4.15d). This causes a lower TMR ratio compared to bottom pinned structure.

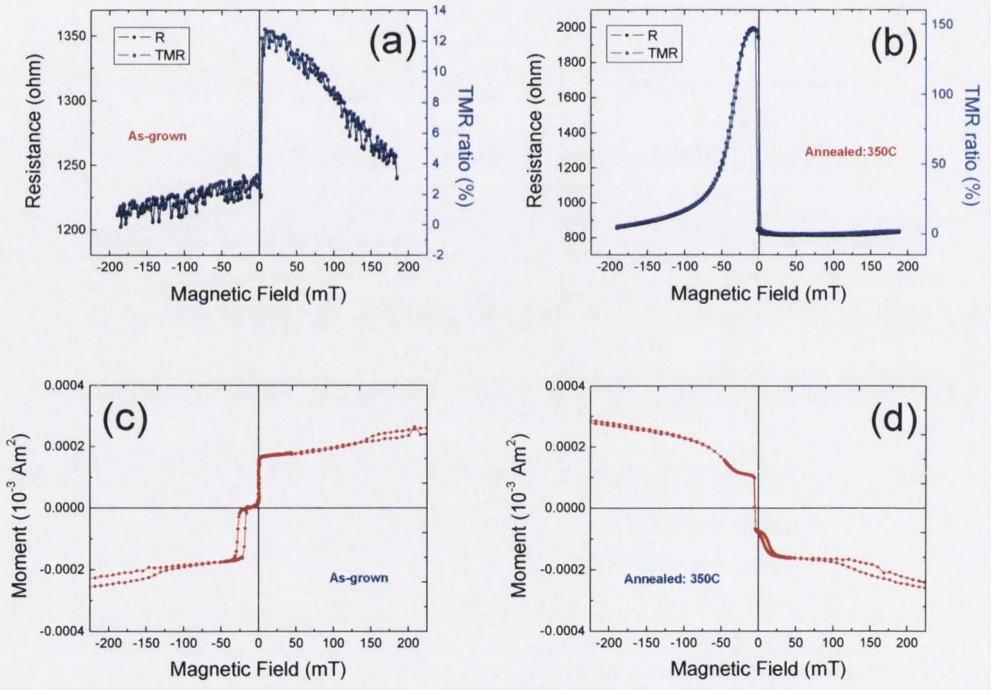

Figure 4. 16. Magnetoresistance and magnetic moment measurements of as-grown (a and c) and annealed (b and d) samples of a MgO MTJ using bottom pinning with a synthetic antiferromagnet.

The reduction in the exchange bias is probably due to lower blocking temperature of IrMn when it is grown on top of CoFeB. IrMn shows very high

exchange anisotropy when it has fcc (111) texture. But, it is difficult to obtain this texture on top of an amorphous layer. Low annealing stability of top pinned spin valves using IrMn has also been reported earlier [17].

The magnetoresistance and magnetisation measurements on MTJs which has a bottom pinning with a synthetic antiferromagnet (SAF) are shown in Figure 4.16. It is found that the best structure in terms of the TMR ratio is this pinning system because the CoFe and Ru layers act as a diffusion barrier to Mn atoms that start to diffuse into CoFeB layer during annealing. Similar to simple bottom pinning, the exchange bias and TMR ratio in the as-grown state is very small but they improve significantly after annealing. TMR ratio increases to ~ 150 % with an exchange bias field of ~ 50 mT. Another advantage of SAF pinning is that it cancels the stray field created by the pinned layer. This is very important for STT devices because the coupling of free and pinned layer causes a shift of the free layer loop. Due to its high TMR ratio, high exchange bias and high annealing stability, this pinning structure has been used in most of the MgO based magnetic tunnel junctions in this thesis.

4.4.1.2. The optimization of MgO and CoFeB growth pressures

It is very important to have MgO (001) texture to achieve high TMR ratios in MgO based magnetic tunnel junctions. Therefore, we investigated the effect of growth pressure of MgO on the crystal quality. Model bilayer structures were used for this purpose with SiO_2 / CoFeB / MgO stacking structure. The XRR measurement of SiO_2 / CoFeB (15 nm) / MgO (32.5 nm) bilayer is shown in Figure 4.17a with a fit obtained using Wingixa software. The XRD 2θ scan for MgO (002) peak is

illustrated in Figure 4.17b revealing high quality (001) oriented MgO layer with an FWHM of 0.8°. Figure 4.17c shows the intensity, the full width at half maximum (FWHM) of the MgO (002) diffraction peak and FWHM of the rocking curve (ω scan) as a function of Ar pressure for room temperature deposited sample with the following stack Si / SiO_2 (500) / Ta(5) / CoFeB(3) / MgO (30). The numbers in parenthesis indicate the layer thickness in nm.

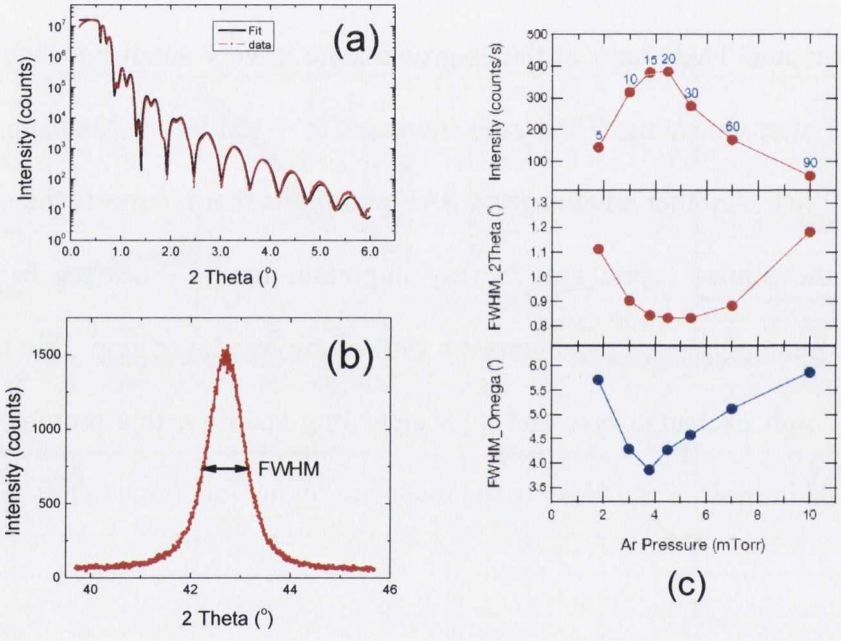

Figure 4. 17. (a) XRR measurement of SiO_2 / CoFeB (15 nm) / MgO (32.5 nm) bilayer showing both measurement and the fit. (b) XRD 2θ peak of MgO (002) plane of the same stack (c) The pressure dependence of intensity and FWHMs of 2θ and ω scans of MgO (002) diffraction peak.

For intensity curves, optimum parameters are in 3.8 - 4.5 mTorr range which corresponds to Ar flow of 15 - 20 sccm. That for the FWHM of the (002) reflection in the 2θ scan, which is related to the grain size of the crystalline MgO, ranges more

broadly. In the ω scan, a minimum value of the FWHM of 3.85° is clearly seen at 3.8 mTorr. The intensity shows its maximum at intermediate Ar pressure, mainly because the mosaicity of MgO film is improved rather than the grain size of crystalline MgO is increased. On the other hand, an Ar flow that is too low (5 sccm) or too high (90 sccm) results in smaller or thinner crystalline MgO. It is known that MgO sputtered on top of an amorphous material initially forms an amorphous MgO layer up to a certain critical thickness then becomes crystalline thereafter [18]. Thus, amorphous MgO is supposed to become dominant for these two extreme Ar flow rates.

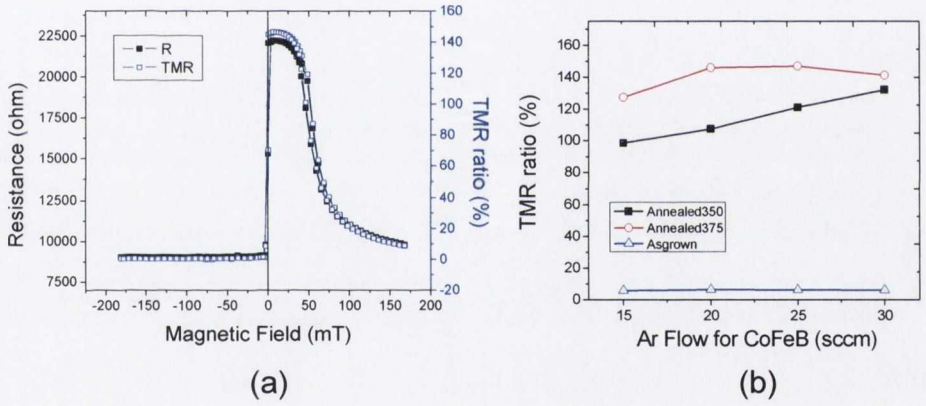

Figure 4. 18. (a) Resistance and TMR vs. H plot of an MgO MTJ annealed at 375 °C. (b) The effect of CoFeB growth pressure on TMR values showing samples with different annealing temperatures.

After careful optimization of barrier growth pressure, the effect of CoFeB growth pressure has been investigated. The XRD method is not appropriate in this case because CoFeB is an amorphous material. Therefore, the fabricated MTJ structures were patterned and MR measurements were performed. Typical room

temperature magnetoresistance and TMR ratio vs. magnetic field (H) plots are shown in Figure 4.18a. That particular sample shows 148 % TMR value and reasonably high exchange bias of 65 mT. On the other hand, Figure 4.18b illustrates the effect of CoFeB growth pressure on TMR values. It was found that the samples grown at 3 mTorr (20 sccm) gives the best results with 148 % TMR at room temperature after annealing at 375 ^{o}C for 1 hour.

4.4.1.3. The optimization of MgO growth temperature

Based on the optimized MgO and CoFeB sputtering pressures, we then varied the substrate temperature during MgO deposition from 290 to 460 ^{o}C. In these samples, we first deposited Ta (5) / CoFeB (3) on Si/SiO_2 substrates at RT and heated the substrate to desired temperature and waited for 30 min to stabilize. Then, the MgO (30) layer is deposited (numbers are thickness values in nm). Samples are characterized by XRD to understand the changes in the crystal structure.

Figure 4.19 illustrates (a) the intensity and (b) FWHM of the MgO (002) 2θ diffraction peak and (c) the FWHM of the rocking curve as a function of the substrate temperature for the sample grown at 3.8 mTorr. In Figure 4.19a, the intensity becomes larger with increasing substrate temperature and then dropped drastically at 460 ^{o}C. Here, optimum parameters are at 385 - 410 ^{o}C. We confirmed that this sudden drop of the intensity at 460 ^{o}C is due to the crystallization of the entire CoFeB layer in the (011) direction from the 2θ scan of the same stack, but with a thicker (40 nm) CoFeB layer. The 2θ scan shows a clear peak just around the position of CoFe (011) diffraction peak. This crystallization of CoFeB (011)

probably occurs before the deposition of MgO, and the MgO is supposed to crystallize in unwanted direction.

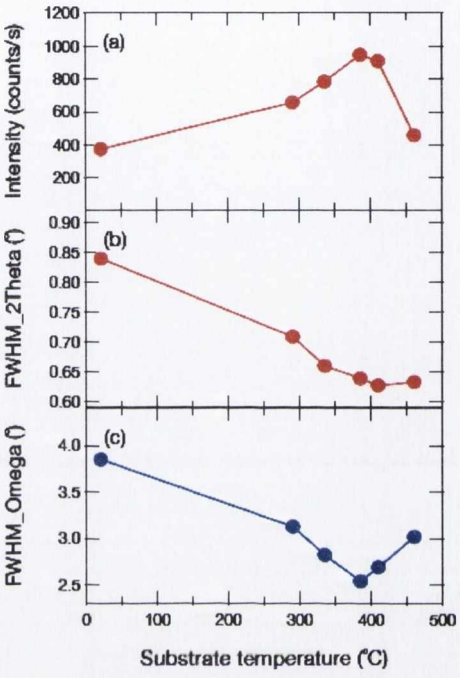

Figure 4. 19. (a) Substrate temperature dependence of (a) the intensity, (b) FWHM of 2θ scan, and (c) FWHM of the rocking curves of the MgO (002) diffraction peak.

Figure 4.19b shows monotonically decreasing FWHM to the end of the temperature range, while Figure 4.19c shows a clear dip in the ω scan at 385 °C. Thus, the optimum condition again seems to be determined by the mosaicity of the MgO. The minimum FWHM of the rocking curve was found to be 2.54°, which is appreciably smaller than the room temperature value, and also than the value of 4.4° previously reported by Ikeda *et al.* [19].

Figure 4.20a shows the dependence of surface root mean square (RMS) roughness on substrate temperature obtained from atomic force microscopy (AFM)

measurements for 0.5 × 0.5 μm^2 scans on each sample. The roughness also shows its minimum at 385 °C which means this temperature is optimum, not only for the crystallinity but also for the surface roughness. Figure 4.20b shows an AFM image of the surface of a much thinner MgO of 3 nm prepared in the optimum conditions. The estimated RMS roughness is less than 0.3 nm (approximately thickness of one atomic layer) which is smooth enough to be used for a tunnel barrier.

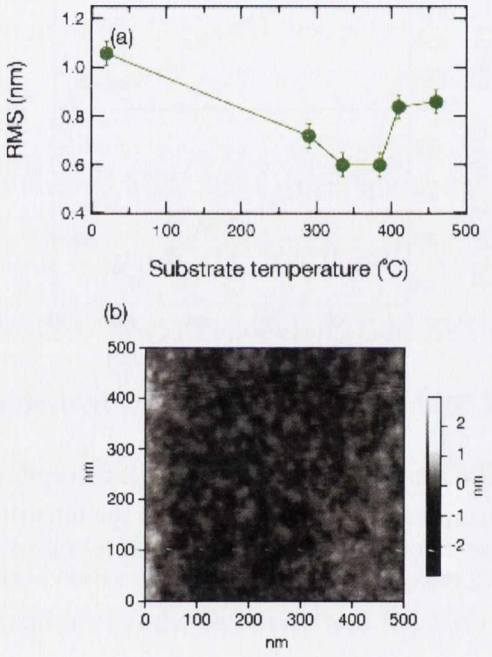

Figure 4. 20. (a) The substrate temperature dependence of root mean square (RMS) roughness. (b) AFM micrograph of MgO 3nm film deposited at optimum conditions.

Although, MgO crystal quality improves with increasing substrate temperature, it is not reflected in TMR ratios. Figure 4.21 reveals the effect of substrate temperature on TMR ratios of MgO MTJs with 2.5 nm MgO layer. TMR ratio decreases monotonically as the substrate temperature is increased. The effect

becomes more pronounced above the crystallization temperature of CoFeB which is > 300 °C. This might be due to random crystallization of bottom CoFeB layer before or during MgO deposition at elevated substrate temperatures. To obtain high TMR, it is important to have (001) crystal matching between MgO and CoFe electrodes. HRTEM images of MTJs with MgO barriers deposited at RT and 385 °C are illustrated in Figure 4.22 (a) and (b), respectively. First striking difference is the thickness of the MgO layer, RT deposited MgO is 2.5 nm (same with designed thickness). It is much thinner for the high T deposited MgO (~ 1.5 nm). The reduced resistance value was observed in magnetoresistance measurements which is consistent with the TEM data.

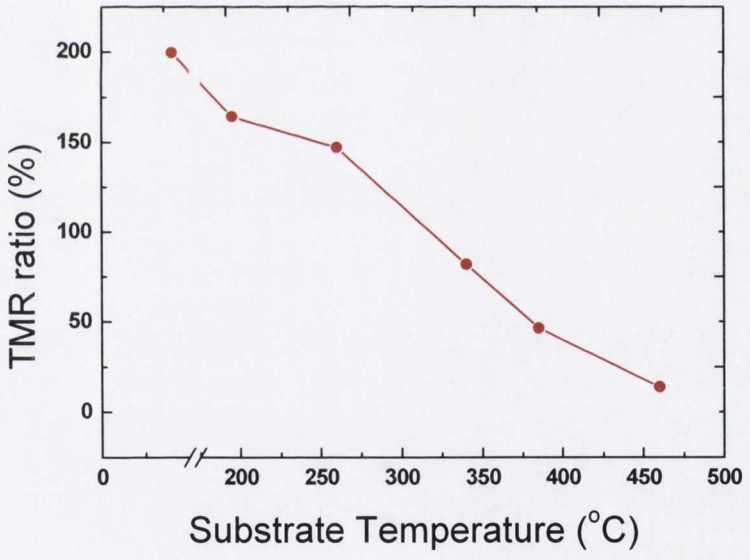

Figure 4. 21. The effect of substrate temperature during MgO deposition on the TMR ratio.

The crystal quality of RT deposited MgO layer seems better than the high T one. The bottom CoFeB layer for the high T sample seems crystallized in a different

fashion (110) which might explain the reduction in TMR ratio. Further elemental investigation of bottom CoFeB/MgO interface is required to have a better understanding of the reason of the decrease in TMR ratio.

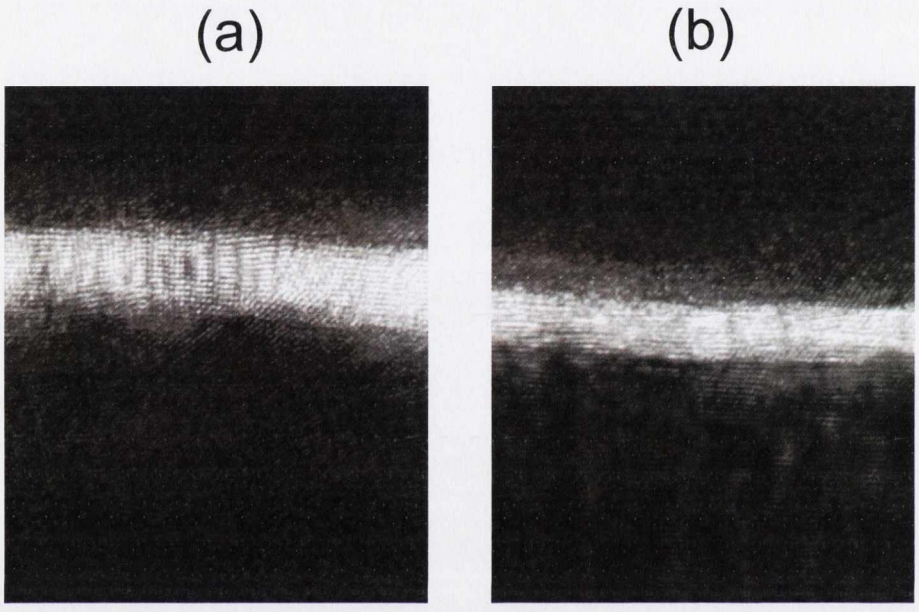

Figure 4. 22. HRTEM images of MTJs with MgO barrier deposited (a) at RT and (b) at 385 ^{0}C.

4.4.1.4. Transmission electron microscope analysis of MTJs

HRTEM micrograph of an as-grown MgO based magnetic tunnel junction is shown in Figure 4.23 indicating individual layers of the stack. All the layers can be identified with a reasonable quality interfaces. The designed thickness values are very similar to real thickness values except for MgO layer which is slightly thicker than designed value of 2.5 nm. It seems that roughness arising from the grain boundaries of the thick Ru contact layer propagates through the layers up to the

bottom CoFeB layer. This roughness does not compromise the uniformity of MgO layer.

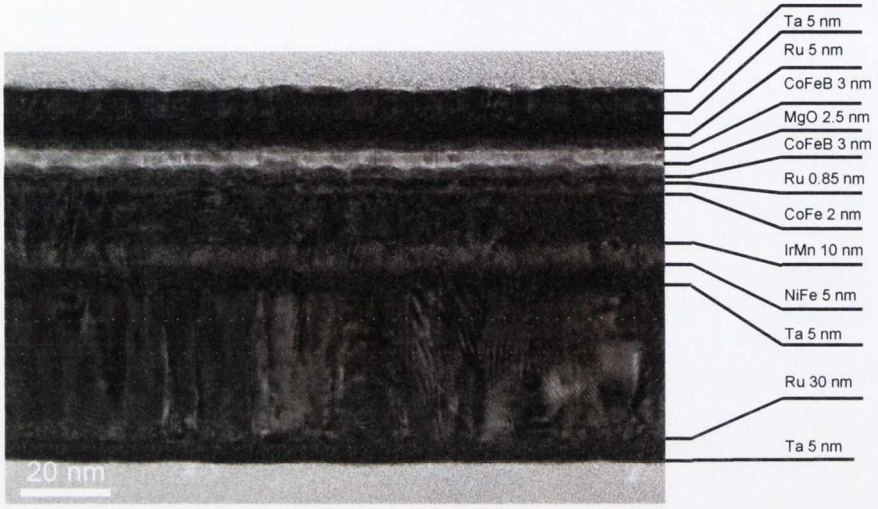

Figure 4. 23. High resolution transmission electron microscope (HRTEM) image of an MgO MTJ showing the individual layers in the stack. Bright layer is the MgO tunnel barrier.

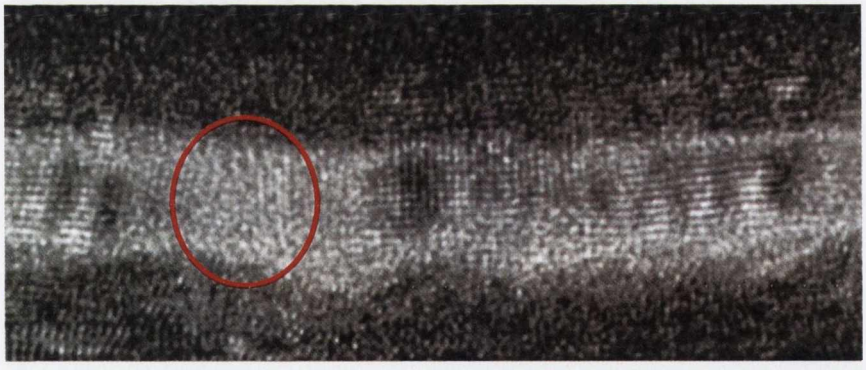

Figure 4. 24. Magnified HRTEM image of the CoFeB / MgO / CoFeB layers of an MgO MTJ. Highly textured MgO layer is clearly observed even in the as-grown state. Red circle indicates an amorphous region in the MgO barrier layer.

The high quality MgO layer is shown in the magnified HRTEM image in Figure 4.24. Mainly (001) texture is clearly observed from the micrograph which was revealed by previous XRD measurements. There are some amorphous areas, indicated with a red circle in the figure, in the MgO layer which also explains lower TMR ratio of our MTJs compared to literature. Further optimization of process parameters is required to improve the MgO quality. On the other hand, the top and bottom CoFeB layers are found to be amorphous in this sample because it is an as-grown MTJ.

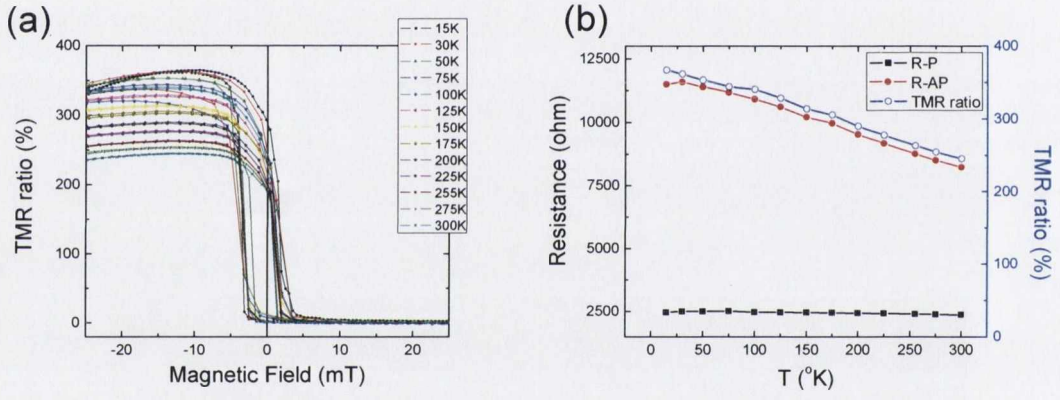

Figure 4. 25. (a) TMR vs. magnetic field graphs obtained at different temperatures between 15 and 300 K. (b) Resistance and TMR ratio vs. T plot of the same MTJ.

4.4.1.5. The effect of temperature on the TMR ratio

The effect of measurement temperature was also investigated on the highest TMR MTJ. Figure 4.25a plots TMR vs. magnetic field curves at different temperatures as low as 15 K. It was found that TMR values increases up to 367 % at

15 K and the increase is mainly due to the increase in the antiparallel resistance of the junction as shown in Figure 4.25b. The parallel resistance does not seem to change as can be seen from the same curve. There are several possible mechanisms that can be responsible for strong temperature dependence of TMR including thermally excited magnons in the FM electrodes, thermal excitation of magnetic impurities / defects in the barrier or at the interfaces and thermal variations of electronic structures at high temperatures.

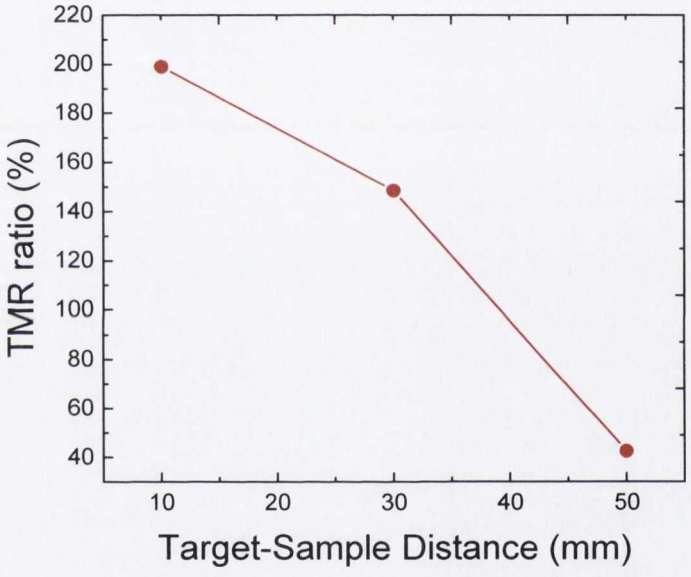

Figure 4. 26. The effect of the target-sample distance of MgO on TMR ratio.

4.4.1.6. The optimization of the target to sample distance for MgO deposition

The other optimization process is the variation of target-sample distance for MgO barrier. Result of these experiments is shown in Figure 4.26. The optimum target-sample distance was found to be 10 mm giving 200 % TMR ratio at room temperature. Further increase of the target distance is detrimental for TMR values.

This is mainly due to the loss of (001) texture in MgO barrier due to very low deposition rate which allows increased interaction of sputtered MgO molecules with H_2O molecules present in the deposition chamber. It is well known that MgO interacts with water molecules and forms a hydroxide (MgOH). Therefore, it is important to have optimized deposition rate especially for non-UHV chambers.

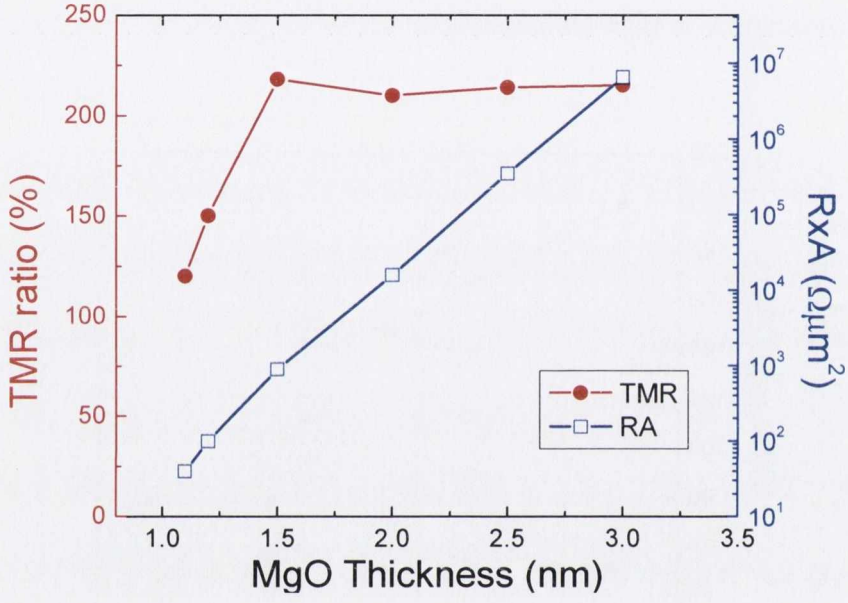

Figure 4. 27. TMR and RA vs. MgO barrier thickness for the samples annealed at 325 °C.

4.4.1.7. The effect of MgO thickness

A further round of determining optimum conditions was carried out: 1) using higher purity CoFeB and MgO targets and 2) fixing all possible leaks in Chamber B to reduce the water vapour in the chamber. Reducing the resistance × area (RA) product of the MTJ structures as well as keeping high TMR ratios are vital for the

spin torque related applications and experiments. Therefore, we studied the effect of MgO thickness on TMR values and the RA product of optimized MTJs. Both results are shown in Figure 4.27. The TMR value of the MTJ seems independent of MgO thickness above 1.2 nm and saturates about 210 % for the samples annealed at 325 ^{o}C. In the case of thin MgO, TMR ratio drops to ~ 150 % due to less spin filtering caused by roughness of the bottom layers. The RA value is exponentially dependent on the barrier thickness due to quantum mechanical tunnelling transport in these devices. Expected linear dependence of MgO thickness on log RA is clearly observed in the graph. An RA value as low as 100 $\Omega\mu m^2$ was achieved for the MTJ with 1.2 nm MgO barrier while keeping 150 % TMR value. Fitting of the log RA vs. MgO thickness curve to the Simmons equation [20] results in φ = ~ 0.35 eV average barrier height for MgO tunnel barrier which is similar to the values reported in literature [21-22].

4.4.1.8. Magnetoresistance and transport characteristics of optimized RF MgO MTJs

After careful optimization of all parameters, we were able to achieve high performance RF MgO MTJs with TMR ratios > 300 % at room temperature. Typical resistance and TMR ratio vs. magnetic field plots of high TMR MgO MTJ sample, annealed at 400 ^{o}C, are given in Figure 4.28 (a) and (b), respectively. The TMR ratio of this particular sample at RT is 287 % and it increases up to 440 % at 25 K which is a factor of 1.5 increase which is typical for MgO based MTJs. The main contribution is from the increase in the antiparallel resistance of the tunnel junction.

The effect of annealing temperature on the TMR ratio and exchange bias field is indicated in Figure 4.29. As usual, the TMR ratio is around ~ 15 % in the as-grown state and rapidly increases above 250 % for annealing temperature of 350 °C. TMR continues to increase until 425 °C when it suddenly drops below 100 % at higher temperatures. This is because of the loss of exchange bias field at high temperatures due to low blocking temperature of IrMn.

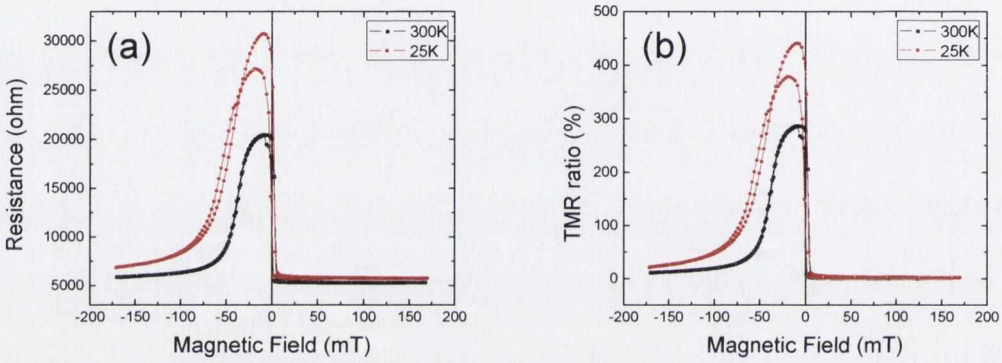

Figure 4. 28. Resistance and TMR ratio vs. magnetic field curves for an optimized MgO MTJ annealed at 400 °C. Room temperature and low temperature measurements are shown.

The change in the exchange bias field is very dramatic as seen in Figure 4.29. The as-grown sample has > 100 mT exchange bias and this decreases continuously with increasing annealing temperature. It is sufficiently high even at temperatures above 400 °C. It almost annihilates at 450 °C due to loss of significant amount of Mn from the IrMn antiferromagnetic layer due to diffusion which is known to start above 300 °C.

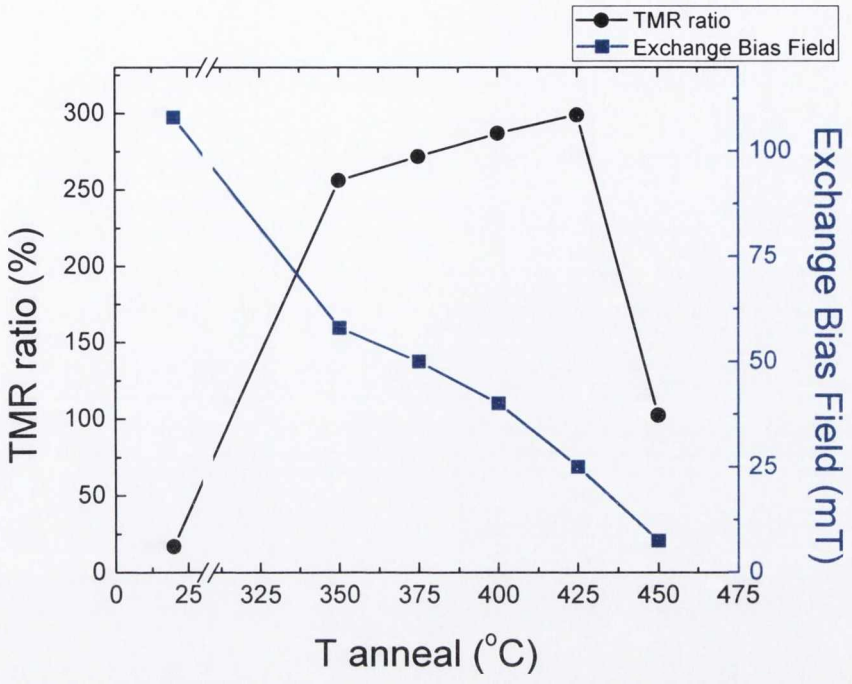

Figure 4. 29. The effect of annealing temperature on the TMR ratio and exchange bias field of MgO MTJs.

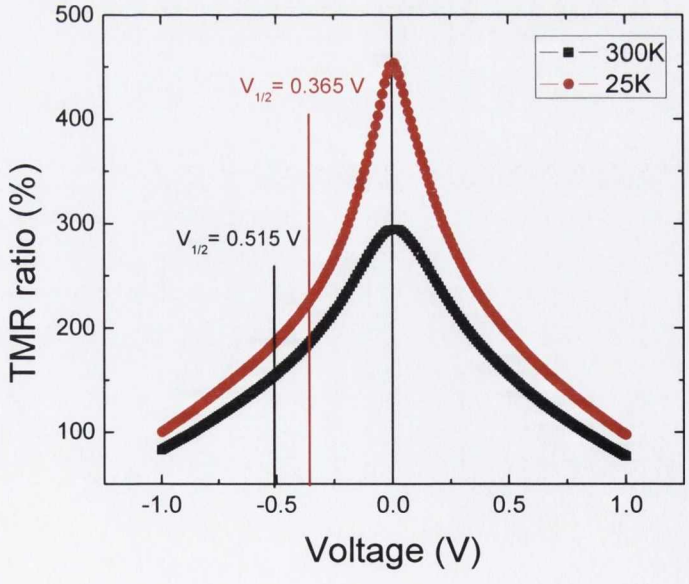

Figure 4. 30. TMR ratio vs. bias voltage curves for an annealed MgO MTJ measured at RT and 25 K.

TMR ratio of MgO MTJs has very strong bias dependence. This is shown in Figure 4.30 for RT and 25 K measurements. At room temperature, TMR ratio decreases to its half value at a bias voltage of 515 mV which is typical for a single barrier MgO MTJ. However, at low temperature, this value drops to 365 mV which suggests that the reduction in the TMR ratio is not related to phonons created at RT. One proposed mechanism for the decrease in TMR ratio as a function of bias is interface magnon excitation [23]. Another mechanism, that is sometimes invoked, is energy dependence in the electronic band structure of the magnetic electrodes [24-25]. A third potential mechanism is the presence of defect states within the tunnel barrier, which may allow an increasing amount of defect-state-assisted tunnel current with increasing junction bias. This type of inelastic tunnel current could effectively dilute the spin polarization of the tunnel current, thereby explaining the decrease in TMR at elevated bias [26]. Third mechanism is likely in our case because our sputtered MgO barrier has a lattice constant higher than bulk which might lead to some defects in the barrier due to strain.

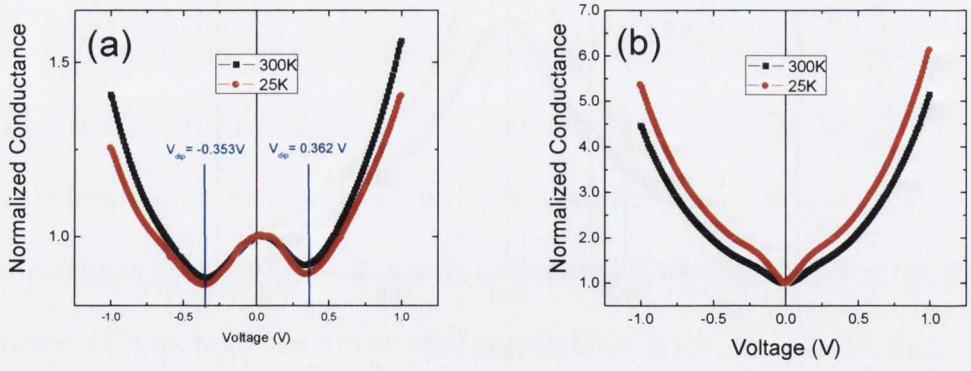

Figure 4. 31. Normalized conductance curves of MgO MTJ obtained from I-V measurements performed at room temperature and 25 K. (a) Parallel and (b) antiparallel state.

Figure 4.31 summarizes the bias dependence of conductance of the annealed MgO MTJ measured at RT and 25 K for parallel and antiparallel alignment of the electrodes. In the parallel state, two almost symmetric dips in positive and negative bias are clearly observed, These are signatures of MgO based magnetic tunnel junctions and previously reported by Matsumoto *et al.* [27-28]. Conductance in the parallel state does not change at low temperature. However, antiparallel conductance shows a clear dip at zero bias which is attributed to zero bias anomaly which is a result of impurities in the barrier layer.

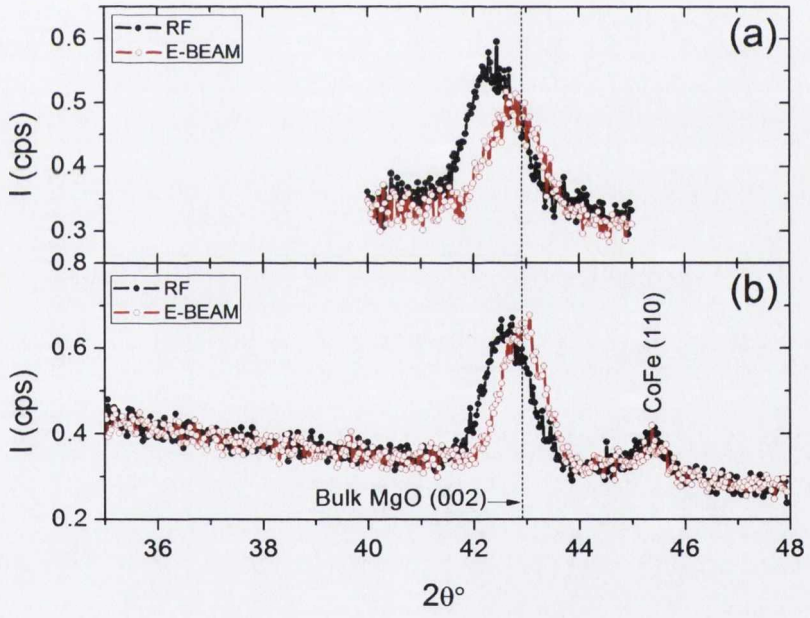

Figure 4. 32. X-ray diffraction data of 10 nm thick RF and EB-MgO sandwiched between CoFeB layers; (a) as-grown, (b) annealed at 400°C for 1 hr. Black line shows the peak position of bulk MgO.

4.4.2. E-beam evaporated MgO MTJs

E-beam evaporation of magnesium oxide is an alternative to RF sputtering. We have achieved high quality MgO (001) textured thin films by e-beam evaporation in our UHV chamber D with a very slow deposition rate (< 5 pm/s). The rest of the stack is deposited by sputtering.

To compare the crystal structure of RF vs. e-beam MgO samples, we fabricated CoFeB (60) / MgO (10) / CoFeB (20) structures and post annealed them at 400 °C for 1 hr (numbers in parenthesis indicate the layer thickness in nm). Figure 4.32 shows 2θ X-ray diffraction scans of these 10 nm thick MgO samples obtained using Cu-$K_{\alpha 1}$ radiation. In the as-grown state, EB-MgO has a d-spacing that is almost exactly the same as that of bulk MgO (a_0 = 0.421 nm) whereas the RF-MgO shows a slight increase in the d-spacing. Upon annealing, both MgO layers have improved crystalline structures, revealed by the identical FWHM values in the 2θ scans (Figure 4.32b). The decrease in the d-spacing of the RF-MgO is 1.07 pm, whereas the decrease in the d-spacing of the e-beam MgO is 0.92 pm after annealing.

Upon annealing, e-beam MgO has the same d-spacing as bulk MgO but the RF-MgO remains at a higher d-spacing as shown in Figure 4.32b. This could be due to different characteristics of the defect and impurity distributions in both samples. To compare the initial growth of e-beam MgO with that of RF-MgO, we attempted to grow it on amorphous thermal SiO_2. Our e-beam MgO would never crystallize on top of SiO_2 unlike RF-MgO, which is known to grow with (001) out of plane texture after forming few nm of amorphous MgO [18]. This indicates that the initial growth characteristics of e-beam MgO are different from those of conventional RF-MgO.

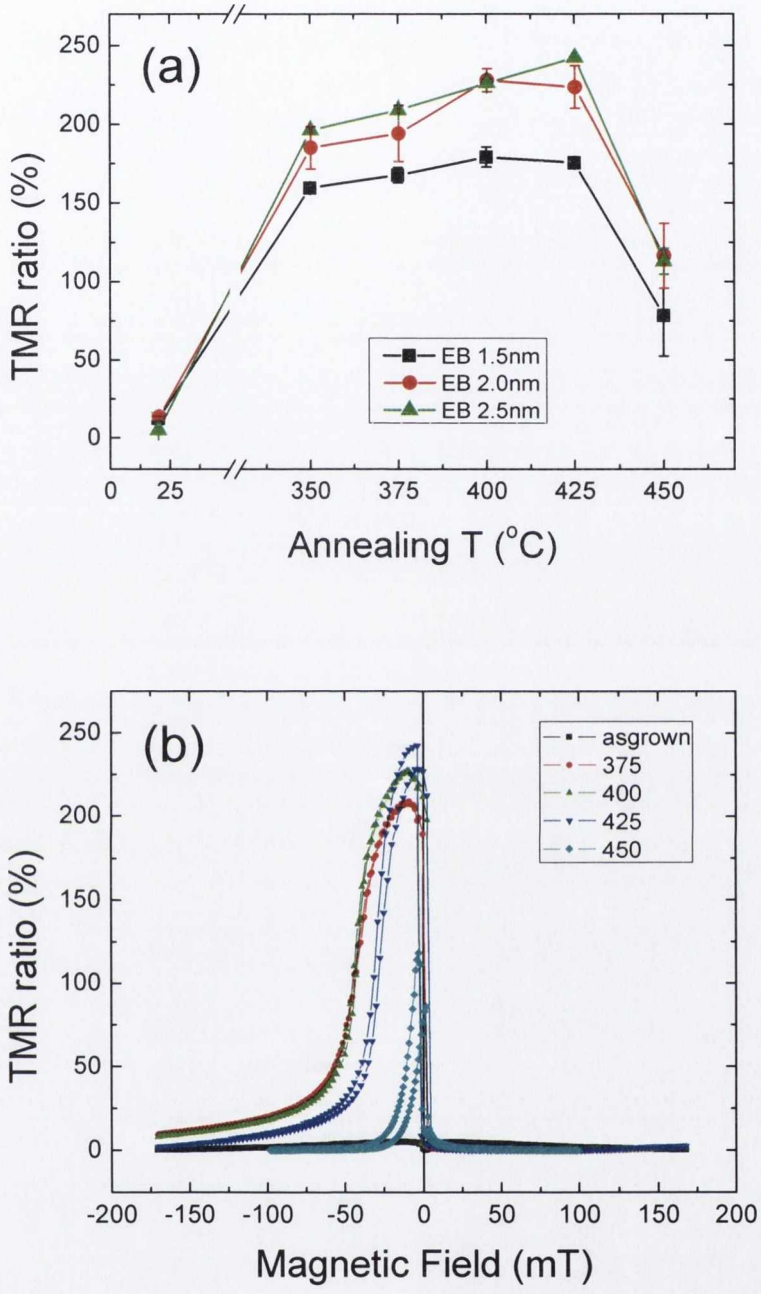

Figure 4. 33. (a) TMR ratio vs. annealing temperature of E-Beam MgO MTJs with different MgO thickness. (b) The effect of annealing temperature on the TMR and exchange bias of the MTJs with 2.5 nm thick e-beam MgO barrier. The reduction in the exchange bias with increasing temperature is clearly observed.

Figure 4.33a summarizes the TMR ratio vs. annealing temperature of e-beam MgO MTJs. In the as-grown state, all samples show low TMR values (~10%) due to incoherent tunnelling and lack of exchange bias. Upon annealing, B diffuses away and a coherent epitaxial structure, confirmed by HR-TEM, is created giving rise to coherent tunnelling and high TMR values. In our samples, we observe an increase in the TMR value up to an annealing temperature of 425°C. The highest TMR (~ 240 %) was observed for the MTJ with a 2.5 nm barrier. TMR values gradually decrease as the MgO thickness is reduced. An MTJ with a 1.2 nm e-beam MgO barrier showed a TMR of ~ 120 % with an RA of 100 $\Omega\mu m^2$.

The exchange bias falls dramatically on annealing above 400 °C (see Figure 4.33b) due to significant loss of Mn from the antiferromagnetic IrMn layer. The higher temperature stability of the AP state and therefore the high TMR in our MTJs is due to the thicker Ru layer in SAF structure, which serves as a barrier for Mn diffusion into MgO barrier [29]. In the case of 450 °C annealing, the exchange bias is almost annihilated and a stable AP configuration is not achieved as shown in Figure 4.33b. We believe the reason for the sudden drop in TMR ratios for the samples annealed at this temperature is mainly due to the lack of a stable AP state.

Figure 4.34 shows the resistance-area (RA) product of e-beam MgO MTJs for both P and AP configurations. The samples show an exponential increase in the RA values with increasing MgO thickness. Straight lines are drawn as guides to the eye to show the exponential increase. The deviations from this line in the low RA regime are common due to the highly pronounced effect of the interfacial roughness for thin barriers. Barrier heights of 0.47 eV for P and 0.49 eV for AP states were calculated from linear fits to the data points for $t_{MgO} \geq 1.5$ nm using Wenzel–Kramer–Brillouin

(WKB) approximation in the low voltage limit [20]. These values are higher than previously reported values for the RF-MgO (0.34 - 0.38 eV) [22] and MBE grown MgO (0.39 eV) [21] barriers, but much smaller than that for an ideal MgO tunnel barrier (3.7 eV) [30]. Significant deviations in the barrier heights of the MgO in MTJs from that of an ideal MgO could be attributed to the oxygen vacancies in the grown barriers [21]. The greater barrier height of the e-beam MgO barrier is most likely due to the lower defect densities compared to the RF-MgO, which reveals itself in the 2θ XRD scans as shown in Figure 4.32. A greater barrier height could be advantageous for sensor and STT applications, where a higher voltage output is required. In addition, our e-beam MgO barrier junctions exhibit lower noise levels on account of the low defect density [31].

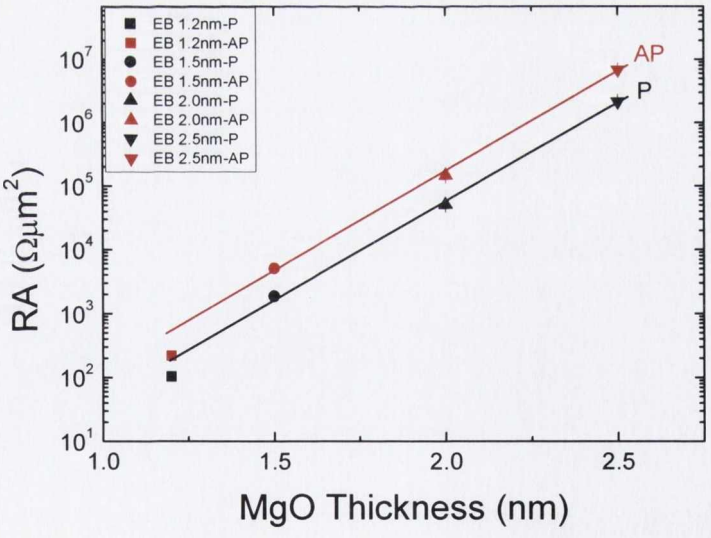

Figure 4. 34. Resistance × area vs. MgO thickness graph. Lines are guide to eye and indicates the deviation at low MgO thickness due to roughness.

4.5. Conclusions

The importance of magnetic dead layers has been identified by investigating the thickness dependence of magnetisation of CoFeB films on various buffer layers such as SiO_2, MgO and Ta. It is found that SiO_2 and Ta buffer layers cause significant dead layers. However, films on MgO buffer became superparamagnetic below 1 nm, but no observable dead layer was measured.

High quality AlO_x based MTJs were fabricated and characterized. TMR ratios exceeding 20 % at RT was observed using CoFe electrodes. It was found that the TMR ratio is independent of the annealing temperature. The effect of oxygen insertion during AlO_x growth was found to be detrimental for TMR in these MTJs due to a dead layer formed at the bottom CoFe / AlO_x interface.

An attempt to create high performance $SrTiO_3$ based MTJ was made but only a low TMR ratio of 2 % at RT was found for the stacks using CoFeB electrodes. The reason for the low TMR ratio is the lack of required (001) crystal matching between the STO barrier and CoFeB electrodes. The TMR ratio could be increased if STO barrier can be grown in (001) orientation with correct stoichiometry.

A large amount of time was devoted to the optimization of high quality MgO based MTJs. The pinning structure, MgO and CoFeB growth pressures, MgO substrate temperature, MgO deposition temperature, MgO target to sample distance, and MgO thickness were all optimized. A very high TMR ratio, exceeding 250 % at RT, was achieved in MgO based MTJs after extensive optimization. We also achieved low RA ($< 50\ \Omega\mu m^2$) MgO MTJs high TMR ratio (> 120 %). These low RA MTJs are essential for spin transfer torque experiments. On the other hand, we

developed high quality e-beam evaporation technique for MgO barrier in UHV condition. The structural properties of the e-beam MgO were found to be very similar to bulk MgO. MTJs with e-beam MgO showed TMR ratios > 240 % at RT which is comparable to what we achieved with sputtered MgO barrier. E-beam evaporation is a simple and inexpensive alternative to sputtering and can be easily implemented for wafer scale production.

4.6. References

1. Parkin, S.S.P., *et al.*, *"Giant tunnelling magnetoresistance at room temperature with MgO (100) tunnel barriers"*, Nat Mater. **3**, 862, (2004).
2. Yuasa, S., *et al.*, *"Giant room-temperature magnetoresistance in single-crystal Fe/MgO/Fe magnetic tunnel junctions"*, Nat Mater. **3**, 868, (2004).
3. Lee, Y.M., *et al.*, *"Effect of electrode composition on the tunnel magnetoresistance of pseudo-spin-valve magnetic tunnel junction with a MgO tunnel barrier"*, Applied Physics Letters. **90**, 212507, (2007).
4. Kurt, H., *et al.*, *"Giant tunneling magnetoresistance with electron beam evaporated MgO barrier and CoFeB electrodes"*, Journal of Applied Physics. **107**, 083920, (2010).
5. Kurt, H., *et al.*, *"Boron diffusion in magnetic tunnel junctions with MgO (001) barriers and CoFeB electrodes"*, Applied Physics Letters. **96**, 262501, (2010).

6. Stamenov, P., K. Oguz, and J.M.D. Coey, *"High-field anisotropy of the tunnelling magnetoresistance of CoFeB/MgO/CoFeB junctions"*, Journal of Magnetism and Magnetic Materials. **322**, 1413, (2010).

7. Scola, J., *et al.*, *"Noise in MgO barrier magnetic tunnel junctions with CoFeB electrodes: Influence of annealing temperature"*, Applied Physics Letters. **90**, 252501, (2007).

8. Wang, Y.-H., *et al.*, *"Interfacial and annealing effects on magnetic properties of CoFeB thin films"*, Journal of Applied Physics. **99**, 08M307, (2006).

9. Jang, Y., *et al.*, *"Magnetic field sensing scheme using CoFeB/MgO/CoFeB tunneling junction with superparamagnetic CoFeB layer"*, Applied Physics Letters. **89**, 163119, (2006).

10. Moodera, J.S., *et al.*, *"Large magnetoresistance at room temperature in ferromagnetic thin film tunnel junctions"*, Physical Review Letters. **74**, 3273, (1995).

11. Miyazaki, T. and N. Tezuka, *"Giant magnetic tunneling effect in Fe/Al2O3/Fe junction"*, Journal of Magnetism and Magnetic Materials. **139**, L231, (1995).

12. Kim, S., *et al.*, *"Effect of plasma oxidation time and annealing condition on the temperature dependence of tunneling magnetoresistance"*, Metals and Materials International. **9**, 57, (2003).

13. Kotecki, D.E., *"A review of high dielectric materials for DRAM capacitors"*, Integrated Ferroelectrics: An International Journal. **16**, 1 (1997).

14. Velev, J.P., *et al.*, *"Negative Spin Polarization and Large Tunneling Magnetoresistance in Epitaxial Co|$SrTiO_3$|Co Magnetic Tunnel Junctions"*, Physical Review Letters. **95**, 216601, (2005).

15. Morán, O., R. Hott, and D. Fuchs, *"Study of $SrTiO_3$ thin films grown by sputtering technique for tunnel barriers in quasiparticle injection contacts"*, Thin Solid Films. **517**, 1908, (2009).

16. Shih, W.-C. and W.-H. Yang, *"Preparation of c-axis textured $SrTiO_3$ thin films on Si(1 0 0) substrates by pulsed laser deposition process"*, Physica B: Condensed Matter. **405**, 234, (2010).

17. Anderson, G.W., Y. Huai, and M. Pakala, *"Spin-valve thermal stability: The effect of different antiferromagnets"*, Journal of Applied Physics. **87**, 5726, (2000).

18. Yuasa, S. and D.D. Djayaprawira, *"Giant tunnel magnetoresistance in magnetic tunnel junctions with a crystalline MgO(0 0 1) barrier"*, Journal of Physics D: Applied Physics. **40**, R337, (2007).

19. Ikeda, S., *et al.*, *"Tunnel magnetoresistance in MgO-barrier magnetic tunnel junctions with bcc-CoFe(B) and fcc-CoFe free layers"*, Journal of Applied Physics. **99**, 08A907, (2006).

20. Simmons, J.G., *"Generalized Formula for the Electric Tunnel Effect between Similar Electrodes Separated by a Thin Insulating Film"*, Journal of Applied Physics. **34**, 1793, (1963).

21. Yuasa, S., *et al.*, *"Giant room-temperature magnetoresistance in single-crystal Fe/MgO/Fe magnetic tunnel junctions"*, Nature Materials. **3**, 868, (2004).

22. Hayakawa, J., *et al.*, *"Dependence of giant tunnel magnetoresistance of sputtered CoFeB/MgO/CoFeB magnetic tunnel junctions on MgO barrier thickness and annealing temperature"*, Japanese Journal of Applied Physics, Part 2: Letters. **44**, L587, (2005).

23. Zhang, S., *et al.*, *"Quenching of Magnetoresistance by Hot Electrons in Magnetic Tunnel Junctions"*, Physical Review Letters. **79**, 3744, (1997).

24. Sharma, M., S.X. Wang, and J.H. Nickel, *"Inversion of Spin Polarization and Tunneling Magnetoresistance in Spin-Dependent Tunneling Junctions"*, Physical Review Letters. **82**, 616, (1999).

25. Valenzuela, S.O., *et al.*, *"Spin Polarized Tunneling at Finite Bias"*, Physical Review Letters. **94**, 196601, (2005).

26. Sun, J.Z. and D.C. Ralph, *"Magnetoresistance and spin-transfer torque in magnetic tunnel junctions"*, Journal of Magnetism and Magnetic Materials. **320**, 1227, (2008).

27. Matsumoto, R., *et al.*, *"Tunneling spectra of sputter-deposited CoFeB/MgO/CoFeB magnetic tunnel junctions showing giant tunneling magnetoresistance effect"*, Solid State Communications. **136**, 611, (2005).

28. Matsumoto, R., *et al.*, *"Dependence on annealing temperatures of tunneling spectra in high-resistance CoFeB/MgO/CoFeB magnetic tunnel junctions"*, Solid State Communications. **143**, 574, (2007).

29. Lee, Y.M., *et al.*, *"Giant tunnel magnetoresistance and high annealing stability in CoFeB/MgO/CoFeB magnetic tunnel junctions with synthetic pinned layer"*, Applied Physics Letters. **89**, 042506, (2006).

30. Wulfhekel, W., *et al.*, *"Single-crystal magnetotunnel junctions"*, Applied Physics Letters. **78**, 509, (2001).

31. Diao, Z., *et al.*, *"Reduced low frequency noise in electron beam evaporated MgO magnetic tunnel junctions"*, Applied Physics Letters. **96**, 202506, (2010).

Chapter 5

Low Moment Amorphous Magnetic Materials

5.1. Introduction

Ferromagnetic materials with low saturation magnetisation (M_s) are very important for reducing the critical current density (j_c) for spin transfer torque magnetisation reversal. j_c scales quadratically with the saturation magnetisation of the free layer as discussed in Chapter I. Hence, lower current density values can be obtained using low-magnetisation magnetic materials. Amorphous ferromagnetic alloys are perfect candidates because their saturation magnetisation can easily be controlled. Amorphous metallic ferromagnets are materials which don't possess long range order and they exhibit particular physical characteristics. These materials are widely used in industry due to their excellent properties such as low coercivity, toughness, high metallic resistivity, very low magneto-crystalline anisotropy and high corrosive resistance [1].

The conventional way to fabricate amorphous alloys is the removal of heat from the molten alloy at a rate that is fast enough to prevent crystallization of the melt (rapid solidification). A typical cooling rate should be $>10^5$ ^{o}C/s. This high rate

of heat removal usually dictates that the sample has at least one small dimension to facilitate thermal transfer. Amorphous metallic materials can also be produced by other methods like sputtering, melt spinning, high energy ion bombardment of crystalline alloys, electrodeposition and splat quenching [1].

Amorphous ferromagnetic alloys can be grouped in two: 1) 3d transition metal based alloys and 2) rare-earth metal based ones. In the first case, amorphous state can be stabilized by metalloid (M) insertions like boron (B), carbon (C), silicon (Si), aluminium (Al) and phosphorous (P) into the 3d element (T) in the form $T_{1-x}M_x$ [2]. Metalloid concentration in general should typically be around 20 %. Examples of this type are $(Co_{1-x}Fe_x)_{80}B_{20}$, $Fe_{80}B_{20}$, $Fe_{40}Ni_{40}P_{14}B_6$ and $Co_{74}Fe_5Si_3B_{18}$. In the second class, rare-earth metals (RE) are alloyed with transition metals and metalloids in the form of $RE_{1-x-y}T_xM_y$ with x in range 10 - 25 % and y from 0 - 10 %. Examples are $Gd_{20}Co_{80}$, $Tb_{30}(CoFe)_{70}$ and $Gd_{20}Co_8Fe_{72}$.

5.2. Structure

The structure of amorphous alloys can be described as a dense random packing of hard spheres. However, it is not entirely random, and there is a significant degree of *short-range* order both topological and chemical. The packing of the 3d atoms in amorphous alloys is similar to the random dense-packed Bernal structure (Figure 5.1) [3-4] where the metalloid atoms occupy the larger voids in the random dense-packed arrays of transition metal atoms. Packing fraction (the volume fraction of space occupied by the 3d atoms) of this structure is 0.64 compared to 0.74 of face centred cubic (fcc) or hexagonal closed packed (hcp) and 0.68 of body centred cubic

(bcc) structures. Locally there are dense clusters of 12 or 13 atoms in the random-dense-packing, but these atoms cannot fill space without leaving large interstitial voids. The ratio of atoms to holes is about 4:1. The holes can be blocked by smaller atoms, which stabilize the non-crystalline structure. A typical composition is a-$Fe_{80}B_{20}$, where the covalent boron plugs the holes in the Bernal structure of iron [5].

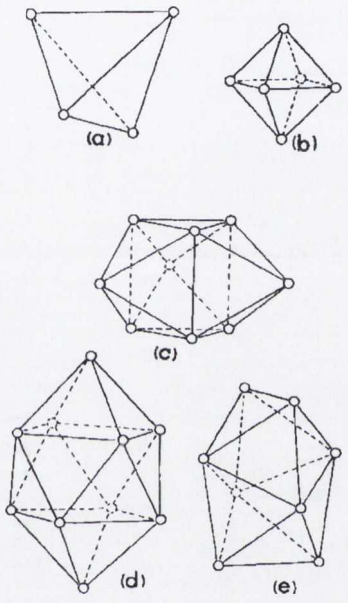

Figure 5. 1. Bernal polyhedra believed to be likely local structural arrangements in amorphous alloys [1].

5.3. Magnetic properties of amorphous ferromagnets

5.3.1. Magnetic moments

The variation of saturation moment per transition-metal atom for amorphous and crystalline alloys as a function of the number of 3d valence electrons is shown in

Figure 5.2 (this is known as Slater-Pauling curve [6-7]). The data are given for the materials of $T_{80}M_{20}$ form. Crystalline alloys apparently have much higher saturation moment, cobalt-iron (CoFe) being the highest (more than $2.4\mu_B$), compared to the amorphous alloys. In the case of amorphous alloys, moment is considerably smaller indicating the presence of metalloid atoms which are needed to stabilize the glassy state. The highest saturation moment is observed in CoFe based ones where it can be larger than 2.0 μ_B for high Fe concentrations.

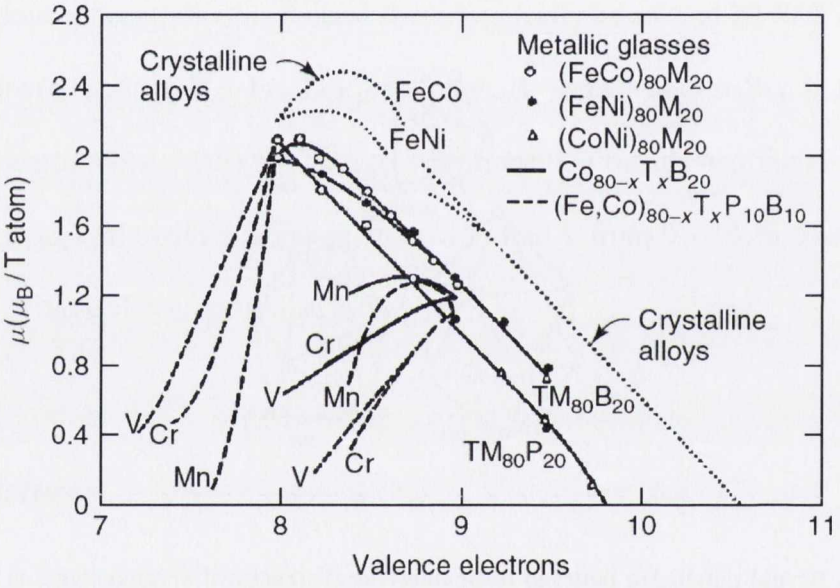

Figure 5. 2 Variation of magnetic moment per transition-metal atom in crystalline and amorphous alloys as a function of number of valence electrons [8].

The effect of early transition metals like chromium (Cr) and vanadium (V) on the saturation moment of amorphous magnetic alloys is drastic, as seen in Figure 5.2. Moment decays rapidly with increasing content of either of these elements. This can

be understood in terms of the virtual-bound-state model, also called magnetic valence model which is discussed in the next section [1, 8-10].

5.3.2. Magnetic valence

The magnetic valence model is a means of predicting the magnetic moment of an alloy based only on the number of electrons. It is based on the assumption of strong ferromagnetism, where the majority spin, ↑ d band, is completely full with five electrons (or else it is entirely empty). Magnetic valence, like ordinary chemical valence, is an integer for each column of the periodic table. To understand its origin, recall that neutrality requires that the total number of valence electrons (up-spin plus down-spin) must equal the chemical valence Z (the nuclear charge minus the number of core electrons) [10]:

$$Z = N^{\uparrow} + N^{\downarrow}. \tag{5.1}$$

The magnetisation M (in units of μ_B) is the corresponding difference:

$$M = N^{\uparrow} - N^{\downarrow} \tag{5.2}$$

where, without loss of generality, we take the majority-spin direction to be "up". Using equation 5.1 to eliminate $N^{\downarrow}$ from equation 5.2, we have

$$M = 2N^{\uparrow} - Z. \tag{5.3}$$

The virtue in focusing on just the up-spin electrons is that, for strong magnets, the number of up-spin electrons $N^{\uparrow}$, can be accurately estimated on the basis of the following fundamental and general considerations. The electronic structure of transition metals consists of a broad sp band cut by five much less dispersive d bands [10]. Now, the defining property of "strong" magnets is that the up-spin d bands lie

entirely above or below the Fermi level, ϵ_F, and therefore contribute either precisely five or precisely zero electrons to $N^{\uparrow}$. We denote this integer contribution of the d band by $N_d^{\uparrow}$ and the small non-integer contribution of the sp band by $N_{sp}^{\uparrow}$ (= $N^{\uparrow}$ - $N_d^{\uparrow}$).

The magnetic valence Z_m, is simply the contribution (according to equation 5.3) of the two integers $N_d^{\uparrow}$ and Z to the magnetisation:

$$Z_m = 2\,N_d^{\uparrow} - Z. \tag{5.4}$$

Since elements to the right of Fe in the periodic table possess filled up-spin d bands, the magnetic valences of Co, Ni, Cu, Zn, ..., Br, and Kr are simply 1, 0, -1, -2, ..., -7, -8. In the late transition metals, the unpolarized sp band contributes 0.3 electrons [11] to $N^{\uparrow}$, giving (via equation 5.3) Co and Ni magnetic moments of ~1.6 μ_B and ~0.6 μ_B respectively. The same argument gives Fe a magnetic valence of 2, and the fact that the magnetisation of Fe (2.2 μ_B) less than 2.6 μ_B reveals the magnetic weakness of Fe: the penetration of the up-spin d band by the Fermi level. The elements Fe, Co and Ni illustrate one virtue of the magnetic-valence concept: the large, but cancelling, contributions to the magnetisation are eliminated, leaving $N_{sp}^{\uparrow}$ and magnetic weakness at centre stage.

In the case of alloys, the average moment per formula is obtained by replacing Z_m by its weighted average value over all atoms present in the alloy:

$$\langle m \rangle = (\langle Z_m \rangle + 2\,N_{sp}^{\uparrow})\,\mu_B. \tag{5.5}$$

In this way, it is possible to estimate the magnetisation of any strong ferromagnetic alloy based on iron, cobalt or nickel. Some magnetic valences are $Z_m = -3$ for B, Y,

La and all rare-earths, −4 for C, Si, Ti, −5 for V, P, −6 for Cr [5]. Additions of the latter elements in particular rapidly destroy the moment.

5.4. Preparation of low magnetisation alloys

Three different low moment ferromagnetic alloy systems were studied in this work. These are $Co_{40}Ni_{40-x}Cr_xB_{20}$, $Co_{40}Fe_{40-x}Ni_xB_{20}$ and $Co_{40}Fe_{40-x}Cr_xB_{20}$. Samples were deposited on SiO_2 / FM (50) or SiO_2 / MgO (2.5) / FM (50) / Ta (5) stacks, FM is the low-moment material and numbers in parentheses indicate the layer thickness in nm. Samples were prepared by co-sputtering from a combination two of $Co_{40}Fe_{40}B_{20}$, $Co_{40}Ni_{40}B_{20}$ and $Co_{40}Cr_{40}B_{20}$ targets. CoNiB and CoCrB targets are used for $Co_{40}Ni_{40-x}Cr_xB_{20}$ films, similarly CoFeB and CoNiB were used for $Co_{40}Fe_{40-x}Ni_xB_{20}$ films and finally CoFeB and CoCrB targets were used for $Co_{40}Fe_{40-x}Cr_xB_{20}$ films. Composition of films was adjusted by carefully arranging the deposition rates of each target. The film composition was determined using energy dispersive x-ray (EDX) technique.

5.5. Magnetic properties of $Co_{40}Ni_{40-x}Cr_xB_{20}$

Figure 5.3 illustrates the room-temperature (RT) magnetisation curves of $Co_{40}Ni_{40-x}Cr_xB_{20}$ films grown on SiO_2 with different Cr concentrations for the as-grown samples. For x = 0, saturation magnetisation is around 400 kA/m and reduces dramatically down to 3 kA/m for x = 13.2 %. Single transition around zero field

indicates a single magnetic phase present in all samples. It is also clear that the Curie temperature of the high Cr concentration sample in the as-grown state is very close to room temperature.

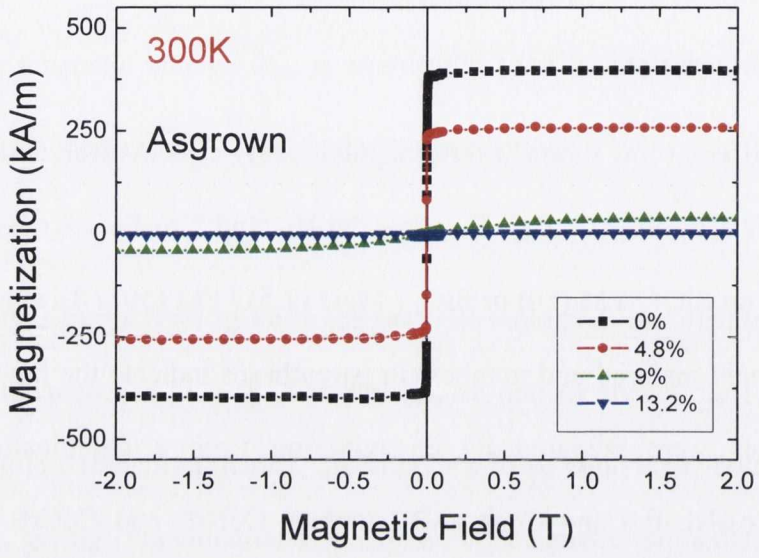

Figure 5. 3. Magnetisation curves of $Co_{40}Ni_{40-x}Cr_xB_{20}$ films with different Cr concentration in the as-grown state measured at RT.

The magnetisation of the annealed samples improves after annealing at 350 ^{o}C for 1 hour as shown in Figure 5.4. For x = 0, saturation magnetisation becomes ~415 kA/m which is slightly larger than the value for the as-grown sample. This indicates some degree of crystallization occurring during annealing which might be associated with boron (B) diffusion into SiO_2. However, increase in the moment is less than 5 % and it is much less than the value for the crystalline $Co_{50}Ni_{50}$ alloy which means the film is still amorphous with considerable boron content.

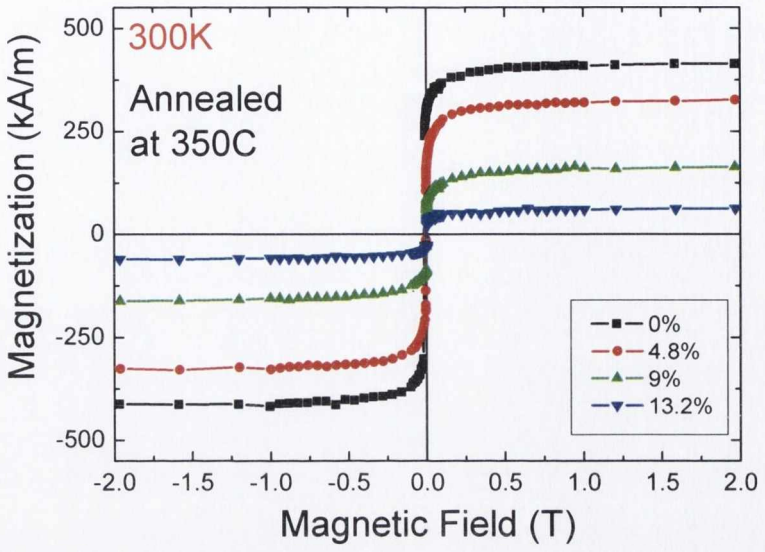

Figure 5. 4. Magnetisation curves of $Co_{40}Ni_{40-x}Cr_xB_{20}$ films with different Cr concentration in the annealed (350 °C for 1 hour) state, measured at RT.

Table 5.1. Summary of saturation magnetisation in kAm^{-1} of annealed $Co_{40}Ni_{40-x}Cr_xB_{20}$ obtained from SQUID measurements at 4 K and RT.

x	M_s (300 K)	M_s (4 K)	ΔM	% Change
0	415.8	532.5	116.7	28
4.8	328.9	422.6	93.7	28
9.0	164.9	330.5	165.6	100
13.2	62.6	206.7	144.1	230

The effect of temperature on the saturation magnetisation of the annealed sample is shown in Figure 5.5. The value of the saturation magnetisation increases considerably at 4 K and increase is almost the same for x = 0 and x = 4.8 as shown in

Table 5.1. This indicates that the magnetic interactions of these films are the same, independent of the amount of Cr. When x is larger than 4.8, the change in the saturation magnetisation at low temperature is significantly larger compared to low concentrations which might be an indication of a change in the Curie temperature. The Curie temperatures for high concentrations might be very close to RT.

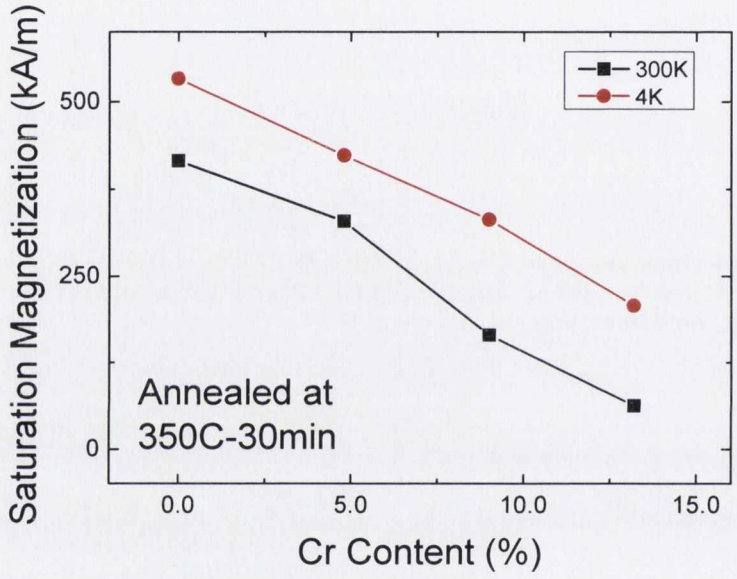

Figure 5. 5. Saturation magnetisation vs. Cr concentration for $Co_{40}Ni_{40-x}Cr_xB_{20}$ films for annealed samples measured at RT and 4 K.

Comparison of saturation magnetisation (μ_B/formula) data of as-grown $Co_{40}Ni_{40-x}Cr_xB_{20}$ films with magnetic valence model is indicated in Figure 5.6. The model gets the right moment for x = 0, but predicts a faster decay with increasing Cr concentration due to high negative magnetic valence of Cr (-6). However, actual films show much smaller reduction in saturation magnetisation with increasing Cr concentration. This might be due to occupancy of the spin ↑ Cr band ($N^{\uparrow} \neq 0$).

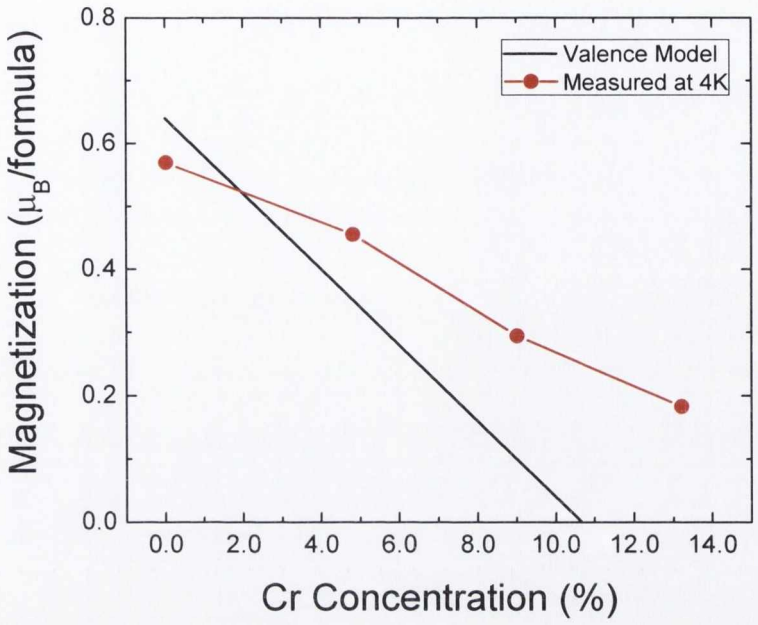

Figure 5. 6. Saturation magnetisation of $Co_{40}Ni_{40-x}Cr_xB_{20}$ films vs. Cr concentration derived from magnetic valence model and from measurement of as-grown film at 4 K.

5.6. Magnetic properties of $Co_{40}Fe_{40-x}Ni_xB_{20}$

$Co_{40}Fe_{40-x}Ni_xB_{20}$ is another low magnetisation amorphous alloy that has been studied in this work. The magnetisation curves of $Co_{40}Fe_{40-x}Ni_xB_{20}$ films grown on SiO_2 are shown in Figure 5.7 for the as-grown samples measured at RT for different Ni concentrations. It seems that Ni substitution is not very effective in terms of reducing the magnetisation of the film. For x = 0, magnetisation of the film is 984 kA/m and reduces slightly to 882 kA/m when x = 21.6. This very small decrease shows that replacing Fe with Ni does not affect the magnetic moments. This result is puzzling because a Ni atom has a much lower moment of 0.6 μ_B compared to moment of an Fe atom (2.2 μ_B). It suggests that a nickel atom slightly increases the

number of $3d^{\uparrow}$ electrons on its iron neighbours. Usually $N^{\uparrow}$ is < 5 for iron, which is a weak ferromagnet.

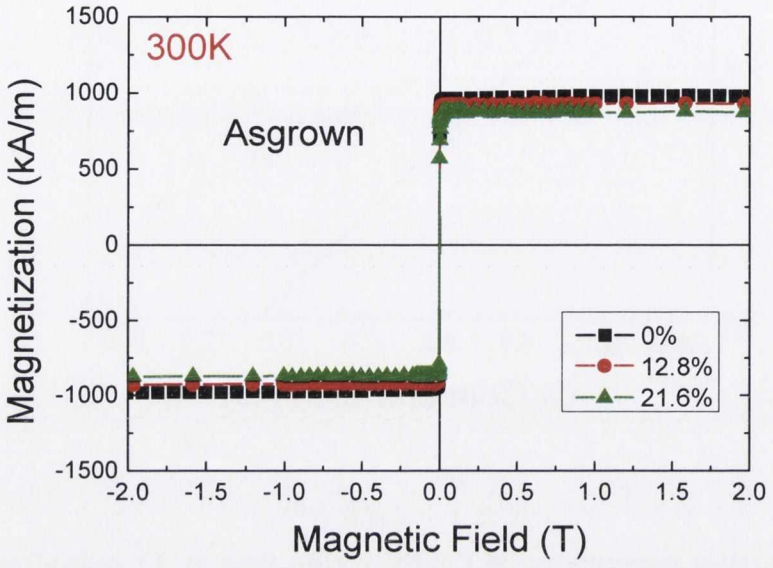

Figure 5. 7. Magnetisation curves of $Co_{40}Fe_{40-x}Ni_xB_{20}$ films with different Ni concentration in the as-grown state measured at RT.

The effect of annealing is very small on the magnetisation of the $Co_{40}Fe_{40-x}Ni_xB_{20}$ as seen in Figure 5.8. Samples are annealed at 350 °C for 1 hour under vacuum. For x = 21.6, magnetisation increases to 924 kA/m which is roughly a 5 % increase compared to the as-grown sample. Similar to $Co_{40}Ni_{40-x}Cr_xB_{20}$ films, this effect might be due to diffusion of boron out of the metal which might lead to some crystallization in the annealed samples. It seems that the crystallization temperature of this alloy is larger than 350 °C, or else longer annealing times are required to completely crystallize the films. It has been also reported that boron requires special cap layers to diffuse into such as tantalum and titanium [12]. Prepared samples were also quite thick (~ 50 nm) for boron to completely diffuse out.

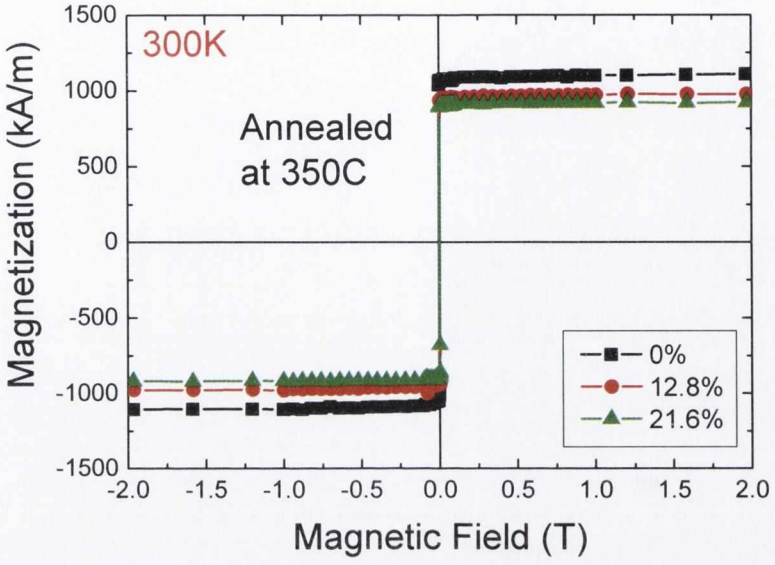

Figure 5. 8. Magnetisation curves of $Co_{40}Fe_{40-x}Ni_xB_{20}$ films with different Ni concentration in the annealed (350 ^{0}C for 1 hour) state measured at RT.

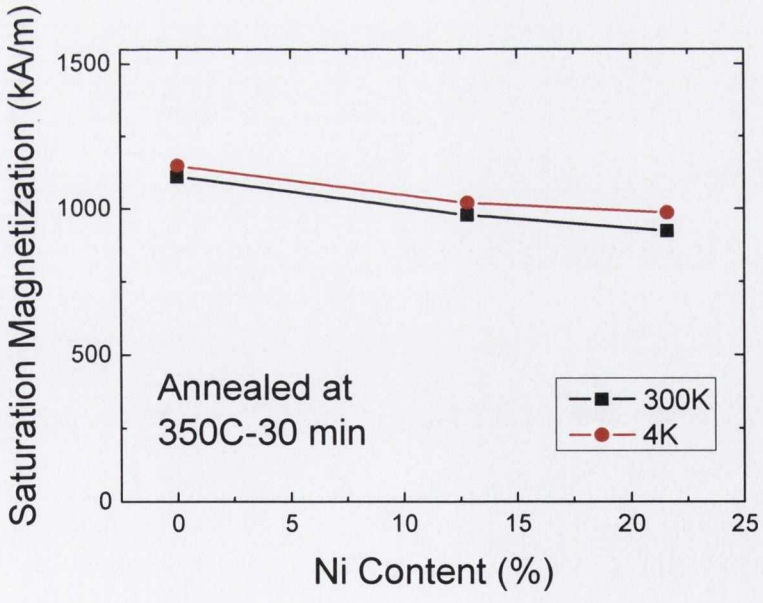

Figure 5. 9. Saturation magnetisation vs. Ni concentration for $Co_{40}Fe_{40-x}Ni_xB_{20}$ films for annealed samples measured at RT and 4 K.

Low-temperature measurements of the annealed films are plotted together with RT measurements in Figure 5.9. The saturation magnetisation of films is slightly higher when the samples are measured at 4 K. Increase of moment is slightly higher for the samples which have Ni substitution. ΔM = [M (4 K) – M (300 K)] is 39 kA/m for x = 0 and 64 kA/m for x = 21.6 which reflects a lower Curie temperature with Ni substitution (Table 5.2). But, overall change in M_s is less than 10 % for all films which indicates that Curie temperatures of these alloys are far above RT.

Table 5. 2. Summary of saturation magnetisation in kAm^{-1} of annealed $Co_{40}Fe_{40-x}Ni_xB_{20}$ obtained from SQUID measurements at 4 K and RT.

x	M_s (300 K)	M_s (4 K)	ΔM	% Change
0	1111.0	1150.0	39.0	3.5
12.8	978.0	1021.0	43.0	4.4
21.6	924.0	988.0	64.0	6.9

The comparison between magnetic valence model and measurements for as-grown $Co_{40}Fe_{40-x}Ni_xB_{20}$ samples is shown in Figure 5.10. Model predicts a larger moment at x= 0 and a large slope. This again can be explained by the fact that iron is a weak ferromagnet, and $N^{\uparrow}$ depends on the composition. It is not exactly 5 for Fe.

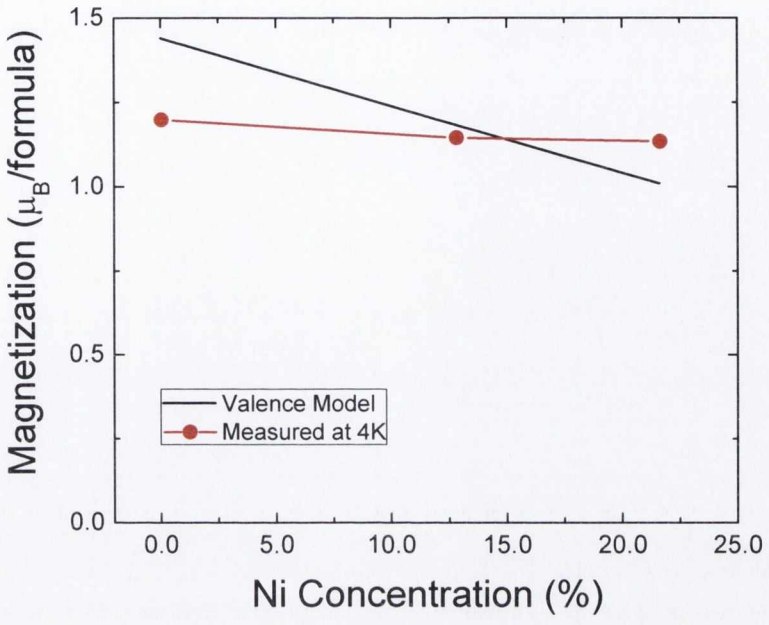

Figure 5. 10. Saturation magnetisation of $Co_{40}Fe_{40-x}Ni_xB_{20}$ films vs. Ni concentration derived from magnetic valence model and from measurement of as-grown films at 4 K.

5.7. Magnetic properties of $Co_{40}Fe_{40-x}Cr_xB_{20}$

$Co_{40}Fe_{40-x}Cr_xB_{20}$ is the best alloy system studied in this work from the point of view of effective reduction in magnetisation. Magnetisation curves of different Cr concentrations of as-grown $Co_{40}Fe_{40-x}Cr_xB_{20}$ films deposited on SiO_2 are shown in Figure 5.11. Magnetisation of the films decreases as the Cr concentration increases with a single transition close to zero magnetic field. This indicates that there is only one magnetic phase present in the samples. For x = 0, saturation magnetisation is 984 kA/m and decreases linearly to 859 kA/m for x = 4.8 and 235 kA/m for x = 18. Similar behaviour was also reported by Kubota *et al.* [13] in $(Co_{75}Fe_{25})_{80-x}Cr_xB_{20}$

films. In their work, magnetisation becomes almost zero for x = 20 at RT but they are reducing both Co and Fe in the alloy. Therefore, it is expected to have a faster decay of magnetisation.

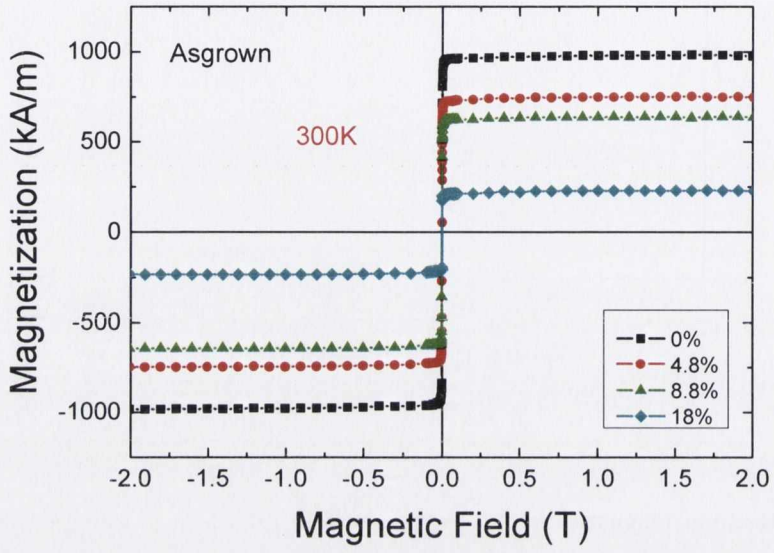

Figure 5. 11. Magnetisation curves of $Co_{40}Fe_{40-x}Cr_xB_{20}$ films with different Cr concentration in the as-grown state measured at RT.

After annealing at 350 °C for 1 hour, magnetisations of all samples considerably increase. RT magnetisation curves of annealed samples are plotted in Figure 5.12. For x = 4, the magnetisation value becomes 910 kA/m after annealing, which is ~ 18 % larger than the value of the amorphous as-grown sample. This increase is due to some structural ordering in the sample via boron diffusion. X-ray diffraction measurements didn't reveal any degree of observable crystallization on these films at this annealing temperature (not shown). Similar to previous alloys, $Co_{40}Fe_{40-x}Cr_xB_{20}$ is also not completely crystallized during annealing due to a lack of

boron getter layer. The single transition around zero field confirms that there is no secondary magnetic phase formation during annealing.

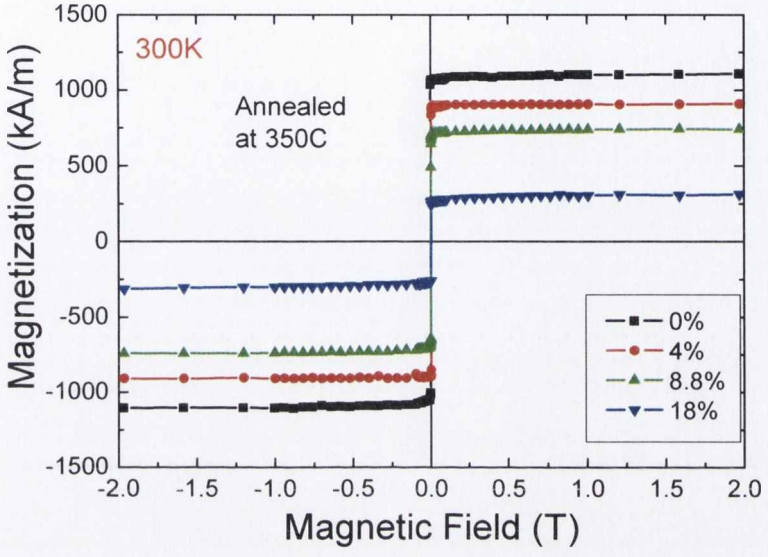

Figure 5. 12. Magnetisation curves of $Co_{40}Fe_{40-x}Cr_xB_{20}$ films with different Cr concentration in the annealed (350 °C for 1 hour) state measured at RT.

Table 5. 3 Summary of saturation magnetisation in kAm^{-1} of annealed $Co_{40}Fe_{40-x}Cr_xB_{20}$ obtained from SQUID measurements at 4 K and RT.

x	M_s (300 K)	M_s (4 K)	ΔM	% Change
0	1111.0	1150.0	39.0	3.5
4.8	909.8	961.7	51.9	5.7
8.8	743.8	816.8	73.0	9.8
18.8	309.7	471.7	162.0	52.3

Low temperature magnetisation measurements reveal a small increase in the saturation magnetisation of samples as shown in Figure 5.13. The increase in the saturation magnetisation becomes larger as the Cr concentration increases, as indicated in Table 5.3. For x = 18.8, the saturation magnetisation increases to more than 50 % of its room temperature value. This is an indication of the lower Curie temperature of samples with higher Cr concentration.

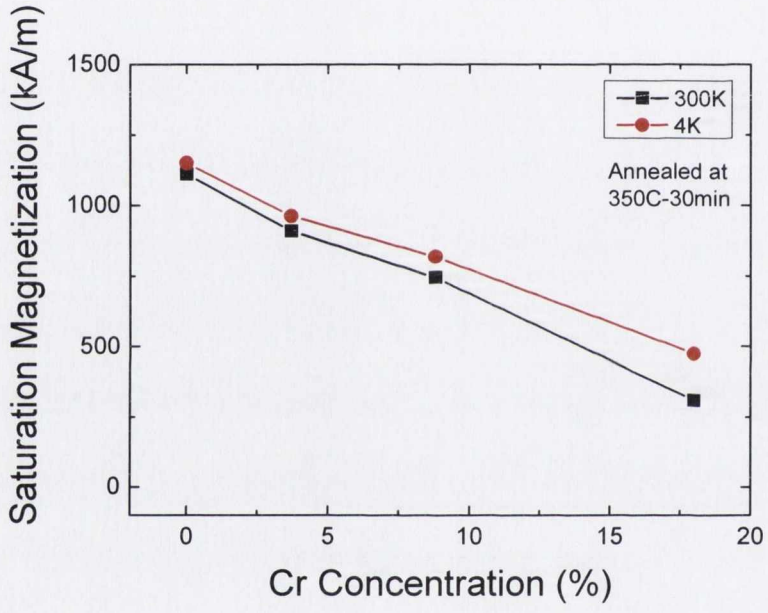

Figure 5. 13. Saturation magnetisation vs. Cr concentration for $Co_{40}Fe_{40-x}Cr_xB_{20}$ films for annealed samples measured at RT and 4 K.

Magnetisations of $Co_{40}Fe_{40-x}Cr_xB_{20}$ samples obtained from magnetic valence model are compared to the measurements of as-grown samples at 4 K in Figure 5.14. The model again predicts significantly a faster linear decay of magnetisation with increasing Cr concentration and disappearance of ferromagnetism at 18 % due to large negative magnetic valence of chromium (-6). Actual magnetisation curve

reduces linearly but the slope is smaller than the model predicts. If the number of electrons in the minority-spin d band are different from the model assumption (5 for Fe, Co; 0 for Cr) discrepancies from model can occur. Another reason for discrepancies is that the Fermi level moves out of the density of states peak responsible for magnetism.

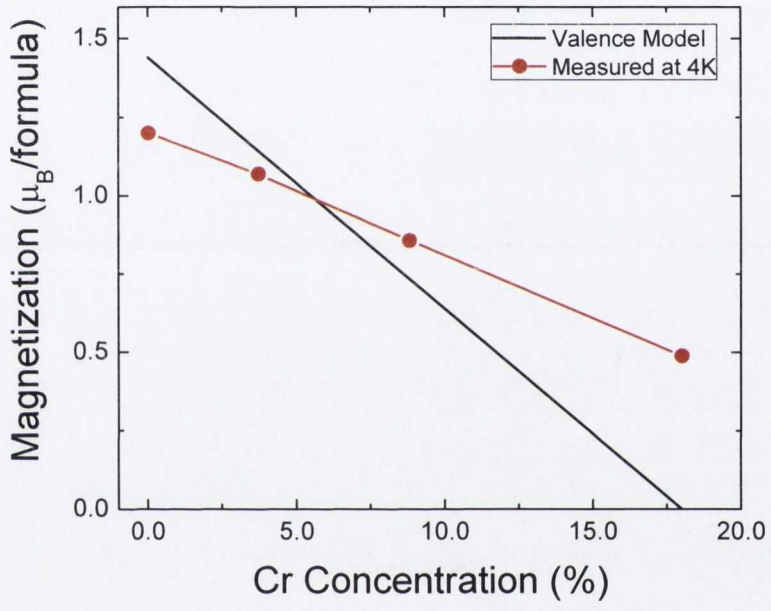

Figure 5. 14. Saturation magnetisation of $Co_{40}Fe_{40-x}Cr_xB_{20}$ films vs. Cr concentration derived from magnetic valence model and from measurement of as-grown film at 4 K.

5.8. Conclusions

Magnetic properties of $Co_{40}Ni_{40-x}Cr_xB_{20}$, $Co_{40}Fe_{40-x}Ni_xB_{20}$ and $Co_{40}Fe_{40-x}Cr_xB_{20}$ low moment amorphous magnetic alloys were studied. $Co_{40}Ni_{40-x}Cr_xB_{20}$ is found to have very low saturation magnetisation which decays very rapidly with

increasing Cr concentration. It is not ideal because very low magnetisation film will have much lower shape anisotropy when it is patterned in to a nanopillar which will reduce the thermal stability of the nano-device. $Co_{40}Fe_{40-x}Ni_xB_{20}$ films showed magnetisation values very similar to $Co_{40}Fe_{40}B_{20}$ which indicated that Ni substitution is not very effective in reducing the moment. Among the three complex alloy systems, $Co_{40}Fe_{40-x}Cr_xB_{20}$ is found to be the best in terms of magnetic properties. Cr substitution linearly reduces the magnetisation of the alloy. Saturation magnetisation of this alloy should be sufficient enough to have reasonable thermal stability for nano-devices.

5.9. References

1. O'Handley, R.C., *"Physics of ferromagnetic amorphous alloys"*, Journal of Applied Physics. **62**, R15, (1987).
2. Luborsky, F.E., *Amorphous Metallic Alloys*. 1983, London: Butterworth & Co Ltd.
3. Bernal, J.D., *"Geometry of the Structure of Monatomic Liquids"*, Nature. **185**, 68, (1960).
4. Bernal, J.D. and J. Mason, *"Packing of spheres: Co-ordination of randomly packed spheres"*, Nature. **188**, 910, (1960).
5. Coey, J.M.D., *Magnetism and Magnetic Materials*. 2009: Cambridge University Press.
6. Slater, J.C., *"The Ferromagnetism of Nickel. II. Temperature Effects"*, Physical Review. **49**, 931, (1936).

7. Pauling, L., *"The Nature of the Interatomic Forces in Metals"*, Physical Review. **54**, 899, (1938).

8. O'Handley, R.C., *Modern Magnetic Materials*. 2000: John Wiley & Sons Inc.

9. Malozemoff, A.P., *et al.*, *"Magnetism of amorphous metal-metal alloys"*, Journal of Magnetism and Magnetic Materials. **35**, 192, (1983).

10. Williams, A., *et al.*, *"Generalized Slater-Pauling curve for transition-metal magnets"*, Magnetics, IEEE Transactions on. **19**, 1983, (1983).

11. V.L. Moruzzi, J.F.J., A.R. Williams., *Calculated electronic properties of metals*. 1978, New York: Pergamon Press.

12. Kurt, H., *et al.*, *"Boron diffusion in magnetic tunnel junctions with MgO (001) barriers and CoFeB electrodes"*, Applied Physics Letters. **96**, 262501, (2010).

13. Kubota, H., *et al.*, *"Reduction in switching current using a low-saturation magnetisation Co-Fe-(Cr, V)-B free layer in MgO-based magnetic tunnel junctions"*, Journal of Applied Physics. **105**, 07D117, (2009).

Chapter 6

Spin Transfer Torque in MgO Based Magnetic Tunnel Junctions

Spin transfer torque magnetisation switching (STS) has been investigated in MgO based nano-MTJs with a view to reduce the critical current density. Two different approaches were used. The first is to reduce the saturation magnetisation of the free layer in single barrier MTJs and the second is to use different device geometries (dual MTJs and MTJs with synthetic antiferromagnetic (SAF) free layer). This chapter is organized as follows: First STS in single barrier MTJs will be discussed including the effect of using low moment free layers, second the effect of using dual MTJs will be described and finally STS in MTJs with a SAF free layer will be explained. Endurance and switching current distribution will also be discussed.

6.1. STS in single barrier MTJs

Spin transfer switching in single barrier magnetic tunnel junctions will be considered first. There are two important parameters governing the observation of spin transfer torque switching in MTJs. The first one is the size of the junction: it

should be small (~ 100 × 200 nm^2) which is achieved by e-beam lithography described in Chapter III. The second one is the resistance × area (RA) product of the MTJ. The RA of the device should be sufficiently small to allow high current densities without damaging the insulating layer. The first devices that we studied had RA values around 220 $\Omega\mu m^2$ and typical resistance and TMR ratio vs. magnetic field curves are shown in Figure 6.1. TMR ratio of the device is more than 200 % and the device size is 160 × 282 nm^2. The MTJ stack is given in Figure 6.2.

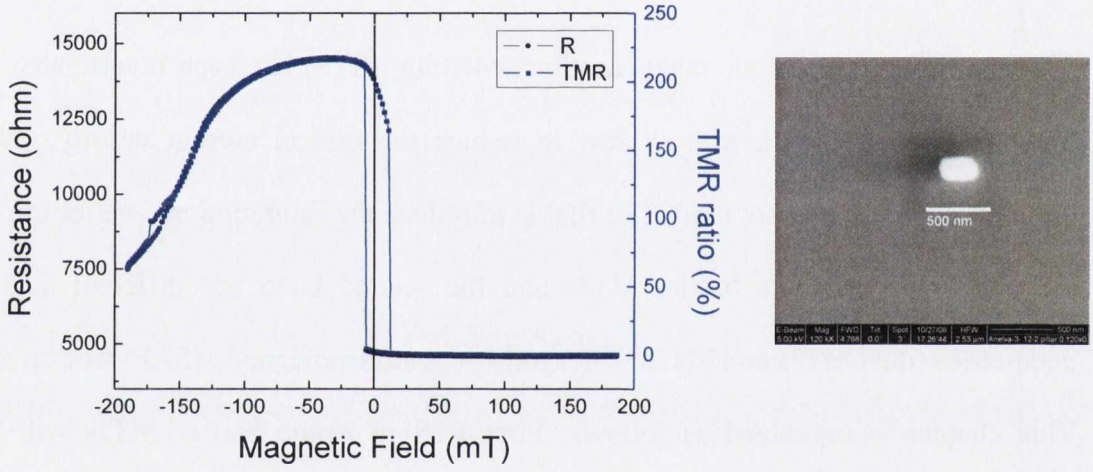

Figure 6. 1. Resistance and TMR ratio vs. magnetic field plot for an MgO based nano-MTJ with an RA = 220 $\Omega\mu m^2$. SEM micrograph on the right shows the e-beam resist pillar exposed for this device. The size of the resist pillar is 160 × 282 nm^2. The sample is annealed at 360 °C.

The DC voltages vs. current measurements of the same device are shown in Figure 6.2 for parallel (P) and anti-parallel (AP) configurations. There are no sharp changes observed in both measurements. The pillar size and the RA value of this device are relatively high, thus it is difficult to obtain high current densities to observe STS. At 1 V bias for P state, the current density reaches only 5 × 10^5 A/cm^2

which is well below the expected critical current density (~ 5 × 10^6 A/cm^2) for this type of device [1-2]. Higher current densities are explored for the same device but when the bias value is above 1.2 V all devices were shorted due to dielectric break-down of the tunnel barrier. This particular device was annealed at 360 °C for 1.5 hours to obtain high TMR ratio.

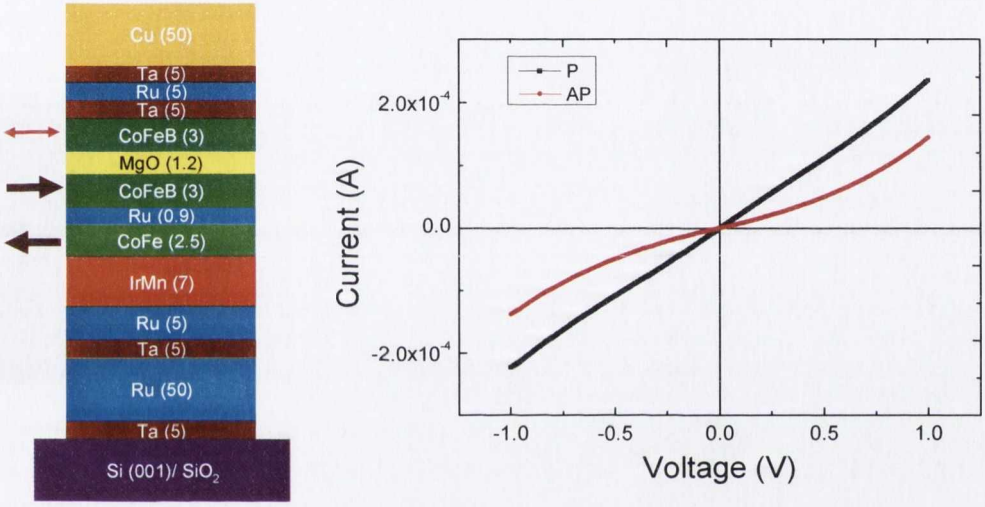

Figure 6. 2. Schematic of the single barrier MTJ stack and I-V plot of a nano-MTJ which is annealed at 360 °C. No sharp changes are observed in the graphs. This shows that current density is not high enough to reverse the magnetisation of the free layer.

In order to observe STS in MgO based single barrier MTJs, we prepared lower RA (≤ 50 Ωμm^2) MTJs and patterned them into nanopillars. The magneto-resistance curve of one of these devices is shown in Figure 6.3. The TMR ratio is > 150 % and RA value is ~ 10 Ωμm^2. The MTJ stack is the same as the previous sample except that the MgO thickness is ~ 1 nm. The free layer is again 3 nm thick and the sample is annealed at 360 °C for 1.5 hours. The minor loop of TMR-H curve

is shown in Figure 6.4. The coercivity of the free layer is 12 mT and a small + 4 mT shift of the loop is observed due to the dipolar coupling between the free and the pinned layer. This coupling is due to the stray field created by the patterned pinned layer and it depends on the milling depth [3]. High coercivity of the free layer indicates that the top CoFeB layer is nicely crystallized after annealing at 360 °C.

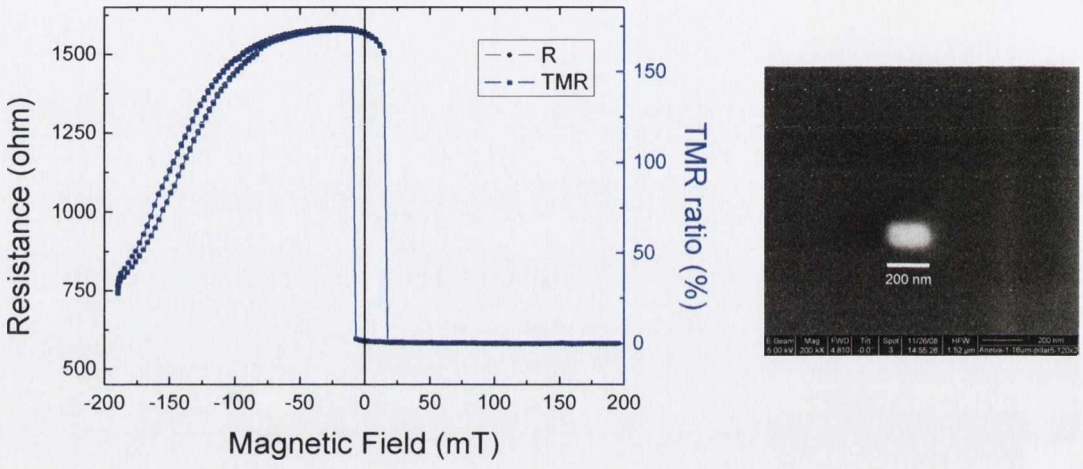

Figure 6. 3. Resistance and TMR ratio vs. magnetic field plot for an MgO based nano-MTJ with an RA = 13 Ωμm^2. SEM micrograph on the right shows the e-beam resist pillar exposed for this device. The size of the resist pillar is 110 × 210 nm^2. The sample is annealed at 360 °C.

Spin transfer torque magnetisation reversal is observed in these single MTJs. Distinct steps in the voltage for positive and negative current in the I-V measurements are the signatures of STS, as shown in Figure 6.5. The positive current is defined such that the electrons flow from pinned to free layer; it stabilizes the P alignment. To observe the STS, we had to apply a small external magnetic field to partially cancel the coupling. We couldn't observe switching when we completely

cancelled the dipolar field. This might be due to high annealing temperature and long annealing time which completely crystallizes the CoFeB free layer. Hence, the magnetisation of the free layer increases significantly. For AP to P switching, + 10 mT external field was applied and J_C^{AP-P} is found to be 2.7 × 10^6 A/cm^2. In the case of the P to AP switch, - 8.8 mT field was applied and switching, J_C^{P-AP}, was observed at 3.3 × 10^6 A/cm^2. For both measurements, the external field is chosen to assist the switching, thus the actual critical current density should be considerably larger [1-2]. The change in the resistance during these measurements is shown in Figure 6.6. Sudden changes at positive and negative currents are clearly observed.

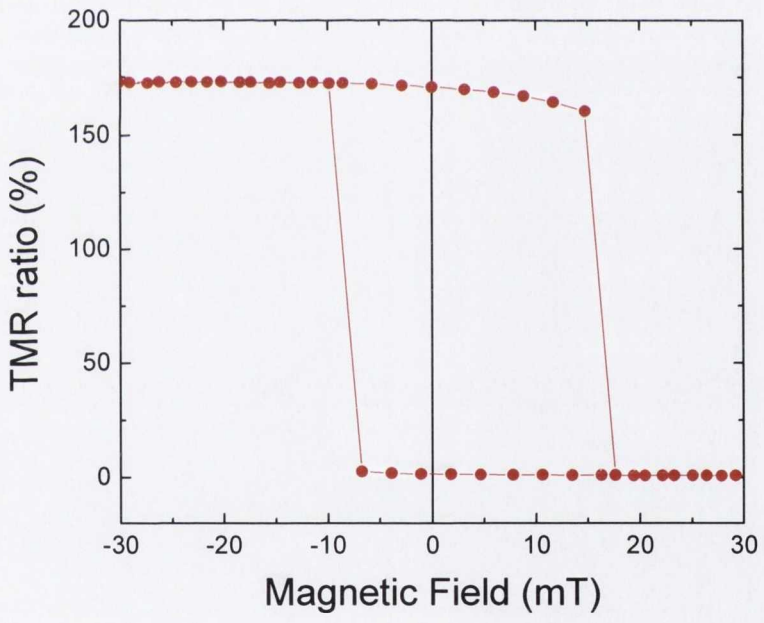

Figure 6. 4. Magneto-resistance curve in low field range for a low RA nano-MTJ showing ~ 175 % TMR ratio at RT.

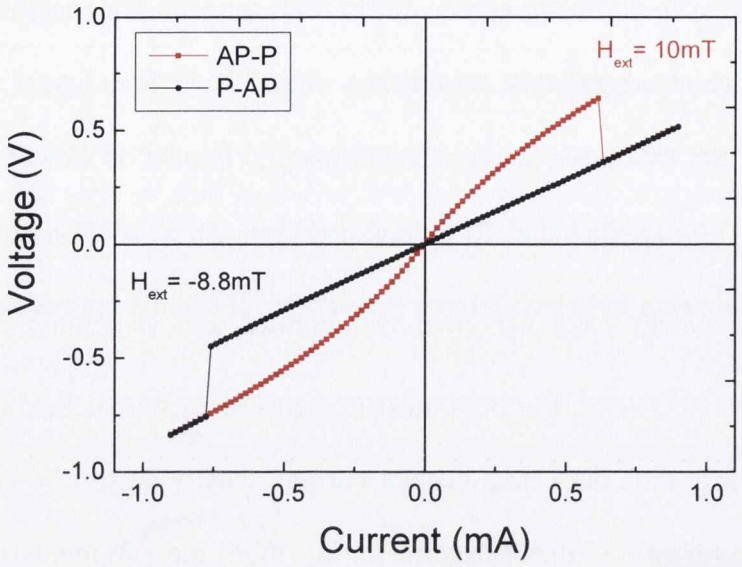

Figure 6. 5. DC voltage vs. current sweep of a nano-MTJ at parallel (red) and anti-parallel (black) states. Different fields applied at different for P and AP states to observe the spin transfer torque magnetisation switching.

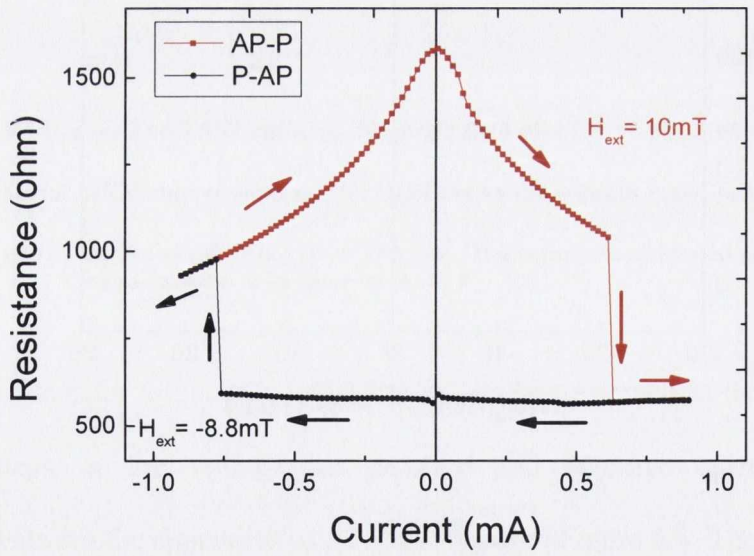

Figure 6. 6. Resistance vs. current measurement on nano-MTJ indicating sharp drops in resistance at positive and negative currents which are due to STS.

Single barrier nano-MTJs with lower annealing temperature and duration are prepared to measure STS when the dipolar coupling is completely cancelled. The lower temperature and duration reduces the crystallization of CoFeB, hence the saturation magnetisation. Therefore, a lower critical current density is expected. The magneto-resistance curve of such a device is shown in Figure 6.7. The annealing temperature is reduced to 325 ^{o}C and annealing time is only 30 mins which is enough to obtain high TMR ratio. This sample shows > 120 % TMR and the RA is ~ 43 $\Omega\mu m^2$.

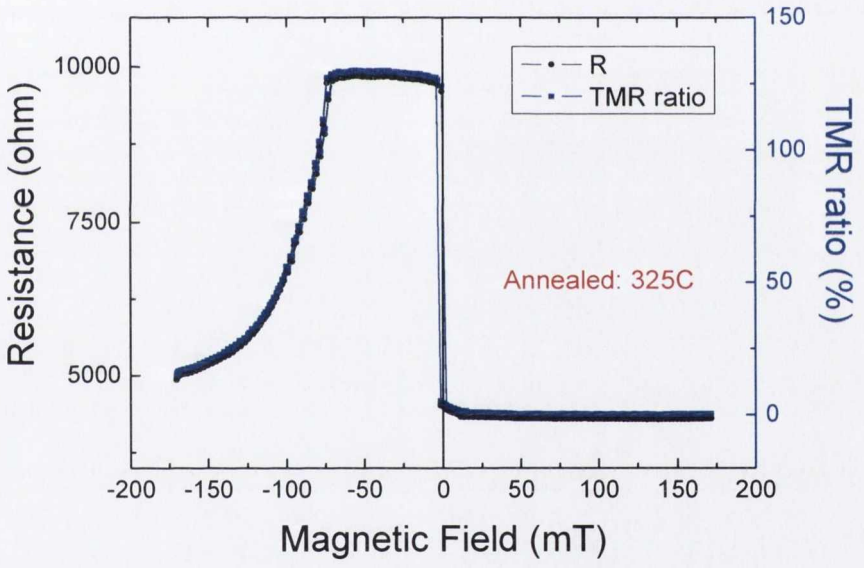

Figure 6. 7. Resistance and TMR ratio vs. magnetic field graphs of an annealed nano-MTJ with RA value of ~ 40 $\Omega\mu m^2$. The size of the nanopillar is 80 × 120 nm^2.

The minor loop of magneto-resistance and the current vs. resistance curves of this device is shown in Figure 6.8 (a) and (b), respectively. A small negative shift (0.8 mT) of the free layer loop is observed in Figure 6.8a due to the orange peel

coupling resulting from the roughness of the underlayers. The coercivity of the free layer is around 1.8 mT which is significantly smaller than the sample annealed at 360 °C. The sharp changes in Figure 6.8a indicate that the device behaves like a single domain particle. The R-I loop of the same device is illustrated in Figure 6.8b, where an external magnetic field of – 0.8 mT is applied during the measurement to cancel the loop shift.

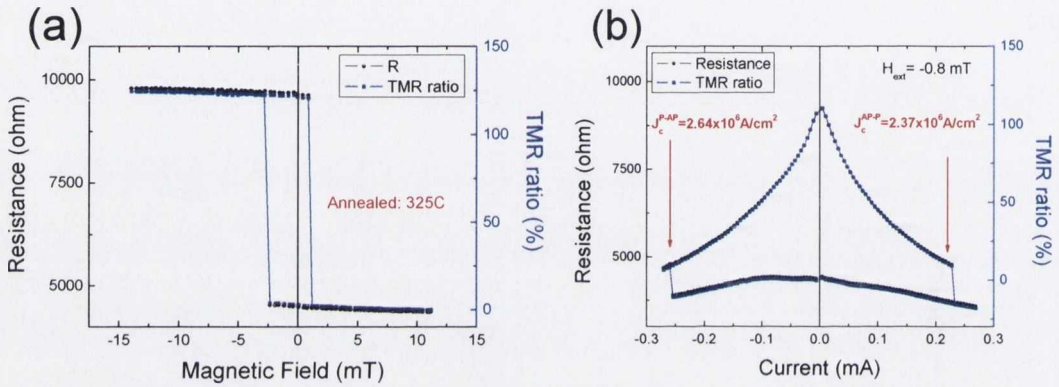

Figure 6. 8. (a) Magneto-resistance curve of a nano-MTJ showing the zero field range. Small shift of the free layer loop is observed due to coupling between free and pinned layers. (b) Resistance and TMR ratio vs. current measurements with an external applied field of - 0.8 mT. Sample is annealed at 325 °C for 30 mins. TMR ratio is > 120 %.

Two abrupt changes in resistance are observed at around + 0.23 mA (I_C^{AP-P}) and – 0.26 mA (I_C^{P-AP}). The corresponding critical current densities are found to be $J_C^{AP-P} = 2.37 \times 10^6$ A/cm^2 and $J_C^{P-AP} = 2.64 \times 10^6$ A/cm^2. The average switching current density , $J_C = \frac{J_C^{AP-P} + J_C^{P-AP}}{2}$, in this sample is 2.5×10^6 A/cm^2 which is slightly lower than for conventionally-processed MgO MTJs because annealing

temperature is 325 °C and annealing time is 30 mins. The TMR ratio from the current curve is very similar to the one obtained from the *R-H* curve which indicates that the magnetisation of the free layer is almost completely reversed by current injection.

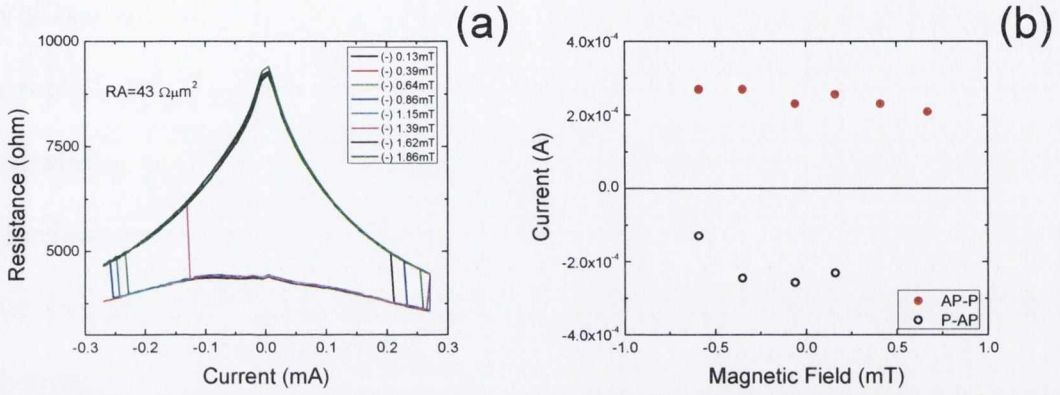

Figure 6. 9. (a) The effect of external magnetic field on the DC current switching of an annealed single barrier MTJ. (b) The change in the switching current vs. nominal magnetic field (H_{ext} - H_{shift}).

The external magnetic field has an important effect on the switching current. Therefore, we investigated it on our devices and it is shown in Figure 6.9. In Figure 6.9a, DC R-I loops are shown for different external magnetic fields. The nominal field felt by the free layer is $H = H_{ext} - H_{shift}$. Switching current vs. nominal field is plotted in Figure 6.9b. As the nominal field increases, I_C^{AP-P} decreases because positive field stabilizes the P state as can be seen in Figure 6.8a. The opposite is observed for I_C^{P-AP}. For large positive and negative nominal fields, switching is not possible because the field enforces only one stable state.

Since a reduced critical current density for low annealing temperatures is observed, we investigated the effect of annealing temperature on the switching current. We annealed different single barrier MTJ devices with the same size and stack for 30 mins under vacuum. The change in the critical current is shown in Figure 6.10. For low annealing temperatures (< 350 °C), J_c is quite low and it is below 2 × 10^6 A/cm^2. As the annealing temperature goes above 350 °C, there is a dramatic increase in the critical current density which is due to the strong increase of the magnetisation of the CoFeB. The switching current density depends quadratically on the magnetisation of the free layer as discussed in Chapter I.

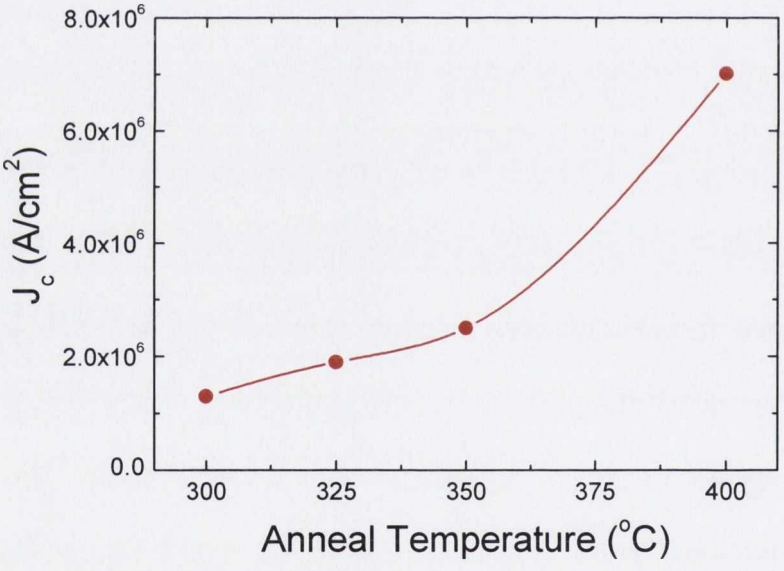

Figure 6. 10. The effect of annealing temperature on the critical current density of single barrier MTJs. Line is a guide to eye.

The effect of measurement time on the critical current density is significant as spin transfer torque magnetisation reversal is a thermally activated process for long

pulse widths (DC measurement is a pulse with infinite width) [4]. Upon varying the current pulse widths, three distinct switching modes is found: thermal activation, dynamic reversal and precessional switching [4]. Different switching modes are shown in Figure 6.11. For a long current pulse (> 50 ns), the magnetisation switching is a thermally activated process. The most interesting switching mode is the dynamic reversal at intermediate current pulses (1 – 50 ns) which corresponds to the operating speed of practical STT-RAM, it is found that the magnetisation reversal is determined both by the initial thermal distribution and the thermal agitation during the switching process. The dynamic reversal is a combination of precessional and thermally activated switching in the nanosecond regime. With a very short current pulse (< 1 ns), the magnetisation switching is mainly dependent on the initial thermal distribution [4]. Therefore, it is essential to understand the effect of measurement time on the switching current. To observe this effect, we used the pulsed current measurements where we changed the pulse width from 1 ms to 1 s.

It is also possible to extract information about the thermal stability (Δ) of nanopillar from these measurements because the current density is given by

$$J_c = J_{c0}\{1 - \frac{1}{\Delta}\ln(\tau / \tau_0)\} \tag{6.1}$$

where τ is the pulse width in seconds, τ_0 is the relaxation time of the free layer magnetisation in seconds (~ 1 ns), and $\Delta = \frac{KV}{k_B T}$ is the thermal stability constant (K is the anisotropy constant, V is the free layer volume, k_B is the Boltzmann's constant and T is the temperature) [5].

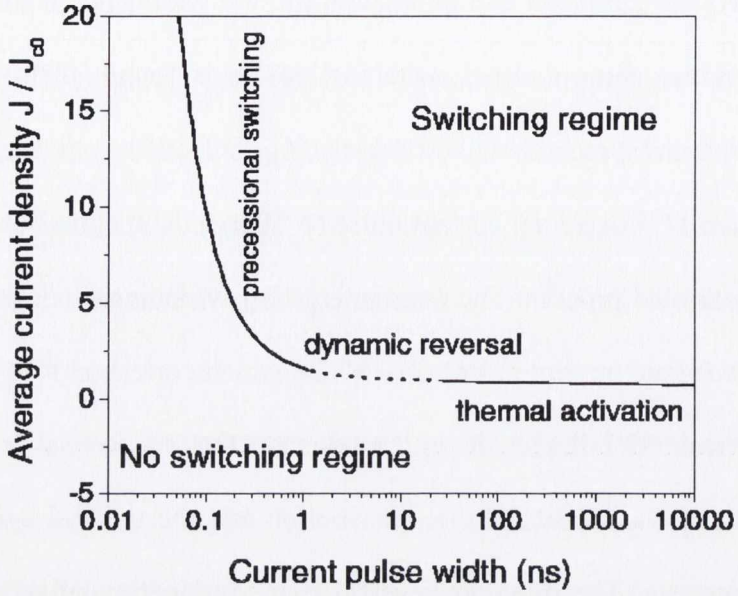

Figure 6. 11. Spin current driven magnetisation switching phase diagram. The three switching modes are thermal activation (solid line), dynamic reversal (dotted line) and precessional switching (thick solid line) [4].

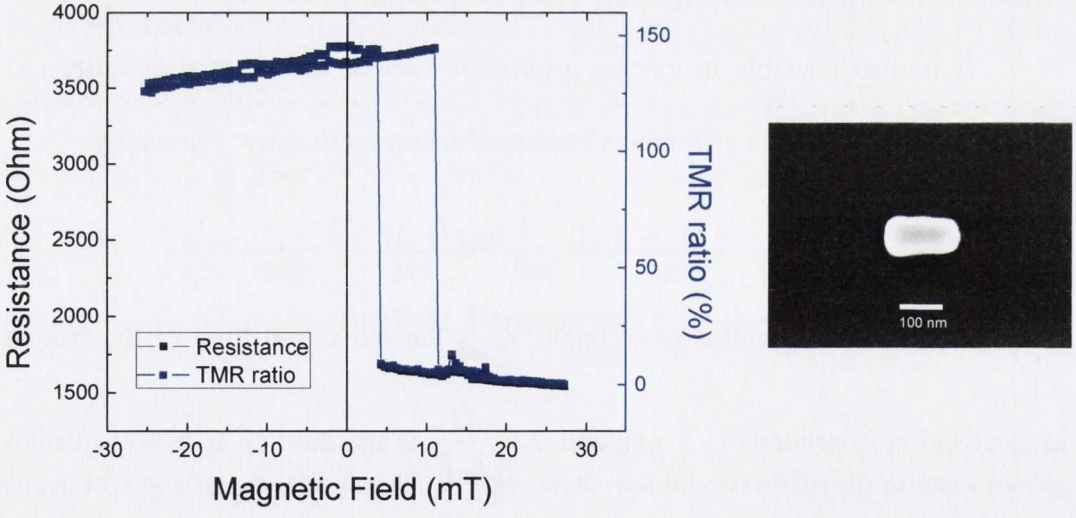

Figure 6. 12. Minor loop of resistance and TMR ratio for a single MTJ with a 2 nm thick free layer annealed at 325 °C for 30 mins. The shift of the loop is due to dipolar coupling. Size of the resist pillar is ~ 90 × 180 nm^2, shown on the right. RA of this device is ~ 24 Ωμm^2.

The magnetoresistance and TMR ratio of a single barrier MTJ device used for pulsed measurements are shown in Figure 6.12. The TMR ratio of this device is around 150 % and RA is ~ 24 $\Omega\mu m^2$ with a size of 90 × 180 nm^2. The larger loop shift (7.5 mT) due to dipolar coupling observed for this device is probably due to long ion milling during patterning. The R-I loop of the device is measured by a 1 s pulse width with an external field of + 6.4 mT and is shown in Figure 6.13. Two abrupt changes in resistance are observed at around + 0.31 mA (I_C^{AP-P}) and – 0.35 mA (I_C^{P-AP}). J_c of this device at 1 s pulse width is calculated to be 2.3 × 10^6 A/cm^2.

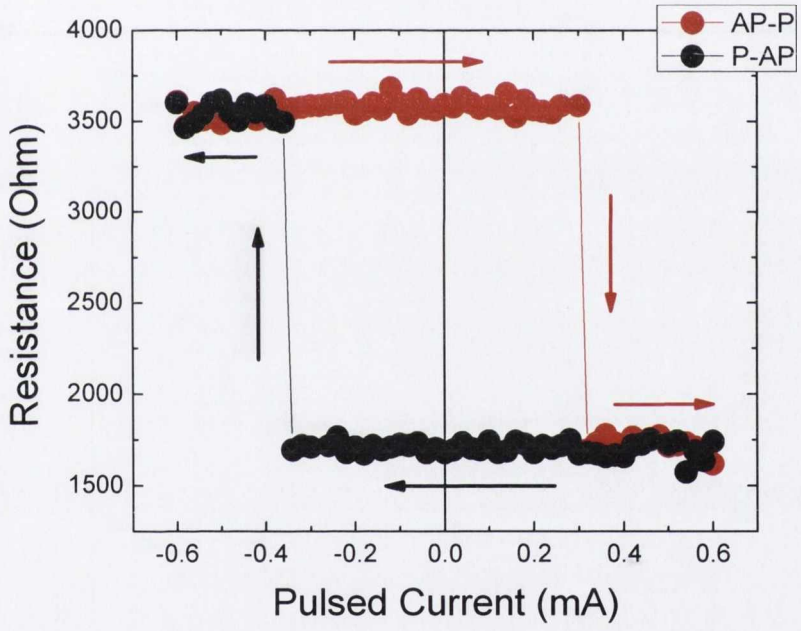

Figure 6. 13. Resistance vs. pulsed current curve of single barrier MTJ. Pulse width is 1 s. Arrows show the sweep directions.

The J_c vs. ln (τ/τ_o) graph is obtained from pulsed measurements by changing the pulse width. Four different pulse widths are used and these are 1, 10, 100 and

1000 ms. The graph is shown in Figure 6.14. It is possible to estimate the intrinsic critical current density (J_{c0}) and the thermal stability constant (Δ) from these measurements using equation 6.1. Intersection of linear fit to y-axis gives the J_{c0} and the slope of the line is equal to $\frac{J_{c0}}{\Delta}$. J_{C0}^{AP-P} is found to be 3.6 × 10^6 A/cm^2 and J_{C0}^{P-AP} is found to be 5 × 10^6 A/cm^2. The thermal stability constant of this device is around 50 and it is sufficient enough to store the information for > 10 years. The operating temperature of the device will determine the minimum thermal stability constant that is required. However, the errors in these extrapolations are fairly large (percentage error in the slope is found to be > 50 %).

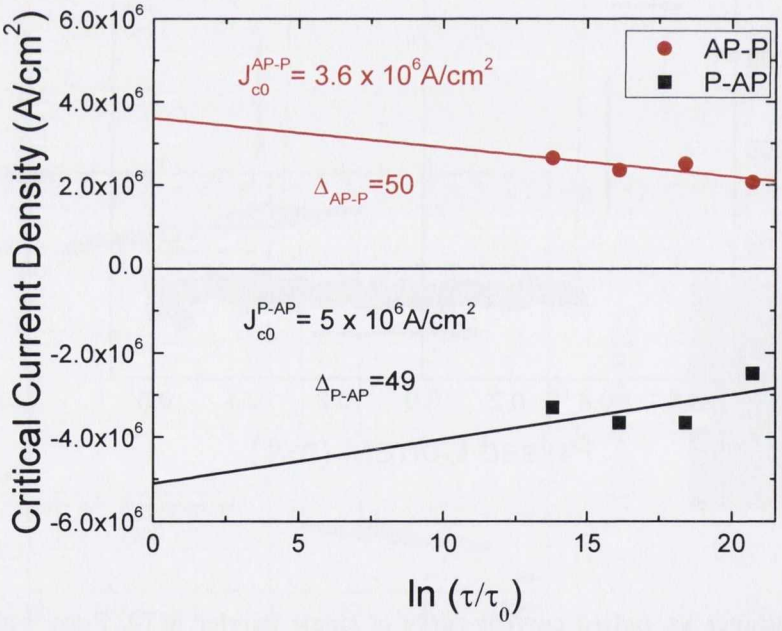

Figure 6. 14. The J_c vs. ln (τ/τ_0) measurement for a single barrier MTJ. All the measurements are done at RT.

6.1.1. Effect of reducing the saturation magnetisation of the free layer

Our primary aim is to reduce the critical current density required for spin transfer torque magnetisation reversal. Therefore, we first investigated the effect of reducing magnetisation of free layer. CoFeB is a very promising material for MgO MTJs and spin transfer torque. It is amorphous and it crystallizes into required phase after annealing. We looked at different alloys systems, similar to CoFeB to reduce the saturation magnetisation of the free layer. These alloys are $Co_{40}Fe_{40-x}Cr_xB_{20}$, $Co_{40}Fe_{40-x}Ni_xB_{20}$, and $Co_{40}Ni_{40-x}Cr_xB_{20}$ and their magnetic properties were presented in Chapter V. All of these alloys are amorphous in the as-grown state. $Co_{40}Fe_{40-x}Cr_xB_{20}$ is the best in terms of reducing the saturation magnetisation. Therefore, we chose $Co_{40}Fe_{40-x}Cr_xB_{20}$ as a low magnetisation free layer. It is very important to keep the TMR ratio high while reducing the saturation magnetisation of the free layer.

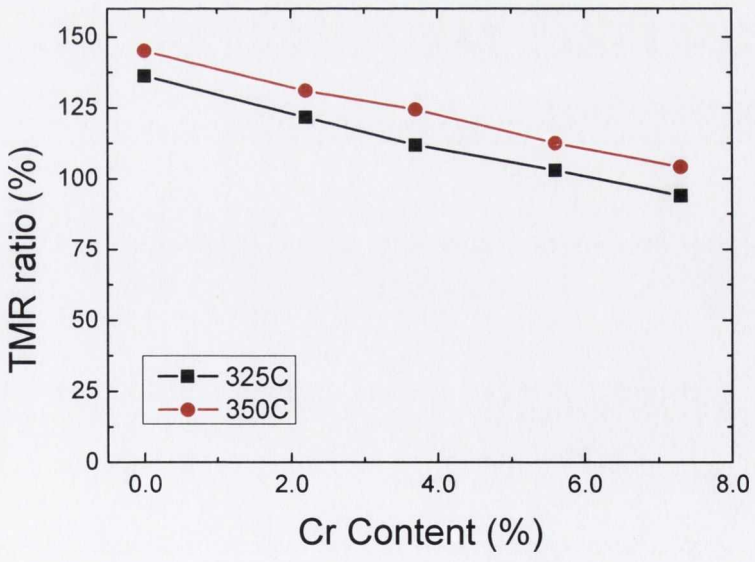

Figure 6. 15. Effect of Cr content on the TMR ratio of MTJs with CoFeCrB free layer. Different annealing temperatures are shown.

The effect of Cr content on the TMR ratio in nano-MTJs with $Co_{40}Fe_{40-x}Cr_xB_{20}$ (2.5 nm) free layer is shown in Figure 6.15. A monotonic decrease in TMR ratio is observed for both of the annealing temperatures. The TMR ratio starts with ~ 150 % for x = 0 and reduces to ~ 100 % for x = 7.5 %. The reduction in the TMR ratio can be explained by a reduction in the tunnelling spin polarization in the MTJ with increasing Cr content.

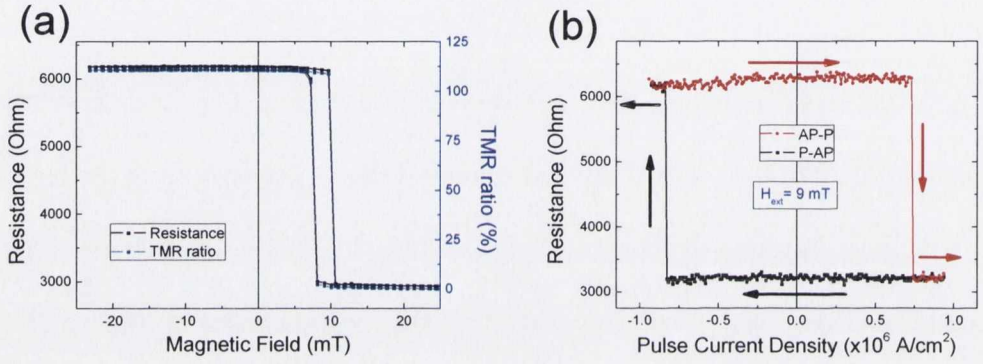

Figure 6. 16. (a) Minor loop of resistance and TMR ratio curves and (b) Pulsed R-J loop of a nano-MTJ with CoFeCrB free layer with 5 % Cr insertion. Pulse width was 1 s during the measurement. Nanopillar size is 80 × 160 nm^2.

Typical magnetoresistance curves of a nano-MTJ with $Co_{40}Fe_{40-x}Cr_xB_{20}$ free layer with x = 5 is shown in Figure 6.16a. The TMR ratio of the device is ~ 110 % and the free layer loop is shifted due dipolar coupling. The shift is + 3.4 mT. Pulsed *R-J* loop of the same device is illustrated in Figure 6.16b. Two distinct changes in resistance are observed around + 7.4 × 10^5 A/cm^2 (J_C^{AP-P}) and – 8.4 x 10^5 A/cm^2 (J_C^{P-AP}). J_c is 7.9 × 10^5 A/cm^2.

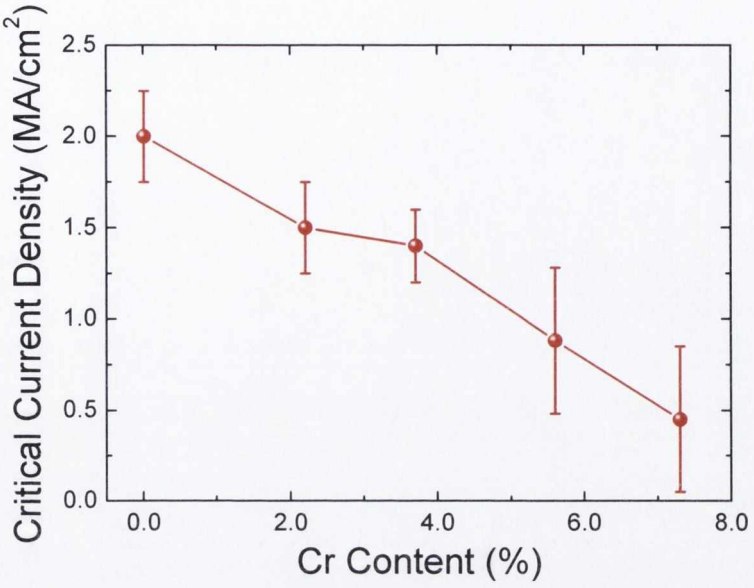

Figure 6. 17. The effect of Cr content on the J_c for the nano-MTJs with $Co_{40}Fe_{40-x}Cr_xB_{20}$ free layer.

As the Cr concentration is increased, the critical current density is progressively reduced as shown in Figure 6.17 for devices annealed at 325 °C for 30 mins. For x = 0, J_c is around 2 × 10^6 A/cm^2 and it falls linearly with increasing Cr insertion. The lowest value of J_c, 5 × 10^5 A/cm^2 is found when x = 7.5. A similar effect is observed by Kubota *et al.* on $(Co_{75}Fe_{25})_{80-x}Cr_xB_{20}$ [6]. They replaced (CoFe) in CoFeB with Cr and reported a decrease of J_{c0} by a factor 2 for 10 % Cr. We observed a reduction in J_c by a factor of 4 for 7.5 % Cr due to the decrease in the saturation magnetisation (M_s) of $Co_{40}Fe_{40-x}Cr_xB_{20}$ free layer which was discussed in Chapter V. It is important to note that the coercivity of the device is also decreased as the Cr content increases. Therefore, it is not possible to use this material with high Cr concentration (> 10 %) for spin transfer torque devices due to the lack of bi-stable state.

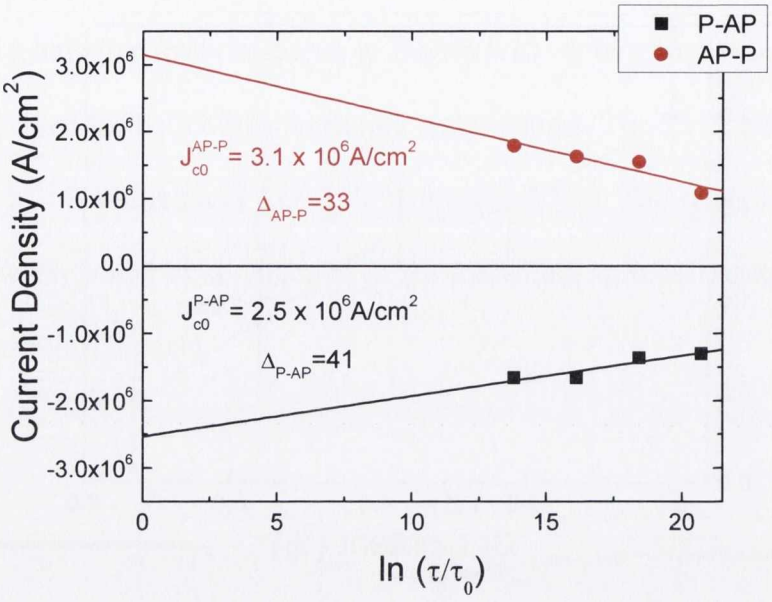

Figure 6. 18. J_c vs. ln (τ/τ_0) for an MTJ with CoFeCrB free layer which has 4 % Cr insertion. Pulse width is varied between 1 ms and 1 s. Sample was annealed at 325 °C for 30 mins. Measurements are performed at RT.

The thermal stability constant (Δ) of these devices is affected because Δ depends on the anisotropy constant (K) and $K = \frac{\mu_0 H_k M_s}{2}$. Hence, if you decrease M_s while maintaining H_k, the K and Δ decrease at the same time. We observed similar behaviour in our devices. J_c vs. ln (τ/τ_0) for an MTJ with CoFeCrB free layer which has 4 % Cr insertion is shown in Figure 6.18. The average thermal stability constant ($\Delta_{av} = \frac{\Delta_{AP-P} + \Delta_{P-AP}}{2}$) is calculated to be 37, which is smaller than the ordinary single barrier MTJ with CoFeB free layer which had Δ_{av} = 50. Even though, Δ is smaller in these devices, it is still high enough sustain information for > 10

years. Furthermore, it can be improved by annealing at higher temperatures or using a synthetic antiferromagnetic free layer.

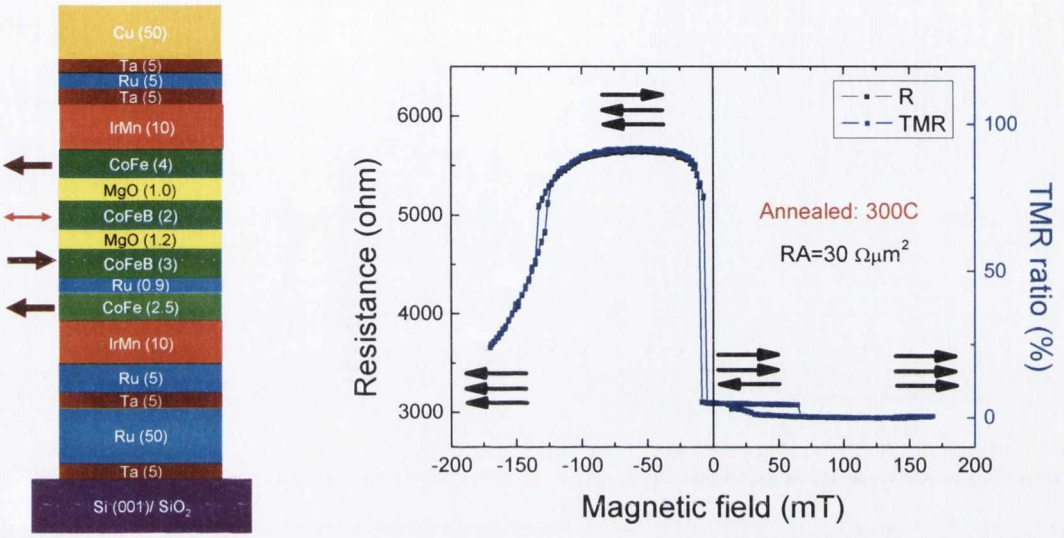

Figure 6. 19. Schematic of the dual barrier MTJ stack and the resistance and TMR ratio vs. magnetic field plot of a nanopillar with the same stack. TMR ratio is around 90 % and RA is ~ 30 Ωμm^2. Arrows indicated the direction of magnetisations of free and pinned layers.

6.2. STS in dual barrier MTJs

Our second approach in reducing the J_c is to increase the spin transfer efficiency term, η. Dual barrier MTJs are predicted to reduce the J_c by a factor of six due to spin transfer efficiency enhancement [7]. The device consists of three ferromagnetic electrodes (2 pinned, 1 free) separated by two tunnel barriers and the two pinned layers are antiparallel (shown in Figure 6.19) and both of the interfaces of the free layer actively generate spin torque. In this type of device, it is important that

the two MgO barrier layers have different thickness (RA); otherwise it is not possible to observe TMR because the resistance change will be zero when the free layer switches direction.

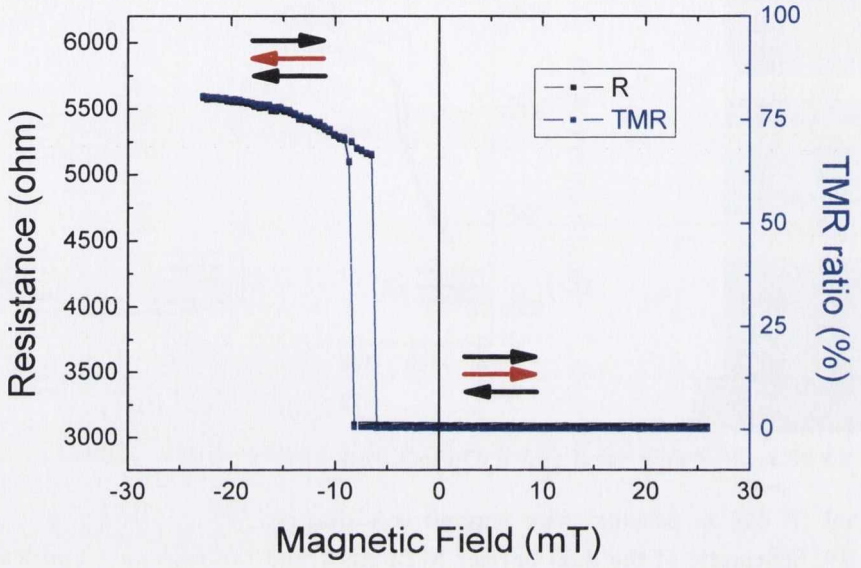

Figure 6. 20. Resistance and TMR ratio minor loop for a dual barrier MTJ nanopillar. Strong coupling (- 7.4 mT) from top pinning layer shifts the free layer loop towards negative field.

Resistance and TMR ratio vs. magnetic field curve of such a device is shown in Figure 6.19. The magnetisation directions of free and pinned layers are shown with black arrows. Four possible alignments with three resistance states are observed in the graph. The lower MgO barrier is designed to be thicker and the RA is dominated by its resistance. For this particular device, TMR ratio is around 90 % and RA is 30 $\Omega\mu m^2$. The sample is annealed at 300 ^{o}C for 30 min and the designed device size is 68 × 160 nm^2.

Figure 6.20 shows the minor loop of the magneto-resistance curves for the same device. The free layer shows a coercivity of 1.1 mT, and the loop is shifted – 7.4 mT due to the strong coupling from the top pinning layer which had to be completely milled during patterning. The TMR ratio at this field region is around 75 % because the bottom part of the MTJ stays in antiparallel orientation as indicated in Figure 6.20. The TMR ratio is similar to what is reported in literature [8].

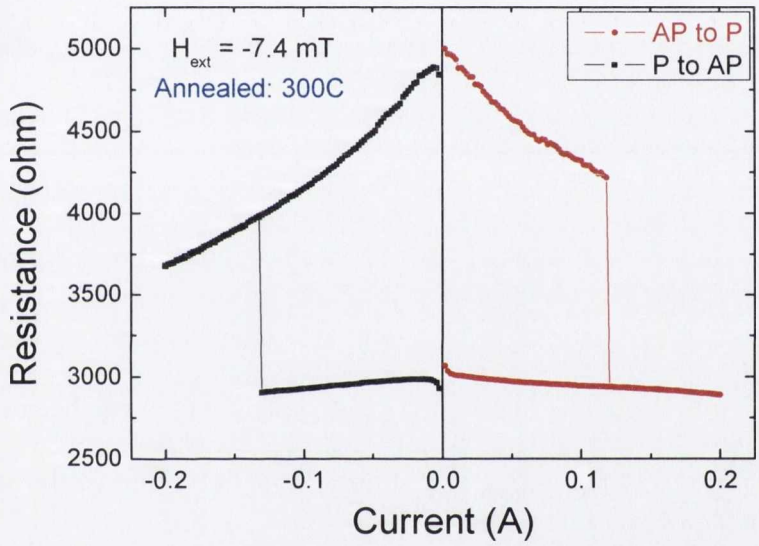

Figure 6. 21. DC resistance vs. current graphs of a dual barrier MTJ nanopillar for P and AP states. Sharp changes in resistance for positive and negative current are due to STS. The sample was annealed at 300 °C for 30 mins. Sample size is 68 × 160 nm^2.

The DC *R-I* loop of the dual MTJ is shown in Figure 6.21 when an external field of -7.4 mT is applied. Abrupt resistance changes are observed around + 0.12 mA (I_C^{AP-P}) and – 0.13 mA (I_C^{P-AP}).The room-temperature switching current density J_c is calculated from I_c to be 4.6 × 10^5 A/cm^2. This value is slightly lower than the

value reported by Diao *et al.* which is 5.2×10^5 A/cm^2 [8]. The improved value in our measurement might be due to higher TMR ratio and low annealing temperature (300 °C) in our device. It is expected that J_c can be further reduced by the use of a low-moment free layer.

6.3. STS in MTJs with SAF free layer

It is critical to maintain high thermal stability while reducing the J_c. It is possible to realize this by utilizing a synthetic antiferromagnetic / ferromagnetic / ferrimagnetic free layer in MTJ stack. A synthetic magnet is composed of two ferromagnets separated by a ruthenium (Ru) layer. Depending on the thickness of the Ru layer coupling can be ferromagnetic or antiferromagnetic and this is referred as oscillatory interlayer exchange coupling [9]. This type of MTJs has been reported to have high thermal stability compared to ordinary MTJs with almost the same/lower J_c [5, 10-13]. J_c is reduced due to the decreased effective volume under the large spin accumulation at the CoFeB/Ru interface [5].

We have fabricated MTJs with a synthetic antiferromagnetic free layer where the top and bottom CoFeB is 1.8 nm and Ru is 0.9 nm as shown in Figure 6.22. Ru 0.9 nm is found to give the highest antiferromagnetic indirect exchange coupling from our previous experiments. This device has a TMR ratio of > 120 % and the RA is 10 Ωμm^2. This particular sample was annealed at 360 °C. The magnetoresistance curves are shown in Figure 6.22. A small shift (5.4 mT) of free layer loop is observed. The nominal device size is 100×208 nm^2.

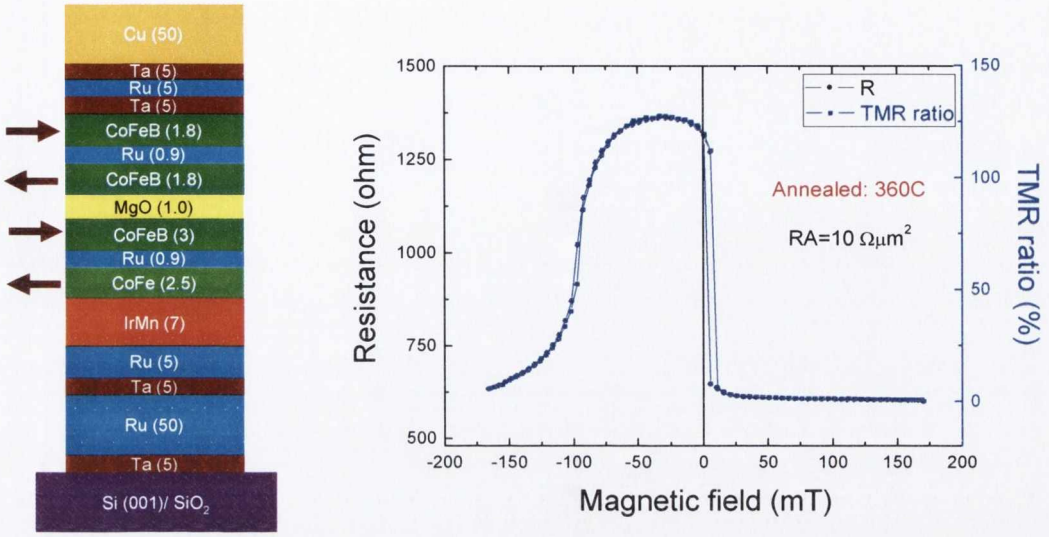

Figure 6. 22. Schematic of an MTJ with a SAF free layer. The resistance and TMR ratio vs. magnetic field plot of a nanopillar with SAF free layer is shown on the right. This sample is annealed at 360 °C for 1.5 hours and RA is ~ 10 Ωμm^2. The size of the nanopillar is 100 × 208 nm^2 (data courtesy Dr. Gen Feng).

The DC *R-I* loop of this nano-MTJ is shown in Figure 6.23 when the external field of 5.4 mT is applied. Abrupt resistance changes are observed around + 0.25 mA (I_C^{AP-P}) and – 0.28 mA (I_C^{P-AP}). The room-temperature switching current density J_c is calculated from I_c to be 1.3 × 10^6 A/cm^2. This value is 2-3 times lower than single barrier MTJs with a 2 nm free layer as also shown by several other groups.

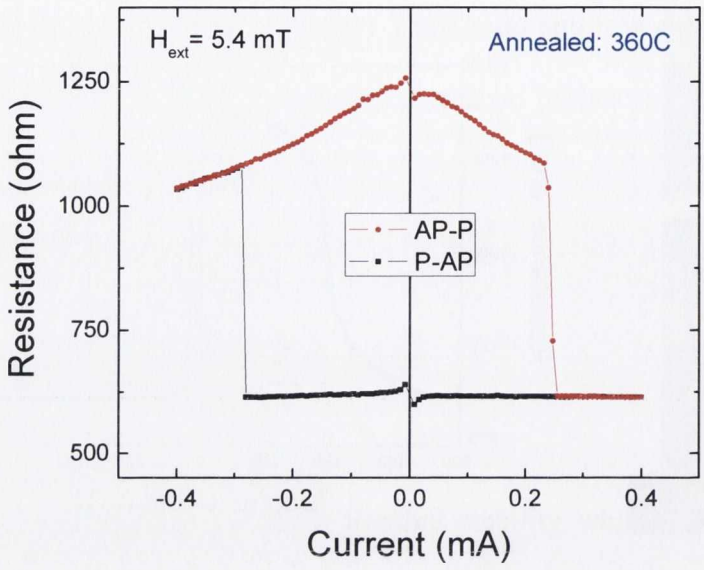

Figure 6. 23. DC resistance vs. current graphs of a MTJ nanopillar with a SAF free layer for P and AP states. Abrupt changes in resistance for positive and negative currents are due to current switching (data courtesy Dr. Gen Feng).

6.4. Repeated switching measurements

Endurance and critical current distribution are important parameters for the application of spin transfer magnetisation switching in possible memory technologies. Therefore, we investigated the effect of consecutive switching events on the switching current distribution, switching probability, resistance and TMR ratio.

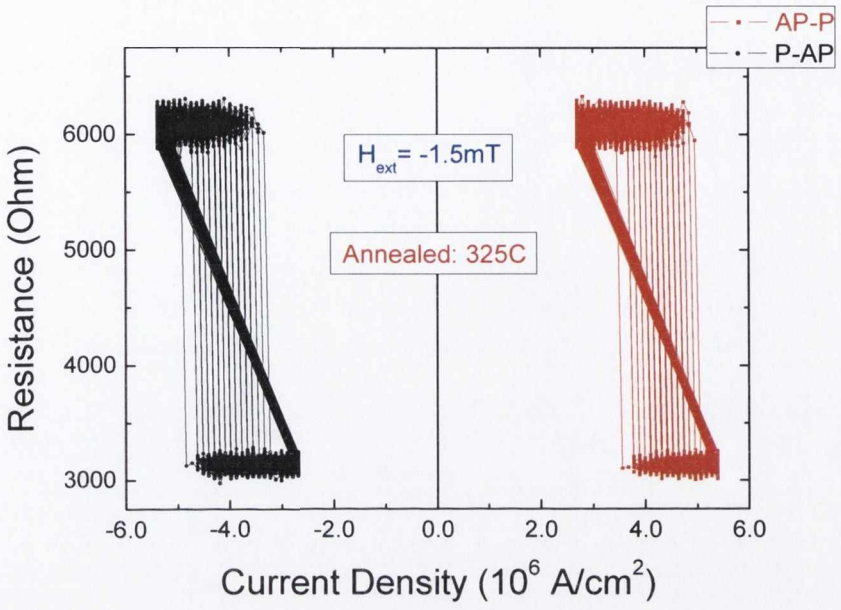

Figure 6. 24. Resistance vs. current density measurements on a dual barrier nano-MTJ. Measurement is repeated for 500 times for both P and AP states. Nominal device size is 60 × 155 nm^2.

Repeated R-J loops for a dual barrier MTJ is shown in Figure 6.24. 500 consecutive measurements are obtained using 1 ms current pulses. The current is swept with 10 μA resolution. Therefore, switching occurs at discrete current values which are defined by the current increment. Only a small range of positive and negative current values are scanned to prevent junction from overheating. The TMR ratio of this sample is > 100 % and RA is 30 Ωμm^2. Nominal size of the device is 60 × 155 nm^2. The resistance in P and AP states and the TMR ratio of the device remained unchanged during these measurements which indicate the reliability of the MgO tunnel barrier. On the other hand, it is found that the critical current density varied significantly during the course of the measurement. This distribution is shown in Figure 6.25 for AP-P and P-AP switching events. Both of the distributions can be

fit by Gaussian distribution function with the peak positions at 4.35 × 10^6 A/cm^2 and -4.24 × 10^6 A/cm^2 for AP-P and P-AP switchings, respectively. FWHM of the peaks are 7.1 × 10^5 for AP-P and 6.4 × 10^5 for P-AP switchings.

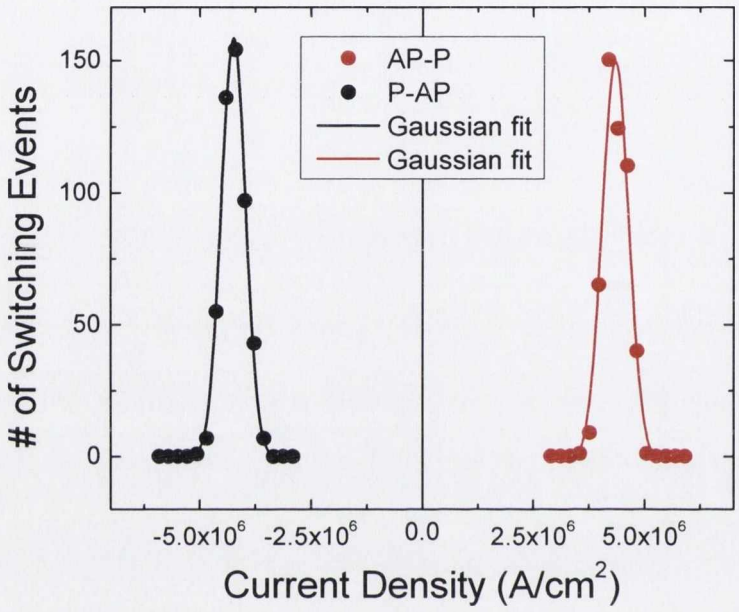

Figure 6. 25. Number of switching events vs. current density for a dual barrier nano-MTJ. Distributions fit well to Gaussian distrubution.

Switching probability is calculated from the switching current distributions and plotted in Figure 6.26. Probability is 0 below 3.5 × 10^6 A/cm^2 for both AP-P and P-AP events and rapidly increases above this value. It reaches 100 % around 5 × 10^6 A/cm^2 for both switching events. It is very useful to analyze the probability to decide what current value should be used to read / write the information in a memory device. It also determines the margin for read and write current values.

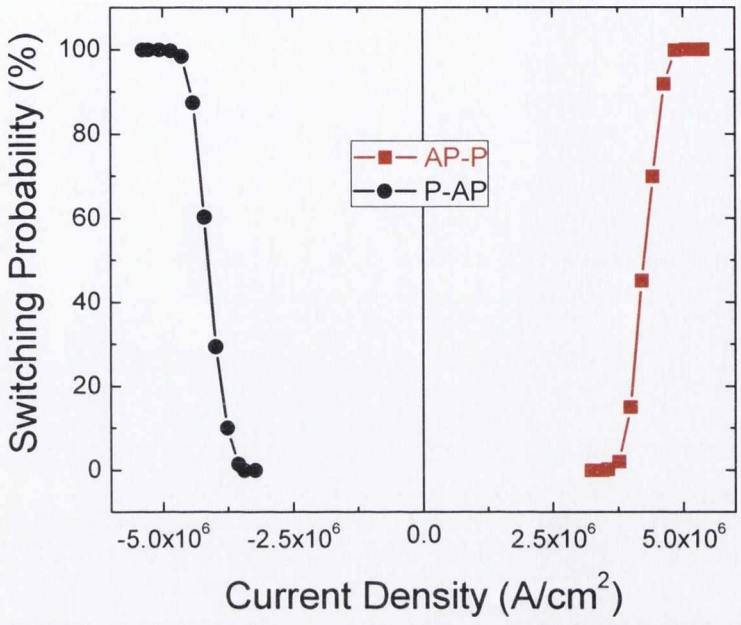

Figure 6. 26. Switching probability of a dual barrier nano-MTJ obtained from switching distributions.

6.5. Conclusions

In conclusion, we demonstrated the spin transfer torque magnetisation reversal in three different MgO-based magnetic tunnel junction devices, namely single barrier MTJ, dual barrier MTJ and MTJ with SAF free layer. We reduced the critical current density in single barrier MTJs to 5×10^5 A/cm^2 using CoFeCrB free layer. The effect of using dual barrier stack was shown to reduce the current density by a factor of 3 due to increase in the torque efficiency. We also demonstrated the reduction of current density in MTJs with SAF free layer. The effect of consecutive switchings is found to be minimal on resistance and TMR ratio of our devices.

6.6. References

1. Kubota, H., *et al.*, *"Evaluation of Spin-Transfer Switching in CoFeB/MgO/CoFeB Magnetic Tunnel Junctions"*, Japanese Journal of Applied Physics. **44**, L1237, (2005).
2. Diao, Z., *et al.*, *"Spin transfer switching and spin polarization in magnetic tunnel junctions with MgO and AlO_x barriers"*, Applied Physics Letters. **87**, 232502, (2005).
3. Fukumoto, Y. and A. Kamijo, *"Effect of Milling Depth of the Junction Pattern on Magnetic Properties and Yields in Magnetic Tunnel Junctions"*, Japanese Journal of Applied Physics. **41**, L183, (2002).
4. Diao, Z. and et al., *"Spin-transfer torque switching in magnetic tunnel junctions and spin-transfer torque random access memory"*, Journal of Physics: Condensed Matter. **19**, 165209, (2007).
5. Hayakawa, J., *et al.*, *"Current-Induced Magnetisation Switching in MgO Barrier Magnetic Tunnel Junctions With CoFeB-Based Synthetic Ferrimagnetic Free Layers"*, Magnetics, IEEE Transactions on. **44**, 1962, (2008).
6. Kubota, H., *et al.*, *"Reduction in switching current using a low-saturation magnetisation Co-Fe-(Cr, V)-B free layer in MgO-based magnetic tunnel junctions"*, Journal of Applied Physics. **105**, 07D117, (2009).
7. Berger, L., *"Multilayer configuration for experiments of spin precession induced by a dc current"*, Journal of Applied Physics. **93**, 7693, (2003).

8. Diao, Z., *et al.*, *"Spin transfer switching in dual MgO magnetic tunnel junctions"*, Applied Physics Letters. **90**, 132508, (2007).

9. Bloemen, P.J.H., *et al.*, *"Oscillatory interlayer exchange coupling in Co/Ru multilayers and bilayers"*, Physical Review B. **50**, 13505, (1994).

10. Hayakawa, J., *et al.*, *"Current-Induced Magnetisation Switching in MgO Barrier Based Magnetic Tunnel Junctions with CoFeB/Ru/CoFeB Synthetic Ferrimagnetic Free Layer"*, Japanese Journal of Applied Physics. **45**, L1057, (2006).

11. Yakata, S., *et al.*, *"Thermal stability and spin-transfer switchings in MgO-based magnetic tunnel junctions with ferromagnetically and antiferromagnetically coupled synthetic free layers"*, Applied Physics Letters. **95**, 242504, (2009).

12. Yakata, S., *et al.*, *"Enhancement of Thermal Stability Using Ferromagnetically Coupled Synthetic Free Layers in MgO-Based Magnetic Tunnel Junctions"*, Magnetics, IEEE Transactions on. **46**, 2232, (2010).

13. Sugano, R., *et al.*, *"Effect of Interlayer Coupling of Synthetic Ferrimagnetic Free Layer on Current Induced Magnetisation Switching in MTJs"*, Magnetics, IEEE Transactions on. **46**, 2136, (2010).

Chapter 7

Conclusions and Future Work

7.1. Conclusions

We can reproducibly grow MgO barrier magnetic tunnel junctions (MTJ) with excellent tunnelling magnetoresistance and low RA product in the Shamrock sputtering system. Our group was the first in Europe to achieve a high TMR > 200 % and even now there are fewer than ten laboratories in the world who can do this.

Novel MgO barriers have been produced by e-beam evaporation and they are comparable to those made by sputtering. MTJ with e-beam MgO showed TMR ratios > 200% and they exhibit considerably low noise. The process should be suitable for up-scaling the wafer-scale production.

Much effort was devoted to developing an e-beam process to produce the MgO nanopillars. The minimum size we can achieve with SEM exposure is 70 × 70 nm^2. Smaller sizes may require a dedicated e-beam lithography tool. The low yield, which was a big problem with the lift-off process, should be improved by implementing a chemical mechanical polishing (CMP) step.

The goal of reducing the critical current density below 10^6 A/cm^2 was successfully achieved by three different methods: The first one is using low moment free layers in single barrier MTJs, the second one is using dual barrier MTJs and the third one is the use of MTJs with a synthetic antiferromagnetic free layer. Of the three methods, first one was found to be the best. The use of low moment chromium substituted CoFeB alloy is novel and promises a low switching current density, $j_c = 5 \times 10^5$ A/cm^2.The new alloy is promising for in-plane STT-MRAM.

7.2. Future Work

The reduction in the current density for STS in MTJs with CoFeCrB free layer is mainly due to reduced M_s. But the change in the damping coefficient has to be investigated. It can be measured by ferromagnetic resonance (FMR) measurements. These measurements will be performed on the thin films of low moment alloy systems that are studied in this work. It will be possible to better quantify the effect of reduction in M_s after these radio frequency measurements and determine the damping coefficient.

Nanopillar fabrication using lift-off has been a low yield process which has to be improved to increase the reproducibility of the measurements. The chemical mechanical polishing (CMP) is an alternative method with high yield. Implementing CMP into nanopillar patterning process is essential for future work on nanopillars.

Spin torque related dynamics was not explored in this study. These measurements might give access to better understanding of spin transfer torque

related effects. Therefore, high frequency response of nanopillar devices will be also explored in the near future.

In this thesis, the focus has been on device structures with in-plane anisotropy ferromagnets. However, for future scalability, it seems that it will be necessary to realize similar devices with perpendicular anisotropy ferromagnets and lower critical current densities are predicted for STS in these systems. It is also possible to obtain high thermal stability constant for the same device size due to high anisotropy of these materials. Candidate systems are $L1_0$ alloys (FePt, CoPt and CoPd) and multilayer stacks based on Pd, Pt, and Ni (Co/Pt, CoFe/Pt, CoFe/Pd, Co/Ni and etc). But, it is difficult at present to combine these systems with MgO barrier and achieve high TMR ratio in MTJs. This will be achieved in future, and then these systems have to be thoroughly investigated to see how to employ them into magnetic tunnel junctions.

Publications

1. H. Kurt, K. Rode, K. Oguz, M. Boese, C.C. Faulkner, J.M.D. Coey, "*Boron Diffusion in Magnetic Tunnel Junctions with MgO (001) Barriers and CoFeB Electrodes*", Applied Physics Letters, **96**, 262501, (2010).
2. C. Fowley, N. Decorde, K. Oguz, K. Rode, H. Kurt, J.M.D. Coey, "*Perpendicular Magnetic Anisotropy in CoFeB/Pd Bi-layers*", IEEE Transactions on Magnetics, **46**, 2116, (2010).
3. H. Kurt, K. Oguz, T. Niizeki, J.M.D. Coey, "*Giant Tunneling Magnetoresistance with Electron Beam Evaporated MgO Barrier and CoFeB Electrodes*", Journal of Applied Physics, **107**, 083920, (2010).
4. P. Stamenov, K. Oguz, J. M. D. Coey, "*High-field Anisotropy of the Tunnelling Magnetoresistance of CoFeB/MgO/CoFeB Junctions*", Journal of Magnetism and Magnetic Materials, **322**, 1413, (2010).
5. Q.L. Ma, J.F. Feng, Gen Feng, K. Oguz, X.F. Han, J.M.D. Coey, "*Annealing Effect on Tunneling Magnetoresistance in MgO-based Magnetic Tunnel Junctions with FeMn Exchange-bias Layer*", Journal of Magnetism and Magnetic Materials, **322**, 108, (2010).
6. G. Szulczewski, H. Tokuc, K. Oguz, J.M.D. Coey, "*Magnetoresistance in Magnetic Tunnel Junctions with an Organic Barrier and an MgO Spin Filter*" Applied Physics Letters, **95**, 202506, (2009).

7. K. Oguz and J.M.D. Coey, *Room-temperature Magnetoresistance in CoFeB/STO/CoFeB Magnetic Tunnel Junctions*, Journal of Magnetism and Magnetic Materials, **321**, 1009, (2009).

8. K. Oguz, P. Jivrajka, M.Venkatesan, G. Feng, and J.M.D. Coey, "*Magnetic Dead Layers in Sputtered $Co_{40}Fe_{40}B_{20}$ Films*", Journal of Applied Physics, **103**, 07B526, (2008).

Appendix

Spin curves of the lithography resists

The spin curves for resists that are used for photo and e-beam lithography in this work are given in Figures A1, A2 and A3. S1813 G2 as a positive and AZ nLOF 2070 as negative photoresists are used in the photolithography processes. E-beam resist was TOK- TGMR EN103 PE negative resist and both of the viscosities were tested for the best performance. Low viscosity one is better in terms of resolution but lift-off is more difficult.

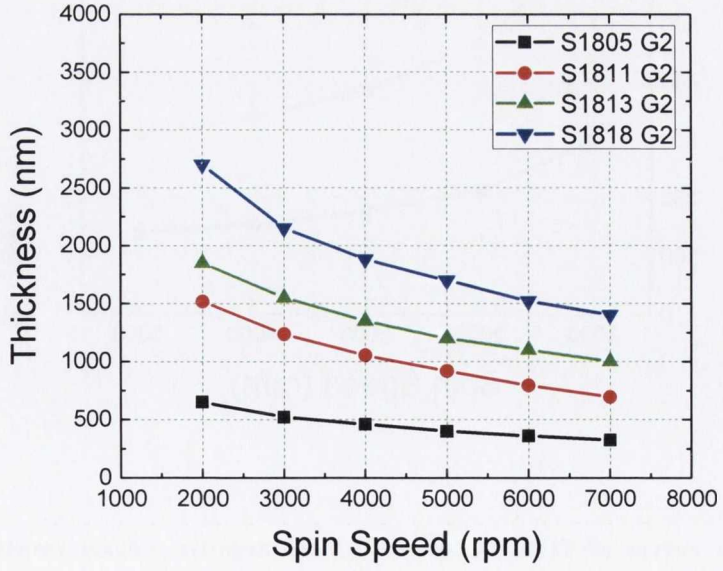

Figure A. 1. Spin curves of S1800 G2 series positive photoresists.

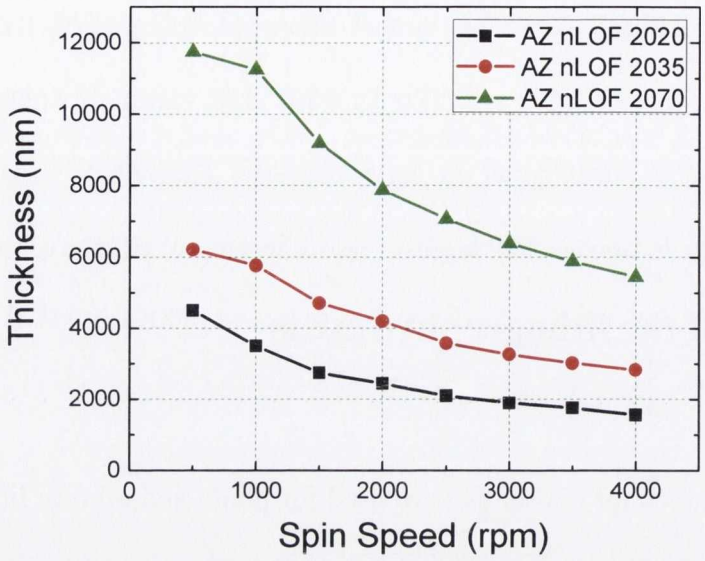

Figure A. 2. Spin curves of AZ nLOF series negative photoresists.

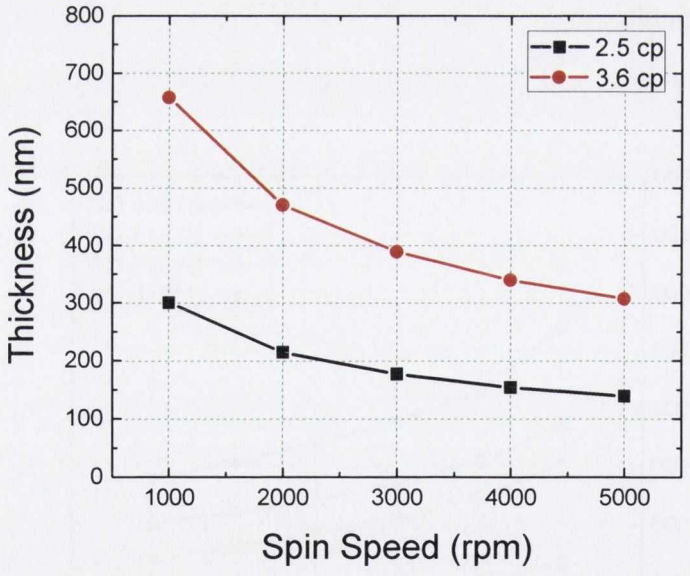

Figure A. 3. Spin curves of TOK TGMR-EN103 PE negative e-beam resists for different viscosities.